Argelander-Institut für Astronomie
Universität Bonn

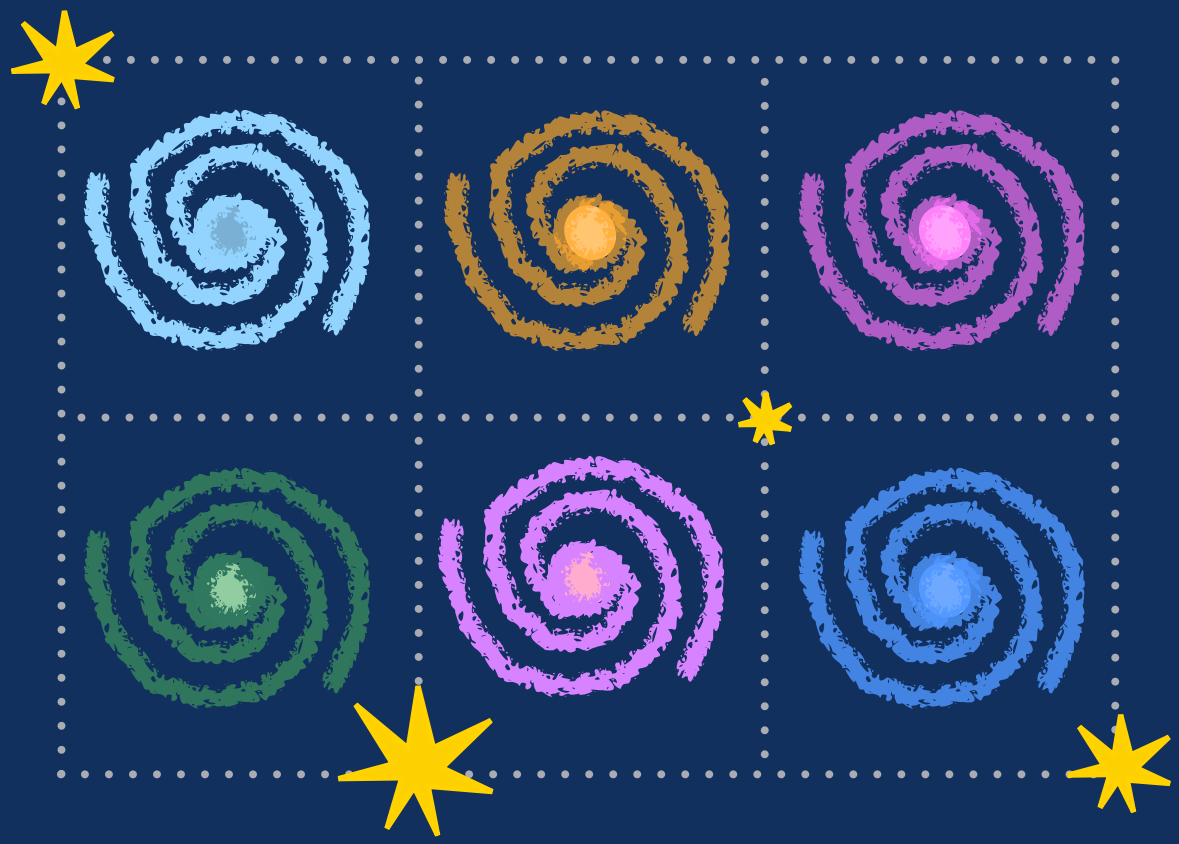

A census on the gas content of star-forming galaxies over the past 11 billion years of the universe

Tsan-Ming Wang
2024

A census on the gas content of star-forming galaxies over the past 11 billion years of the universe

Dissertation
zur
Erlangung des Doktorgrades (Dr. rer. nat.)
der
Mathematisch-Naturwissenschaftlichen Fakultät
der
Rheinischen Friedrich-Wilhelms-Universität Bonn

von
Tsan-Ming Wang
aus
Taichung, Taiwan

Bonn, December 2023

Angefertigt mit Genehmigung der Mathematisch-Naturwissenschaftlichen Fakultät der Rheinischen Friedrich-Wilhelms-Universität Bonn

1. Gutachter:	Prof. Dr. Frank Bertoldi
2. Gutachter:	Prof. Dr. Frank Bigiel
Tag der Promotion:	10.07.2024
Erscheinungsjahr:	2024

Abstract

With the advent of the Atacama Large Millimeter/submillimeter Array (ALMA), we now have the opportunity to measure the physical properties of the cold, dense, star-forming interstellar medium (ISM) even in distant, high-redshift galaxies. This dissertation documents measurements of the mean molecular gas mass, $M_{\rm gas}$, and apparent size of star-forming galaxies (SFGs) at different cosmological epochs, for galaxies over a wide range of total stellar mass, $M_\star$, and in different star formation modes, normal vs. starburst. This contributes to constrain the physical mechanisms that regulate star formation throughout cosmic history.

It has been known that most of the SFGs follow a tight correlation between total star formation rate and total stellar mass, the so-called main sequence (MS) of SFGs. I selected a sample of mass-complete MS galaxies and measured their mean $M_{\rm gas}$ and size using a Fourier-domain stacking analysis. Based on the measurements, I determined the mean molecular gas fraction, $M_{\rm gas}/M_\star$, and the mean molecular gas depletion time, $M_{\rm gas}$/ star formation rate (SFR), of these SFGs. I found that MS galaxies exhibit a constant mean molecular gas depletion time of ~400 million years over cosmic time, while their mean molecular gas fraction decreases by a factor of ~24 over the past 11 billion years. These findings suggest that cold gas must be continuously accreted to MS galaxies from the cosmic web to sustain star formation on timescales of giga-years, and that the evolution of MS galaxies is predominantly regulated by variations in their gas content. The mean gas sizes of MS galaxies remain constant (~2.2 kpc) across all stellar masses and throughout cosmic time, which is smaller than the mean size of their monochromatic optical emissions, but similar to the mean size of their stellar mass distributions. This suggests negative radial gradient of the dust attenuation in MS galaxies.

By integrating the gas mass, size, and star formation rate of MS galaxies, I investigated the relation between their gas mass surface density and the SFR surface density, known as the Kennicutt-Schmidt relation. An universal slope of ~1.13 in log-space across cosmic time is found, which implies that the increase in mean molecular gas depletion time of observed over the past 11 Gyr is due to a decrease in the gas surface density.

On the origin of a ~0.3 dex scatter in the SFR on the MS at a given redshift and $M_\star$, I found that SFGs located on the lower envelop of the MS have lower molecular gas fraction and longer depletion time, while SFGs located on the upper envelope have higher gas mass fractions and shorter depletion time. This suggests that small variations in the SFR of SFGs during their long-term evolution within the MS are regulated by disturbances acting on short timescales, such as minor mergers and violent disk instabilities.

At any redshift and total stellar mass, a subset of SFGs have star formation rates of more than a factor of three higher than those of MS galaxies. These are the so-called starburst galaxies, which I have found to exhibit complex optical morphologies indicative of merger events that appear as infall of gas into deeper gravitational potentials, as evidenced by more compact gas sizes (~1.4 kpc). This infalling gas scenario is supported by my finding that starburst galaxies have larger molecular gas fractions than MS galaxies, because neutral hydrogen gas would lose its angular momentum and fall into the deeper gravitational potentials, transforming into a molecular phase.

List of Publications

This dissertation research project resulted in two first-author, peer-reviewed and published publications that are listed below.

1. **Wang T.-M.**, Magnelli B., Schinnerer E., Liu D., Modak Z. A., Jiménez-Andrade E. F., Karoumpis C., Kokorev V., and Bertoldi F. (2022), *A^{3}COSMOS: A census on the molecular gas mass and extent of main-sequence galaxies across cosmic time*, Astronomy & Astrophysics, 660, A142.

   Author's Contribution: Wang performed the stacking analysis on the ALMA data and the scientific analysis under the supervision of Magnelli and Bertoldi. Modak provided the script for simulating ALMA observations to test the stacking analysis. The other co-authors contributed to the interpretation of the results and provided comments and revisions to the final manuscript.

2. **Wang T.-M.**, Magnelli B., Schinnerer E., Liu D., Jiménez-Andrade E. F., Karoumpis C., Adscheid S., and Bertoldi F. (2023), *A^{3}COSMOS: Dissecting the gas content of star-forming galaxies across the main sequence at 1.2 $\leq z <$ 1.6*, Astronomy & Astrophysics, 47219-23, in print.

   Author's Contribution: Wang performed the stacking analysis on the ALMA data and performed the scientific analysis under the supervision of Magnelli and Bertoldi. The other coauthors contributed to the interpretation of the results and provided comments and revisions to the final manuscript.

Contents

CHAPTER 1

Introduction

Mankind has been interested in the secrets of the heavens for thousands of years. In fact, the history of mankind is as long as the history of astronomy. In the last few hundred years, advances in telescope technology have allowed us to observe sources that are more distant and less luminous than what can be seen with the human eye. We are now able to constrain the evolutionary history of galaxies over cosmic time by observing the light emitted by their various components, i.e., stars, black holes, and the interstellar medium. However, the underlying mechanisms that drive this evolution are not fully understood. This is partly due to difficulties in measuring the fuel for star formation, i.e. the molecular gas, in distant galaxies. The main goal of this thesis work has been to address these limitations by measuring the gas mass and size of galaxies over a wide range of redshifts and stellar masses using the most powerful interferometric telescope to date, the Atacama Large Millimeter/submillimeter Array (ALMA), and an innovative Fourier space-based stacking analysis. Such measurements provide key constraints on our understanding of the underlying mechanisms that drive galaxy evolution over cosmic time.

In the following sections, I will introduce the general background of this doctoral research. In Sect. 1.1, I first present our current understanding of cosmology, spanning the epoch from the Big Bang to the emergence of the first light. In Sect. 1.2, I introduce the various physical properties of galaxies that can be revealed through the investigation of their Spectral Energy Distribution (SED). Finally, in Sect. 1.3, I summarize the evolutionary scenario of galaxies across cosmic times, as revealed by the past investigations of their different components.

1.1 From the Big Bang to the first light

Our Universe emerged from an initial state of extreme density and temperature known as the Big Bang around 13.8 billion years ago (e.g., Planck Collaboration et al., 2020). From this moment on, the Universe underwent a rapid expansion phase, the so called inflation (e.g., Kawasaki et al., 2005; Planck Collaboration et al., 2020, and Fig. 1.1). The ΛCDM cosmological model elegantly describes this cosmic evolution, with Λ representing dark energy and CDM symbolizing cold dark matter (e.g., Planck Collaboration et al., 2016; Planck Collaboration et al., 2020). Dark energy, which accounts for roughly 68% of the total mass-energy budget of the Universe, opposes gravity and causes the Universe to expand at an accelerating rate (e.g., Brax, 2018). This concept is supported by Hubble's law, which relates galactic distances and recessional velocities, indicating an expanding Universe (e.g., Riess et al., 2019; Pesce et al., 2020; Shajib et al., 2023). In contrast, CDM, accounting for roughly 27% of the total mass-energy budget, is hypothesized to be made up of cold, non-relativistic, and collisionless particles (e.g., Ostriker, 1993; Weinberg et al., 2015;

Rodrıguez-Montoya et al., 2020). The existence of CDM was first substantiated by empirical evidence from galactic rotation curves, which exhibit discrepancies between the mass inferred from the orbital velocity of stars and the visible baryonic mass (Babcock, 1939; van de Hulst et al., 1957; Rubin, 1983). This suggests a significant amount of unseen mass and leads to the postulation of dark matter (e.g., Jovanović, 2017; Bertone and Hooper, 2018; Mancera Piña et al., 2022).

As the Universe expanded following the Big Bang, both its density and temperature steadily decreased. The Cosmic Microwave Background (CMB) bears witness to this epoch. Characterized as nearly uniform black-body radiation, the CMB has an observed temperature of about 2.7 Kelvin (K). This corresponds to an effective temperature of $> 10^4$ K when at a redshift $z > 4{,}000$, serving as evidence of the early state of the Universe (see Durrer, 2015, for a review). As the Universe cooled to temperatures below ~3000 K, baryonic matter began to form neutral hydrogen (H I) atoms (e.g., Ahn and Smith, 2018), marking the epoch of recombination at z~1100. Further cosmic expansion caused these hydrogen atoms to cool, and their peak black-body radiation to fell into the infrared (IR) wavelength. This period, devoid of visible light to human observers, is known as the Dark Ages (see Miralda-Escudé, 2003, for a review). During this era, dark matter began to profoundly shape the structure of the Universe by forming dark matter halos via gravitational collapse. Simulations and observations in the large-scale structures support this hypothesis (see Peebles, 1980; Coles, 2001, for a review). The dark matter halos, with high gravitational potential, could further attract H I atoms. These atoms would later transform into molecular hydrogen (H_2) gas, leading to the formation of molecular clouds. These clouds serve as ideal environments for star formation. A contracting (non-magnetized) molecular cloud could collapse, causing its core temperature to rise, once it reaches its Jeans mass,

$$M_J \approx 2M_\odot \cdot \left(\frac{c_s}{0.2\,\mathrm{km/s}}\right)^3 \left(\frac{n}{10^3\mathrm{cm}^{-3}}\right)^{-\frac{1}{2}}, \tag{1.1}$$

where $M_\odot$ represents the solar mass, c_s is the gaseous sound speed, and n denotes the gas number density, with respect to the mean mass per particle. As the temperature in the collapsing core rises, molecular hydrogen transitions back into ionized hydrogen. Once the core temperature exceeds a few million K, enabling hydrogen atoms to overcome the energy barrier, nuclear fusion is initiated, leading to the formation of stars.

The birth of the first generation of stars, the Population III stars, signaled the end of the Dark Ages and the beginning of the epoch of reionization at z ~20 (see Zaroubi, 2013, for a review). Theoretical studies propose that these massive ($> 100M_\odot$), short-lived, and metal-free stars (e.g., Schaerer, 2002; Fraser et al., 2017; Lazar and Bromm, 2022; Klessen and Glover, 2023; Larkin et al., 2023) were born when the total mass of a dark matter halo reached around $10^6 M_\odot$ (see Bromm and Yoshida, 2011, for a review). The end of the life of these stars led to Population III supernovae, resulting in the first creation and ejection of heavy elements, such as, Carbon (C), Oxygen (O), Silicon (Si), and Iron (Fe), into the interstellar medium (e.g., Padmanabhan and Loeb, 2022). However, since these ejections took place in the shallow gravitational potential of this $\sim 10^6 M_\odot$ dark matter halo, they likely removed most of the gas and thus halted any subsequent star formation. Studies suggest that the first galaxies were born at z ~10 with total dark matter halo mass $> 10^8 M_\odot$, i.e., when their gravitational potential is strong enough to hold the gas and sustain self-regulated star formation (e.g., Bromm and Yoshida, 2011; Chen et al., 2022). The continuous radiation from generations of stars gradually ionized the hydrogen in the Universe, marking the end of the reionization epoch, when the intergalactic medium (IGM) was fully ionized, around z ~6 (e.g., Fan et al., 2003; Yang et al., 2020; Simmonds et al., 2023).

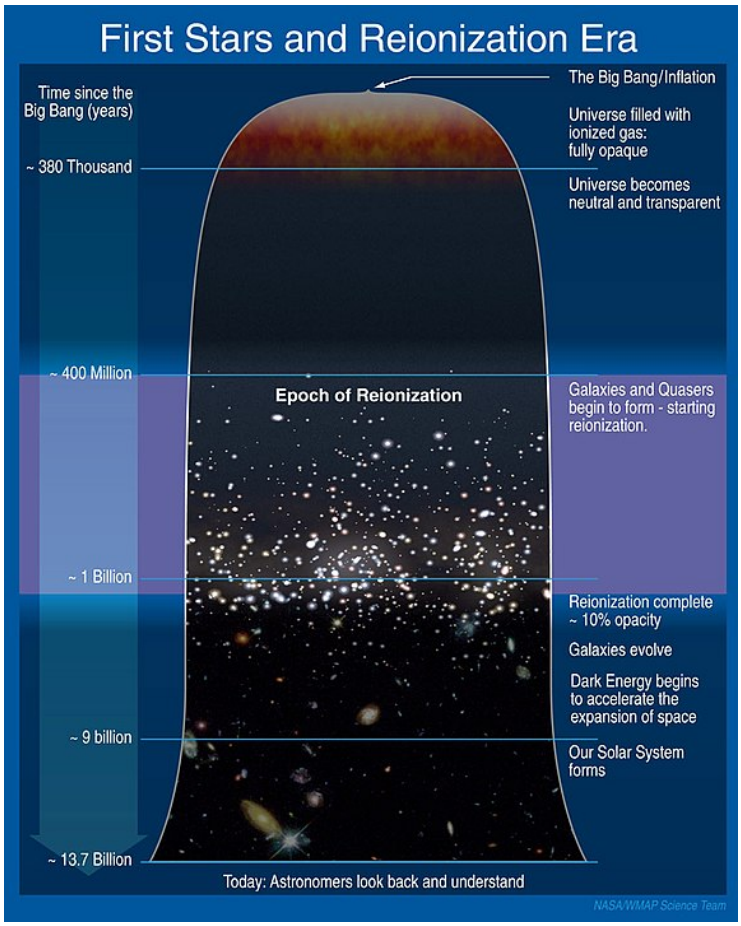

Figure 1.1: The story of our Universe. In between the Big Bang and the formation of the first galaxies (z ~10), our Universe underwent the epoch of recombination (from z ~1,100 to z ~200), Dark Ages (from z ~200 to z ~20), and the epoch of reionization (from z ~20 to z ~6). Figure taken from Caltech and NASA webpage (http://imagine.gsfc.nasa.gov/docs/sats_n_data/satellites/jwst_darkages.html).

1.2 To diagnose the physical properties of galaxies

Following their formation, galaxies undergo diverse evolutionary stages, leading eventually to the diversity of galaxies we observe today in the local universe. However, given the complex conditions within the interstellar medium (ISM) of galaxies, creating a succinct theory that captures their evolution and reproduce the observed diversity in shape and colors of local galaxies is challenging. As a result, accurately measuring the physical properties (e.g., their stellar mass, star formation rate, molecular gas mass, and size) of a large samples of galaxies across cosmic time is essential to refine theories and simulations of galaxy evolution. Typically, the physical properties of galaxies are inferred through the study of their SED. The SED illustrates how light energy is distributed across different wavelengths, ranging from X-ray to radio (e.g., Fig. 1.2 for a typical star-forming galaxy, Bruzual and Charlot, 2003; da Cunha et al., 2008; da Cunha et al., 2015). Below, I introduce different physical properties of galaxies that are essential for this doctoral research and how they can be inferred from the modeling of their SED.

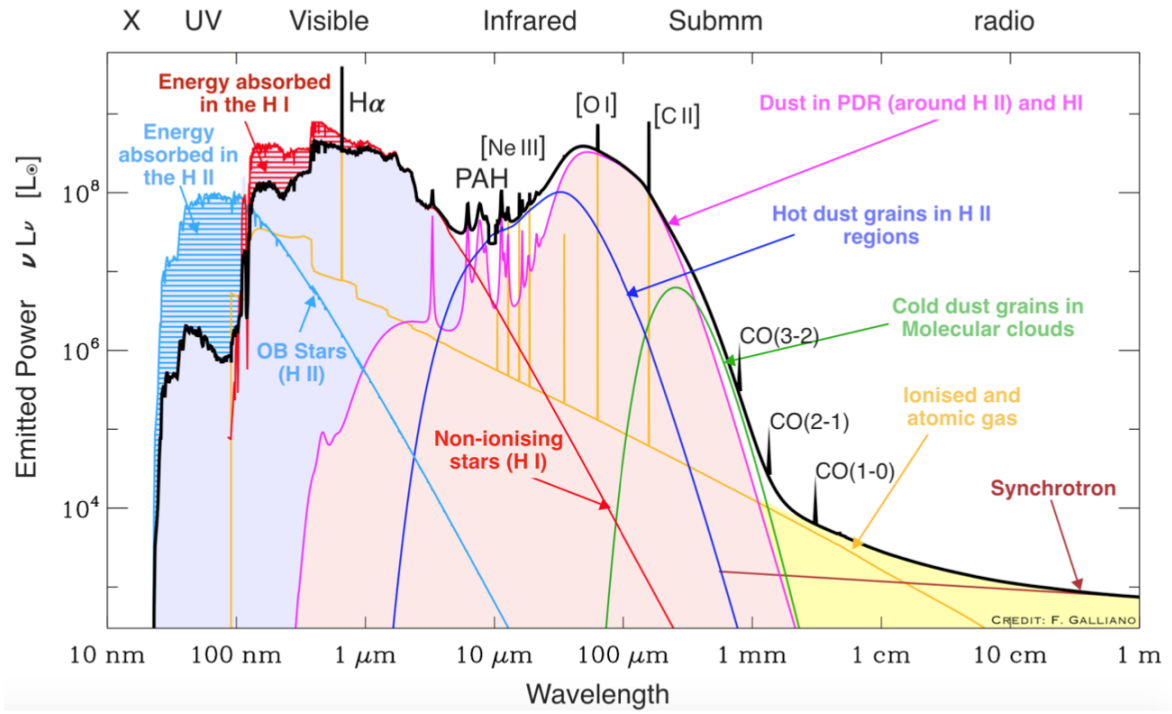

Figure 1.2: Energy distribution of a typical star-forming galaxy at different wavelengths. Several signature emissions reflecting the physical conditions of a galaxy can be observed, e.g., continuum emission at optical/near-IR wavelengths indicates the amount of stars (red line; see Sect. 1.2.1), at UV wavelengths reflects the unobscured star formation (blue line; see Sect. 1.2.2), and at FIR/millimeter wavelengths reveals the amount of dust (green line; see Sect. 1.2.3), which correlates with the gas content. Figure adapted from Galliano et al. (2008).

1.2.1 Stellar mass

Stars are a main constituency of the baryonic matter content of the universe. They are the end point of the evolution of matter from the diffuse gas phase to self-gravitating molecular clouds, and they are the sources of all heavy elements beyond Lithium. The total mass in all stars of a galaxy is a key indicator of its evolution history, and thus a prime observable.

Stars have masses ranging from 0.08 $M_\odot$ to ~150 $M_\odot$ (e.g., Kumar, 1963; Figer, 2005), where the upper mass limit depends strongly on the the metallicity, which refers to the abundance of elements heavier than helium, of the gas they form from. Stars are historically classified in various spectral classes that are sorted in their initial mass. The O and B stars are the most rare and massive stars, with masses > 6 $M_\odot$. Due to their intense nuclear fusion, their lifespans are short, typically no more than ~100 million years (e.g., Arabadjis and Richstone, 1998; Crowther, 2012; Aschenbrenner et al., 2023). The most massive stars, although rare, outshine the more numerous low-mass stars in any young stellar population. The total luminosity of a young star forming region can therefore be related to the total star formation rate (see Sect. 1.2.2), but is unrelated to the total stellar mass that a galaxy has accumulated over billions of years. In contrast, stars with masses < 6 $M_\odot$ are numerous, have a long lifespan (e.g., Wolfe et al., 2010, stars with a mass equivalent to our sun live up to ~10 billion years). When < 6 $M_\odot$ stars evolve to their end phases, they become red giants, a phase that can last for more than a gigayear (e.g., Wu et al., 2018). Red giants emit brightly in the near-infrared spectrum (see the red curve, i.e., non-ionising stars, in Fig. 1.2),

making this emission a good tracer for the total stellar mass of a galaxy. Observational studies use SED fitting of the entire stellar population of a galaxy to convert the optical/near-infrared (near-IR) emission into stellar masses (e.g., Song et al., 2016; Lower et al., 2020; Robertson et al., 2023). This method uses specific stellar initial mass functions convolved with single star spectra, and assumes some star formation history to construct a multitude of SED models. It fits multi-band observational data to these models to determine the corresponding stellar mass. This approach allows for the measurement of the stellar mass of galaxies across diverse populations and distances. In this doctoral research, the stellar masses of galaxies are determined using such an SED fitting approach. In the COSMOS field, where I conducted this study and which benefits from observations in more than 20 spectral bands ranging from the ultraviolet (UV) to near-IR (see Sect. 2.2), the uncertainties on the derived stellar masses are estimated to be less than 0.1 dex (e.g., Laigle et al., 2016; Weaver et al., 2021).

1.2.2 Star formation rate

The total star formation rate is a measure of the instantaneous rate of star formation, i.e., the growth rate of the mass in all stars. It can be derived by assuming an initial mass function that describes the initial mass distribution for a population of stars during star formation, and using emission from sources that show evidence of recent star formation.

The short-lived O- and B-type stars that form from dense molecular clouds in regions of high gas mass density (i.e., particle number density > 10^4 cm^{-3} (e.g., McKee and Ostriker, 2007; Parmentier et al., 2011)) serve as effective tracers of the SFR of a galaxy. These massive stars undergo intense nuclear fusion and have temperatures exceeding 10,000K in their atmospheres, primarily emitting radiation in the UV wavelength (see light-blue curve, i.e., OB stars, in Fig. 1.2). Madau et al. (1998) provided a widely-used calibration to estimate the SFR of a galaxy,

$$\mathrm{SFR_{UV}}[M_\odot\,\mathrm{yr}^{-1}] = 1.4\times10^{-28} L_\nu[\mathrm{ergs\,s^{-1}\,Hz^{-1}}], \tag{1.2}$$

where L_ν is the monochromatic luminosity observed at wavelengths 1,500 to 2,800 Å, where, in the absence of dust attenuation (see below), the UV spectrum of a star forming galaxy is nearly flat. A part of the energetic radiation of O and B stars (wavelength <912Å can ionize the surrounding hydrogen gas, creating so called HII regions. Free electrons can recombine with these ionized hydrogens, and transition to lower energy levels. When they transition from the energy level n=3 to n=2, they emit line radiation at 6,564 Å(see Fig. 1.2), known as the Hα emission. This optical emission line is bright in star-forming galaxies (SFGs) and can also be used as a tracer to probe the SFR of galaxies (e.g., Kennicutt, 1998a; Pflamm-Altenburg et al., 2007; Domınguez Sánchez et al., 2012; Domınguez Sánchez et al., 2014). The Hα recombination emission trace even more instantaneous (massive) star formation than the UV luminosity, and the conversion from its luminosity to SFR is given by Kennicutt (1998a) as

$$\mathrm{SFR_{H\alpha}}[M_\odot\,\mathrm{yr}^{-1}] = 7.9\times10^{-42} L_{\mathrm{H}\alpha}[\mathrm{ergs\,s^{-1}}], \tag{1.3}$$

where $L_{\mathrm{H}\alpha}$ is the luminosity of the Hα emission line.

The radiation emitted from young star forming regions is dominated by that of the most massive stars, although they contribute only a small share in the total stellar mass. The stellar radiation is partially absorbed by the dense dusty clouds surrounding massive star-forming regions (e.g., Draine, 2003). This radiation absorbed by dust grains heats them and the absorbed energy is re-emitted as thermal radiation at IR to sub-millimeter wavelengths (see pink and dark blue curves in Fig. 1.2). Therefore, to accurately determine the total SFR of a galaxy, studies combine measurements at both UV and IR wavelengths (e.g.,

Kennicutt, 1998a; Elbaz et al., 2007; Wuyts et al., 2011). For example, Kennicutt (1998a) provided a calibration based on observations in both the UV and IR to estimate the SFR of a galaxy,

$$\mathrm{SFR}_{\mathrm{UV+IR}}[M_\odot\,\mathrm{yr}^{-1}] = 1.09\times10^{-10}(L_{\mathrm{IR}}[L_\odot] + 3.3\times L_{2800}[L_\odot]), \tag{1.4}$$

where $L_{2800} = \nu L_\nu$ (2,800 Å) and L_{IR} is the total IR luminosity of a galaxy, integrated from 8-1,000 μm. In this case, the IR luminosity can be determined either by renormalizing IR SED templates (e.g., Wuyts et al., 2011; Kirkpatrick et al., 2012) to a single mid-IR band observation or by fitting these IR SED templates to multiple far-IR band observations. High redshift galaxies are found to be very dusty and thus have a large fraction (>50%) of their UV emission absorbed by dust (e.g., Magnelli et al., 2011; Wuyts et al., 2011; Pannella et al., 2015). The use of the approach that combines UV and IR measurements to calculate the SFR of high redshift galaxies is therefore crucial. When applicable, this is the method I have chosen in my work.

1.2.3 Gas mass

Hydrogen is the most basic and abundant element in our Universe, making up to ~75% of the baryonic mass in the ISM (e.g., Obreschkow and Rawlings, 2009). The neutral (HI) and molecular (H_2) forms of hydrogen are crucial components of the ISM, as they fuel galaxy growth through star formation. Below, I briefly describe the HI and H_2 gas components of the ISM and discuss methods to measure them observationally.

Neutral hydrogen

Galaxies initially grow in baryonic mass by accreting ionized gas from the intergalactic medium, through gas streams in large cosmic filaments. This gas turns neutral as it accumulates in galaxies, and in their later evolutionary stages, most disk galaxies maintain a large, thick disk of neutral hydrogen that can extend well beyond the stellar disk. This neutral gas can condense to form molecular clouds from which stars form. This conversion from atomic to molecular is most efficient in the inner, central part of galaxies. HI is the most common form of cold gas in the Universe at all epochs, and is the foundational ingredient of the cosmic baryon cycle and of star formation.

The 21 cm emission line serves as a tracer for these HI gas (e.g., Kerp et al., 2016; Di Teodoro and Peek, 2021), which originates from the change in the spin orientation of an electron relative to the proton within a hydrogen atom. The probability for this transition is very small as it takes ~11 million years (Myr) for a hydrogen atom to spontaneously undergo this transition (see Saintonge and Catinella, 2022, for a review). Despite this low probability, the high abundance wide spread emission of HI make this emission line sufficiently bright to be easily detected even with small radio telescopes in our own galaxy. Measurements of the 21 cm emission line can be used to determine the total HI gas mass in distant galaxies,

$$M_{\mathrm{HI}}[M_\odot] = \frac{2.356\times10^5}{(1+z)^2}(D_L[\mathrm{Mpc}])^2\int S_\nu[\mathrm{Jy}]\,d\nu, \tag{1.5}$$

here D_L is the luminosity distance and S_ν is the flux density over the emission line spectrum. Using 21 cm measurements, we know that HI gas contributes up to 80% of the hydrogen mass in SFGs of the local Universe (e.g., Obreschkow and Rawlings, 2009; Fletcher et al., 2021; Saintonge and Catinella, 2022). Accounting for the HI gas is thus important when exploring the physics regulating star formation in SFGs. Unfortunately, in the high redshift Universe ($z > 1.0$), measuring the 21 cm emission line in a galaxy becomes increasingly difficult with available technology, due to sensitivity limits and terrestrial

radio frequency interference. Consequently, indirect probes of HI gas, such as measuring the UV damped Lyman-alpha absorbing lines of high-redshift galaxies, are used to measure the comoving, average HI mass density at high redshifts. Using such an approach, Bauermeister et al. (2010, and references therein) found that there is very little evolution of HI comoving mass density from z ~0 to z ~4. Given the findings that the molecular gas mass density increases significantly with redshift (e.g., Liu et al., 2019b; Magnelli et al., 2020; Tacconi et al., 2020), in this doctoral research, I have made an approximation of molecular hydrogen gas mass ~ total hydrogen gas mass within high-redshift SFGs, which is consistent with other high-redshift galaxy studies.

Molecular hydrogen

Due to the symmetrical structure of the H_2 molecule, it lacks a dipole moment and therefore does not emit electric dipole, but only faint quadrupole radiation. Moreover, the energy for the first excited rotational level of H_2 molecule is relatively high, corresponding to 510 K and emission at 28 μm so that the bulk of molecular gas, which is at temperature well below 100K, does not radiate strongly. Molecular hydrogen is therefore difficult to be measured directly. The second-most abundant molecule in galaxies, CO, is commonly used as proxy for the dense molecular gas within galaxies (see Bolatto et al., 2013, for a review). The relative intensities of different transition lines of CO molecules yield information about the physical condition in the ISM of a galaxy, specifically the density and temperature (e.g., Seaquist et al., 2006; Narayanan and Krumholz, 2014; Zhao et al., 2016). For a given transition, above the so called critical density the rate of collisional excitation to an upper level exceeds the rate of spontaneous radiative de-excitation. The critical density for the lowest CO rotational transition line, CO (J=1-0), is n ~2×10^3 cm^{-3} at 100 K (e.g., Narayanan and Krumholz, 2014), which makes this line a sensitive tracer of the the bulk of the molecular gas in galaxies (e.g., Wang and Hwang, 2020; den Brok et al., 2021; Teng et al., 2023; Zhang and Ho, 2023). However, this line is typically optically thick, which makes it more complicated to interpret. In the local Universe, studies attempt to build a simple empirical relation that relates the CO (J=1-0) luminosity, $L_{\rm CO}$, of a galaxy (equally that of a resolved molecular cloud) to its molecular gas mass, $M_{\rm gas}$, using a mass-to-light conversion factor, $\alpha_{\rm CO}$,

$$M_{\rm gas} = \alpha_{\rm CO}\, L_{\rm CO}. \tag{1.6}$$

It was empirically found that $\alpha_{\rm CO}$ varies between ~0.2 and ~20 (K km s^{-1} pc^2)$^{-1}$, depending on the physical properties of galaxies (e.g., Sandstrom et al., 2013; Bolatto et al., 2013), such as metallicity, gas temperature and density, and intensity of the radiation field. Using the lowest CO rotational line to measure the molecular gas masses for a significant, representative sample of high redshift SFGs is inefficient, because this would require relatively long observing time. Besides, the applicability of $\alpha_{\rm CO}$ derived from local galaxies to high-redshift SFGs, given differing ISM conditions, remains a topic of debate (e.g., Srianand et al., 2008; Papadopoulos et al., 2012).

To measure more efficiently the molecular gas mass in high-redshift SFGs, recent studies have proposed an approach based on dust emission (see green curve, i.e., cold dust grains in molecular clouds, in Fig. 1.2). Dust and molecular gas are closely linked, not only because dust grains catalyze the formation of H_2 (e.g., Hollenbach and Salpeter, 1971), but generally dust and gas is well mixed with constant relative abundance, irrespective of the gas phase.

An simple empirical approach uses the narrow-band flux density of the dust mm-wavelength emission spectrum, thus measuring in the the Rayleigh–Jeans (RJ) part of the thermal (modified black-body) emission spectrum (e.g., Scoville et al., 2014; Scoville et al., 2016; Liu et al., 2019b; Magnelli et al., 2020; Millard

et al., 2020; Dye et al., 2022). The measured RJ flux density can be related to a molecular gas mass using an empirical light-to-gas mass relation. Hughes et al. (2017, hereafter H17) compare the CO (J=1-0) luminosity and rest-frame luminosity at 850 μm (i.e., $L_{850}^{\rm rest}$) of local galaxies, assuming a constant $\alpha_{\rm CO}$=6.5(K km s^{-1} pc^2)$^{-1}$, and calibrate the $L_{850}^{\rm rest}$-to-H_2 gas mass relation,

$$\log_{10} M_{\rm H_2} = (0.92 \pm 0.02) \log_{10} L_{850}^{\rm rest} - (17.31 \pm 0.59), \tag{1.7}$$

where $M_{\rm H_2}$ is in $M_\odot$ and $L_{850}^{\rm rest}$ is in erg s^{-1} Hz^{-1}. Using RJ flux densities and a light-to-gas mass relation is now widely used in high-redshift studies, because of its simplicity and convenience. Specifically, it allows one to constrain the gas mass of a SFGs with little observing time, a few minutes compared to more than half an hour required when using CO lines.

However, studies have found that the gas-to-dust mass ratio within galaxies increases as their metallicity decreases (e.g., Rémy-Ruyer et al., 2014). An approach that assumes a constant light-to-gas mass ratio might not be suitable for high-redshift and low-stellar mass galaxies, which typically have lower metallicity (e.g., Mannucci et al., 2010; Curti et al., 2023; Nakajima et al., 2023). Therefore, an alternative approach that first measures the dust mass, $M_{\rm dust}$, and then applies a metallicity-dependent $M_{\rm dust}$-to-gas mass relation has been developed. The dust mass can be measured by either applying multi-wavelength dust SED fits (e.g., Hunt et al., 2019; Kokorev et al., 2021; Suzuki et al., 2021), using an optically thin approximation that assumes a mass-weighted mean dust temperature of 25 K (e.g., Magnelli et al., 2020), or scaling the SED template to the observed RJ flux density and applying a total IR luminosity $L_{\rm IR}$-to-dust mass relation (e.g., Béthermin et al., 2012, hereafter B12). The obtained dust mass can then be converted into molecular gas mass using locally calibrated $M_{\rm dust}$-to-gas mass relations. For example, Leroy et al. (2011, hereafter L11) use high-resolution observations of five local group galaxies to calibrate a metallicity-dependent $M_{\rm dust}$-to-gas mass relation,

$$\log(M_{\rm gas}/M_\odot) = \log(M_{\rm dust}/M_\odot) + 9.4 - 0.85(12 + \log({\rm O/H})), \tag{1.8}$$

where the gas-phase metallicity, 12+log(O/H), can be inferred using the redshift- and stellar mass-dependent relation given by, e.g., Liu et al. (2019b), the so-called mass-metallicity relation,

$$12 + \log({\rm O/H}) = \begin{cases} a & \text{when } \log(M_\star/M_\odot) \geq b(z), \\ a - 0.087(\log(M_\star/M_\odot) - b(z))^2 & \text{otherwise,} \end{cases} \tag{1.9}$$

where $a = 8.74$ and $b(z) = 10.4 + 4.46\log(1+z) - 1.78(\log(1+z))^2$.

Studies that use approaches based on dust emissions to measure the gas mass of high-redshift SFGs typically use the molecular gas mass as an approximation of the total hydrogen gas mass (i.e., $M_{\rm gas}^{\rm dust} = M_{\rm H2}+M_{\rm HI} \sim M_{\rm H2}$; e.g., Liu et al., 2019b; Magnelli et al., 2020; Tacconi et al., 2020). This is because the HI gas mass is difficult to measure at $z > 1.0$ and the molecular gas mass density is found to increase significantly with redshift (Tacconi et al., 2020). The approximation is supported by CO measurements that trace only the molecular phase, which tend to agree well with dust-based measurements (e.g., Genzel et al., 2015; Scoville et al., 2016; Scoville et al., 2017; Tacconi et al., 2018; Tacconi et al., 2020).

1.3 Evolution of galaxies

Over the past decades, studies have examined how the physical properties of galaxies (e.g., stellar mass, SFR, molecular gas mass, and size) change over cosmic time, shedding light on our understanding of galaxy

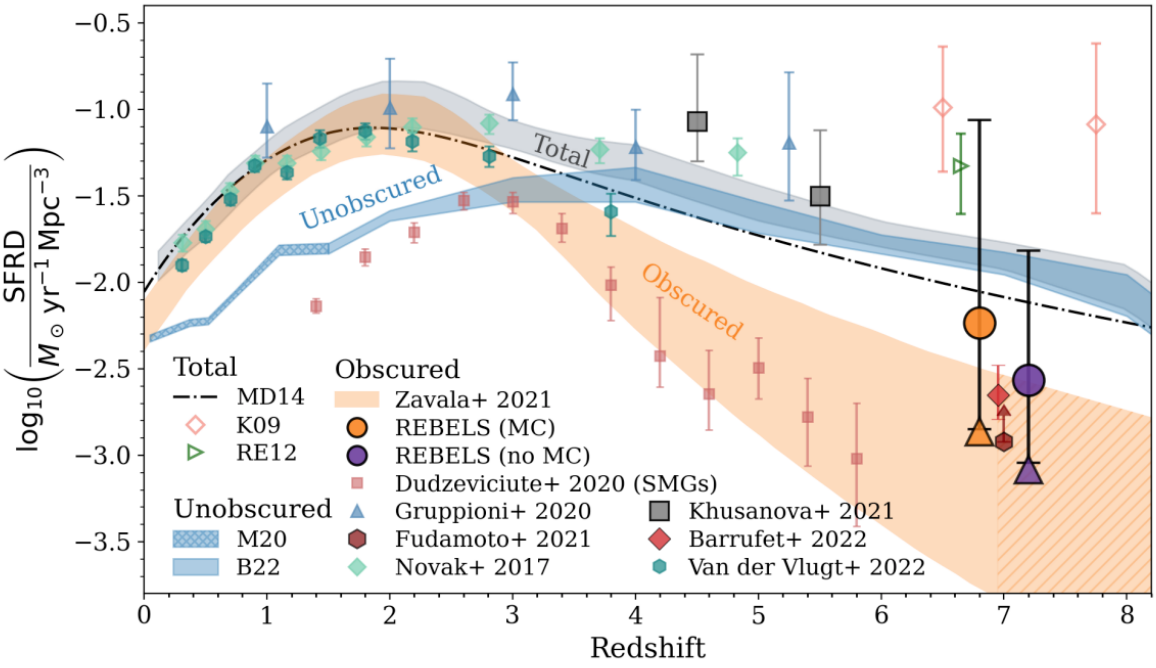

Figure 1.3: Cosmic SFRD from literature studies. Total cosmic SFRD from Madau and Dickinson (2014, black dashed line), Kistler et al. (2009, purple diamonds), and Robertson and Ellis (2012, green triangle). Dust-unobscured cosmic SFRD from Moutard et al. (2020, denoted M20 in the legend) and Bouwens et al. (2022, denoted B22 in the legend). Dust-obscured cosmic SFRD from Zavala et al. (2021, orange shaded region), Dudzevičiūtė et al. (2020, pink squares), Gruppioni et al. (2020, blue triangles), Fudamoto et al. (2021, brown hexagon), Novak et al. (2017, green diamonds), Khusanova et al. (2021, gray squares), Barrufet et al. (2023, red diamond), van der Vlugt et al. (2022, green hexagons), and Algera et al. (2023, purple and orange data points). Figure taken from Algera et al. (2023).

evolution. In the following, I will describe several key findings from these studies and discuss some of their limitations and how my research has sought to alleviate them.

1.3.1 Cosmic evolution of star formation

A simple, yet powerful, way to understand the evolutionary history of galaxies is to study the global star formation of the universe per unit comoving volume (the so-called star formation rate density; SFRD), and to examine its evolution over cosmic time (e.g., Madau and Dickinson, 2014; Novak et al., 2017; Liu et al., 2018; Gruppioni et al., 2020; Leslie et al., 2020; Katsianis et al., 2021; Picouet et al., 2023). Madau and Dickinson (2014) provided a comprehensive review of cosmic SFRD across all redshifts. They found that the cosmic SFRD increases rapidly after the earliest galaxy formation epochs, then peaks at $z \sim 2$ (the so-called cosmic noon), and subsequently decreases by a factor of ~ 10 to the present day value (Fig. 1.3). To parameterize this evolution, they proposed the empirical relation

$$\mathrm{SFRD} = 0.015 \frac{(1+z)^{2.7}}{1+[(1+z)/2.9]^{5.6}}\, M_\odot\,\mathrm{year}^{-1}\,\mathrm{Mpc}^{-3}. \tag{1.10}$$

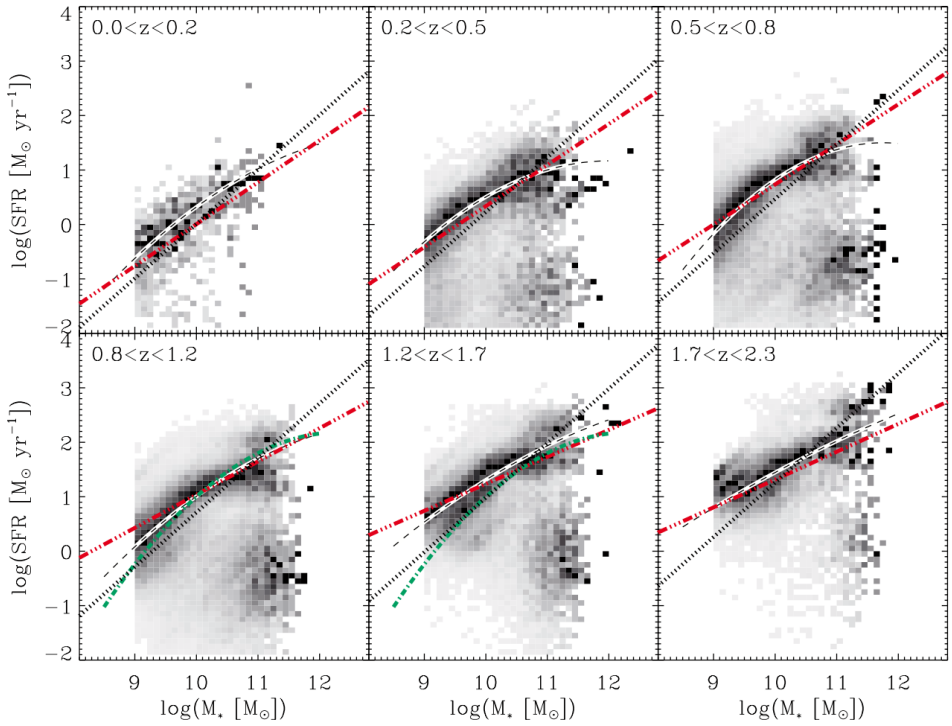

Figure 1.4: Number density of galaxies in the stellar mass-SFR plane. The darkest pixels show the highest number density of galaxies within that particular stellar mass bin. The black dashed lines with white background show the second-order polynomial function fitted to the MS as found by Magnelli et al. (2014). Lines represent the MS determined by Elbaz et al. (2011, dotted black), Rodighiero et al. (2010, red dot-dashed), and Whitaker et al. (2012, green dot-dashed). One can directly observe that the normalization of the MS increases with redhsifts. Figure taken from Magnelli et al. (2014).

By integrating this empirical relation across cosmic time, they derived the cosmic stellar mass density. They concluded that ~50% and ~25% of the current observable stellar mass was formed between the epoch of reionization and z ~1.3 and z ~2.0 (i.e., cosmic noon), respectively. While most recent studies support the above empirical relation for $z < 3$ (e.g., Novak et al., 2017; Liu et al., 2018; Gruppioni et al., 2020; Leslie et al., 2020; Katsianis et al., 2021), some discrepancies exist at $z > 3$. In fact, several recent studies suggest higher SFRDs when both dust-obscured and unobscured data are combined (e.g., Fig. 1.3, Gruppioni et al., 2020; Katsianis et al., 2021; Khusanova et al., 2021; Algera et al., 2023). This discrepancy may arise from the fact that Madau and Dickinson (2014) rely solely on uncertain dust attenuation-corrected UV emission to constrain the SFRD for $z > 3$. Their estimates may thus miss a population of high-redshift dusty SFGs.

1.3.2 Stellar mass–SFR plane

While the cosmic SFRD is well constrained up to z ~8 (see Fig. 1.3), details in the mechanisms that drive the rise and fall of the cosmic SFRD are uncertain. To gain further insight into these mechanisms, one should first study the SFR and stellar mass of each individual galaxy, as this allows us to determine where star formation is primarily taking place.

Numerous studies show that galaxies can be divided into three populations on the SFR-stellar mass plane. The largest population contributes about 80% of the cosmic SFRD, and exhibits a tight, nearly

linear (in log-space) correlation between its SFR and stellar mass, the so-called main-sequence (MS) of SFGs (Fig. 1.4; e.g., Elbaz et al., 2011; Whitaker et al., 2012; Schreiber et al., 2015; Leslie et al., 2020; Delvecchio et al., 2021). Several important features were found for the MS. First, for a given stellar mass and redshift, the MS exhibits a constant scatter of ∼0.3 dex in the SFR. Second, the normalization of the MS is found to increase by a factor of 20 from the present day to the cosmic noon (i.e., z ∼2). Third, a bend and flattening of the SFR at high stellar masses has been observed for the MS galaxies, with the bending stellar mass increasing with redshift and becoming less obvious at $z > 2.5$.

The second population on the SFR-stellar mass plane are galaxies with intense star formation activity. These galaxies are offset above the MS with ΔMS ($\log_{10}(\mathrm{SFR}/\mathrm{SFR}_{\mathrm{MS}})$) > 0.7, the so-called starburst galaxies (e.g., Rodighiero et al., 2011; Schreiber et al., 2015; Silverman et al., 2018). Starburst galaxies are rare, accounting for only 5% of the SFG population, but contribute to 10% of the SFRD at all redshifts (e.g., Sargent et al., 2012; Lamastra et al., 2013). Observations and simulations suggest that starburst galaxies could be induced by mergers, galaxy interactions, or disk instabilities (e.g., Porter et al., 2014; Wilkinson et al., 2018; Calabrò et al., 2019; Cibinel et al., 2019; Renaud et al., 2022). With their intense star formation, starburst galaxies are likely to have a relatively short lifespan, i.e., < 300 Myr (e.g., Schawinski et al., 2014; Bergvall et al., 2016; Dıaz-Garcıa and Knapen, 2020; Rinaldi et al., 2022).

The third population of galaxies is found ∼1 dex below the MS on the SFR-stellar mass plane, predominantly at the high end of the stellar mass. These are referred to as quiescent galaxies (e.g., Valentino et al., 2020; Lustig et al., 2023; Suzuki et al., 2022). Characterized by limited ongoing star formation (e.g., Young et al., 2011; Gobat et al., 2020; Caliendo et al., 2021), they are dominated by old stellar populations (e.g., Dıaz-Garcıa et al., 2019; Buzzo et al., 2022), resulting in a predominantly red color. Furthermore, these galaxies are more likely to be found in dense environments (e.g., Strazzullo et al., 2019; Noordeh et al., 2021; Buzzo et al., 2022), such as the centers of galaxy clusters.

Simulations attempt to interpret the mechanisms behind the characteristics of the MS, starburst, and quiescent galaxies. For the scatter of ∼0.3 dex in MS galaxies, simulations by Tacchella et al. (2016) suggest that its origin could be a complex combination of several phenomena: galaxies on the MS could experience cycles of compaction (increasing ΔMS) and depletion (decreasing ΔMS) phases (Fig. 1.5). For the observed increase in MS normalization with redshift, simulations interpret this by the cosmic evolution of the accretion rate of gas from the IGM onto MS galaxies (e.g., Bouché et al., 2010; Lilly et al., 2013; Peng and Maiolino, 2014). For the flattening of the MS, studies use the mass-quenching model (e.g., Peng et al., 2010; Nelson et al., 2018; Wright et al., 2019) to explain such a discovery. In the mass-quenching model, galaxies accumulate stellar mass over cosmic time. When their halo mass is < $10^{10.5} M_{\odot}$, the gravitational potential of these galaxies allows for efficient accretion of gas from the IGM. This supports the ongoing star formation in these galaxies, resulting in a linear correlation between their stellar mass and SFR over cosmic time. However, as these galaxies evolve over a few gigayears (Gyrs), they become increasingly massive. Once their halo mass > $10^{10.5} M_{\odot}$, various mechanisms, such as the activity of their AGN or heating due to their elevated gravitational potential, act to reduce the further accretion of the fuel for star formation from the IGM (e.g., Dekel and Birnboim, 2006; Rodrıguez Montero et al., 2019; Donnari et al., 2021). These mechanisms would therefore reduce star formation in these massive galaxies. For starbursts, simulations suggest that they result from an increase in the star formation efficiency (SFE) of galaxies (e.g., Di Matteo et al., 2007; Sargent et al., 2014). However, other simulations suggest that an increase in star formation fuel, specifically the molecular gas, is necessary to trigger such intense star formation (e.g., Sparre et al., 2022). Finally, the formation of quiescent galaxies is simulated to result from the quenching of SFGs by the growth of their hot halos, preventing further cold gas accretion, depletion of the surrounding gas, AGN activity, or merger events (e.g., Fig. 1.6, Tacchella et al., 2016; Man and Belli, 2018; Noordeh et al., 2021; Gómez-Guijarro et al., 2022; Park et al., 2022; Walters et al., 2022).

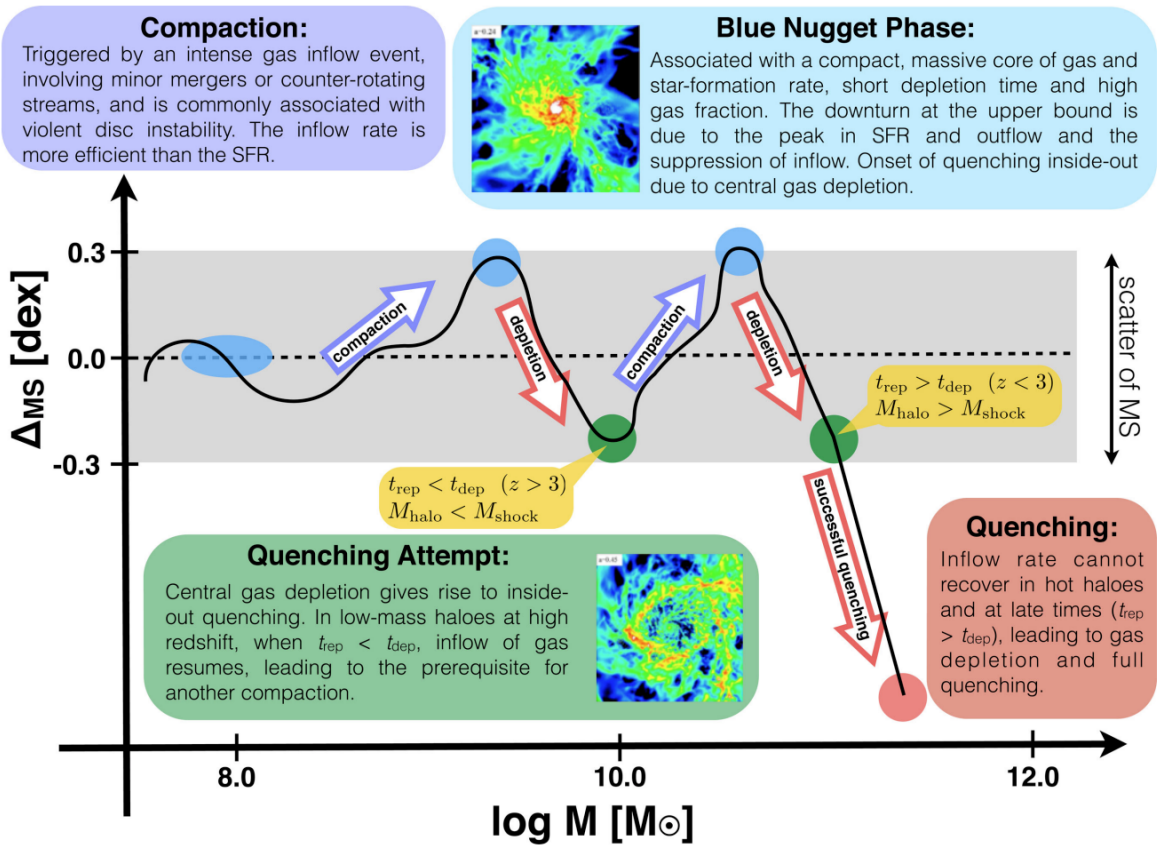

Figure 1.5: Schematic of the mechanisms driving the dispersion of the MS and the quenching of SFGs. Figure taken from Tacchella et al. (2016).

Common to all these theories is that the evolution of MS, starburst, and quiescent galaxies is regulated by their gas content. Unfortunately, until recently, most of these theoretical studies lacked direct observational constraints on the gas content of high-redshift SFGs and could neither be confirmed nor refuted. To overcome this limitation, accurate measurements of the molecular gas mass and size of high-redshift SFGs are essential.

1.3.3 Gas mass within galaxies

Simulations predict that the gas content within SFGs plays an essential role in regulating their evolution (e.g., Sargent et al., 2012; Tacchella et al., 2016). Accurate measurements of the gas mass in SFGs therefore provide crucial observational constraints for distinguishing between different evolutionary scenarios (e.g., Sargent et al., 2014; Schinnerer et al., 2016; Miettinen et al., 2017a; Scoville et al., 2017; Tacconi et al., 2020; Liu et al., 2019b), and thus improve our understanding of galaxy evolution. At the beginning of my doctoral research, the most advanced studies on this topic by Liu et al. (2019b, Fig. 1.7) and Tacconi et al. (2020) have already started to investigate the gas mass of individual SFGs across different redshifts, stellar masses, and ΔMSs. Across different redshifts, they measured a relatively constant molecular gas fraction, $\mu_{mol} = M_{gas}/M_{\star}$, for massive SFGs at $z > 2$, but a decrease of this fraction by a factor of ∼20 from $z \sim 2$ to $z \sim 0$. They also found that the molecular depletion time, $\tau_{mol} = M_{gas}/SFR = 1/SFE$, for

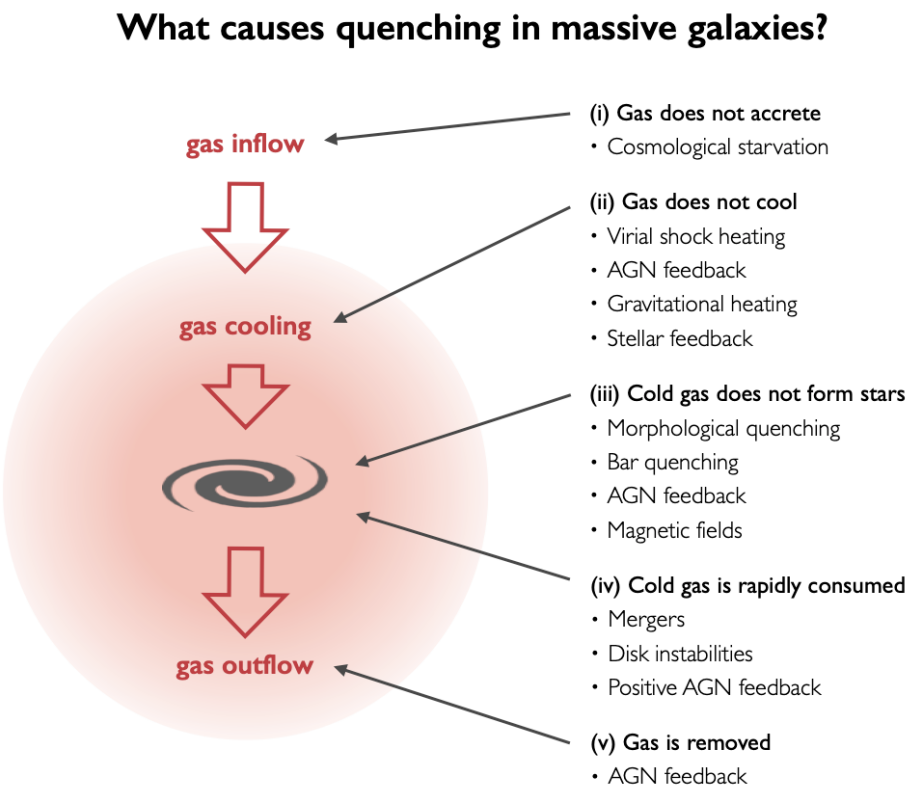

Figure 1.6: Schematic diagram listing the quenching mechanisms in massive galaxies. Figure taken from Man and Belli (2018).

SFGs gradually decreases by a factor of ~3 from 1.5 Gyr at z ~0 to 600 Myr at z>1.5. Most of these results have been interpreted mainly in the light of gas regulator models (e.g., Bouché et al., 2010; Lilly et al., 2013; Peng and Maiolino, 2014). In this model, the continuous accretion of fresh gas from the cosmic web is required to sustain galaxy growth. Without this, galaxies would cease star formation and become "red and dead" within the typical depletion timescale of their gas reservoir, which is ~600 Myr at z>1.5. Across different stellar masses, they found that the molecular gas fraction of SFGs decreases as their stellar mass increases. This finding supports the mass-quenching model (see the previous section; e.g., Peng et al., 2010; Nelson et al., 2018; Wright et al., 2019). Finally, across different ΔMSs, the insight provided by these studies was very limited due to their sparse sampling of the ΔMS < 0 parameter space. Nevertheless, extrapolations made in these studies suggest that the molecular gas fraction and depletion time of SFGs increase and decrease, respectively, as their ΔMS increases. This implies that variations in both the gas content and SFE influence the transition of SFGs from the MS to the starburst regime, as predicted by the simulation of Tacchella et al. (2016, Fig. 1.5).

The above observational studies provide insight into the gas content of galaxies across different redshifts, stellar masses, and ΔMSs. However, they have significant limitations that affect the reliability of their conclusions. First, they typically suffer from small number statistics, especially when splitting galaxies into different redshift, stellar mass, and ΔMS bins. Second, their samples are drawn from parent samples with complex selection criteria, potentially biasing the measured mean molecular gas mass. Third, they are mainly limited to galaxies that are bright enough to be individually-detected in the (sub)mm observations

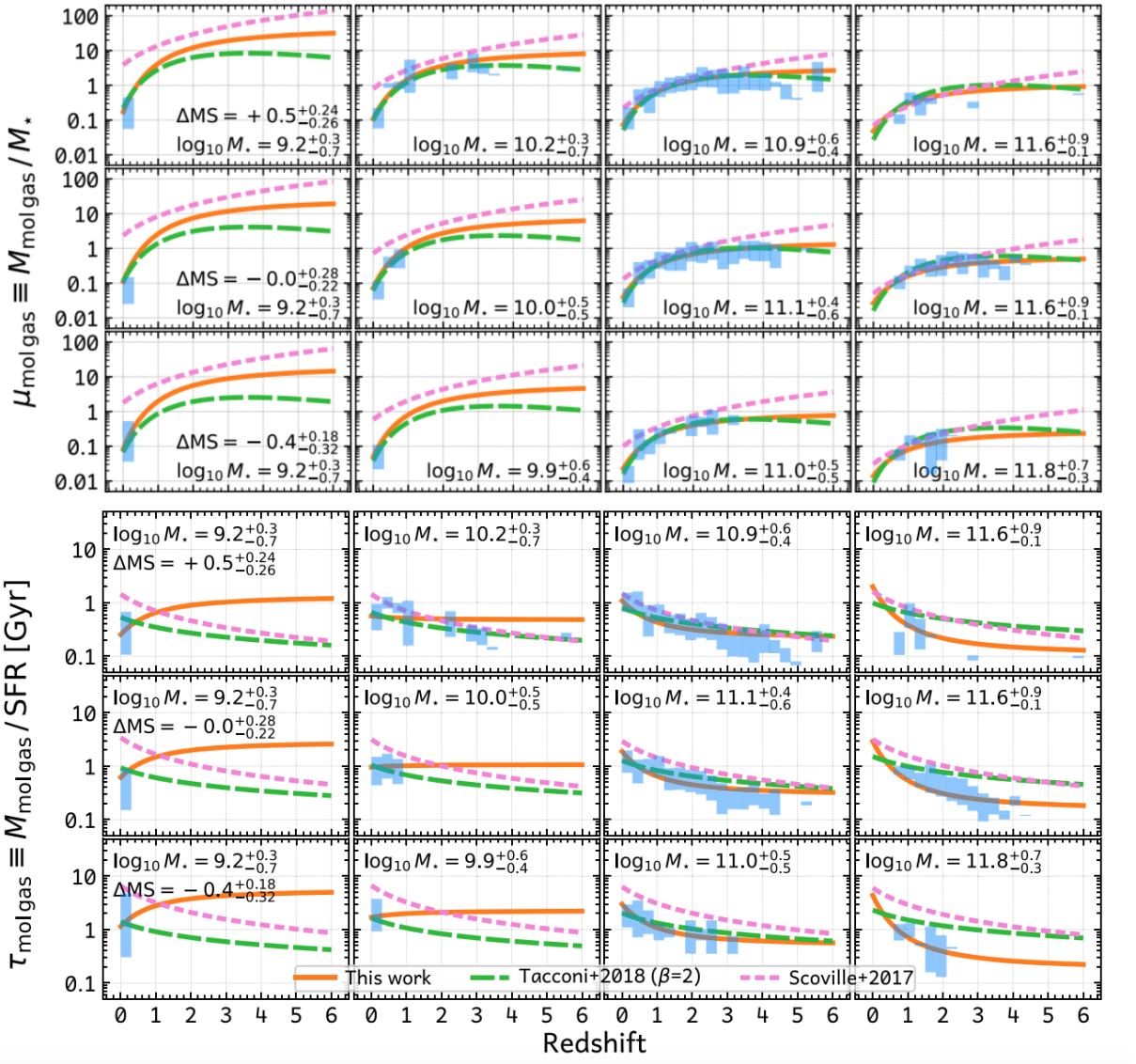

Figure 1.7: Redshift evolution of molecular gas fraction and depletion time. (*top*) The cosmic evolution of the mean molecular gas fraction in SFGs observed and fitted in Scoville et al. (2017, pink lines), Tacconi et al. (2018, green lines), and Liu et al. (2019b, orange lines). Different sub-panels correspond to different stellar mass (from left to right) and ΔMS (from bottom to top). The blue shaded regions display the distribution of measurements conducted by Liu et al. (2019b). (*bottom*) Similar to the top panel, but for the mean molecular gas depletion time. Figure taken from Liu et al. (2019b).

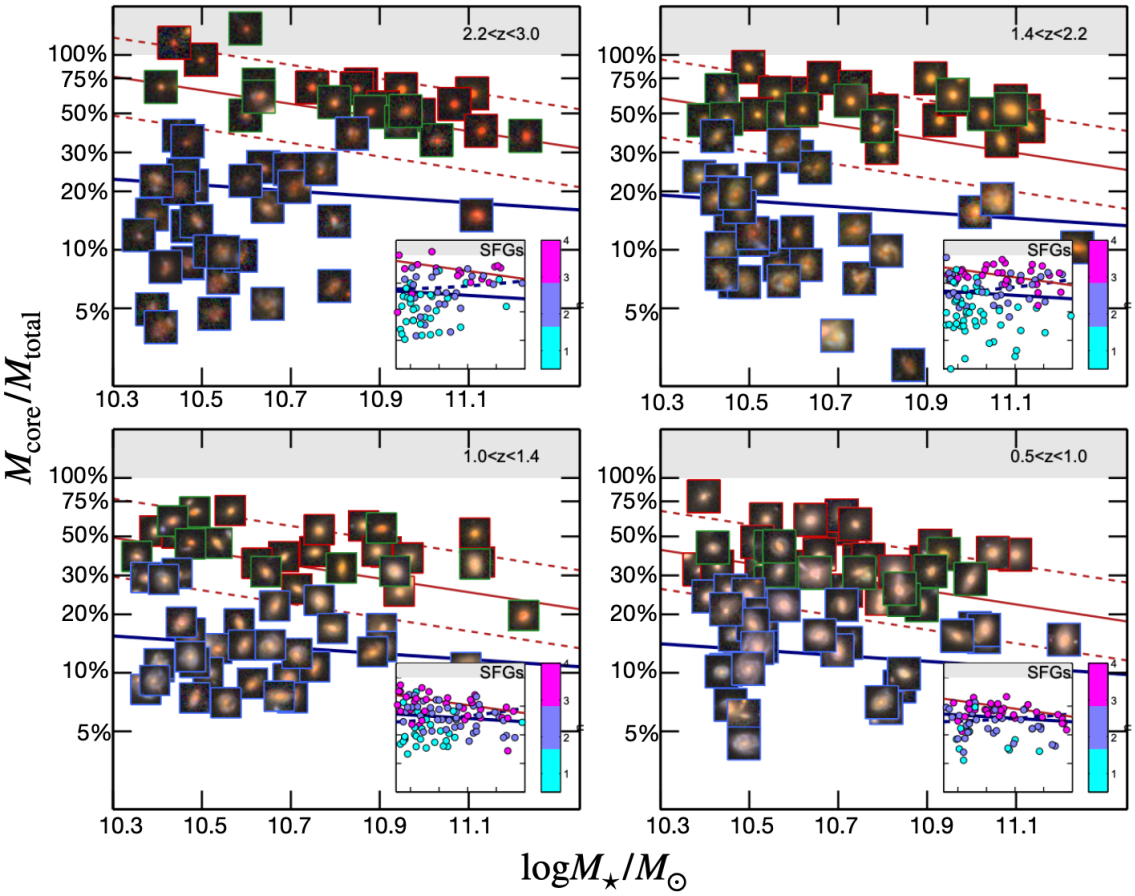

Figure 1.8: Core to total mass ratio vs. stellar mass for a group of galaxies. Different panels show different redshift bins. Red, green, and blue frame outside the stamps show galaxies that are classified as quenched, compact and MS. Blue and red solid lines show the best fit stellar mass-core to total mass ratio relations for SFG and quiescent galaxies at each redshift bin. Red dashed lines are the threshold that was used to define compact SFGs. Sub panels display the Sérsic index for all massive SFGs. Figure taken from Venemans et al. (2017).

used to infer their gas mass. These limitations restrict their scope to luminous, i.e., gas-rich, SFGs with $M_\star > 10^{10.5} M_\odot$. This implies that at the beginning of my doctoral research, our understanding of the gas content in SFGs was biased, leaving the gas content of low stellar mass, high-redshift, and low ΔMS galaxies mostly unknown. This can be observed in Fig. 1.7 where the molecular gas fraction at $M_\star < 10^{10.5} M_\odot$, $z > 1$, and ΔMS < 0.3 is based only on extrapolation. The primary aim of this doctoral research is to overcome these limitations by using an innovative Fourier space-based stacking analysis of a large dataset of ALMA observations (see Sect. 2.3.1 and Sect. 2.1) to measure the gas content of a mass-complete sample of SFGs, probing a board range of different physical properties (e.g., redshift, stellar mass, and ΔMS).

1.3.4 Sizes of star forming galaxies

To gain a better understanding of the mechanisms that drive the evolution of SFGs, it is also crucial to investigate how galaxies develop their structure and thus measure in particular their rest-frame optical size, i.e, the distribution of their stars. The optical size of SFGs was found to increase as redshift decreases and

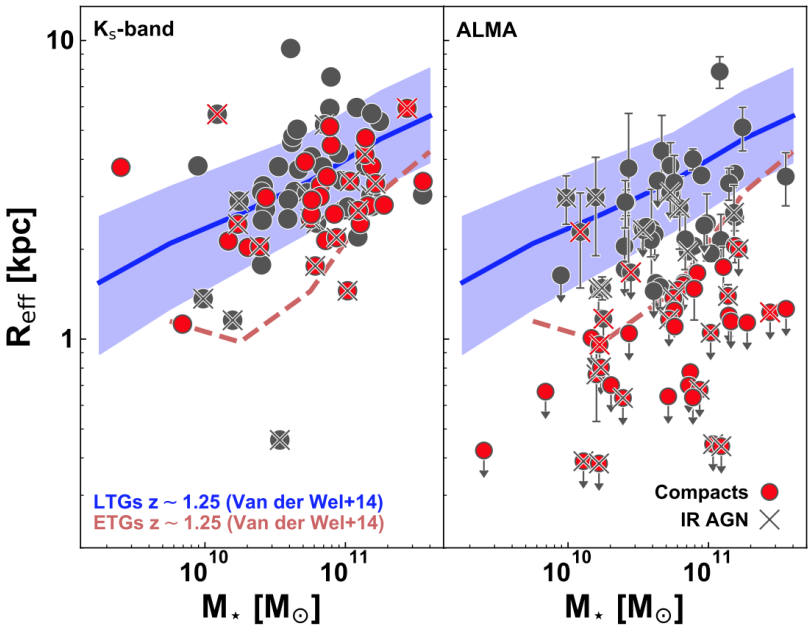

Figure 1.9: Relation between stellar mass and effective radius (left panel for K_s-band and right panel for ALMA observations) for z ~1.25 galaxies. Blue lines and shaded regions represent the van der Wel et al. (2014) relation and their scatter for SFGs at z ~1.25. Red dashed lines display the van der Wel et al. (2014) relation for early-type galaxies. Red filled circles denote compact galaxies. Crosses above the data points indicate the classification of AGN. Figure taken from Puglisi et al. (2021).

stellar mass increases (e.g., van der Wel et al., 2014; Suess et al., 2019b; Suess et al., 2019a; Yang et al., 2021). This suggests that SFGs grow up their size as they evolve along the MS (e.g., van Dokkum et al., 2013; van Dokkum et al., 2015). In addition, SFGs are found to have larger optical size (e.g., Lang et al., 2014; van der Wel et al., 2014; Barro et al., 2017; Suess et al., 2019a; Yang et al., 2021) and to possess a lower core stellar mass surface density (Σ_1) within a 1 kpc radius (e.g., Fig. 1.8, Tacchella et al., 2015; Venemans et al., 2017; Mosleh et al., 2017; Suess et al., 2021) than quiescent galaxies. These findings imply that SFGs must undergo a compaction phase before they quench into quiescent galaxies (e.g., Cheung et al., 2012; Barro et al., 2017; Venemans et al., 2017). While the aforementioned studies have measured how the stellar structures of SFGs change with redshift and along the MS, they do not explain how these changes occurred.

To delve deeper into the mechanisms underlying the size evolution of the stellar component of SFGs, some studies investigate the distribution of ongoing star formation within SFGs by measuring the size of their Hα emission. They found that the Hα size of SFGs is slightly larger than their optical size, with the difference becoming less pronounced at lower stellar masses (e.g., Nelson et al., 2016; Wilman et al., 2020; Matharu et al., 2022). However, simulations suggest that the central regions of high-redshift SFGs are dusty (Popping et al., 2022), as also supported by recent observation with the JWST (Nelson et al., 2023). This makes correcting for dust attenuation in size measurements from Hα emission at high redshifts challenging. Having in mind the effect of dust and the extreme difficulty of correcting for it, other studies have used ALMA and VLA observations in the FIR and radio wavelengths to determine the dust-unbiased size of star-forming regions in high-redshift SFGs. They found that the star-forming regions in some SFGs with $M_\star \geq 10^{10.5} M_\odot$ were more compact than their rest-frame optical size (e.g., Fig. 1.9, Elbaz

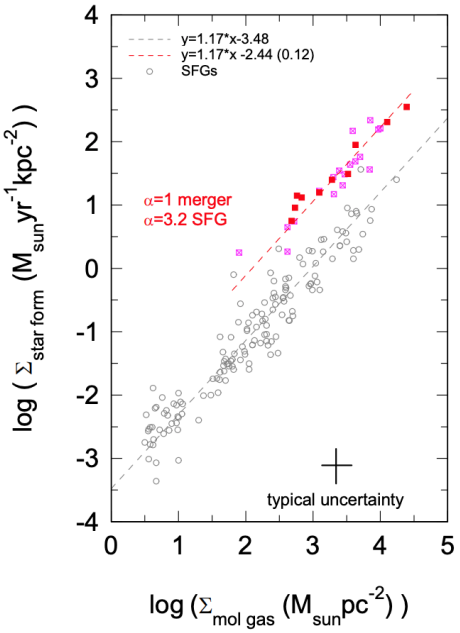

Figure 1.10: The KS relation for SFGs and merger galaxies up to z ~3.5. Open circles represent the SFGs. Magenta and red squares display the local and z > 1 merger galaxies, respectively. Gray dashed line represents the fitting result for SFGs. Red dashed lines show the fitting result for merger galaxies, assuming different values of $\alpha_{\rm CO}$ for SFGs and mergers. Figure taken from Genzel et al. (2010).

et al., 2018; Jiménez-Andrade et al., 2019; Jiménez-Andrade et al., 2021; Tadaki et al., 2020; Puglisi et al., 2021; Gómez-Guijarro et al., 2022). These findings contradict the observational results from Hα size, and this centrally enhanced star formation in SFGs is typically interpreted as the result of cold gas being accreted into their central regions, which then forms their stellar bulges (e.g., Zolotov et al., 2015; Tacchella et al., 2016). However, these studies face the same challenges as those mentioned previously concerning the gas mass of SFGs. In general, the sample that are used in these morphological studies are mainly restricted to small or biased (e.g., radio-selected, ALMA-selected, or optically-selected) samples, and thus not representative of the entire SFG population. Therefore, many questions remain unanswered regarding the morphological evolution of SFGs across cosmic time, particularly concerning where star formation occurs in relation to their stellar components. The secondary goal of this doctoral research is to investigate the star-forming size of a mass-complete sample of SFGs, probing a broad range in redshift, stellar mass, and ΔMS.

1.3.5 Kennicutt-Schmidt relation

By integrating the aforementioned measurements, i.e., SFR, gas mass, and star-forming size of high-redshift SFGs, one can examine how their SFR density scales with their gas mass density. The seminal research on this topics by Schmidt (1959) revealed a power law correlation, characterized by an index of ~ 2, between the SFR volume density ($\rho_{\rm SFR}$) and gas volume density ($\rho_{\rm gas}$) within the Galactic plane. This index suggested a specific physical condition within star-forming regions. To gain deeper insight into the mechanisms driving star formation, Kennicutt (1998b) assumed a fixed gas scale height and proposed a relation between the SFR surface density ($\Sigma_{\rm SFR}$) and gas mass surface density ($\Sigma_{M_{\rm mol}}$), the so called

Kennicutt-Schmidt (KS) relation, for a group of normal and starburst galaxies,

$$\log_{10}(\Sigma_{\rm SFR}\,[M_\odot\,{\rm yr}^{-1}\,{\rm kpc}^{-2}]) = \alpha\cdot\log_{10}(\Sigma_{M_{\rm mol}}\,[M_\odot\,{\rm pc}^{-2}]) + C, \tag{1.11}$$

where α is the power law index and C is the normalization. They found that α=1.4, which supports a scenario in which the SFR in self-gravitating disks scales with the ratio of $\rho_{\rm gas}$ to its free-fall timescale (i.e., $\propto \rho_{\rm gas}^{-0.5}$). Following Kennicutt (1998b), numerous studies on various scales, environments, galactics and extragalactics have revealed that the power law index of the KS relation might not be equal to 1.4 but vary between 0.75 to 2 (e.g., Wong and Blitz, 2002; Schuster et al., 2007; Bigiel et al., 2008; Leroy et al., 2013; Momose et al., 2013; Miura et al., 2014; Shetty et al., 2014; Wilson et al., 2019; Wang and Hwang, 2020; Ellison et al., 2021; Pessa et al., 2021; Sánchez et al., 2021). However, at large scale, i.e., > 100 pc, Bigiel et al. (2008) used observational data in a broad range of $\Sigma_{M_{\rm mol}}$, $\Sigma_{\rm SFR}$, and H I surface densities, which considered different ISM conditions (e.g., metallicity, stellar surface density, gas pressure, and galactic rotation), and found an α = 1.0. They concluded that their result on the $\Sigma_{\rm SFR}$-$\Sigma_{M_{\rm mol}}$ scaling relation reflects the filling factor of GMCs within the beam, rather than indicating changes in the physical conditions within the star-forming regions. In addition, they argued that data from normal galaxies should not be mixed with those from starburst galaxies due to their different star formation environments (e.g., Gao and Solomon, 2004; Rosolowsky and Blitz, 2005). This is the main reason their result contradicts the findings of Schmidt (1959), who found an α = 1.4. Recent studies support the conclusion of Bigiel et al. (2008), extending the measurement of the global scale KS relation up to z ∼5 (e.g., Fig. 1.10, Genzel et al., 2010; Miettinen et al., 2017b). When splitting the data into normal and starburst galaxies, they found that the power law index of the KS relation appeared to be near-unity for both types of galaxies, with the only difference being in their normalization. This supports a scenario in which the evolution of MS galaxies across cosmic time is primarily influenced by variations in their gas content rather than by changes in SFE, except in cases where their SFE is boosted by a factor of > 5 due to major merger-induced starbursts. However, Genzel et al. (2010) and Miettinen et al. (2017b) used a very limited sample of galaxies to constrain the KS relation. In addition, their results did not seem to agree with the conclusion of Liu et al. (2019b) and Tacconi et al. (2020), who find that the intense star-forming activity in starbursts is attributed not only to higher SFE but also to a higher gas mass fraction. Therefore, at the beginning of this doctoral research, it remains unclear whether the near-unity KS relation can be universally applied to galaxies across all redshifts, stellar masses, and ΔMSs. The tertiary objective of my doctoral research is to tackle this unresolved question.

CHAPTER 2

Data and methods

The above studies have revealed general aspects of galaxy evolution. However, many questions remain unanswered due to our limited understanding of the gas mass and size of high-redshift SFGs. In order to go beyond the existing literature, I first collected SFG observations from the most advanced interferometric telescope, ALMA, focusing on those SFGs that were also covered by a deep panchromatic near-infrared optical catalog, from which the stellar mass and SFR of the galaxies could be accurately inferred. This allows me to obtain mass complete galaxy samples. Finally, I developed an innovative Fourier-domain stacking analysis to measure the gas content and size of a mass-complete sample of SFGs and to carefully study the dependences of these gas reservoir properties on the stellar mass, cosmic time, and star formation mode of the galaxies using a Bayesian statistical approach.

In the following sections, I present the basic details of the instruments, data, and statistical approaches used for the research presented in this dissertation. In Sect. 2.1, I introduce the interferometric telescope used in my study and describe how it produces observational data. In Sect. 2.2, I present the data set used to infer the physical properties of my galaxy sample. Finally, in Sect. 2.3, I present the statistical approaches used to obtain the mean molecular gas mass of SFGs and to constrain their cosmic evolution.

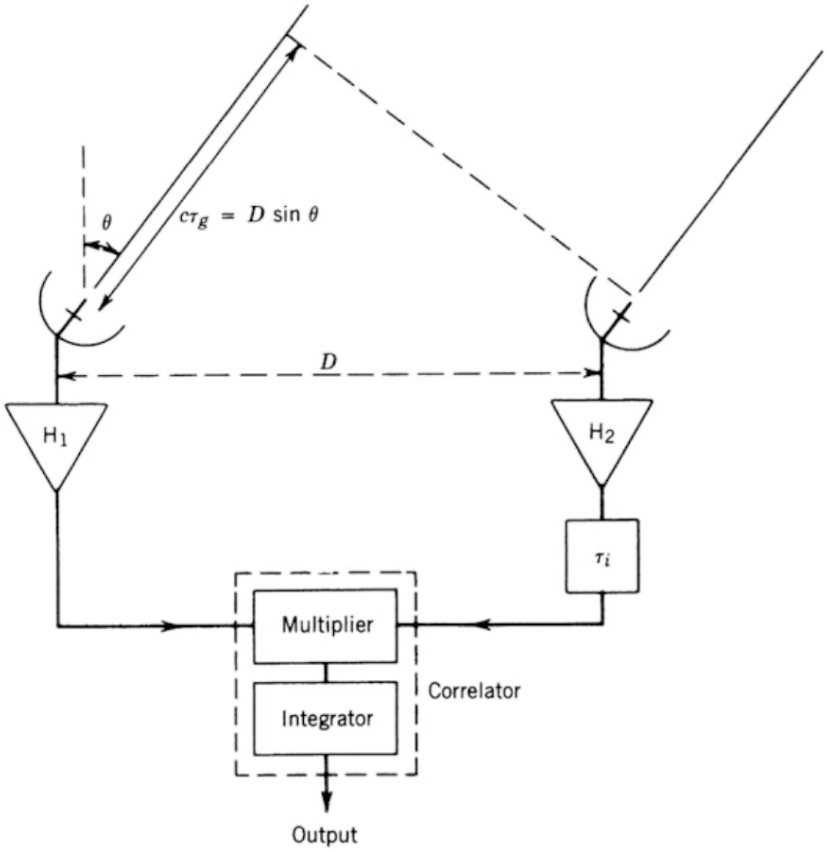

Figure 2.1: Schematic of an interferometric telescope. Several important elements of interferometric telescopes are illustrated in the figure, including the distance between two single-dish telescopes (baseline, D), source position (θ), optical path length ($D\sin\theta$), bandpass amplifiers (H1 and H2), geometric time delay (τ_g), instrumental time delay (τ_i), and correlator. Figure taken from Thompson et al. (2017).

2.1 ALMA

To measure the molecular gas mass and size of SFGs, I used their RJ dust continuum flux as a proxy (see Sect. 1.2.3). This requires a telescope operating in the (sub)millimeter wavelength range. Considering the typical angular size of the star forming region of SFGs (i.e. ∼0.4 arcsec for SFGs with $R_{\rm eff}$ ∼1.5 kpc at z ∼1.25, see Fig. 1.9), a telescope with high angular resolution ($\theta_{\rm angular}$) is required. The angular resolution of telescopes can be expressed as

$$\theta_{\rm angular} = 1.22\frac{\lambda}{D}, \tag{2.1}$$

where λ is the observed wavelength and D is the aperture diameter of the telescope. For the same aperture size, telescopes observing at 1 mm have an angular resolution that is ×1000 worse than those observing at 1 μm. Building a large-aperture single-dish telescope is always challenging, given the gravitational distortions, surface accuracy, and structural and material limitations. Even the largest single-dish telescope on Earth, the Five-hundred-meter Aperture Spherical Telescope, has an aperture diameter of "only" 500 m. To achieve high angular resolution in the submillimeter to radio wavelength range, the interferometric

Table 2.1: ALMA working band and their basic information (taken from https://www.eso.org/public/teles-instr/alma/receiver-bands/).

ALMA band	Wavelength coverage (mm)	Noise Temperature (K) specification	Frequency (GHz)	First light
1	6-8.6	32	35-50	2011
2	2.6-4.5	47	67-116	TBD
3	2.6-3.6	60	84-116	2009
4	1.8-2.4	82	125-163	2013
5	1.4-1.8	105	163-211	2016
6	1.1-1.4	136	211-275	2009
7	0.8-1.1	219	275-373	2009
8	0.6-0.8	292	385-500	2013
9	0.4-0.5	261	602-720	2011
10	0.3-0.4	344	787-950	2012

technique is used. The simplest interferometric telescope consists of a pair of antennas (Fig. 2.1), whose distance is usually called the baseline D. An advanced interferometric telescope typically contains multiple antennas, thus forming multiple baselines. By carefully processing the data collected from these antennas, one can synthesize a virtual telescope with an aperture diameter equal to the length of the longest baseline. The submillimeter interferometer ALMA follows this principle and is the one I made use of for my work.

Located in the Atacama Desert at an altitude of 5,000 meters, ALMA began observations in 2009. ALMA has a total of 66 antennas: 54 of them have a diameter of 12 m, while 12 have a diameter of 7 m. Among these antennas, fifty 12 m antennas can be flexibly moved to achieve the desired angular resolution, with the longest baseline reaching up to 16 km, providing the highest angular resolution (as fine as 20 mas at 230 GHz). However, performing observations with such long baselines faces the problem of missing flux. This problem arises because interferometric telescopes are more sensitive to structures in the source that have a size corresponding to the scales sampled by these baselines. Thus, extended structures (e.g. $> 4''.3$ at 110 GHz) corresponding to the scales sampled by shorter baselines are poorly imaged. Therefore, the remaining four 12 m and twelve 7 m antennas are configured in a special fixed short baseline configuration known as the Atacama Compact Array (ACA) (Iguchi et al., 2009). The ACA is designed to capture the flux from low spatial frequency Fourier components. Note that in this dissertation I did not include ALMA datasets observed with the ACA because the missing scales are beyond the angular size of high redshift SFGs. In addition to its high angular resolution, ALMA also has high spectral resolution (as accurate as 3.8 kHz) and working bands from 35 to 950 GHz. Details about the different bands and the corresponding noise temperature and frequency can be found in Tab. 2.1.

From signal to visibility

In each of ALMA's antennas, several physical properties are recorded during the observations. For example, each antenna measures the amplitude of the incoming signal, including not only the signal from the target source, but also the signal from so-called calibration sources, for which the emission properties (shape and flux density) are well known and can be used to calibrate the data, as will be introduced below. In addition, the time difference of the wavefronts of the signal reaching each antenna is recorded, depending on the position of the source in the sky (θ, see Fig. 2.1). The time difference can be calculated by dividing the optical path length ($D\sin\theta$) by the speed of light. By taking into account the frequency of the observation,

this time difference can be translated into a phase difference. This phase difference is a key parameter when combining data from different ALMA antennas. For each pair of ALMA antennas, the recorded data are processed by a correlator, which computes the cross-correlation function as a function of the time lag between antennas and generates the data for that baseline. These data record the spatial coherence of the incoming radiation, i.e. amplitude and phase, as a function of the baseline length and the orientation of the observation, the so-called visibility. The visibility $V(u,\ v,\ w)$ can be expressed as

$$V(u,\ v,\ w) = \int \int I(x,\ y) e^{-2\pi i \left(ux+vy+w(\sqrt{1-x^2-y^2}-1)\right)}\, dx\, dy \tag{2.2}$$

where I is the sky brightness distribution, x and y are directional cosines measured with respect to the axes u and v, and w is in the direction orthogonal to the $(u,\ v)$ plane.

Calibration

After the observations are made, several calibrations must be performed on the raw visibilities to ensure that the final data products are scientifically reliable. For example, a bandpass calibration corrects for frequency-dependent effects because antenna receivers have slightly different sensitivities at different frequencies. This calibration relies on a known source (i.e., the calibrator) with a well-understood spectrum. By comparing the observed spectrum with that expected from the bandpass calibrator, we can determine the response of the antennas at different frequencies. Flux calibration also converts the digital signal to absolute units of flux density, typically in Janskys (1 Jy=10^{-26}W $\cdot$ m^{-2} $\cdot$ Hz^{-1}). This calibration relies on a calibrator with a known and very stable emission, such as quasars and planets. By comparing the observed signal with that expected from the flux calibrator, we can determine the conversion applied to the data. Finally, gain calibration ensures that the visibilities are consistently scaled across the different observing conditions encountered during an observing run, which can last from a few minutes to hundreds of minutes. The gain of an antenna, which refers to its ability to convert incoming electromagnetic waves into electrical signals, can vary due to changes in temperature, humidity, and the performance of electronic components during the observation. This calibration relies on the regular observation of a phase calibrator with a known emission. Once the variations in gain are known, corrections are applied to the data. By measuring the variation in the phase of the calibrator at each antenna, the phases of the signal from the target source can then be accurately calibrated.

Imaging

Once the calibrations have been performed, one can obtain an image that represents the convolution of the spatial coherence function with the sampling function. This is the so-called "dirty" image, which is produced by applying the Fourier transform to the visibilities. The term "dirty" refers to the fact that the image contains sidelobes resulting from the response of the interferometer (the sampling function). Algorithms are applied to the dirty image to remove these sidelobes and to obtain an image with the correct intensity distribution, known as the "clean" image. The technique developed by Högbom (1974) is the most widely used. This algorithm identifies the brightest peak in the dirty image, subtracts a point spread function (often called the dirty beam, i.e., the sampling function) centered on that peak, and adds the subtracted function to a clean component list. This process is repeated iteratively until the peaks across the dirty image are less than the threshold (usually $\geq 3\sigma$ of the rms on the dirty image), creating a clean component list that models the true sky brightness distribution. Finally, by convolving this clean component list with the so-called clean beam, which is a Gaussian function with the same FWHM as the dirty beam

but without its sidelobes, and adding it to the residuals from the dirty image, one can obtain the cleaned image without sidelobes.

ALMA data in this doctoral research

For this doctoral thesis, I used all available ALMA band-6 and -7 archive data observed in the Cosmic Evolution Survey (COSMOS) field (see Sect. 2.2 for details). These two bands operate at wavelengths between 0.8 and 1.4 mm, allowing me to capture the RJ tail emission from the cold dust in galaxies (see Sect. 1.2.3 and the green line in Fig. 1.2). I then decided to keep only the data observed after ALMA Cycle 2. This is because the calibration software used by ALMA (i.e., the Common Astronomy Software Applications (CASA) package (McMullin et al., 2007)) has only converged on the definition of how it weights data when it is used to perform calibrations at the different visibilities after Cycle 2. The early versions of CASA assumed that the data sets were uniformly sampled in time and frequency and adopted a global weighting scale factor. This assumption did not affect the fidelity of calibration and imaging within a single ALMA project. However, when merging datasets from different ALMA projects with different bandwidths and channel counts, this assumption could lead to incongruent weight scales. Therefore, after ALMA Cycle 2, CASA adopted channel-dependent weights. This allows the combination of different ALMA projects with different channel sensitivities and bases. Since the stacking analysis in this dissertation relies on combining multiple datasets from different ALMA projects observed in different cycles, I limited my analysis to those datasets observed after Cycle 2.

2.2 The COSMOS field

To study the evolutionary history of galaxies for this thesis, I needed to focus on a region of the sky with deep panchromatic observations that would allow me to obtain the physical properties of galaxies over a wide range of cosmic time. My preferred choice is therefore the COSMOS field, which covers an area of about two square degrees of the sky, centered at R.A. (J2000) = $10^{h}00^{m}28.6^{s}$, Dec. = $+02^{\circ}12'21.0''$ (Scoville et al., 2007). This field is one of the largest ever surveyed by *HST*, and it has been observed by several telescopes at different wavelengths, ranging from X-ray (e.g., XMM-Newton; Cappelluti et al., 2009), ultraviolet (e.g., GALEX; Zamojski et al., 2007), optical (e.g., Koekemoer et al., 2007; Taniguchi et al., 2007), IR (e.g., *Spitzer*; Sanders et al., 2007), up to radio wavelengths (e.g., VLA; Schinnerer et al., 2010; Smolčić et al., 2017). This makes the COSMOS field an ideal region to study the evolutionary history of galaxies.

Optical source catalog

To obtain the stellar mass and the dust-free SFR of SFGs, in my first publication I relied on the COSMOS2015 catalog (Laigle et al., 2016). This catalog collects for the first time the X-ray to mid-IR (MIR) photometry for more than half a million galaxies within the COSMOS field. The studies associated with this catalog have used these photometric measurements to constrain the photometric redshifts, stellar masses, and dust-free SFRs of galaxies using the method described in Sections 1.2.1 and 1.2.2, respectively. After the completion of my first publication, the latest COSMOS2020 catalog (Weaver et al., 2021) became available, which I used in my second publication. This catalog uses similar approaches as the COSMOS2015 catalog to determine the physical properties of galaxies within the COSMOS field. However, this latest catalog offers many advances. It uses observations from *Gaia* to align the astrometry, resulting in an absolute astrometric uncertainty of 20 milliarcseconds. In addition, a new photometric extraction tool (`THE FARMER`)

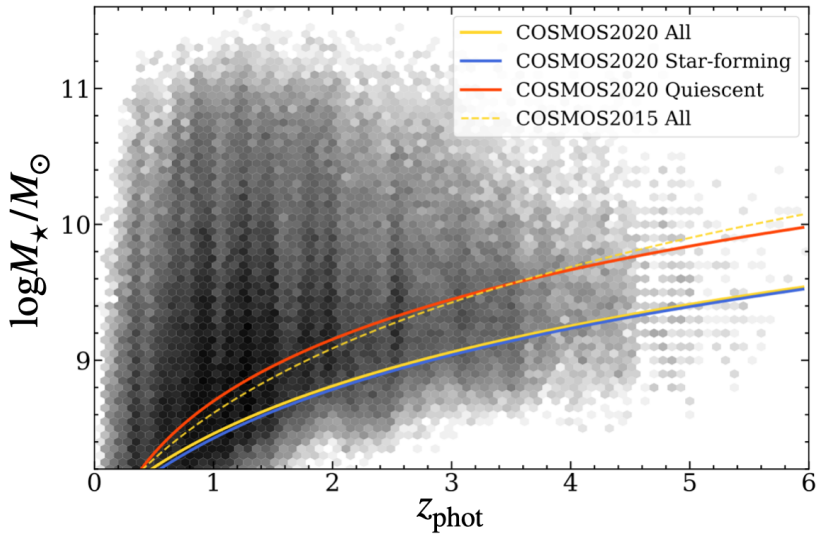

Figure 2.2: Mass completeness versus redshift in the COSMOS2020 catalog. Lines show the mass completeness limits for different types of galaxies in the COSMOS2015 and COSMOS2020 catalogs. The mass completeness limits have improved by ~0.5 dex from the COSMOS2015 to COSMOS2020 catalog at z ~3, due to advancements in photometric extraction in these latest catalog. Figure taken from Weaver et al. (2021).

was developed to refine the photometry of the galaxies. This enhancement has significantly improved the reliability of the measured photometric redshifts, e.g. galaxies with i-band apparent magnitudes between 25.0 and 27.0 have a redshift precision ($\Delta z/(1+z)$) of 0.036. In addition, this advance has reduced the uncertainties in the estimated stellar masses to less than 0.1 dex. The COSMOS2020 catalog achieves mass completeness down to $M_\star \sim 10^9 M_\odot$ even at z ~3 (Fig. 2.2).

Infrared source catalog

To constrain the dust-obscured SFR of SFGs, I used the super-deblended catalog published by Jin et al. (2018). This catalog established a state-of-the-art point spread function (PSF) fitting method to accurately measure the MIR to (sub)millimeter photometry of sources, even when the target source may be blended with nearby sources in the image due to the limited spatial resolution of infrared telescopes. I obtained the infrared luminosities of SFGs by fitting their MIR and/or FIR SEDs to the template of Chary and Elbaz (2001). The measured infrared luminosities were then converted to dust-obscured SFR using equation 1.4 from section1.2.2.

A^{3}COSMOS project

To measure the mean molecular gas content and size of SFGs by stacking analysis, I used the calibrated visibilities that were collected by the Automated mining of the ALMA Archive in the COSMOS field project (A^{3}COSMOS; Fig. 2.3, Liu et al., 2019a; Adscheid, 2023). This project starts with the collection of all publicly available ALMA archival data, including band-6 and -7 observations, which are typically used to detect dust emission in SFGs. These data were then calibrated and cleaned using the CASA package and scripts compiled by the ALMA observatory. As more ALMA data are released, the database of the A^{3}COSMOS project continues to grow. This project performs a blind search for continuum emission

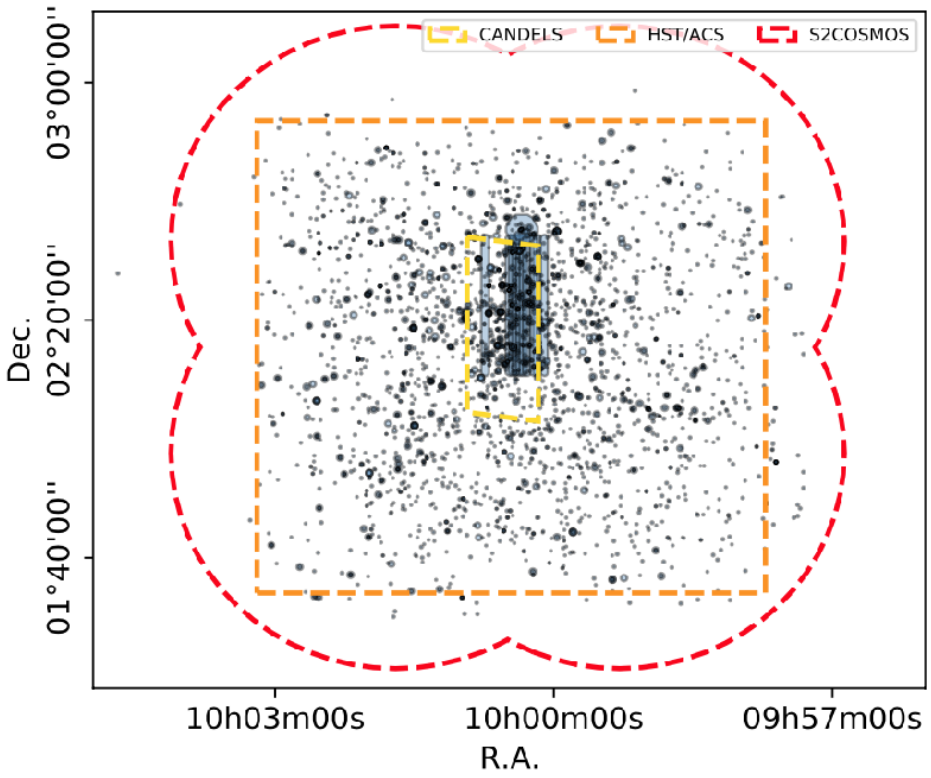

Figure 2.3: Coverage of all ALMA observations collected in the A^{3}COSMOS project until 06.06.2022. Blue shaded rectangles and blue circles are the fields with archive data from mapping and pointed observations, respectively. The size of each circle corresponds to the FWHM of the primary beam of the observation. Dashed lines display the outlines of the survey field from CANDELS (Grogin et al., 2011, yellow), COSMOS HST/ACS (Koekemoer et al., 2007, orange), and S2COSMOS (Simpson et al., 2019, red). Figure provided by Adscheid (2023).

from sources with signal-to-noise (S/N) ratio > 4.35 on the cleaned ALMA images. They then used the MAGPHYS SED fitting (da Cunha et al., 2008; da Cunha et al., 2015) to determine the physical properties, such as, stellar mass, SFR, and total IR luminosity, of the sources, resulting in the A^{3}COSMOS catalog. All the calibrated visibilities, cleaned images, and the value-added source catalog provided by the A^{3}COSMOS project can be easily accessed through a single portal.

2.3 Statistical approaches

While the A^{3}COSMOS catalog provides measurements of dust emission for massive galaxies through single detections with high significance (i.e., S/N > 4.35), only a few high redshift SFGs with $M_\star < 10^{11} M_\odot$ are detected individually in the ALMA archive. This is due to the fact that such galaxies are very faint at submillimeter wavelengths and thus difficult to detect individually. For example, at $z \sim 3$, only ~10% of the $M_\star \sim 10^{10.75} M_\odot$ SFGs have an S/N > 4 on the maps. To retrieve the faint emission of these SFGs and to measure their mean molecular gas mass and size, I used a stacking analysis. I then constrained the cosmic evolution of the mean molecular gas fraction and depletion time of these SFGs using a Bayesian statistical approach. Details of these statistical approaches are presented below.

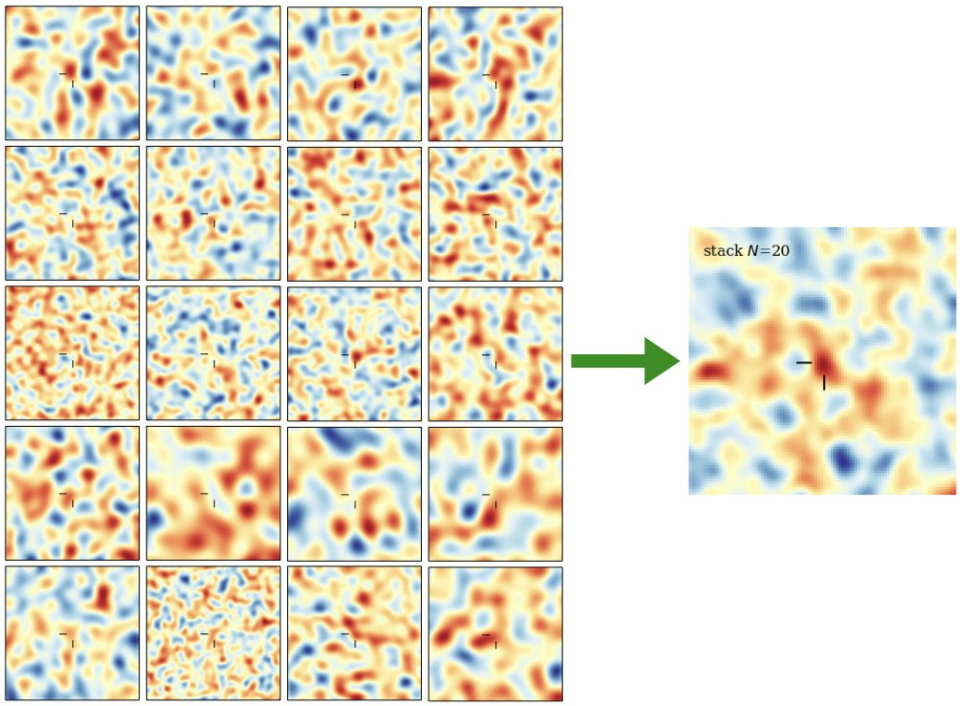

Figure 2.4: Illustration of image domain stacking analysis. The images on the left show 20 simulated ALMA observational images with the same spatial resolution but different noise, each 6 × 6 arcsec in size, with a modeled galaxy in the center. The image on the right shows the stacked result, obtained by stacking the 20 images on the left to improve the S/N of the stacked galaxies.

2.3.1 Stacking analysis

Assuming that the sources are unresolved or barely resolved, my stacking analysis groups them in a meaningful way (e.g., into bins of redshift and stellar mass), and averages the pixel values either by mean or median (e.g., Dole et al., 2006; Zheng et al., 2006; Magnelli et al., 2014; Scoville et al., 2014; Magnelli et al., 2015; Schreiber et al., 2015; Lindroos et al., 2016; Magnelli et al., 2020).

The simplest way to stack data sets is to perform the analysis in the image domain (e.g., Fig. 2.4). The pixel intensity in the stacked image can be calculated as,

$$I_{\rm stack} = \frac{\Sigma\, I_i\, \sigma_i^{-2}}{\Sigma \sigma_i^{-2}}, \tag{2.3}$$

where I_i is the pixel intensity of the i-th galaxy and σ_i is the noise level in the image of the i-th galaxy. This reduces the background noise in the stacked image and improves the S/N. However, image domain stacking only applies to data sets observed at the same frequency and angular resolution. It cannot be used to stack data from the A^{3}COSMOS project, which contains observations from different ALMA projects using different frequency settings and different array configurations, resulting in different angular resolutions in the images. Therefore, in my research, I developed a Fourier domain stacking analysis that can stack data sets from different ALMA projects. Since different galaxies were observed at different frequencies, I used the MS and starburst SED templates from Béthermin et al. (2012) and calculated the SED template flux

density ratio between the $850\times(1+z)\mu$m and the observed wavelength of the galaxy of interest,

$$\Gamma^{\rm SED} = S^{\rm SED}_{\nu_{850\times(1+z)\mu m}} \,/\, S^{\rm SED}_{\nu_{\rm obs}}. \tag{2.4}$$

With this, I scaled the ALMA visibility amplitudes from flux density ($S^{\rm ALMA}_{\nu_{\rm obs}}$) to rest-frame 850$\mu$m luminosity,

$$L_{\nu_{850\mu{\rm m,rest}}} = 4\,\pi\, D_{\rm L}^2\, S^{\rm ALMA}_{\nu_{\rm obs}} \Gamma^{\rm SED} / \,(1+z), \tag{2.5}$$

where $D_{\rm L}$ is the luminosity distance of the galaxy of interest. The above rescaling of the ALMA visibilities was done using the CASA tasks `gencal` and `applycal`. Since the galaxy of interest may not be located at the phase center during the observations, using the CASA package `STACKER` (Lindroos et al., 2015) I shifted the phase center of the visibilities to the coordinates of the galaxy,

$$V_{\rm shifted}(u,v,w) = V(u,v,w)\, e^{2\pi i B\cdot(\hat{S}_0-\hat{S}_k)/\lambda} / A_N(\hat{S}_k)\ , \tag{2.6}$$

where $V(u,v,w)$ is the visibilities, $\hat{S}_0$ is a unit vector pointing to the original phase center, $\hat{S}_k$ is a unit vector pointing to the position of the stacked galaxy, $\mathrm{A}_N(\hat{S}_k)$ is the primary beam attenuation in the direction of $\hat{S}_k$, B is the visibility baseline. Finally, I concatenated these visibilities together using the CASA task `concat`. Details of the scripts for the above process are presented in the Appendix A.

Rest-frame 850 μm luminosity and size

The rest-frame 850 μm luminosity and size of the stacked galaxy were measured using two different approaches. First, I measured them in the Fourier domain by fitting a single component model, either a Gaussian disk or a point source, to the stacked visibilities using the CASA task `uvmodelfit`. Alternatively, I measured them in the image domain by using the CASA task `tclean` to image the stacked data set. I selected Briggs natural weighting and cleaned the image down to a 3σ threshold, and fit a single 2D component model to the cleaned image using the Python Blob Detector and Source Finder (`PyBDSF`) package (Mohan and Rafferty, 2015). After the measurements, I define the effective radius of the stacked galaxy, $R_{\rm eff} \approx FWHM/2.43$, following Jiménez-Andrade et al. (2019). Here, $FWHM$ denotes the beam-deconvolved full width at half maximum of the major axis output by `uvmodelfit` or `PyBDSF`. I then expressed the mean size of the stacked galaxy in terms of circularized radii, $R^{\rm circ}_{\rm eff}$,

$$R^{\rm circ}_{\rm eff} = R_{\rm eff} \times \sqrt{\frac{b}{a}}, \tag{2.7}$$

where b/a is the axis ratio measured with `uvmodelfit` or `PyBDSF`. Note that the rest-frame 850 μm luminosity and size obtained with `uvmodelfit` and `PyBDSF` agree within the uncertainties.

From rest-frame 850 μm luminosity to molecular gas mass

I converted the rest-frame 850 μm luminosity measurements to molecular gas mass. I follow the gas mass conversions as previously introduced in Sect. 1.2.3. In the first paper of my doctoral research (Sect. 3 and Appendix B), I used the H17 approach. This approach was chosen because I wanted to compare my results with those of Liu et al. (2019b), who also used the H17 method to estimate the molecular gas mass of SFGs. However, as pointed out in Sect. 1.2.3, this approach, which assumes a constant light-to-gas mass ratio, may not be suitable for high-redshift and low-stellar-mass galaxies due to their lower metallicities. Therefore, in

the second paper of this doctoral research (Sect. 4 and Appendix C), I used the B12 and L11 approaches instead.

2.3.2 MCMC analysis

In order to accurately constrain the cosmic evolution of the mean molecular gas fraction and depletion time of SFGs as a function of their stellar mass and redshift, it is crucial to carefully choose the approach to perform the fit. The simplest approach to numerically test the goodness of fit of a model to the data is to find the minimum value of Pearson's chi-squared test,

$$\chi^2 = \Sigma \frac{(O_i - E_i)^2}{E_i}, \tag{2.8}$$

where χ^2 is Pearson's cumulative test statistic, O_i is the i-th observation, and E_i is the expected value from the model corresponding to the same variables as O_i. However, this approach has its limitations, especially when the given variables do not follow a normal distribution.

To address this issue, in this doctoral research, I used the Markov Chain Monte Carlo (MCMC) method – a Bayesian statistical technique – to find the best fit. In this context, the Markov chain implies that the i-th sample (for $i > 1$) is generated randomly but depends on the state reached in the (i-1)-th sample, i.e., the sample generated during the process are autocorrelated. The Monte Carlo in this context refers to the use of random sampling and probabilistic reasoning to estimate parameters. I use the Python package `emcee` (Foreman-Mackey et al., 2013) to perform the MCMC fit.

CHAPTER 3

A^{3}COSMOS: A census on the molecular gas mass and extent of main-sequence galaxies across cosmic time (Summary)

This chapter is a summary of the article published in Astronomy and Astrophysics (A&A) as:

Wang, T.-M., Magnelli B., Schinnerer E., Liu D., Modak Z. A., Jiménez-Andrade E. F., Karoumpis C., Kokorev V., and Bertoldi F. (2022), A&A, 660, A142.

In this publication, I performed the stacking analysis on the ALMA dataset and the conducted scientific analysis under the supervision of Magnelli and Bertoldi. Modak provided the script for simulating ALMA observations to test the stacking analysis. The other co-authors contributed to the interpretation of the results and provided comments and revisions to the final manuscript. The refereed article can be found in Appendix B of this document, while the open access version is found under the reference arXiv:2201.12070v1.

3.1 Context

To understand the evolutionary history of SFGs over cosmic time, precise measurements of the gas reservoir that fuels their star formation are required. Although some studies have attempted to measure these physical properties of SFGs at different redshifts, stellar masses, and ΔMSs (e.g., Carilli and Walter, 2013; Sargent et al., 2014; Schinnerer et al., 2016; Miettinen et al., 2017a; Scoville et al., 2017; Tacconi et al., 2018; Tacconi et al., 2020; Gowardhan et al., 2019; Liu et al., 2019b; Wiklind et al., 2019; Cassata et al., 2020), they all show evidence of selection bias in their galaxy samples (Fig. 3.1). Indeed, it is difficult to detect the gas reservoir of high redshift and low stellar mass SFGs individually, which makes the measurement of the mean molecular gas mass of SFGs with a mass complete sample challenging.

3.2 Aims

We aim to constrain for the first time the cosmic evolution of the mean molecular gas mass and size of a mass complete sample of SFGs with $M_\star > 10^{10} M_\odot$ at $0.4 < z < 3.6$.

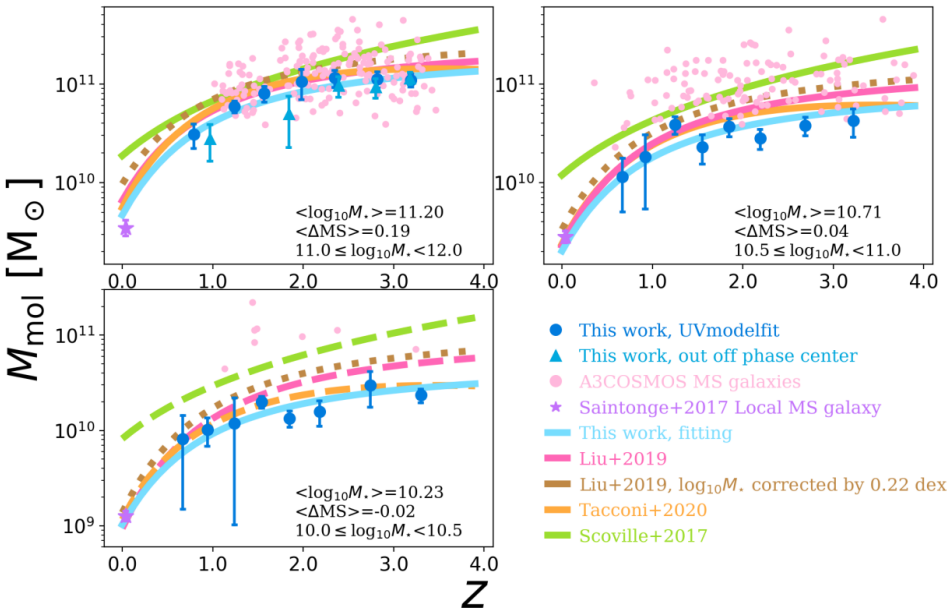

Figure 3.1: Illustration of the selection bias in galaxy samples in literature studies. The panels show the redshift evolution of the molecular gas mass in MS galaxies at different stellar masses. Symbols for lines and data points are shown in the legend. One can directly observe that MS galaxies detected individually in ALMA images (pink circles) are biased towards high stellar masses, high ΔMSs, and low redshifts. This figure is taken from Wang et al. (2022).

3.3 Methods

In the COSMOS2015 catalog, we obtained the stellar mass and redshift of SFGs and selected only those above the mass completeness limits of this catalog. The SFR of these SFGs was calculated following the ladder of the SFR indicator as advocated by Wuyts et al. (2011). We used the MS calibration of Leslie et al. (2020) and kept only SFGs with -0.5 ≤ ΔMS < 0.5. These SFGs were then matched with all available ALMA band-6 and -7 observations from the A^{3}COSMOS project, retaining only those observed by ALMA. We developed an innovative Fourier domain stacking analysis and applied it to this ALMA dataset. This stacking analysis, performed on the Rayleigh-Jeans dust continuum emission, allows us to measure the mean molecular gas mass and size of MS galaxies at the redshift and stellar mass where galaxies are difficult to detect individually. Finally, the empirical relationship between the cosmic evolution of the mean molecular gas mass and the depletion time is derived using the Markov chain Monte Carlo method.

3.4 Results

The molecular gas mass of MS galaxies evolves with redshift and stellar mass. The mean molecular gas fraction of MS galaxies decreases by a factor of ~ 24 from $z \sim 3.2$ to $z \sim 0$ at all stellar masses. At a given redshift, it decreases with stellar mass at about the same rate as the decrease in the specific star formation rate (SFR/$M_\star$) of MS galaxies. The molecular gas depletion time of MS galaxies remains roughly constant at $z > 0.5$ with a value of 300–500 Myr, but increases by a factor of ~ 3 from $z \sim 0.5$ to $z \sim 0$. The star-forming size of MS galaxies remains roughly constant over cosmic time and stellar mass, with an average circularized half-light radius of ~2.2 kpc. Combining these measurements, we derived the KS

relation, i.e. the $\Sigma_{M_{\rm mol}} - \Sigma_{\rm SFR}$ relation, of MS galaxies and found a slope of ~ 1.13.

3.5 Conclusions

At first order, at high redshifts and low stellar masses, our measured mean molecular gas masses of MS galaxies are generally lower than predictions from previous studies. This discrepancy can be explained by the fact that those studies were largely biased towards individually detected MS galaxies with massive gas reservoirs (e.g. Fig. 3.1). The molecular gas content of MS galaxies regulates their star formation over cosmic time, with variations in their star formation efficiency playing a secondary role. This finding is supported by an apparently universal MS-only and near-unity slope of the KS relation, which is also found in Genzel et al. (2010) and Miettinen et al. (2017b). Continuous cold gas accretion to MS galaxies is required to sustain their star formation throughout their > Gyr evolution. Without such cold gas accretion, their star formation would cease in a few hundred million years, as indicated by their short mean molecular gas depletion times. Finally, the compact FIR sizes of MS galaxies relative to their optical sizes, as discovered in our study, could indicate the formation of galaxy bulges (e.g., Fisher, 2006; Zolotov et al., 2015; Goldbaum et al., 2016; Tacchella et al., 2016; Tonini et al., 2016).

CHAPTER 4

A^{3}COSMOS: Dissecting the gas content of star-forming galaxies across the main sequence at 1.2 ≤ z < 1.6 (Summary)

This chapter is a summary of the article published in Astronomy and Astrophysics (A&A) with reference:

Wang T.-M., Magnelli B., Schinnerer E., Liu D., Jiménez-Andrade E. F., Karoumpis C., Adscheid S., and Bertoldi F. (2023), A&A, 47219-23 (in print).

In this publication, I performed the stacking analysis on the ALMA data and the scientific analysis under the supervision of Magnelli and Bertoldi. The other coauthors contributed to the interpretation of the results and provided comments and revisions to the final manuscript. The published article can be found in Appendix C of this thesis, while the open access version can be found under reference arXiv:2311.11832v1.

4.1 Context

At all redshifts, most SFGs reside on the main sequence (MS), which has a scatter of ~0.3 dex in the SFR (e.g., Schreiber et al., 2015; Leslie et al., 2020; Leja et al., 2022; Popesso et al., 2023). However, some of SFGs are outliers with extreme star formation (e.g., Schreiber et al., 2015; Silverman et al., 2018). To deepen our understanding of the mechanisms driving these features, it is essential to study the gas mass and size of SFGs across a board range of ΔMS with mass-complete samples. However, due to instrumental limitations, such a study has not yet been conducted.

4.2 Aims

The aim of this work is to understand the physical mechanisms that drive the scatter of the MS and starburst with a group of mass-complete $M_\star > 10^{9.5} M_\odot$ SFGs at $1.2 \leq z < 1.6$.

4.3 Methods

We selected SFGs and obtained their stellar mass and redshift from the COSMOS2020 catalog, and calculated their SFRs following the ladder of SFR indicator as advocated by Wuyts et al. (2011). The ΔMS of these SFGs were defined following the MS calibration of Leslie et al. (2020). We cross-matched

these SFGs with the available ALMA band-6 and -7 observations from the A^{3}COSMOS project, keeping only those that have been observed by ALMA. Applying the Fourier-domain stacking analysis to ALMA datasets, it allows us to accurately measure the mean molecular gas mass and size of SFGs down to stellar mass $\sim 10^{9.5} M_{\odot}$, where none of the MS galaxies can be individually detected in their ALMA images. For our selected SFGs, we also apply an image-domain stacking analysis on their *HST* i-band and UltraVISTA J- and K_s-band images. This enables us to probe the distribution of their stellar components. The stellar mass size of MS galaxies is acquired by applying the $R_{\rm half-stellar-light}$-to-$R_{\rm half-stellar-mass}$ conversion at rest 5000 angstrom of Suess et al. (2019a) to their rest-frame optical sizes. We then compare the modeled stellar mass size of MS galaxies to their star-forming size derived from our ALMA stacking analysis.

4.4 Results

The mean molecular gas fraction of SFGs increases by a factor of ∼1.4 as they move across the MS (from ΔMS∼-0.2 to ΔMS∼0.2), while the mean molecular gas depletion time decreases by a factor of ∼1.8 simultaneously. The mean molecular gas fraction of MS galaxies decreases by a factor of ∼7 as stellar mass increases from $M_{\star} \sim 10^{9.7} M_{\odot}$ to $\sim 10^{11.3} M_{\odot}$, while their mean molecular gas depletion time remains roughly constant across all stellar massed. The majority of galaxies on the MS have $R_{\rm FIR} \approx R_{\rm stellar}$. As SFGs transition from the MS to the starburst region (from ΔMS∼0 to ΔMS∼0.7), their mean molecular gas fraction increases by a factor of ∼2.1, and their mean molecular gas depletion time decreases by a factor of ∼3.3. This is accompanied by a transformation in their optical morphology from disk-like to merger-like and a decrease in star-forming size from ∼2.5kpc to ∼1.4kpc. MS galaxies exhibit a larger size dispersion compared to that of starburst galaxies. This may hint at hidden starburst within the MS. Finally, MS and starburst galaxies follow the same KS relation, i.e., the $\Sigma_{M_{\rm mol}} - \Sigma_{\rm SFR}$ relation, with an inferred slope of ∼1.13.

4.5 Conclusions

The scatter on the MS is caused by variations in both the star formation efficiency and molecular gas fraction of galaxies. Our findings support the simulation of Tacchella et al. (2020), which suggests that SFGs may cycle through complex star formation mechanisms over several Gyr. In their simulation, the star formation efficiency of MS galaxies can be elevated due to minor mergers or disk instabilities, leading to an increase in their ΔMS (e.g., Cacciato et al., 2012; Dekel and Burkert, 2014; Lapiner et al., 2023). Conversely, star formation within MS galaxies can reduce their gas fraction, thus decreasing their SFR and ΔMS (e.g., Feldmann and Mayer, 2015; Spilker et al., 2019). On the MS, the mean molecular gas fraction decreases with increasing stellar mass. This could be linked to variations in their cold gas accretion and can explain the origin of the bending of the MS (e.g., Daddi et al., 2022). Our finding that MS galaxies have $R_{\rm FIR} \approx R_{\rm stellar}$, but a much larger optical size, indicates that they have strong radial dust attenuation gradient. Finally, our observations suggest that strarburst are induced by major mergers. In this process, the star formation efficiency and molecular gas fraction increase. The latter can be understood as the surrounding H I gas of the SFGs could become unstable during the merger and fall into the central region of the merger system (e.g., Weston et al., 2017; Blumenthal and Barnes, 2018; Sivasankaran et al., 2022), transforming into additional molecular gas content (e.g., Yu et al., 2022).

CHAPTER 5

Summary and outlook

5.1 Summary

By integrating the results of this dissertation with those from the literature, we can get a clearer picture of the evolutionary history of our universe. Galaxies are thought to have formed at $z \sim 10$ (e.g., Bromm and Yoshida, 2011; Chen et al., 2022) and later evolved mostly in isolation. They continue to accrete fresh gas from the cosmic web, which fuels their star formation during their evolution, as suggested by observations of their gas content (e.g., Liu et al., 2019b; Tacconi et al., 2020; Wang et al., 2022; Wang et al., 2023).

In chapter 3 I examined the evolution of MS galaxies at $0.4 \leq z < 3.6$, focusing on their mean molecular gas fraction and depletion time. Between $z \sim 3.6$ and $z \sim 0.4$, they maintain a relatively high and stable mean molecular gas fraction and a short and constant mean molecular gas depletion time, i.e., 300–500 Myr, indicating the need for cold accretion from the cosmic web. For a given redshift, galaxies with higher stellar mass tend to have lower mean molecular gas fractions. This finding supports the interpretation that the flattening of the MS at high masses is due to a decrease in their gas accretion rate, which could be related to the mass-quenching model (e.g., Peng et al., 2010; Nelson et al., 2018; Wright et al., 2019). In measuring the size of these MS galaxies, I found that their star-forming size is constant, i.e. ~2.2kpc, and compact at all redshifts and stellar masses. This is often interpreted as the accretion of cold gas into their center, forming the stellar bulges (e.g., Fisher, 2006; Zolotov et al., 2015; Goldbaum et al., 2016; Tacchella et al., 2016; Tonini et al., 2016). Overall, the evolution of MS galaxies in this cosmic epoch is primarily dominated by variations in their gas accretion rate and content, as supported by my finding of a near-unity KS relation slope of ~1.13.

In chapter 4 I studied the same physical properties as in chapter 3, but for $M_\star \geq 10^{9.5} M_\odot$ SFGs at $z \sim 1.4$ and $-0.7 \leq \Delta\text{MS} < 1.3$. Across the MS, i.e. from $\Delta\text{MS} \sim -0.2$ to $\Delta\text{MS} \sim 0.2$, the mean molecular gas fraction of SFGs increases by a factor of ~1.4, while their depletion time decreases by a factor of ~1.8. This reflects a complex star formation scenario as suggested by Tacchella et al. (2020). For example, the star formation efficiency of MS galaxies can be enhanced by small mergers or disk instabilities, increasing their ΔMS (e.g., Cacciato et al., 2012; Dekel and Burkert, 2014; Lapiner et al., 2023). Conversely, star formation can reduce the gas fraction of MS galaxies, thereby decreasing their SFR and ΔMS (e.g., Feldmann and Mayer, 2015; Spilker et al., 2019). MS galaxies can experience these cycles over a few Gyr.

In some rare cases, MS galaxies move into the starburst region, i.e. from $\Delta\text{MS} \sim 0$ to $\Delta\text{MS} \sim 0.7$, via mergers, as revealed by our morphology measurements. This process includes an increase in the mean molecular gas content by a factor of ~2.1, a decrease in the mean molecular gas depletion time by a factor of ~3.3, and a decrease in star formation size from ~2.5 kpc to ~1.4 kpc.

The increased molecular gas content and decreased star formation region size indicate instability in the surrounding H I gas. This gas loses its angular momentum during galaxy collisions, falls into the deep gravitational potential region of the system (e.g., Weston et al., 2017; Blumenthal and Barnes, 2018; Sivasankaran et al., 2022), and changes into additional molecular gas (e.g., Yu et al., 2022). This highly unstable molecular gas then turns into stars, but with a higher star formation efficiency than that observed in MS galaxies.

Finally, I measured the optical size of SFGs, modeled their half-mass size, and found that their half-mass size is similar to their star-forming extend, but smaller than their optical size. I conclude that this relatively large optical size reflects strong dust extinction within SFGs (e.g., Popping et al., 2022).

5.2 Outlook

The Fourier domain stacking analysis developed in this thesis allows us to accurately measure the mean molecular gas mass and size of SFGs over a wide range of redshifts, stellar masses, and ΔMS. However, several questions remain unanswered, in particular those related to gas mass and size measurements of galaxies at redshifts, stellar masses, and ΔMS beyond the limits explored in this work. This is mainly due to insufficient ALMA data observed in the COSMOS field, i.e. the signal-to-noise ratio of the stacked image correlates with the square of the number of visibilities used in the stacking analysis. As more ALMA data observed in the COSMOS field become available in the future, and with the advent of next-generation telescopes, I expect that these unresolved issues can be addressed. Below, I outline some remaining questions that could be addressed in the future using the statistical approach developed during my Ph.D. work.

What role does the gas content of SFGs play during morphological quenching?

Studies have found that the morphological distribution of galaxies (i.e., the percentage of galaxies that are disks, spheroids, irregular, or bulge+disk) depends on redshift and stellar mass (e.g., Ferreira et al., 2022; Huertas-Company et al., 2023). The morphology of a galaxy reflects the dynamics of its internal components, such as stars and gas, and could be related to its star formation evolution, including disk formation by gas accretion or destruction by mergers. Leslie et al. (2020) found that the mass quenching of SFGs is associated with a change in their morphology. In particular, bulge-dominated late-type galaxies contribute more to the total SFR at low redshifts and high stellar masses. This could be related to the morphological quenching model (e.g., Martig et al., 2013), where bulge-dominated SFGs stabilize their molecular clouds and thus regulate star formation. To confirm this interpretation, one needs to categorize galaxies based on their morphology, stellar mass, and SFR, and then study their gas mass and size. However, this categorization would divide galaxies into bins, thereby reducing the signal-to-noise ratio of the stacked galaxy. Therefore, such a study has not yet been done.

What are the mechanisms that trigger starbursts at redshifts beyond the scope of this study?

The cosmic major merger fraction has been studied in the literature (e.g., Xu et al., 2012; Tasca et al., 2014; Ventou et al., 2017; Duncan et al., 2019; Romano et al., 2021). These studies found that the major merger fraction increases dramatically from z ~0 to z ~3, and decreases smoothly from z ~3 to z ~6. Their results suggest a variation in the environments of galaxies at different cosmic times. In this dissertation, I have successfully linked starburst galaxies to merger events and explored the mechanisms that trigger starbursts at z ~1.4. However, it remains unclear whether my conclusions apply to starburst galaxies at other redshifts.

Future studies using more ALMA datasets containing high-redshift SFGs with a large dynamical range in their ΔMS can address this issue. This will be made possible in particular by future deep and large surveys with JWST, such as the COSMOS Web program (Casey et al., 2023).

What are the physical mechanisms that trigger star formation in SFGs at their birth?

In this thesis, I have provided precise gas mass measurements for a group of mass-complete SFGs with redshifts up to z ~3.6 and stellar masses down to $M_\star \sim 10^{9.5} M_\odot$. This allows us to understand a part of the evolutionary history of SFGs. However, it is not clear whether my results can be applied to the very beginning of galaxy formation at z ~10 and with total halo mass ~$10^8 M_\odot$ (e.g., Bromm and Yoshida, 2011; Chen et al., 2022). In addition, studies have argued that the RJ dust continuum approach may not be suitable for measuring the gas mass in SFGs at $z > 5$ (e.g., Zhang et al., 2016; Vizgan et al., 2022), because the cold dust in SFGs could thermally couple with the increasing CMB temperature. They suggest that the measurement of the ionized carbon (C II) emission line at rest-frame 158 μm could be a promising approach to estimate the gas mass of high redshift SFGs (e.g., Dessauges-Zavadsky et al., 2020; Vizgan et al., 2022; Heintz et al., 2023). Future studies could potentially address this issue by applying a stacking analysis to the C II emission line data from a group of mass-complete high redshift SFGs, especially as more ALMA datasets are released.

Bibliography

Adscheid, S. (2023), "A^{3}COSMOS 2.0: Continuum Source Catalogues and Multi-band Number Counts".

Ahn, K. and B. D. Smith (2018), *Formation of First Galaxies inside Density Peaks and Voids under the Influence of Dark Matter-Baryon Streaming Velocity. I. Initial Condition and Simulation Scheme*, ApJ **869**, 76 76.

Algera, H. S. B. et al. (2023), *The ALMA REBELS survey: the dust-obscured cosmic star formation rate density at redshift 7*, MNRAS **518** 6142.

Arabadjis, J. S. and D. O. Richstone (1998), *The Dynamical Evolution of Dense Rotating Systems: Paper II. Mergers and Stellar Evolution*, arXiv e-prints, astro-ph/9810193 astro.

Aschenbrenner, P., N. Przybilla and K. Butler (2023), *Quantitative spectroscopy of late O-type main-sequence stars with a hybrid non-LTE method*, A&A **671**, A36 A36.

Babcock, H. W. (1939), *The rotation of the Andromeda Nebula*, Lick Observatory Bulletin **498** 41.

Barro, G. et al. (2017), *Structural and Star-forming Relations since $z \sim 3$: Connecting Compact Star-forming and Quiescent Galaxies*, ApJ **840**, 47 47.

Barrufet, L. et al. (2023), *The ALMA REBELS Survey: the first infrared luminosity function measurement at z 7*, MNRAS **522** 3926.

Bauermeister, A., L. Blitz and C.-P. Ma (2010), *The Gas Consumption History to Redshift 4*, ApJ **717** 323.

Bergvall, N. et al. (2016), *Local starburst galaxies and their descendants. Statistics from the Sloan Digital Sky Survey*, A&A **587**, A72 A72.

Bertone, G. and D. Hooper (2018), *History of dark matter*, Reviews of Modern Physics **90**, 045002 045002.

Béthermin, M. et al. (2012), *A Unified Empirical Model for Infrared Galaxy Counts Based on the Observed Physical Evolution of Distant Galaxies*, ApJ **757**, L23 L23.

Bigiel, F. et al. (2008), *The Star Formation Law in Nearby Galaxies on Sub-Kpc Scales*, AJ **136** 2846.

Blumenthal, K. A. and J. E. Barnes (2018), *Go with the Flow: Understanding inflow mechanisms in galaxy collisions*, MNRAS **479** 3952.

Bolatto, A. D., M. Wolfire and A. K. Leroy (2013), *The CO-to-H_2 Conversion Factor*, ARA&A **51** 207.

Bouché, N. et al. (2010), *The Impact of Cold Gas Accretion Above a Mass Floor on Galaxy Scaling Relations*, ApJ **718** 1001.

Bouwens, R. J., G. Illingworth, R. S. Ellis, P. Oesch and M. Stefanon (2022), *z 2-9 Galaxies Magnified by the Hubble Frontier Field Clusters. II. Luminosity Functions and Constraints on a Faint-end Turnover*, ApJ **940**, 55 55.

Brax, P. (2018), *What makes the Universe accelerate? A review on what dark energy could be and how to test it*, Reports on Progress in Physics **81**, 016902 016902.

Bromm, V. and N. Yoshida (2011), *The First Galaxies*, ARA&A **49** 373.

Bruzual, G. and S. Charlot (2003), *Stellar population synthesis at the resolution of 2003*, MNRAS **344** 1000.

Buzzo, M. L. et al. (2022), *The stellar populations of quiescent ultra-diffuse galaxies from optical to mid-infrared spectral energy distribution fitting*, MNRAS **517** 2231.

Cacciato, M., A. Dekel and S. Genel (2012), *Evolution of violent gravitational disc instability in galaxies: late stabilization by transition from gas to stellar dominance*, MNRAS **421** 818.

Calabrò, A. et al. (2019), *Merger induced clump formation in distant infrared luminous starburst galaxies*, A&A **632**, A98 A98.

Caliendo, J. N. et al. (2021), *Early Science with the Large Millimeter Telescope: Constraining the Gas Fraction of a Compact Quiescent Galaxy at $z = 1.883$*, ApJ **910**, L7 L7.

Cappelluti, N. et al. (2009), *The XMM-Newton wide-field survey in the COSMOS field. The point-like X-ray source catalogue*, A&A **497** 635.

Carilli, C. L. and F. Walter (2013), *Cool Gas in High-Redshift Galaxies*, ARA&A **51** 105.

Casey, C. M. et al. (2023), *COSMOS-Web: An Overview of the JWST Cosmic Origins Survey*, ApJ **954**, 31 31.

Cassata, P. et al. (2020), *ALMA Reveals the Molecular Gas Properties of Five Star-forming Galaxies across the Main Sequence at 3*, ApJ **891**, 83 83.

Chary, R. and D. Elbaz (2001), *Interpreting the Cosmic Infrared Background: Constraints on the Evolution of the Dust-enshrouded Star Formation Rate*, ApJ **556** 562.

Chen, K.-J. et al. (2022), *Impact of the Population III Supernova Remnants on the Primeval Galaxy Formation*, arXiv e-prints, arXiv:2211.06016 arXiv:2211.06016.

Cheung, E. et al. (2012), *The Dependence of Quenching upon the Inner Structure of Galaxies at $0.5 <= z < 0.8$ in the DEEP2/AEGIS Survey*, ApJ **760**, 131 131.

Cibinel, A. et al. (2019), *Early- and late-stage mergers among main sequence and starburst galaxies at $0.2 \leq z \leq 2$*, MNRAS **485** 5631.

Coles, P. (2001), "Large-scale Structure, Theory and Statistics", *Phase Transitions in the Early Universe: Theory and Observations*, ed. by H. J. de Vega, I. M. Khalatnikov and N. G. Sanchez, vol. 40 217.

Crowther, P. (2012), *Birth, life and death of massive stars*, Astronomy and Geophysics **53** 4.30.

Curti, M. et al. (2023), *The chemical enrichment in the early Universe as probed by JWST via direct metallicity measurements at $z \sim 8$*, MNRAS **518** 425.

da Cunha, E. et al. (2015), *An ALMA Survey of Sub-millimeter Galaxies in the Extended Chandra Deep Field South: Physical Properties Derived from Ultraviolet-to-radio Modeling*, ApJ **806**, 110 110.

da Cunha, E., S. Charlot and D. Elbaz (2008), *A simple model to interpret the ultraviolet, optical and infrared emission from galaxies*, MNRAS **388** 1595.

Daddi, E. et al. (2022), *The bending of the star-forming main sequence traces the cold- to hot-accretion transition mass over $0 < z < 4$*, A&A **661**, L7 L7.

Dekel, A. and A. Burkert (2014), *Wet disc contraction to galactic blue nuggets and quenching to red nuggets*, MNRAS **438** 1870.

Dekel, A. and Y. Birnboim (2006), *Galaxy bimodality due to cold flows and shock heating*, MNRAS **368** 2.

Delvecchio, I. et al. (2021), *The infrared-radio correlation of star-forming galaxies is strongly $M_\star$-dependent but nearly redshift-invariant since $z \sim 4$*, A&A **647**, A123 A123.

den Brok, J. S. et al. (2021), *New constraints on the ^{12}CO(2-1)/(1-0) line ratio across nearby disc galaxies*, MNRAS **504** 3221.

Dessauges-Zavadsky, M. et al. (2020), *The ALPINE-ALMA [C II] survey. Molecular gas budget in the early Universe as traced by [C II]*, A&A **643**, A5 A5.

Di Matteo, P., F. Combes, A. .-. Melchior and B. Semelin (2007), *Star formation efficiency in galaxy interactions and mergers: a statistical study*, A&A **468** 61.

Di Teodoro, E. M. and J. E. G. Peek (2021), *Radial Motions and Radial Gas Flows in Local Spiral Galaxies*, ApJ **923**, 220 220.

Dıaz-Garcıa, L. A. et al. (2019), *Stellar populations of galaxies in the ALHAMBRA survey up to $z \sim 1$. IV. Properties of quiescent galaxies on the stellar mass-size plane*, A&A **631**, A158 A158.

Dıaz-Garcıa, S. and J. H. Knapen (2020), *Gas fractions and depletion times in galaxies with different degrees of interaction*, A&A **635**, A197 A197.

Dole, H. et al. (2006), *The cosmic infrared background resolved by Spitzer. Contributions of mid-infrared galaxies to the far-infrared background*, A&A **451** 417.

Domınguez Sánchez, H. et al. (2012), *Comparison of star formation rates from Hα and infrared luminosity as seen by Herschel*, MNRAS **426** 330.

Domınguez Sánchez, H. et al. (2014), *Herschel far-IR counterparts of SDSS galaxies: analysis of commonly used star formation rate estimates*, MNRAS **441** 2.

Donnari, M. et al. (2021), *Quenched fractions in the IllustrisTNG simulations: the roles of AGN feedback, environment, and pre-processing*, MNRAS **500** 4004.

Draine, B. T. (2003), *Interstellar Dust Grains*, ARA&A **41** 241.

Dudzevičiūtė, U. et al. (2020), *An ALMA survey of the SCUBA-2 CLS UDS field: physical properties of 707 sub-millimetre galaxies*, MNRAS **494** 3828.

Duncan, K. et al. (2019), *Observational Constraints on the Merger History of Galaxies since $z \approx 6$: Probabilistic Galaxy Pair Counts in the CANDELS Fields*, ApJ **876**, 110 110.

Durrer, R. (2015), *The cosmic microwave background: the history of its experimental investigation and its significance for cosmology*, Classical and Quantum Gravity **32**, 124007 124007.

Dye, S. et al. (2022), *A high-resolution investigation of the multiphase ISM in a galaxy during the first two billion years*, MNRAS **510** 3734.

Elbaz, D. et al. (2007), *The reversal of the star formation-density relation in the distant universe*, A&A **468** 33.

Elbaz, D. et al. (2011), *GOODS-Herschel: an infrared main sequence for star-forming galaxies*, A&A **533**, A119 A119.

Elbaz, D. et al. (2018), *Starbursts in and out of the star-formation main sequence*, A&A **616**, A110 A110.

Ellison, S. L. et al. (2021), *The ALMaQUEST Survey - V. The non-universality of kpc-scale star formation relations and the factors that drive them*, MNRAS **501** 4777.

Fan, X. et al. (2003), *A Survey of z>5.7 Quasars in the Sloan Digital Sky Survey. II. Discovery of Three Additional Quasars at z>6*, AJ **125** 1649.

Feldmann, R. and L. Mayer (2015), *The Argo simulation - I. Quenching of massive galaxies at high redshift as a result of cosmological starvation*, MNRAS **446** 1939.

Ferreira, L. et al. (2022), *The JWST Hubble Sequence: The Rest-Frame Optical Evolution of Galaxy Structure at* $1.5 < z < 8$, arXiv e-prints, arXiv:2210.01110 arXiv:2210.01110.

Figer, D. F. (2005), *An upper limit to the masses of stars*, Nature **434** 192.

Fisher, D. B. (2006), *Central Star Formation and PAH Profiles in Pseudobulges and Classical Bulges*, ApJ **642** L17.

Fletcher, T. J., A. Saintonge, P. S. Soares and A. Pontzen (2021), *The cosmic abundance of cold gas in the local Universe*, MNRAS **501** 411.

Foreman-Mackey, D., D. W. Hogg, D. Lang and J. Goodman (2013), *emcee: The MCMC Hammer*, PASP **125** 306.

Fraser, M., A. R. Casey, G. Gilmore, A. Heger and C. Chan (2017), *The mass distribution of Population III stars*, MNRAS **468** 418.

Fudamoto, Y. et al. (2021), *Normal, dust-obscured galaxies in the epoch of reionization*, Nature **597** 489.

Galliano, F., E. Dwek and P. Chanial (2008), *Stellar Evolutionary Effects on the Abundances of Polycyclic Aromatic Hydrocarbons and Supernova-Condensed Dust in Galaxies*, ApJ **672** 214.

Gao, Y. and P. M. Solomon (2004), *The Star Formation Rate and Dense Molecular Gas in Galaxies*, ApJ **606** 271.
Genzel, R. et al. (2010), *A study of the gas-star formation relation over cosmic time*, MNRAS **407** 2091.
Genzel, R. et al. (2015), *Combined CO and Dust Scaling Relations of Depletion Time and Molecular Gas Fractions with Cosmic Time, Specific Star-formation Rate, and Stellar Mass*, ApJ **800**, 20 20.
Gobat, R., G. Magdis, C. D'Eugenio and F. Valentino (2020), *The evolution of the gas fraction of quiescent galaxies modeled as a consequence of their creation rate*, A&A **644**, L7 L7.
Goldbaum, N. J., M. R. Krumholz and J. C. Forbes (2016), *Mass Transport and Turbulence in Gravitationally Unstable Disk Galaxies. II: The Effects of Star Formation Feedback*, ApJ **827**, 28 28.
Gómez-Guijarro, C. et al. (2022), *GOODS-ALMA 2.0: Starbursts in the main sequence reveal compact star formation regulating galaxy evolution prequenching*, A&A **659**, A196 A196.
Gowardhan, A. et al. (2019), *High Gas Fraction in a CO-detected Main-sequence Galaxy at $z > 3$*, ApJ **875**, 6 6.
Grogin, N. A. et al. (2011), *CANDELS: The Cosmic Assembly Near-infrared Deep Extragalactic Legacy Survey*, ApJS **197**, 35 35.
Gruppioni, C. et al. (2020), *The ALPINE-ALMA [CII] survey. The nature, luminosity function, and star formation history of dusty galaxies up to z 6*, A&A **643**, A8 A8.
Heintz, K. E. et al. (2023), *The Gas and Stellar Content of a Metal-poor Galaxy at $z = 8.496$ as Revealed by JWST and ALMA*, ApJ **944**, L30 L30.
Högbom, J. A. (1974), *Aperture Synthesis with a Non-Regular Distribution of Interferometer Baselines*, A&AS **15** 417.
Hollenbach, D. and E. E. Salpeter (1971), *Surface Recombination of Hydrogen Molecules*, ApJ **163** 155.
Huertas-Company, M. et al. (2023), *Galaxy Morphology from $z \sim 6$ through the eyes of JWST*, arXiv e-prints, arXiv:2305.02478 arXiv:2305.02478.
Hughes, T. M. et al. (2017), *VALES - III. The calibration between the dust continuum and interstellar gas content of star-forming galaxies*, MNRAS **468** L103.
Hunt, L. K. et al. (2019), *Comprehensive comparison of models for spectral energy distributions from 0.1 μm to 1 mm of nearby star-forming galaxies*, A&A **621**, A51 A51.
Iguchi, S. et al. (2009), *The Atacama Compact Array (ACA)*, PASJ **61** 1.
Jiménez-Andrade, E. F. et al. (2019), *Radio continuum size evolution of star-forming galaxies over $0.35 < z < 2.25$*, A&A **625**, A114 A114.
Jiménez-Andrade, E. F. et al. (2021), *The VLA Frontier Field Survey: A Comparison of the Radio and UV/Optical Size of $0.3 \lesssim z \lesssim 3$ Star-forming Galaxies*, ApJ **910**, 106 106.
Jin, S. et al. (2018), *"Super-deblended" Dust Emission in Galaxies. II. Far-IR to (Sub)millimeter Photometry and High-redshift Galaxy Candidates in the Full COSMOS Field*, ApJ **864**, 56 56.
Jovanović, M. (2017), *Two regimes of galaxy dynamics: mass models of NGC 5055 and DDO 154*, MNRAS **469** 3564.
Katsianis, A., X. Yang and X. Zheng (2021), *The Observed Cosmic Star Formation Rate Density Has an Evolution that Resembles a $\Gamma(a, bt)$ Distribution and Can Be Described Successfully by Only Two Parameters*, ApJ **919**, 88 88.
Kawasaki, M., K. Kohri and T. Moroi (2005), *Big-bang nucleosynthesis and hadronic decay of long-lived massive particles*, Phys. Rev. D **71**, 083502 083502.
Kennicutt Robert C., J. (1998a), *Star Formation in Galaxies Along the Hubble Sequence*, ARA&A **36** 189.
– (1998b), *The Global Schmidt Law in Star-forming Galaxies*, ApJ **498** 541.
Kerp, J. et al. (2016), *A survey of HI gas toward the Andromeda galaxy*, A&A **589**, A120 A120.

Khusanova, Y. et al. (2021), *The ALPINE-ALMA [CII] survey. Obscured star formation rate density and main sequence of star-forming galaxies at $z > 4$*, A&A **649**, A152 A152.

Kirkpatrick, A. et al. (2012), *GOODS-Herschel: Impact of Active Galactic Nuclei and Star Formation Activity on Infrared Spectral Energy Distributions at High Redshift*, ApJ **759**, 139 139.

Kistler, M. D., H. Yüksel, J. F. Beacom, A. M. Hopkins and J. S. B. Wyithe (2009), *The Star Formation Rate in the Reionization Era as Indicated by Gamma-Ray Bursts*, ApJ **705** L104.

Klessen, R. S. and S. C. O. Glover (2023), *The first stars: formation, properties, and impact*, arXiv e-prints, arXiv:2303.12500 arXiv:2303.12500.

Koekemoer, A. M. et al. (2007), *The COSMOS Survey: Hubble Space Telescope Advanced Camera for Surveys Observations and Data Processing*, ApJS **172** 196.

Kokorev, V. I. et al. (2021), *The Evolving Interstellar Medium of Star-forming Galaxies, as Traced by Stardust*, ApJ **921**, 40 40.

Kumar, S. S. (1963), *The Structure of Stars of Very Low Mass.*, ApJ **137** 1121.

Laigle, C. et al. (2016), *The COSMOS2015 Catalog: Exploring the $1 < z < 6$ Universe with Half a Million Galaxies*, ApJS **224**, 24 24.

Lamastra, A., N. Menci, F. Fiore and P. Santini (2013), *The interaction-driven starburst contribution to the cosmic star formation rate density*, A&A **552**, A44 A44.

Lang, P. et al. (2014), *Bulge Growth and Quenching since $z = 2.5$ in CANDELS/3D-HST*, ApJ **788**, 11 11.

Lapiner, S. et al. (2023), *Wet compaction to a blue nugget: a critical phase in galaxy evolution*, MNRAS **522** 4515.

Larkin, M. M., R. Gerasimov and A. J. Burgasser (2023), *Characterization of Population III Stars with Stellar Atmosphere and Evolutionary Modeling and Predictions of their Observability with the JWST*, AJ **165**, 2 2.

Lazar, A. and V. Bromm (2022), *Probing the initial mass function of the first stars with transients*, MNRAS **511** 2505.

Leja, J. et al. (2022), *A New Census of the $0.2 < z < 3.0$ Universe. II. The Star-forming Sequence*, ApJ **936**, 165 165.

Leroy, A. K. et al. (2011), *The CO-to-H_2 Conversion Factor from Infrared Dust Emission across the Local Group*, ApJ **737**, 12 12.

Leroy, A. K. et al. (2013), *Molecular Gas and Star Formation in nearby Disk Galaxies*, AJ **146**, 19 19.

Leslie, S. K. et al. (2020), *The VLA-COSMOS 3 GHz Large Project: Evolution of Specific Star Formation Rates out to $z \sim 5$*, ApJ **899**, 58 58.

Lilly, S. J., C. M. Carollo, A. Pipino, A. Renzini and Y. Peng (2013), *Gas Regulation of Galaxies: The Evolution of the Cosmic Specific Star Formation Rate, the Metallicity-Mass-Star-formation Rate Relation, and the Stellar Content of Halos*, ApJ **772**, 119 119.

Lindroos, L., K. K. Knudsen, W. Vlemmings, J. Conway and I. Martı-Vidal (2015), *Stacking of large interferometric data sets in the image- and uv-domain - a comparative study*, MNRAS **446** 3502.

Lindroos, L. et al. (2016), *Estimating sizes of faint, distant galaxies in the submillimetre regime*, MNRAS **462** 1192.

Liu, D. et al. (2018), *"Super-deblended" Dust Emission in Galaxies. I. The GOODS-North Catalog and the Cosmic Star Formation Rate Density out to Redshift 6*, ApJ **853**, 172 172.

Liu, D. et al. (2019a), *Automated Mining of the ALMA Archive in the COSMOS Field (A^3COSMOS). I. Robust ALMA Continuum Photometry Catalogs and Stellar Mass and Star Formation Properties for ~700 Galaxies at $z = 0.5$-6*, ApJS **244**, 40 40.

Liu, D. et al. (2019b), *Automated Mining of the ALMA Archive in the COSMOS Field (A^3COSMOS). II. Cold Molecular Gas Evolution out to Redshift 6*, ApJ **887**, 235 235.

Lower, S. et al. (2020), *How Well Can We Measure the Stellar Mass of a Galaxy: The Impact of the Assumed Star Formation History Model in SED Fitting*, ApJ **904**, 33 33.

Lustig, P. et al. (2023), *Massive quiescent galaxies at z 3: A comparison of selection, stellar population, and structural properties with simulation predictions*, MNRAS **518** 5953.

Madau, P. and M. Dickinson (2014), *Cosmic Star-Formation History*, ARA&A **52** 415.

Madau, P., L. Pozzetti and M. Dickinson (1998), *The Star Formation History of Field Galaxies*, ApJ **498** 106.

Magnelli, B. et al. (2011), *Evolution of the dusty infrared luminosity function from $z = 0$ to $z = 2.3$ using observations from Spitzer*, A&A **528**, A35 A35.

Magnelli, B. et al. (2014), *The evolution of the dust temperatures of galaxies in the SFR-M_* plane up to $z \sim 2$*, A&A **561**, A86 A86.

Magnelli, B. et al. (2015), *The far-infrared/radio correlation and radio spectral index of galaxies in the SFR-M_* plane up to $z\sim2$*, A&A **573**, A45 A45.

Magnelli, B. et al. (2020), *The ALMA Spectroscopic Survey in the HUDF: The Cosmic Dust and Gas Mass Densities in Galaxies up to $z \sim 3$*, ApJ **892**, 66 66.

Man, A. and S. Belli (2018), *Star formation quenching in massive galaxies*, Nature Astronomy **2** 695.

Mancera Piña, P. E. et al. (2022), *The impact of gas disc flaring on rotation curve decomposition and revisiting baryonic and dark matter relations for nearby galaxies*, MNRAS **514** 3329.

Mannucci, F., G. Cresci, R. Maiolino, A. Marconi and A. Gnerucci (2010), *A fundamental relation between mass, star formation rate and metallicity in local and high-redshift galaxies*, MNRAS **408** 2115.

Martig, M. et al. (2013), *The ATLAS^{3D} project - XXII. Low-efficiency star formation in early-type galaxies: hydrodynamic models and observations*, MNRAS **432** 1914.

Matharu, J. et al. (2022), *CLEAR: The Evolution of Spatially Resolved Star Formation in Galaxies between $0.5 \lesssim z \lesssim 1.7$ Using Hα Emission Line Maps*, ApJ **937**, 16 16.

McKee, C. F. and E. C. Ostriker (2007), *Theory of Star Formation*, ARA&A **45** 565.

McMullin, J. P., B. Waters, D. Schiebel, W. Young and K. Golap (2007), "CASA Architecture and Applications", *Astronomical Data Analysis Software and Systems XVI*, ed. by R. A. Shaw, F. Hill and D. J. Bell, vol. 376, Astronomical Society of the Pacific Conference Series 127.

Miettinen, O. et al. (2017a), *An ALMA survey of submillimetre galaxies in the COSMOS field: Physical properties derived from energy balance spectral energy distribution modelling*, A&A **606**, A17 A17.

Miettinen, O. et al. (2017b), *On the Kennicutt-Schmidt scaling law of submillimetre galaxies*, A&A **602**, L9 L9.

Millard, J. S. et al. (2020), *S2COSMOS: Evolution of gas mass with redshift using dust emission*, MNRAS **494** 293.

Miralda-Escudé, J. (2003), *The Dark Age of the Universe*, Science **300** 1904.

Miura, R. E. et al. (2014), *Enhancement of CO(3-2)/CO(1-0) Ratios and Star Formation Efficiencies in Supergiant H II Regions*, ApJ **788**, 167 167.

Mohan, N. and D. Rafferty (2015), *PyBDSF: Python Blob Detection and Source Finder*, Astrophysics Source Code Library, record ascl:1502.007.

Momose, R. et al. (2013), *Star Formation on Subkiloparsec Scale Triggered by Non-linear Processes in Nearby Spiral Galaxies*, ApJ **772**, L13 L13.

Mosleh, M. et al. (2017), *Connection between Stellar Mass Distributions within Galaxies and Quenching Since $z = 2$*, ApJ **837**, 2 2.

Moutard, T. et al. (2020), *UV and U-band luminosity functions from CLAUDS and HSC-SSP - I. Using four million galaxies to simultaneously constrain the very faint and bright regimes to $z \sim 3$*, MNRAS **494** 1894.

Nakajima, K. et al. (2023), *JWST Census for the Mass-Metallicity Star-Formation Relations at z=4-10 with the Self-Consistent Flux Calibration and the Proper Metallicity Calibrators*, arXiv e-prints, arXiv:2301.12825 arXiv:2301.12825.

Narayanan, D. and M. R. Krumholz (2014), *A theory for the excitation of CO in star-forming galaxies*, MNRAS **442** 1411.

Nelson, D. et al. (2018), *The abundance, distribution, and physical nature of highly ionized oxygen O VI, O VII, and O VIII in IllustrisTNG*, MNRAS **477** 450.

Nelson, E. J. et al. (2023), *JWST Reveals a Population of Ultrared, Flattened Galaxies at $2 \lesssim z \lesssim 6$ Previously Missed by HST*, ApJ **948**, L18 L18.

Nelson, E. J. et al. (2016), *Where Stars Form: Inside-out Growth and Coherent Star Formation from HST Hα Maps of 3200 Galaxies across the Main Sequence at $0.7 < z < 1.5$*, ApJ **828**, 27 27.

Noordeh, E. et al. (2021), *Quiescent galaxies in a virialized cluster at redshift 2: evidence for accelerated size growth*, MNRAS **507** 5272.

Novak, M. et al. (2017), *The VLA-COSMOS 3 GHz Large Project: Cosmic star formation history since z 5*, A&A **602**, A5 A5.

Obreschkow, D. and S. Rawlings (2009), *Understanding the H_2/HI ratio in galaxies*, MNRAS **394** 1857.

Ostriker, J. P. (1993), *Astronomical tests of the cold dark matter scenario.*, ARA&A **31** 689.

Padmanabhan, H. and A. Loeb (2022), *Signatures of population III supernovae at Cosmic Dawn: the case of GN-z11-flash*, General Relativity and Gravitation **54**, 24 24.

Pannella, M. et al. (2015), *GOODS-Herschel: Star Formation, Dust Attenuation, and the FIR-radio Correlation on the Main Sequence of Star-forming Galaxies up to z 4*, ApJ **807**, 141 141.

Papadopoulos, P. P., P. van der Werf, E. Xilouris, K. G. Isaak and Y. Gao (2012), *The Molecular Gas in Luminous Infrared Galaxies. II. Extreme Physical Conditions and Their Effects on the X_{co} Factor*, ApJ **751**, 10 10.

Park, M. et al. (2022), *On the formation of massive quiescent galaxies with diverse morphologies in the TNG50 simulation*, MNRAS **515** 213.

Parmentier, G., J. Kauffmann, T. Pillai and K. M. Menten (2011), *Volume density thresholds for overall star formation imply mass-size thresholds for massive star formation*, MNRAS **416** 783.

Peebles, P. J. E. (1980), *The large-scale structure of the universe*.

Peng, Y.-j. and R. Maiolino (2014), *From haloes to Galaxies - I. The dynamics of the gas regulator model and the implied cosmic sSFR history*, MNRAS **443** 3643.

Peng, Y.-j. et al. (2010), *Mass and Environment as Drivers of Galaxy Evolution in SDSS and zCOSMOS and the Origin of the Schechter Function*, ApJ **721** 193.

Pesce, D. W. et al. (2020), *The Megamaser Cosmology Project. XIII. Combined Hubble Constant Constraints*, ApJ **891**, L1 L1.

Pessa, I. et al. (2021), *Star formation scaling relations at ~100 pc from PHANGS: Impact of completeness and spatial scale*, A&A **650**, A134 A134.

Pflamm-Altenburg, J., C. Weidner and P. Kroupa (2007), *Converting Hα Luminosities into Star Formation Rates*, ApJ **671** 1550.

Picouet, V. et al. (2023), *HSC-CLAUDS survey: The star formation rate functions since $z \sim 2$ and comparison with hydrodynamical simulations*, A&A **675**, A164 A164.

Planck Collaboration et al. (2016), *Planck 2015 results. XIII. Cosmological parameters*, A&A **594**, A13 A13.

Planck Collaboration et al. (2020), *Planck 2018 results. VI. Cosmological parameters*, A&A **641**, A6 A6.

Popesso, P. et al. (2023), *The main sequence of star-forming galaxies across cosmic times*, MNRAS **519** 1526.

Popping, G. et al. (2022), *The dust-continuum size of TNG50 galaxies at z = 1-5: a comparison with the distribution of stellar light, stars, dust, and H_2*, MNRAS **510** 3321.

Porter, L. A., R. S. Somerville, J. R. Primack and P. H. Johansson (2014), *Understanding the structural scaling relations of early-type galaxies*, MNRAS **444** 942.

Puglisi, A. et al. (2021), *Submillimetre compactness as a critical dimension to understand the main sequence of star-forming galaxies*, MNRAS **508** 5217.

Rémy-Ruyer, A. et al. (2014), *Gas-to-dust mass ratios in local galaxies over a 2 dex metallicity range*, A&A **563**, A31 A31.

Renaud, F., Á. Segovia Otero and O. Agertz (2022), *The merger-starburst connection across cosmic times*, MNRAS **516** 4922.

Riess, A. G., S. Casertano, W. Yuan, L. M. Macri and D. Scolnic (2019), *Large Magellanic Cloud Cepheid Standards Provide a 1% Foundation for the Determination of the Hubble Constant and Stronger Evidence for Physics beyond ΛCDM*, ApJ **876**, 85 85.

Rinaldi, P. et al. (2022), *The Galaxy Starburst/Main-sequence Bimodality over Five Decades in Stellar Mass at z ≈ 3-6.5*, ApJ **930**, 128 128.

Robertson, B. E. et al. (2023), *Identification and properties of intense star-forming galaxies at redshifts z > 10*, Nature Astronomy **7** 611.

Robertson, B. E. and R. S. Ellis (2012), *Connecting the Gamma Ray Burst Rate and the Cosmic Star Formation History: Implications for Reionization and Galaxy Evolution*, ApJ **744**, 95 95.

Rodighiero, G. et al. (2010), *The first Herschel view of the mass-SFR link in high-z galaxies*, A&A **518**, L25 L25.

Rodighiero, G. et al. (2011), *The Lesser Role of Starbursts in Star Formation at z = 2*, ApJ **739**, L40 L40.

Rodrıguez Montero, F., R. Davé, V. Wild, D. Anglés-Alcázar and D. Narayanan (2019), *Mergers, starbursts, and quenching in the SIMBA simulation*, MNRAS **490** 2139.

Rodrıguez-Montoya, I., V. Avila-Reese, A. Pérez-Lorenzana and J. Venzor (2020), *Constraints on the Velocity Dispersion of Dark Matter from Cosmology and New Bounds on Scattering from the Cosmic Dawn*, ApJ **894**, 40 40.

Romano, M. et al. (2021), *The ALPINE-ALMA [CII] survey. The contribution of major mergers to the galaxy mass assembly at z ∼ 5*, A&A **653**, A111 A111.

Rosolowsky, E. and L. Blitz (2005), *Giant Molecular Clouds in M64*, ApJ **623** 826.

Rubin, V. C. (1983), *Dark matter in spiral galaxies*, Scientific American **248** 96.

Saintonge, A. and B. Catinella (2022), *The Cold Interstellar Medium of Galaxies in the Local Universe*, ARA&A **60** 319.

Sánchez, S. F. et al. (2021), *The EDGE-CALIFA survey: the local and global relations between Σ_*, Σ_{SFR}, and Σ_{mol} that regulate star formation*, MNRAS **503** 1615.

Sanders, D. B. et al. (2007), *S-COSMOS: The Spitzer Legacy Survey of the Hubble Space Telescope ACS 2 deg^2 COSMOS Field I: Survey Strategy and First Analysis*, ApJS **172** 86.

Sandstrom, K. M. et al. (2013), *The CO-to-H_2 Conversion Factor and Dust-to-gas Ratio on Kiloparsec Scales in Nearby Galaxies*, ApJ **777**, 5 5.

Sargent, M. T., M. Béthermin, E. Daddi and D. Elbaz (2012), *The Contribution of Starbursts and Normal Galaxies to Infrared Luminosity Functions at z < 2*, ApJ **747**, L31 L31.

Sargent, M. T. et al. (2014), *Regularity Underlying Complexity: A Redshift-independent Description of the Continuous Variation of Galaxy-scale Molecular Gas Properties in the Mass-star Formation Rate Plane*, ApJ **793**, 19 19.

Schaerer, D. (2002), *On the properties of massive Population III stars and metal-free stellar populations*, A&A **382** 28.

Schawinski, K. et al. (2014), *The green valley is a red herring: Galaxy Zoo reveals two evolutionary pathways towards quenching of star formation in early- and late-type galaxies*, MNRAS **440** 889.
Schinnerer, E. et al. (2010), *The VLA-COSMOS Survey. IV. Deep Data and Joint Catalog*, ApJS **188** 384.
Schinnerer, E. et al. (2016), *Gas Fraction and Depletion Time of Massive Star-forming Galaxies at z ∼3.2: No Change in Global Star Formation Process out to z > 3*, ApJ **833**, 112 112.
Schmidt, M. (1959), *The Rate of Star Formation.*, ApJ **129** 243.
Schreiber, C. et al. (2015), *The Herschel view of the dominant mode of galaxy growth from z = 4 to the present day*, A&A **575**, A74 A74.
Schuster, K. F., C. Kramer, M. Hitschfeld, S. Garcia-Burillo and B. Mookerjea (2007), *A complete ^{12}CO 2-1 map of M 51 with HERA. I. Radial averages of CO, H I, and radio continuum*, A&A **461** 143.
Scoville, N. et al. (2007), *The Cosmic Evolution Survey (COSMOS): Overview*, ApJS **172** 1.
Scoville, N. et al. (2014), *The Evolution of Interstellar Medium Mass Probed by Dust Emission: ALMA Observations at z = 0.3-2*, ApJ **783**, 84 84.
Scoville, N. et al. (2016), *ISM Masses and the Star formation Law at Z = 1 to 6: ALMA Observations of Dust Continuum in 145 Galaxies in the COSMOS Survey Field*, ApJ **820**, 83 83.
Scoville, N. et al. (2017), *Evolution of Interstellar Medium, Star Formation, and Accretion at High Redshift*, ApJ **837**, 150 150.
Seaquist, E. R., S. W. Lee and G. H. Moriarty-Schieven (2006), *A High-Resolution Map of ^{12}CO J = 6-5 Emission in the Starburst Galaxy M82*, ApJ **638** 148.
Shajib, A. J. et al. (2023), *TDCOSMO. XII. Improved Hubble constant measurement from lensing time delays using spatially resolved stellar kinematics of the lens galaxy*, A&A **673**, A9 A9.
Shetty, R. et al. (2014), *Indications of a sub-linear and non-universal Kennicutt-Schmidt relationship*, MNRAS **437** L61.
Silverman, J. D. et al. (2018), *The Molecular Gas Content and Fuel Efficiency of Starbursts at z ∼ 1.6 with ALMA*, ApJ **867**, 92 92.
Simmonds, C. et al. (2023), *The ionizing photon production efficiency at z 6 for Lyman-alpha emitters using JEMS and MUSE*, MNRAS **523** 5468.
Simpson, J. M. et al. (2019), *The East Asian Observatory SCUBA-2 Survey of the COSMOS Field: Unveiling 1147 Bright Sub-millimeter Sources across 2.6 Square Degrees*, ApJ **880**, 43 43.
Sivasankaran, A. et al. (2022), *Simulations of black hole fueling in isolated and merging galaxies with an explicit, multiphase ISM*, MNRAS **517** 4752.
Smolčić, V. et al. (2017), *The VLA-COSMOS 3 GHz Large Project: Continuum data and source catalog release*, A&A **602**, A1 A1.
Song, M. et al. (2016), *The Evolution of the Galaxy Stellar Mass Function at z = 4-8: A Steepening Low-mass-end Slope with Increasing Redshift*, ApJ **825**, 5 5.
Sparre, M. et al. (2022), *Gas flows in galaxy mergers: supersonic turbulence in bridges, accretion from the circumgalactic medium, and metallicity dilution*, MNRAS **509** 2720.
Spilker, J. S., R. Bezanson, B. J. Weiner, K. E. Whitaker and C. C. Williams (2019), *Evidence for Inside-out Galaxy Growth and Quenching of a z ∼ 2 Compact Galaxy From High-resolution Molecular Gas Imaging*, ApJ **883**, 81 81.
Srianand, R., P. Noterdaeme, C. Ledoux and P. Petitjean (2008), *First detection of CO in a high-redshift damped Lyman-α system*, A&A **482** L39.
Strazzullo, V. et al. (2019), *Galaxy populations in the most distant SPT-SZ clusters. I. Environmental quenching in massive clusters at 1.4 ≲ z ≲ 1.7*, A&A **622**, A117 A117.
Suess, K. A., M. Kriek, S. H. Price and G. Barro (2019a), *Half-mass Radii for ∼7000 Galaxies at 1.0 ≤ z ≤ 2.5: Most of the Evolution in the Mass-Size Relation Is Due to Color Gradients*, ApJ **877**, 103 103.

Suess, K. A., M. Kriek, S. H. Price and G. Barro (2019b), *Half-mass Radii of Quiescent and Star-forming Galaxies Evolve Slowly from $0 \lesssim z \leq 2.5$: Implications for Galaxy Assembly Histories*, ApJ **885**, L22 L22.

– (2021), *Dissecting the Size-Mass and Σ_1-Mass Relations at $1.0 < z < 2.5$: Galaxy Mass Profiles and Color Gradients as a Function of Spectral Shape*, ApJ **915**, 87 87.

Suzuki, T. L. et al. (2021), *Dust, Gas, and Metal Content in Star-forming Galaxies at $z \sim 3.3$ Revealed with ALMA and Near-IR Spectroscopy*, ApJ **908**, 15 15.

Suzuki, T. L. et al. (2022), *Low Star Formation Activity and Low Gas Content of Quiescent Galaxies at $z = 3.5$-4.0 Constrained with ALMA*, ApJ **936**, 61 61.

Tacchella, S. et al. (2015), *Evidence for mature bulges and an inside-out quenching phase 3 billion years after the Big Bang*, Science **348** 314.

Tacchella, S., J. C. Forbes and N. Caplar (2020), *Stochastic modelling of star-formation histories II: star-formation variability from molecular clouds and gas inflow*, MNRAS **497** 698.

Tacchella, S. et al. (2016), *The confinement of star-forming galaxies into a main sequence through episodes of gas compaction, depletion and replenishment*, MNRAS **457** 2790.

Tacconi, L. J. et al. (2018), *PHIBSS: Unified Scaling Relations of Gas Depletion Time and Molecular Gas Fractions*, ApJ **853**, 179 179.

Tacconi, L. J., R. Genzel and A. Sternberg (2020), *The Evolution of the Star-Forming Interstellar Medium Across Cosmic Time*, ARA&A **58** 157.

Tadaki, K.-i. et al. (2020), *Structural Evolution in Massive Galaxies at $z \sim 2$*, ApJ **901**, 74 74.

Taniguchi, Y. et al. (2007), *The Cosmic Evolution Survey (COSMOS): Subaru Observations of the HST Cosmos Field*, ApJS **172** 9.

Tasca, L. A. M. et al. (2014), *Evidence for major mergers of galaxies at $2 \lesssim z < 4$ in the VVDS and VUDS surveys*, A&A **565**, A10 A10.

Teng, Y.-H. et al. (2023), *The Physical Drivers and Observational Tracers of CO-to-H_2 Conversion Factor Variations in Nearby Barred Galaxy Centers*, ApJ **950**, 119 119.

Thompson, A. R., J. M. Moran and J. Swenson George W. (2017), *Interferometry and Synthesis in Radio Astronomy, 3rd Edition*.

Tonini, C., S. J. Mutch, D. J. Croton and J. S. B. Wyithe (2016), *The growth of discs and bulges during hierarchical galaxy formation - I. Fast evolution versus secular processes*, MNRAS **459** 4109.

Valentino, F. et al. (2020), *Quiescent Galaxies 1.5 Billion Years after the Big Bang and Their Progenitors*, ApJ **889**, 93 93.

van de Hulst, H. C., E. Raimond and H. van Woerden (1957), *Rotation and density distribution of the Andromeda nebula derived from observations of the 21-cm line*, Bull. Astron. Inst. Netherlands **14** 1.

van der Vlugt, D. et al. (2022), *An Ultra-deep Multiband Very Large Array (VLA) Survey of the Faint Radio Sky (COSMOS-XS): New Constraints on the Cosmic Star Formation History*, ApJ **941**, 10 10.

van der Wel, A. et al. (2014), *3D-HST+CANDELS: The Evolution of the Galaxy Size-Mass Distribution since $z = 3$*, ApJ **788**, 28 28.

van Dokkum, P. G. et al. (2013), *The Assembly of Milky-Way-like Galaxies Since $z \sim 2.5$*, ApJ **771**, L35 L35.

van Dokkum, P. G. et al. (2015), *Forming Compact Massive Galaxies*, ApJ **813**, 23 23.

Venemans, B. P. et al. (2017), *The Compact, ~1 kpc Host Galaxy of a Quasar at a Redshift of 7.1*, ApJ **837**, 146 146.

Ventou, E. et al. (2017), *The MUSE Hubble Ultra Deep Field Survey. IX. Evolution of galaxy merger fraction since $z \approx 6$*, A&A **608**, A9 A9.

Vizgan, D. et al. (2022), *Tracing Molecular Gas Mass in z 6 Galaxies with [C II]*, ApJ **929**, 92 92.

Walters, D., J. Woo and S. L. Ellison (2022), *Quenching time-scales in the IllustrisTNG simulation*, MNRAS **511** 6126.

Wang, T.-M. and C.-Y. Hwang (2020), *Influence of velocity dispersions on star-formation activities in galaxies*, A&A **641**, A24 A24.

Wang, T.-M. et al. (2022), *A^{3}COSMOS: A census on the molecular gas mass and extent of main-sequence galaxies across cosmic time*, A&A **660**, A142 A142.

Wang, T.-M. et al. (2023), *A^{3}COSMOS: Dissecting the gas content of star-forming galaxies across the main sequence at 1.2 ≤ z < 1.6*, arXiv e-prints, arXiv:2311.11832 arXiv:2311.11832.

Weaver, J. R. et al. (2021), "COSMOS2020: A next-generation catalog to explore the 1 < z < 8 universe", *American Astronomical Society Meeting Abstracts*, vol. 53, American Astronomical Society Meeting Abstracts 215.06 215.06.

Weinberg, D. H., J. S. Bullock, F. Governato, R. Kuzio de Naray and A. H. G. Peter (2015), *Cold dark matter: Controversies on small scales*, Proceedings of the National Academy of Science **112** 12249.

Weston, M. E. et al. (2017), *Incidence of WISE -selected obscured AGNs in major mergers and interactions from the SDSS*, MNRAS **464** 3882.

Whitaker, K. E., P. G. van Dokkum, G. Brammer and M. Franx (2012), *The Star Formation Mass Sequence Out to z = 2.5*, ApJ **754**, L29 L29.

Wiklind, T. et al. (2019), *Evolution of the Gas Mass Fraction of Progenitors to Today's Massive Galaxies: ALMA Observations in the CANDELS GOODS-S Field*, ApJ **878**, 83 83.

Wilkinson, C. L., K. A. Pimbblet, J. P. Stott, C. G. Few and B. K. Gibson (2018), *Evolution of starburst galaxies in the Illustris simulation*, MNRAS **479** 758.

Wilman, D. J. et al. (2020), *The Regulation of Galaxy Growth along the Size-Mass Relation by Star Formation, as Traced by Hα in KMOS^{3D} Galaxies at 0.7 ≲ z ≲ 2.7*, ApJ **892**, 1 1.

Wilson, C. D., B. G. Elmegreen, A. Bemis and N. Brunetti (2019), *The Kennicutt-Schmidt Law and Gas Scale Height in Luminous and Ultraluminous Infrared Galaxies*, ApJ **882**, 5 5.

Wolfe, A., E. F. Guinan, K. M. Datin, L. E. DeWarf and S. G. Engle (2010), "Are Main-Sequence K-type Stars the "Goldilocks" Stars for Hosting Long-term Habitable Planets", *American Astronomical Society Meeting Abstracts #215*, vol. 215, American Astronomical Society Meeting Abstracts 423.10 423.10.

Wong, T. and L. Blitz (2002), *The Relationship between Gas Content and Star Formation in Molecule-rich Spiral Galaxies*, ApJ **569** 157.

Wright, R. J. et al. (2019), *Quenching time-scales of galaxies in the EAGLE simulations*, MNRAS **487** 3740.

Wu, Y. et al. (2018), *Mass and age of red giant branch stars observed with LAMOST and Kepler*, MNRAS **475** 3633.

Wuyts, S. et al. (2011), *On Star Formation Rates and Star Formation Histories of Galaxies Out to z ∼3*, ApJ **738**, 106 106.

Xu, C. K. et al. (2012), *Major-merger Galaxy Pairs in the COSMOS Field—Mass-dependent Merger Rate Evolution since z = 1*, ApJ **747**, 85 85.

Yang, J. et al. (2020), *Measurements of the z ∼ 6 Intergalactic Medium Optical Depth and Transmission Spikes Using a New z > 6.3 Quasar Sample*, ApJ **904**, 26 26.

Yang, L. et al. (2021), *The evolution of the size-mass relation at z = 1-3 derived from the complete Hubble Frontier Fields data set*, MNRAS **501** 1028.

Young, L. M. et al. (2011), *The ATLAS^{3D} project - IV. The molecular gas content of early-type galaxies*, MNRAS **414** 940.

Yu, Q. et al. (2022), *On the H I Content of MaNGA Major Merger Pairs*, ApJ **934**, 114 114.

Zamojski, M. A. et al. (2007), *Deep GALEX Imaging of the COSMOS HST Field: A First Look at the Morphology of z ∼0.7 Star-forming Galaxies*, ApJS **172** 468.

Zaroubi, S. (2013), "The Epoch of Reionization", *The First Galaxies*, ed. by T. Wiklind, B. Mobasher and V. Bromm, vol. 396, Astrophysics and Space Science Library 45.

Zavala, J. A. et al. (2021), *The Evolution of the IR Luminosity Function and Dust-obscured Star Formation over the Past 13 Billion Years*, ApJ **909**, 165 165.

Zhang, L. and L. C. Ho (2023), *Estimating Molecular Gas Content in Galaxies from Polycyclic Aromatic Hydrocarbon Emission*, ApJ **943**, 1 1.

Zhang, Z.-Y. et al. (2016), *Gone with the heat: a fundamental constraint on the imaging of dust and molecular gas in the early Universe*, Royal Society Open Science **3**, 160025 160025.

Zhao, Y. et al. (2016), *ALMA Imaging of the CO (6-5) Line Emission in NGC 7130**, ApJ **820**, 118 118.

Zheng, X. Z. et al. (2006), *Detecting Faint Galaxies by Stacking at 24 μm*, ApJ **640** 784.

Zolotov, A. et al. (2015), *Compaction and quenching of high-z galaxies in cosmological simulations: blue and red nuggets*, MNRAS **450** 2327.

APPENDIX A

Script for the stacking analysis

Here I present details on the script that I used to perform Fourier-domain stacking in my research work (see Sect. 2.3.1). This script should be executed under CASA version 4.6.0.

I include the python packages that are used in this script Lindroos et al. (2015).

```
import numpy as np
import stacker
import stacker.uv
from scipy.io.idl import readsav
```

For each galaxy, I calculate $\Gamma^{\rm SED}$ from eq. 2.4 using the SED templates of Béthermin et al. (2012) and interpolation.

```
lambda_obs=(3.0*10**8/frequency)*10**6
lambda_850=850.0*(1+redshift)
# frequency: the observed frequency in Hz.
# redshift: the redshift of the target galaxy.
SED_lambda=readsav('SED_z.save')['lambda_grids']
SED_z_grid=readsav('SED_z.save')['z_grids']
SED_lower=readsav('SED_z.save')['snu_grids_ms'][SED_number]
# call SED wavelength grids, in unit of μm, SED redshift grids,
# and SED flux grids at a given redshift, in unit of Jy.
f_predict_obs_SED_lower=np.interp(lambda_obs,SED_lambda,SED_lower)
f_predict_850_SED_lower=np.interp(lambda_850,SED_lambda,SED_lower)
# obtain the SED flux at the observed wavelength and 850 μm using interpolation.
frec_lower=f_predict_850_SED_lower/f_predict_obs_SED_lower
# calculate Γ^SED at a given redshift grid.
SED_upper=readsav('SED_z.save')['snu_grids_ms'][SED_number+1]
# call SED flux grids for the next redshift.
f_predict_obs_SED_upper=np.interp(lambda_obs,SED_lambda,SED_upper)
f_predict_850_SED_upper=np.interp(lambda_850,SED_lambda,SED_upper)
# obtain the SED flux at the observed wavelength and 850 μm using interpolation.
frec_upper=f_predict_850_SED_upper/f_predict_obs_SED_upper
# calculate Γ^SED at the next redshift grid.
```

gamma_SED=np.interp(age_obs,[age_upper,age_lower],[frec_big,frec_small])
obtain the final $\Gamma^{\rm SED}$ at the redshift of the target source using interpolation.
age: the corresponding cosmic age at a give redshift in year.

I then use $\Gamma^{\rm SED}$ to scale the amplitude of ALMA visibilities to the rest-frame 850 μm luminosity, using CASA tasks `gencal` and `applycal`.

scale=1.0/np.sqrt((4*np.pi*(DL)2*gamma_SED/(1+redshift)))**
define the scaling factor with $\Gamma^{\rm SED}$ and here DL is the luminosity distance in meter.
gencal(vis=vis, caltable=caltable, caltype='amp', spw=spw, parameter=scale)
vis: visibility. caltable: calibration table. spw: spectral window.
applycal(vis=vis, spw=spw, gaintable=caltable)
split(vis=vis, outputvis='vis_amp_shifted', datacolumn='corrected')
split the result after applying CASA task `gencal` and `applycal`.

I use stacker to shift the phase center of the visibilities to the coordinates of the galaxy.

flux['uv']=stacker.uv.stack(coordinate,inputvis='vis_amp_shifted', outputvis='stack_output',datacolumn='data')
coordinate: the coordinate of the galaxy.

Finally, I stack the visibilities of the galaxies using the CASA task `concat`.

concat(vis=vislist,concatvis='uvstacked.ms')
vislist: list of visibilities to stack.

APPENDIX B

A^{3}COSMOS: A census on the molecular gas mass and extent of main-sequence galaxies across cosmic time

The publication *Wang et al. A&A (2022), 660A, 142W* is reproduced below in its original form with permission by ESO.

A&A 660, A142 (2022)
https://doi.org/10.1051/0004-6361/202142299

Astronomy & Astrophysics

A^{3}COSMOS: A census on the molecular gas mass and extent of main-sequence galaxies across cosmic time

Tsan-Ming Wang (王贊銘)[1], Benjamin Magnelli[1,2], Eva Schinnerer[3], Daizhong Liu[4], Ziad Aziz Modak[1], Eric Faustino Jiménez-Andrade[5], Christos Karoumpis[1], Vasily Kokorev[6,7], and Frank Bertoldi[1]

[1] Argelander-Institut für Astronomie, Universität Bonn, Auf dem Hügel 71, 53121 Bonn, Germany
e-mail: twan@uni-bonn.de
[2] AIM, CEA, CNRS, Université Paris-Saclay, Université Paris Diderot, Sorbonne Paris Cité, 91191 Gif-sur-Yvette, France
[3] Max-Planck-Institut für Astronomie, Königstuhl 17, 69117 Heidelberg, Germany
[4] Max-Planck-Institut für extraterrestrische Physik, Gießenbachstraße 1, 85748 Garching b. München, Germany
[5] National Radio Astronomy Observatory, 520 Edgemont Road, Charlottesville 22903, USA
[6] Cosmic Dawn Center (DAWN), Copenhagen, Denmark
[7] Niels Bohr Institute, University of Copenhagen, Lyngbyvej 2, 2100 Copenhagen Ø, Denmark

Received 24 September 2021 / Accepted 17 January 2022

ABSTRACT

Aims. We aim to constrain for the first time the mean mass and extent of the molecular gas of a mass-complete sample of normal $>10^{10}\,M_\odot$ star-forming galaxies at $0.4 < z < 3.6$.
Methods. We apply an innovative *uv*-based stacking analysis to a large set of archival Atacama Large Millimeter/submillimeter Array (ALMA) observations using a mass-complete sample of main-sequence (MS) galaxies. This stacking analysis, performed on the Rayleigh-Jeans dust continuum emission, provides accurate measurements of the mean mass and extent of the molecular gas of galaxy populations, which are otherwise individually undetected.
Results. The molecular gas mass of MS galaxies evolves with redshift and stellar mass. At all stellar masses, the molecular gas fraction decreases by a factor of ∼24 from $z \sim 3.2$ to $z \sim 0$. At a given redshift, the molecular gas fraction of MS galaxies decreases with stellar mass at roughly the same rate that their specific star-formation rate (SFR/$M_\star$) decreases. The molecular gas depletion time of MS galaxies remains roughly constant at $z > 0.5$ with a value of 300–500 Myr, but increases by a factor of ∼3 from $z \sim 0.5$ to $z \sim 0$. This evolution of the molecular gas depletion time of MS galaxies can be predicted from the evolution of their molecular gas surface density and a seemingly universal MS-only $\Sigma_{M_{\rm mol}} - \Sigma_{\rm SFR}$ relation with an inferred slope of ∼1.13, the so-called Kennicutt–Schmidt (KS) relation. The far-infrared size of MS galaxies shows no significant evolution with redshift or stellar mass, with a mean circularized half-light radius of ∼2.2 kpc. Finally, our mean molecular gas masses are generally lower than previous estimates, likely due to the fact that literature studies were largely biased toward individually detected MS galaxies with massive gas reservoirs.
Conclusions. To first order, the molecular gas content of MS galaxies regulates their star formation across cosmic time, while variation in their star-formation efficiency plays a secondary role. Despite a large evolution of their gas content and star-formation rates, MS galaxies have evolved along a seemingly universal MS-only KS relation.

Key words. galaxies: evolution – galaxies: high-redshift – galaxies: ISM

1. Introduction

Understanding galaxy evolution across cosmic time is one of the key topics of modern astronomy. One very successful approach for addressing this vast and important question is to assemble and study large and representative samples of galaxies through deep multiwavelength extragalactic surveys. Using this approach, much has been learned over the last few decades about the global star-formation history of the Universe. The cosmic star-formation rate density (SFRD) increases from early cosmic times, $z \sim 2$, and decreases by a factor of 10 by $z \sim 0$ (Madau & Dickinson 2014). About 80% of this star formation takes place in relatively massive galaxies ($>10^{10}\,M_\odot$) that reside on the so-called main sequence (MS) of star-forming galaxies (SFGs; e.g., Noeske et al. 2007; Rodighiero et al. 2011; Sargent et al. 2012). This MS denotes the tight correlation that exists between the stellar mass ($M_\star$) and star-formation rate (SFR) of galaxies, which is observed up to $z \sim 4$ (e.g., Brinchmann et al. 2004; Pannella et al. 2009; Magdis et al. 2010; Zahid et al. 2012; Kashino et al. 2013; Whitaker et al. 2014; Sobral et al. 2014; Speagle et al. 2014; Johnston et al. 2015; Tomczak et al. 2016; Bourne et al. 2017; Pearson et al. 2018; Popesso et al. 2019; Leslie et al. 2020). The existence of the MS, with its constant scatter of 0.3 dex and a normalization that decreases by a factor of 20 from $z \sim 2$ to $z \sim 0$, suggests that most SFGs are isolated and secularly evolving with long (>1 Gyr) star-forming duty cycles. On the contrary, galaxies above the MS (∼5% of the SFG population; Luo et al. 2014) seem to be mostly associated with short, intense starbursts triggered by major mergers and contribute only 10% to the SFRD at all redshifts (e.g., Sargent et al. 2012). While the evolution of the MS and SFRD across cosmic time is observationally well established up to $z \sim 2$, the mechanisms driving their evolution remain poorly constrained. At $z > 2$, our understanding is even more limited because observations obtained from different rest-frame frequencies (i.e., ultraviolet, far-infrared, or radio) provide a somewhat discrepant view of the exact evolution of the SFRD (e.g., Bouwens et al. 2015; Novak et al. 2017; Liu et al. 2018; Gruppioni et al. 2020).

To shed light on the physical processes that regulate star formation across cosmic time, it is paramount to obtain a precise

measurement of the molecular gas content of local and high-redshift galaxies. Indeed, molecular gas fuels star formation, as revealed by the tight correlation between gas mass and SFR surface densities, the so-called Kennicutt–Schmidt (KS) relation (Kennicutt 1998a). Molecular hydrogen (H_2) is the most abundant constituent of molecular gas, but it is difficult to observe due to its lack of a dipole moment. For this reason, the carbon monoxide (CO) molecule, which is the most abundant and readily observable constituent of molecular gas, is usually used to trace the molecular gas content of galaxies (see Bolatto et al. 2013, for a review). However, even with the Atacama Large Millimeter/submillimeter Array (ALMA), obtaining such measurements for $z > 2.0$ MS galaxies with stellar masses of $\sim 10^{10}\,M_\odot$ still requires an hour of observing time per object. The CO molecule is thus still poorly suited for the study of large and representative samples of high-redshift galaxies. Therefore, in recent years, an alternative approach of focusing on high-redshift galaxies has emerged, which relies on dust mass measurements and a standard gas-to-dust mass ratio calibrated in the local Universe. These gas mass measurements, inferred from either multiwavelength dust spectral energy distribution (SED) fits (e.g., Magdis et al. 2012; Magnelli et al. 2012b, 2014; Santini et al. 2014; Tan et al. 2014; Béthermin et al. 2015; Berta et al. 2016; Hunt et al. 2019) or single Rayleigh–Jeans (RJ) flux density conversion (e.g., Scoville et al. 2014, 2016; Groves et al. 2015; Schinnerer et al. 2016; Kaasinen et al. 2019; Liu et al. 2019b; Magnelli et al. 2020; Millard et al. 2020), were shown to be surprisingly accurate when compared to state-of-the-art CO measurements (e.g., Genzel et al. 2015; Scoville et al. 2016, 2017; Tacconi et al. 2018, 2020).

This dust-based approach has since allowed the measurement of the gas content of hundreds of high-redshift SFGs. It was found that the gas fraction of massive SFGs (i.e., $M_{\rm gas}/M_*$) is relatively constant at $z > 2$ but decreases significantly from $z \sim 2$ to $z \sim 0$ (Carilli & Walter 2013; Sargent et al. 2014; Schinnerer et al. 2016; Miettinen et al. 2017b; Scoville et al. 2017; Tacconi et al. 2018, 2020; Gowardhan et al. 2019; Liu et al. 2019b; Wiklind et al. 2019; Cassata et al. 2020). This evolution follows that of the normalization of the MS and implies that the star-formation efficiency (SFE; i.e., SFR/$M_{\rm gas}$) in these galaxies remains relatively constant across cosmic time. This finding is confirmed by the global evolution of the co-moving gas mass density, which resembles that of the SFRD (Magnelli et al. 2020). At any redshift, the depletion time ($t_{\rm depl} = 1/{\rm SFE}$) of the gas reservoirs of massive SFGs is found to be relatively short, on the order of ∼0.5–1 Gyr. Without continuous replenishment of their gas reservoirs, star formation in massive MS galaxies would thus cease within ∼0.5–1 Gyr, in tension with the existence of the MS itself (i.e., long star-forming duty cycles). The continuous accretion of fresh gas from the intergalactic or circum-galactic medium would thus be the main parameter regulating star formation across cosmic time, as also suggested by hydro-dynamical simulations (e.g., Faucher-Giguère et al. 2011; Walther et al. 2019).

While all these previous studies provided key information for our understanding of galaxy evolution, they all suffer from a set of limitations. Firstly, all relied on samples of a few hundred to at most a thousand galaxies and thus suffered from small number statistics, especially because these samples were further split into numerous redshift, stellar mass, and ΔMS ($\Delta{\rm MS} = \log_{10}({\rm SFR}/{\rm SFR_{MS}})$) bins. Secondly, all these studies were based on subsets of galaxies drawn from a parent sample using complex underlying selection functions. Each subsample could thus still fail to provide a complete and representative view of the gas content of high-redshift galaxies. This likely explains in part why these studies agreed qualitatively but disagree quantitatively on the exact redshift evolution of the gas content of massive galaxies (see Liu et al. 2019b). Finally, and most importantly, these studies relied mainly on individually detected galaxies and were thus limited to the high-mass end ($>10^{10.5}\,M_\odot$) of the SFG population. While constraining the gas content of massive galaxies is important, extending our knowledge toward lower stellar masses is crucial because the bulk of the star-formation activity of the Universe is known to take place in $10^{10\cdots10.5}\,M_\odot$ galaxies (e.g., Karim et al. 2011; Leslie et al. 2020). The gas properties of these crucial low-mass high-redshift SFGs thus remain largely unknown simply because most are individually undetected, even in deep ALMA observations.

To statistically retrieve the faint emission of this SFG population, one can perform a stacking analysis. Indeed, by grouping galaxies in meaningful ways (e.g., in bins of redshift and stellar mass) and by stacking their observations (e.g., summing or averaging), one effectively increases the observing time toward this galaxy population and can thus infer their average properties. The noise in the stacked image decreases as the root square of the number of stacked galaxies, and thus large samples can lead to robust detections of previously individually undetected galaxy populations. Such a statistical approach applied to, for example, *Spitzer*, *Herschel*, or ALMA images has proven to be extremely powerful and to push measurements well below the conventional instrumental and confusion noise limits of these observatories (e.g., Dole et al. 2006; Zheng et al. 2006; Magnelli et al. 2014, 2015, 2020; Scoville et al. 2014; Schreiber et al. 2015; Lindroos et al. 2016). Although stacking over the entire ALMA archive provides a unique opportunity to study the gas mass content of low-mass high-redshift SFGs, it also presents two challenges when compared to standard stacking analyses performed with *Spitzer*, *Herschel*, or single ALMA projects, as the ALMA archival data are heterogeneous in terms of observed frequencies and spatial resolution. While stacking data obtained at different observing frequencies simply implies a rescaling of each individual data set to a common rest-frame luminosity frequency using locally calibrated submillimeter SEDs, stacking data with different spatial resolutions is a more uncommon challenge that has only rarely been tackled in the literature (e.g., Lindroos et al. 2016; Chang et al. 2020). It can, however, be easily addressed thanks to the very nature of ALMA observations. Indeed, while combining observations with different spatial resolutions would involve very uncertain and complex convolutions in the image domain, combining them in the *uv* domain is strictly equivalent to performing aperture synthesis on a single object (e.g., Lindroos et al. 2016; Chang et al. 2020).

In this work, we aim at mitigating most of the limitations that affect current studies of the gas properties of high-redshift SFGs by applying an innovative *uv*-based stacking analysis to a large set of ALMA observations toward a mass-complete sample of $M_\star > 10^{10}\,M_\odot$ MS galaxies. This sample is drawn from one of the largest, yet still deep, multiwavelength extragalactic surveys, the Cosmic Evolution Survey 2015 (COSMOS-2015) catalog (Laigle et al. 2016). The stellar masses and redshifts of our galaxies were taken directly from the COSMOS-2015 catalog, while their SFRs were estimated from their COSMOS-2015 rest-ultraviolet, mid-infrared (MIR), and far-infrared (FIR) photometry following the ladder of SFR indicators of Wuyts et al. (2011). From this mass-complete sample of MS galaxies, we only kept those with an ALMA archival band-6 or band-7 coverage as assembled by the Automated mining of the ALMA Archive in the COSMOS field (A^{3}COSMOS) project (Liu et al. 2019a).

This mass-complete sample of MS galaxies was then subdivided into several redshift and stellar mass bins, and a measurement of their mean molecular gas mass and size was performed using a *uv*-based stacking analysis of their ALMA observations. This stacking analysis allows for accurate mean gas mass and size measurements even at low stellar masses where galaxies are too faint to be individually detected by ALMA. Our results provide, for the first time, robust RJ-based constraints on the mean cold gas mass of a mass-complete sample of $M_\star > 10^{10}\,M_\odot$ galaxies up to $z \sim 3$. Combined with their mean FIR size measurements, this yields the first stringent constraint of the KS relation at high redshift.

The structure of the paper is as follows: in Sect. 2 we introduce the ALMA data used in our study and our mass-complete sample of MS galaxies; in Sect. 3 we describe the method used to estimate the mean gas mass and size of a given galaxy population, stacking their ALMA observations in the *uv* domain; in Sect. 4 we present our results, and we discuss them in Sect. 5; finally, in Sect. 6 we summarize our findings and present our conclusions.

Throughout the paper, we assume a flat Λ cold dark matter cosmology with $H_0 = 67.8\,\mathrm{km\,s^{-1}\,Mpc^{-1}}$, $\Omega_M = 0.308$, and $\Omega_\Lambda = 0.692$ (Planck Collaboration XIII 2016). All stellar masses and SFRs are provided assuming a Chabrier (2003) initial mass function.

2. Data

2.1. The A^{3}COSMOS data set

The A^{3}COSMOS project aims at homogeneously processing (i.e., calibration, imaging and source extraction) of all ALMA projects targeting the COSMOS field that are publicly available, and providing these calibrated visibilities, cleaned images, and value-added source catalog via a single access portal (Liu et al. 2019a). In our analysis we use the A^{3}COSMOS 20200310 version[1], that is, all ALMA projects publicly available over the COSMOS field as of 10 March 2020. This database contains 80 independent ALMA projects with band-6 and/or band-7 observations. The interferometric calibration was performed by the A^{3}COSMOS project using the Common Astronomy Software Applications (CASA) package (McMullin et al. 2007) and the calibration scripts provided by the ALMA observatory. During this calibration step, a weight is assigned to each calibrated visibility and this weight is key for the accuracy of our stacking analysis (see Sect. 3.2). Unfortunately, the definition of these weights changed between the CASA versions used for the ALMA cycles 0, 1, and 2, and those used for ALMA cycles >3. For this reason, we excluded from our analysis all cycle 0, 1, and 2 ALMA projects. Our final database contains 64 ALMA projects, 39 in band-6 and 25 in band-7. These projects include 1893 images (equivalently ALMA pointings), which contain a total of 1002 sources with $>4.35\sigma$ (Liu et al. 2019a).

2.2. Our sample

COSMOS is a deep extragalactic blind survey of two square degrees on the sky centered at RA (J2000) = $10^{\mathrm{h}}00^{\mathrm{m}}28.6^{\mathrm{s}}$, Dec = $+02°12'21.0''$ (Scoville et al. 2007). This survey has been carried out over 46 broad and narrow bands probing the entire electromagnetic spectrum, from X-ray (e.g., *XMM-Newton*; Cappelluti et al. 2009), ultraviolet (e.g., GALEX; Zamojski et al. 2007), optical (e.g., Koekemoer et al. 2007; Taniguchi et al. 2007), infrared (e.g., *Spitzer*; Sanders et al. 2007), to radio wavelengths (e.g., VLA; Schinnerer et al. 2010; Smolčić et al. 2017). These observations have triggered numerous spectroscopic follow-up studies, providing nowadays more than 10 000 spectroscopic redshifts for galaxies over this field. From all these photometric and spectroscopic multiwavelength coverage, Laigle et al. (2016) built the reference COSMOS-2015 catalog, providing the photometry, redshift (photometric or spectroscopic), stellar mass, and SFR of more than half a million of galaxies. From their careful analysis, Laigle et al. (2016) classified galaxies into quiescent and star-forming based on a standard rest-frame near-ultraviolet-*r*/*r*-*J* selection method. The mass-completeness of their SFGs is down to stellar masses of $\sim 10^{9.3}\,M_\odot$ at $z < 1.75$ and $\sim 10^{9.9}\,M_\odot$ at $z < 3.50$ (see their Table 6). Here we select only SFGs above their mass-completeness limit. Moreover, to avoid contamination from active galactic nuclei (AGNs), we exclude from our analysis all galaxies classified as AGNs based on their X-Ray luminosity ($L_X \geq 10^{42}\,\mathrm{erg\,s^{-1}}$; Szokoly et al. 2004) using the latest COSMOS X-ray catalog of Marchesi et al. (2016). After the selection of SFGs and exclusion of AGNs, our parent sample is left with 515 465 galaxies (green contours in Fig. 1). We note that photometric redshifts in the COSMOS-2015 catalog are highly reliable even up to the redshift limit of our study (i.e., $z = 3.6$), with a redshift accuracy of $\sigma_{\delta z/(1+z)} \sim 0.028$ (Laigle et al. 2016).

To select from this parent sample galaxies residing within the MS of SFGs, one needs to accurately measured their SFRs. The COSMOS-2015 catalog provides such estimates but those are solely based on optical-to-near-infrared SED fits performed by Laigle et al. (2016). While reliable for stellar masses with $M_\star < 10^{11}\,M_\odot$ and moderately SFGs, observations from the *Herschel* Space Observatory have unambiguously demonstrated that such measurements are inaccurate for starbursting or massive SFGs, in which star formation can be heavily dust-enshrouded (e.g., Wuyts et al. 2011; Qin et al. 2019). To accurately measure the SFR of all galaxies in our parent sample, we thus used the approach advocated by Wuyts et al. (2011): applying to each galaxy the best dust-corrected star-formation indicator available (the so-called ladder of SFR indicator; see below for details). The SFR of galaxies for which infrared observations were available, were obtained by combining their un-obscured and obscured SFRs, following Kennicutt (1998b) for a Chabrier (2003) initial mass function,

$$\mathrm{SFR_{UV+IR}}[M_\odot\,\mathrm{yr^{-1}}] = 1.09\times10^{-10}(L_{\mathrm{IR}}[L_\odot]+3.3\times L_{\mathrm{UV}}[L_\odot]), \quad (1)$$

where the rest-frame L_{UV} at 2300 Å was taken from the COSMOS-2015 catalog, and the rest-frame $L_{\mathrm{IR}} = L(8-1000\,\mu\mathrm{m})$ was calculated from their MIR/FIR photometry[2]. For galaxies with multiple FIR photometry in the COSMOS-2015 catalog[3], we estimated their L_{IR} by fitting their *Herschel*-Photodetector Array Camera and Spectrometer (PACS) and *Herschel*-Spectral and Photometric Imaging Receiver (SPIRE) flux

[1] A^{3}COSMOS 20200310 version: https://sites.google.com/view/a3cosmos/data/dataset_v20200310

[2] Among the 3037 galaxies of our final sample (see below), 972 (32%) have MIR 24 μm photometry and among those 482 (16%) have multiple FIR photometry. Among the 1376 galaxies of our final sample with stellar mass $>10^{10}\,M_\odot$ (those detectable by our stacking analysis; see Sect. 4), 852 (62%) have MIR 24 μm photometry and among those 461 (33%) have multiple FIR photometry.

[3] The *Herschel* photometry in the COSMOS-2015 catalog is based on the 24 μm prior source extraction performed by the PEP (Lutz et al. 2011) and HerMES (Oliver et al. 2012) consortia.

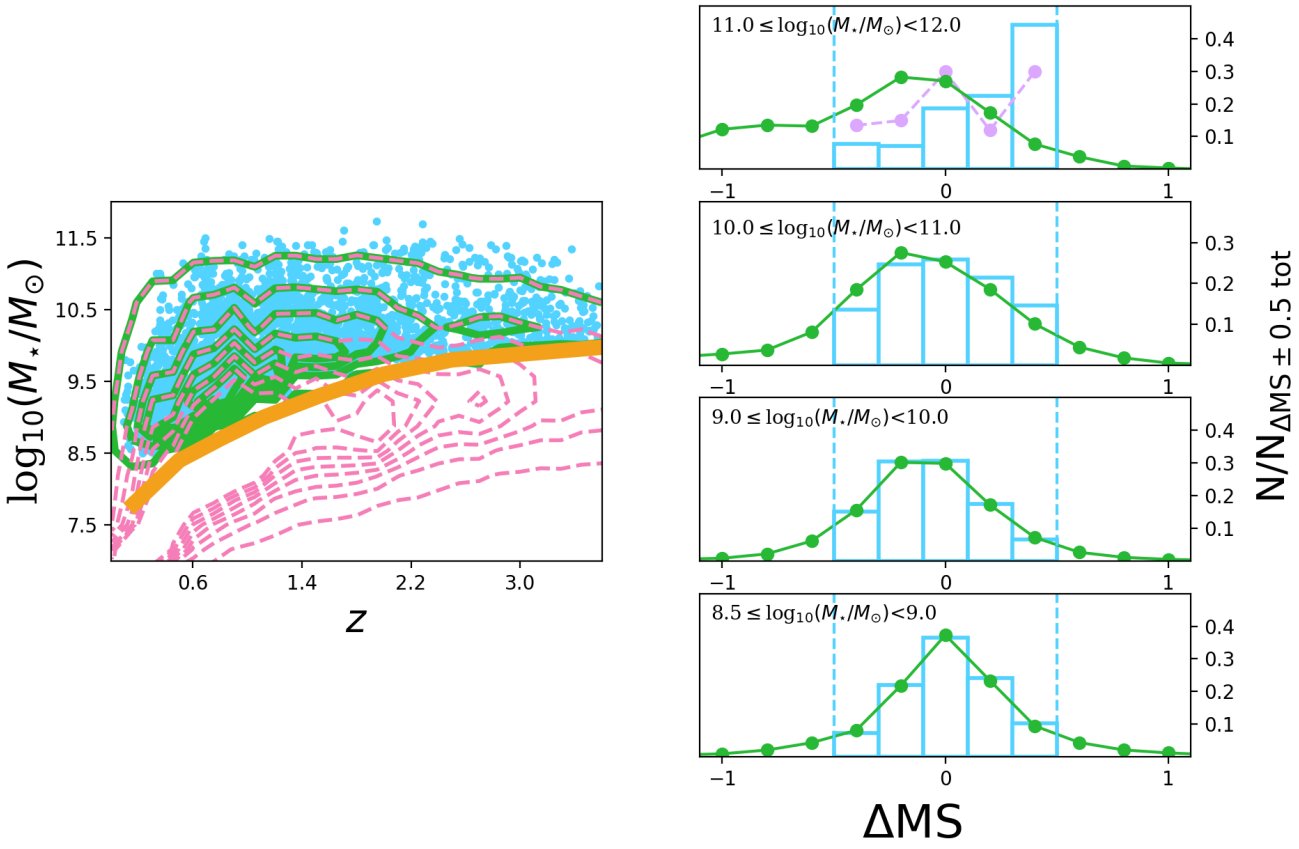

Fig. 1. Completeness and relative ΔMS distribution in our final sample. *Left*: Stellar mass and redshift distribution in our final ALMA-covered mass-complete sample of MS galaxies (blue dots). The dashed pink contours display the number density of SFGs in Laigle et al. (2016), i.e., our parent sample of SFGs. The pink contour levels are in steps of 500 from 200 to 3700 galaxies per z–$\log_{10} M_\star$ bin of size 0.14 and 0.15, respectively. The solid orange line represents the stellar mass completeness limit of SFGs in Laigle et al. (2016). The green contour shows the number density of SFGs in Laigle et al. (2016) above this stellar mass completeness limit, i.e., our parent mass-complete sample. The green contour levels are in steps of 500 from 200 to 3700 galaxies per z–$\log_{10} M_\star$ bin of size 0.14 and 0.15, respectively. *Right*: Relative ΔMS distribution in our final ALMA-covered mass-complete sample of MS galaxies (blue histogram) and our mass-complete parent sample of SFGs (green histogram) in different stellar mass bins. In the highest stellar mass bin, the dashed purple line shows the relative ΔMS distribution after having rejected from our final sample all ALMA primary targets, i.e., galaxies at the phase center of the ALMA observation. The vertical dashed blue lines display the ±0.5 dex interval used to defined MS galaxies. Over this interval, the integral of each histogram is equal to one. This normalization is needed to compare our final and mass-complete parent samples, which contain 3037 and 515 465 galaxies, respectively.

densities (Lutz et al. 2011; Oliver et al. 2012) with the SED template library of Chary & Elbaz (2001). For galaxies without a multiple FIR photometry but an MIR 24 μm detection in the COSMOS-2015 catalog, we estimated their $L_{\rm IR}$ by scaling the MS SED template of Elbaz et al. (2011) to their 24 μm flux densities (Le Floc'h et al. 2009). This particular MS SED template was chosen because it provides accurate 24 μm-to-$L_{\rm IR}$ conversions over the redshift and stellar mass ranges probed in our study (Elbaz et al. 2011). For galaxies without any MIR or FIR photometry, we used the SFRs measured by Laigle et al. (2016) and which were obtained by fitting their optical-to-near-infrared photometry with the Bruzual & Charlot (2003) SED model. We verified that toward intermediate SFRs – that is, where the fraction of galaxies with an MIR/FIR detection starts to decrease (i.e., $0 < \log(\mathrm{SFR_{IR+UV}}) < 1.5$) – our ultraviolet-plus-infrared-based SFR measurements agree with those solely based on this optical-to-near-infrared SED fits, with a median $\log(\mathrm{SFR_{IR+UV}/SFR_{SED}})$ of $0.09^{+0.39}_{-0.53}$ (Fig. 2). This agreement ensures a smooth transition between the different steps of our ladder of SFR indicators. Also, among the 269 galaxies of our final sample with stellar masses $>10^{10}\,M_\odot$ (that is, those detectable by our stacking analysis; see Sect. 4) and with SFR $>$ $100\,M_\odot\,\mathrm{yr}^{-1}$, only 54 have their SFRs solely based on their SED fits and thus potentially underestimated by ∼0.3–0.5 dex (see Fig. 2). Finally, we note that at high SFRs, where a high fraction of galaxies are individually detected by ALMA, our SFRs agree with those from the A^{3}COSMOS catalog, that is, inferred with Multi-wavelength Analysis of Galaxy Physical Properties (MAGPHYS; da Cunha et al. 2008, 2015) SED fitting combining the COSMOS-2015 photometry with super-deblended *Herschel* (Jin et al. 2018) and ALMA photometry.

From their redshift, stellar mass, and SFR, we can measure the offset of each of these galaxies from the MS: $\Delta\mathrm{MS} = \log(\mathrm{SFR}(z, \mathrm{SM})/\mathrm{SFR_{MS}}(z, \mathrm{SM}))$. To this end, we used the MS calibration of Leslie et al. (2020), as it is also based on the mass-complete COSMOS-2015 catalog:

$$\log(\mathrm{SFR_{MS}}(z, \mathrm{SM})) = S_0 - a_1 t - \log\left(1 + \left(\frac{10^{M'_t}}{10^{M}}\right)\right), \qquad M'_t = M_0 - a_2 t, \tag{2}$$

where M is $\log(M_\star/M_\odot)$, t is the age of the Universe in Gyr, $S_0 = 2.97$, $M_0 = 11.06$, $a_1 = 0.22$, and $a_2 = 0.12$. Our mass-complete sample of MS galaxies was then constructed by selecting galaxies with ΔMS between −0.5 and 0.5 (e.g., Rodighiero et al. 2014). This sample contains 92 739 galaxies.

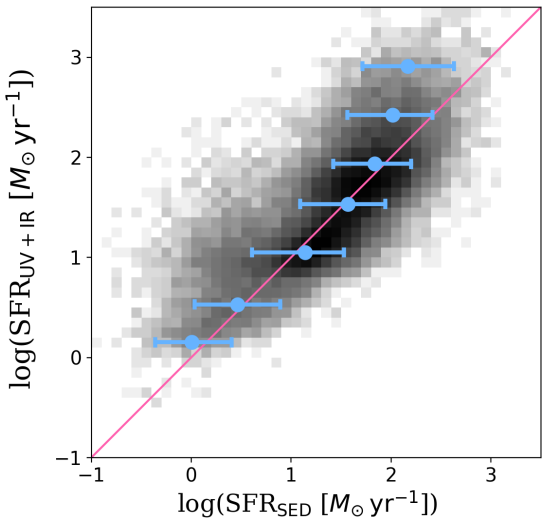

Fig. 2. Comparison of the SFRs obtained from the COSMOS-2015 catalog, i.e., SFR_{SED}, to the SFRs obtained from the ladder of SFR, i.e., SFR_{UV+IR}. Number densities are displayed in log-scale. Blue circles represent the median value of $\log(SFR_{SED})$ in $\log(SFR_{UV+IR})$ bins, starting from −0.25 dex and with a bin size of 0.5 dex. Error bars correspond to the 16th and 84th percentiles. The pink line is the one-to-one relation.

Finally, from this mass-complete sample of MS galaxies, we selected those with an ALMA band-6 (~243 GHz) or band-7 (~324 GHz) coverage in the A^{3}COSMOS database (see Sect. 2.1). Here, we only consider galaxies well within the ALMA primary beam (i.e., where the primary beam response is higher than 0.5). This conservative primary beam cut was used because uncertainties in the primary beam response far from the phase center can significantly affect our stacking analysis (see Sect. 3.2). In addition, to avoid contamination by bright neighboring sources, we excluded from our analysis galaxy pairs (<2.″0) with $S^1_{ALMA}/S^2_{ALMA} > 2$ or $M^1_\star/M^2_\star > 3$ (for ALMA undetected galaxies, assuming a first-order $M_{gas} - M_\star$ correlation). About 8% of our galaxies are excluded by these criteria. However, we note that most of these excluded galaxy pairs (~95%) are due to projection effects ($\Delta z > 0.05$). This implies that the exclusion of these galaxies does not introduce any biases into our final ALMA-covered mass-complete sample of MS galaxies. There are 3,037 galaxies in this final sample. The left panel of Fig. 1 shows the stellar mass and redshift distribution of our parent and final samples. Our final sample probes a broad range in redshifts and stellar masses, similar to that probed by our parent sample. We verified that our parent and final samples have consistent stellar mass, redshift and L_{IR} distributions, with Kolmogorov–Smirvov probabilities of 99%, 99%, and 96% of being drawn from the same distribution, respectively.

The ALMA archive cannot be treated as a real blind survey and thus our ALMA coverage selection criteria could have introduced a bias in our final ALMA-covered mass-complete MS galaxy sample. As an example (though rather unrealistic), if all ALMA projects in COSMOS would have targeted MS galaxies with $\Delta MS = 0.3$ dex, our final sample would naturally be biased toward this population and thus not be representative of the entire MS galaxy population. A simple way to test the presence of such bias is to compare the ΔMS distributions of our final and parent samples for different stellar mass bins (Fig. 1; right panels). As expected, our parent sample (green histogram) exhibits in all stellar mass bins a Gaussian distribution centered at 0 and with a 0.3 dex dispersion. At low stellar masses ($M_\star < 10^{10.0}\,M_\odot$), our final sample follows the same distribution, with a Kolmogorov–Smirvov 99% probability of being drawn from the same sample (this finding remaining true even if we further divide these stellar mass bins into several redshift bins). Indeed, in these low stellar mass bins, only 5% of our galaxies are located at the phase center of the ALMA image and thus were the primary target of the ALMA observations. However, we note that in the highest stellar mass bins the ΔMS distribution of our final sample is significantly skewed toward high ΔMS values (this finding is still true if we further divide these stellar mass bins into several redshift bins). In these stellar mass bins, about 63% of our galaxies are the primary targets of the ALMA observations (i.e., located at the phase center), and thus potentially affected by complex and uncontrollable selection biases. Excluding these primary targets from our galaxy sample yields ΔMS distribution in much better agreement with those of our parent sample. In the rest of our analysis, at high masses, we show our stacking results before and after excluding these primary-target galaxies. In addition, we account for these ΔMS distributions while fitting the cosmic and stellar mass evolution of the mean molecular gas content of MS galaxies.

3. Method

ALMA has revolutionized the study of high-redshift SFGs at (sub)millimeter wavelengths. Nevertheless, even with its unparallel sensitivity, ALMA cannot detect within a reasonable observing time MS galaxies with $M_\star < 10^{10.5}\,M_\odot$ at $z > 0.5$. Consequently, despite including all individually detected galaxies within the A^{3}COSMOS images (i.e., primary targets and serendipitous detections), the final sample of Liu et al. (2019b) is still mostly restricted to the high-mass end of the SFG population. The emission of such low-mass high-redshift SFGs captured within these images is too faint to be individually detected, and thus remains unexploited. To statistically retrieve the faint emission of this SFG population, we need to perform a stacking analysis. As already mentioned, stacking over the entire A^{3}COSMOS data set presents two challenges when compared to standard stacking analysis performed with *Spitzer*, *Herschel*, or individual ALMA projects. Indeed, the A^{3}COSMOS database is heterogeneous in terms of observed frequencies and spatial resolution. The frequency-heterogeneity problem is simply solved by a prior rescaling of each individual data set to a common rest-frame luminosity frequency using locally calibrated submillimeter SEDs (Sect. 3.1), while the spatial resolution-heterogeneity problem is solved by performing our stacking analysis in the *uv* domain (Sect. 3.2).

In the following, we describe in detail the different steps of our stacking analysis, while the validation of this methodology via Monte Carlo simulations is presented in Appendix A.

3.1. From observed-frame flux densities to rest-frame luminosities

The A^{3}COSMOS observations were performed at different frequencies and the galaxies to be stacked also lie at slightly different redshifts. Therefore, prior to proceeding with our stacking analysis, we needed to convert the ALMA observations of a given galaxy from observed flux density to its rest-frame luminosity at 850 μm (i.e., L^{rest}_{850}). To do so, we used the MS SED templates of Béthermin et al. (2012), which accurately capture the monotonic increase in the dust temperature of MS galaxies with redshift (e.g., Magdis et al. 2012; Magnelli et al. 2014). First, we computed the SED template luminosity ratio at rest-frame

850 μm and the observed rest-frame wavelength of the galaxy of interest,

$$\Gamma^{\rm SED} = L^{\rm SED}_{850}/L^{\rm SED}_{\lambda_{\rm obs}/(1+z)}. \quad (3)$$

The observed ALMA visibility amplitudes toward this galaxy (i.e., $|V(u,v,w)|_{\lambda_{\rm obs}}$) – which are in units of flux density – were then converted into rest-frame 850 μm luminosity following

$$|L(u,v,w)|^{\rm rest}_{850} = 4\,\pi\,D_L^2 \times |V(u,v,w)|_{\lambda_{\rm obs}} \times \Gamma^{\rm SED}/(1+z), \quad (4)$$

where D_L is the luminosity distance of the galaxy of interest. This rescaling of the amplitude (and weights) of the ALMA visibilities was performed for each stacked galaxy using the CASA tasks `gencal` and `applycal`.

3.2. Stacking in the uv domain

Stacking in the *uv* domain relies on the exact same principle as aperture synthesis. The only difference is that one combines multiple baselines pointing at the same galaxy population instead of multiple baselines pointing at the same galaxy. The tools or tasks needed to perform stacking in the *uv* domain are thus all readily available in CASA. For each of our stellar mass-redshift bin and each galaxy within these bins, we proceeded as follow. First, we time- and frequency-averaged their measurement set, producing one averaged visibility per ALMA scan (lasting typically 30 s and originally divided into ten 3-second integration bins) and ALMA spectral window (probing typically 2 GHz and originally divided into hundreds of channels). This step, which was performed using the CASA task `split`, is crucial to keep the volume of our final stacked measurement sets within current computing capabilities. These averaged visibilities were then rescaled from observed-frame flux density into rest-frame 850 μm luminosity using the CASA tasks `gencal` and `applycal` (see Sect. 3.1). Finally, the phase center of these averaged and rescaled visibilities were shifted to the coordinate of the stacked galaxy. This step was performed using the CASA package `STACKER` (Lindroos et al. 2015) following

$$L_{\rm shifted}(u,v,w)^{\rm rest}_{850} = L(u,v,w)^{\rm rest}_{850}\,\frac{1}{A_N(\hat{S}_k)}\,e^{\frac{2\pi}{\lambda}iB\cdot(\hat{S}_0-\hat{S}_k)}, \quad (5)$$

where $L(u,v,w)^{\rm rest}_{850}$ is the averaged and rescaled visibility, $\hat{S}_0$ is a unit vector pointing to the original phase center, $\hat{S}_k$ is a unit vector pointing to the position of the stacked galaxy, $A_N(\hat{S}_k)$ is the primary beam attenuation in the direction $\hat{S}_k$, B is the baseline of the visibility. The final stacked measurement set of a given stellar mass-redshift bin was then obtained by concatenating the shifted, rescaled, and averaged visibilities (i.e., $L_{\rm shifted}(u,v,w)^{\rm rest}_{850}$) of all galaxies within this bin using the CASA task `concat`. Because all these steps were performed in CASA, the original weights of all visibilities (i.e., those accounting for their system temperature, channel width, integration time…) were properly renormalized and could thus be used for the forthcoming *uv*-model fit and image processing.

To measure the stacked rest-frame 850 μm luminosity of each of our stellar mass–redshift bins (i.e., $L^{\rm stack}_{850}$), we used two different approaches. First, we extracted this information from the *uv* domain by fitting a single component model to the stacked measurement set. This fit was performed using the CASA task `uvmodelfit`, assuming a single Gaussian component and fixing its position to the stacked phase center. Second, we measured $L^{\rm stack}_{850}$ from the image domain. To do so, we imaged the stacked measurement set with the CASA task `tclean`, using Briggs natural weighting and cleaning the image down to 3σ. Then, we fitted a 2D Gaussian model to the cleaned image using the Python Blob Detector and Source Finder (`PyBDSF`) package (Mohan & Rafferty 2015). For all our stellar mass–redshift bins, these two approaches agreed within the uncertainties.

Our *uv*-domain and image-domain fits provide us also with the mean size (or upper limit) of the galaxy population in a given stellar mass–redshift bin. From the intrinsic (i.e., beam-deconvolved) full width at half maximum (FWHM) of the major axis outputted by `uvmodelfit` or `PyBDSF`, we define the effective – equivalently half-light – radius ($R_{\rm eff}$) of the stacked population following Jiménez-Andrade et al. (2019) (i.e., $R_{\rm eff} \approx FWHM/2.43$). Then, we express these mean size measurements in form of circularized radii, $R^{\rm circ}_{\rm eff}$,

$$R^{\rm circ}_{\rm eff} = R_{\rm eff} \times \sqrt{\frac{b}{a}}, \quad (6)$$

where b/a is the axis ratio measured with `uvmodelfit` or `PyBDSF`.

Finally, to infer the uncertainties associated with these stacked rest-frame 850 μm luminosity and size measurements, we used a standard resampling method. These uncertainties account not only for the instrumental noise in the stacked measurement set (i.e., the detection significance) but also for the intrinsic distribution of L_{850} and size within the stacked galaxy population. For a stellar mass–redshift bin containing N galaxies, we performed N different realizations of our stacking analysis, removing in each realization one galaxy of the stacked sample. The uncertainties on $L^{\rm stack}_{850}$ and size are then given by the standard deviation of these quantities measured over these realizations multiplied by $\sqrt{N}$. We note that because there is a possible mismatch of $\sim$0.″2 between the stacked optical-based position and the actual (sub)millimeter position of the sources (e.g., Elbaz et al. 2018), the average FIR sizes inferred in our study could be slightly overestimated. This is further discussed in Sect. 4.3.

It should be noted that although some studies have used median stacking to mitigate the contribution of bright outliers to the stacked flux densities (e.g., Algera et al. 2020; Feltre et al. 2020; Fudamoto et al. 2020; Gabányi et al. 2021; Johnston et al. 2021), we decided to perform our analysis using a mean stack; that is to say, in the *uv* domain our models are fitted to the weighted mean visibility amplitudes and our images are created by `tclean` using weighted mean visibilities. This choice was made for the following reasons: (i) the impact of bright outliers is already mitigated by our $-0.5 < \Delta{\rm MS} < 0.5$ selection, which by construction excludes gas-rich starbursts; (ii) the impact of bright outliers is accounted for in our uncertainties (i.e., resampling method); and finally (iii) Schreiber et al. (2015) and Leslie et al. (2020), which thoroughly tested mean and median stacking, concluded both that median stacking is biased toward higher values at low S/N because the median is not a linear operation and that the stacked distribution is intrinsically a log-normal distribution skewed toward bright sources. As a result, median stacked fluxes are difficult to interpret and are often not measuring the median nor mean fluxes, but something in between. We note, however, that the median visibility amplitudes of each of our stacked bins are consistent, within the uncertainties, with the mean visibility amplitudes (see open symbols in Fig. 3).

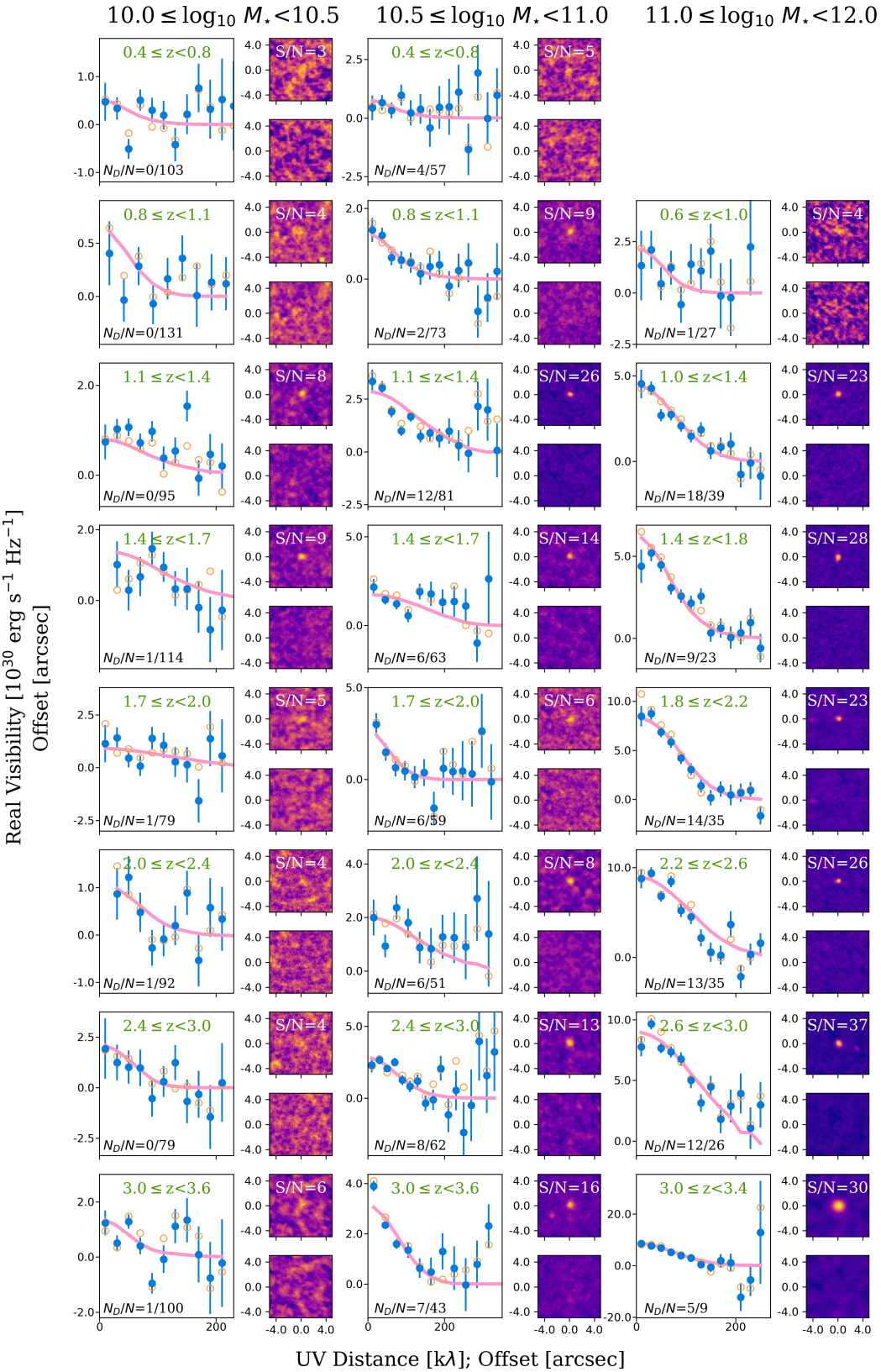

Fig. 3. Results of our stacking analysis for MS galaxies in the *uv* and image domain. For each stellar mass–redshift bin, *the left panel* shows the single component model (solid pink line) fitted to the (stacked) mean visibility amplitudes (filled blue circles) using the `CASA` task `uvmodelfit`. Open orange circles show the median visibility amplitudes, which are consistent, within the uncertainties, with the mean visibility amplitudes. *The top-right and bottom-right panels* show, respectively, the stacked and residual images, the latter being obtained by subtracting from the former the single 2D Gaussian component fitted by `PyBDSF`. The number of individually detected galaxies ($N_{\rm D}$) and the number of stacked galaxies (N) in each stellar mass–redshift bin is reported in the *left panel* (i.e., $N_{\rm D}/N$), while the detection significance i.e., $S/N_{\rm peak}$, is reported in the *upper-right panel*.

3.3. From rest-frame 850 μm luminosities to molecular gas masses

The literature contains a plethora of relations linking molecular gas mass of galaxies with their (sub)millimeter luminosities (e.g., Bourne et al. 2013; Groves et al. 2015; Scoville et al. 2017; Bertemes et al. 2018; Saintonge et al. 2018; Kaasinen et al. 2019). All of them rely on an assumed gas-to-dust mass ratio (or a direct 870 μm luminosity-to-gas mass ratio) that might or might not depend on the metallicity. Liu et al. (2019b) thoroughly studied how these different relations influence our molecular gas mass estimation, using a sample of galaxies down to a stellar mass of $\sim 10^{10.3}\,M_{\odot}$. They found that metallicity-dependent relations (Rémy-Ruyer et al. 2014; Genzel et al. 2015) and the 850 μm luminosity-dependent relation of Hughes et al. (2017) only differ by ∼0.15–0.25 dex (which is comparable to the observed scatter), and that the relation of Hughes et al. (2017) provided the best agreement with local observations (e.g., Bertemes et al. 2018; Saintonge et al. 2018). They concluded that the 850 μm luminosity-dependent relation is thus the most preferable relation for galaxies down to a stellar mass of $M_{\star} \sim 10^{10.3}\,M_{\odot}$ and for which no metallicity measurements are available. Based on their analysis, we decided to use this empirically calibrated relation of Hughes et al. (2017). The mean molecular gas mass of a given galaxy population (i.e., $M_{\rm mol}$) is thus computed from their stacked rest-frame 850 μm luminosities following

$$\log_{10} M_{\rm mol} = (0.93 \pm 0.01) \cdot \log_{10} L_{850} - (17.74 \pm 0.05), \quad (7)$$

where $M_{\rm mol}$ already includes the 1.36 correction factor to account for helium and assumes a CO-to-$M_{\rm mol}$ conversion factor (i.e., $\alpha_{\rm CO}$) of 6.5 $(\mathrm{K\,km\,s^{-1}\,pc^2})^{-1}$.

In Sect. 4.5.1 and Appendix B, we thoroughly present and discuss the impact on our results of using different gas mass calibration relations. In brief, the main conclusions of our paper are not qualitatively affected by this particular choice; the H17 method yields measurements that are bracket by those inferred from other relations. Finally, measurements obtained using H17 are in good agreement with Tacconi et al. (2020) at high stellar masses, where the Tacconi et al. (2020) study can be considered as the reference.

4. Results

The results of our stacking analysis are shown in Fig. 3 and summarized in Table 1. In our highest stellar mass bin (i.e., $10^{11} \leq M_{\star}/M_{\odot} < 10^{12}$; right-most column), the number of stacked sources per redshift bin varies from 9 to 39, with about 37% of them being individually detected. In this stellar mass bin, our stacking analysis yields high significance detections, with peak signal-to-noise ratios ($S/N_{\rm peak}$) greater than 20, except in our lowest redshift bin with $S/N_{\rm peak} \sim 4$. In the *uv* domain, those high significance detections are characterized by a Gaussian-like decrease of the stacked visibility amplitudes with the *uv*-distance, well fitted by our single component model. These galaxy populations are thus detected and spatially resolved by our stacking analysis. In the image domain, this translates into bright spatially resolved phase-center emission (i.e., with a median synthesized beam FWHM of 0.″5 and an median angular size-to-synthesized beam FWHM ratio of 1.5) that is well described by single 2D Gaussian components. In our intermediate stellar mass bin (i.e., $10^{10.5} \leq M_{\star}/M_{\odot} < 10^{11.0}$), the number of stacked sources per redshift bin increases (43–81), while the fraction of them being individually detected decreases to about 10%. As for our highest stellar mass bin, our stacking analysis yields high significance detections (i.e., $S/N_{\rm peak} > 5$) in all of our redshift bins and those are spatially resolved at our median synthesized beam FWHM of 0.″6. Finally, in our lowest stellar mass bin (i.e., $10^{10} \leq M_{\star}/M_{\odot} < 10^{10.5}$), the number of stacked sources per redshift bin increases even further (79–131) and only few of them are individually detected (1%). In this low stellar mass bin, the same patterns are observed, i.e., spatially resolved detections in the *uv* and image domain (with a median synthesize beam FWHM of 0.″7), though at lower significance, i.e., $3 < S/N_{\rm peak} < 9$. This implies that the number of stacked galaxies (controlled by the stellar mass function of MS galaxies) does not increase sufficiently to fully counterbalance the decrease in their molecular gas content with respect to the most massive population. Nevertheless, even in this low stellar mass bin, our stacking analysis yields clear detection ($S/N_{\rm peak} > 3$), especially when considering both the *uv* domain and image-domain constraints. We note that pushing this stacking analysis to lower stellar masses ($M_{\star} < 10^{10}$) did not produce any significant detection. These results are thus not presented here and not discussed further in the paper.

We conclude that our stacking analysis provides robust mean molecular gas mass and FIR size measurements for $M_{\star} > 10^{10}\,M_{\odot}$ MS galaxies from $z \sim 0.4$ to 3.6. Considering that in our highest and lowest stellar mass bins only 37% and ∼1% of these galaxies were individually detected in the A^{3}COSMOS catalog, respectively, our stacking analysis clearly provides the first unbiased ALMA view on the gas content and size of MS galaxies.

4.1. The molecular gas content of MS galaxies

The redshift evolution of the molecular gas mass of MS galaxies inferred from our stacking analysis is shown in Fig. 4. It is compared to analytical predictions from the literature (Scoville et al. 2017; Liu et al. 2019b; Tacconi et al. 2020), individually detected MS galaxies taken from the A^{3}COSMOS catalog (Liu et al. 2019b) and a local reference (i.e., $z \sim 0.03$) taken from Saintonge et al. (2017). In addition, in Fig. 5, we present the evolution of the molecular gas fraction (i.e., $\mu_{\rm mol} = \langle M_{\rm mol}\rangle/\langle M_{\star}\rangle$) of MS galaxies as a function of redshifts and stellar masses. We note that for our galaxies in common with the A^{3}COSMOS catalog, the stellar masses used here (i.e., those from the COSMOS-2015 catalog) are about 0.22 dex lower than those reported in the A^{3}COSMOS catalog. This offset, which is also discussed in Liu et al. (2019b), is likely explained by the fact that stellar masses in the A^{3}COSMOS catalog rely on full optical-to-millimeter energy-balanced SED fits performed with MAGPHYS. While this offset is observed for massive galaxies, it might not be present at $\lesssim 10^{10.5}\,M_{\odot}$, where the number of galaxies available in the A^{3}COSMOS catalog is too scarce to provide meaningful comparison with the COSMOS-2015 catalog. In any case, when comparing our analytical predictions to those from Liu et al. (2019b), we thus show both their original predictions and those inferred by accounting for this systematic 0.22 dex offset.

Our measurements reveal a significant evolution of the molecular gas mass of MS galaxies with both redshifts and stellar masses. For all stellar mass bins, the molecular gas masses of MS galaxies (equivalently molecular gas fraction) increase by a factor of ∼24 from $z \sim 0$ to $z \sim 3.2$. In addition, at a given redshift, the molecular gas masses of MS galaxies significantly increase with stellar masses. This trend is, however, sublinear in the log-log space, which implies that the molecular gas fraction of MS galaxies decreases with stellar mass at a given redshift (Fig. 5). To obtain a more quantitative constraint on the stellar

Table 1. Molecular gas mass and size properties of MS galaxies.

$M_\star$	z	N	N_D	$\langle z\rangle$	$\langle M_\star\rangle$ ($\log_{10}[M_\odot]$)	$\langle$SFR$\rangle$ ($\log_{10}[M_\odot\,\mathrm{yr}^{-1}]$)	$\langle\Delta\mathrm{MS}\rangle$	$\langle\nu_{\rm obs}\rangle$ (GHz)	$\langle L_{850-uv}\rangle$ (10^{30} erg s^{-1} Hz^{-1})	$S/N_{\rm peak}$	$M_{\rm mol-uv}$ ($\log_{10}[M_\odot]$)	$M_{\rm mol-py}$ ($\log_{10}[M_\odot]$)	$\theta^{\rm circ}_{\rm beam}$ (arcsec)	$\theta^{\rm circ}_{\rm mol-uv}$ (arcsec)	$\theta^{\rm circ}_{\rm mol-py}$ (arcsec)	$R^{\rm circ}_{\rm eff-uv}$ (kpc)	$R^{\rm circ}_{\rm eff-py}$ (kpc)
(1)	(2)	(3)	(4)	(5)	(6)	(7)	(8)	(9)	(10)	(11)	(12)	(13)	(14)	(15)	(16)	(17)	(18)
$11.0 \le \log_{10}$	$0.6 \le z < 1.0$	27	1	0.79	11.16	1.58	0.09	298.02	$2.3_{\pm0.7}$	4	$10.5_{\pm0.1}$	$10.4_{\pm0.2}$	0.51	1.10	0.83	$3.0_{\pm1.}$	$2.1_{\pm1.1}$
$M_\star < 12.0$	$1.0 \le z < 1.4$	39	18	1.24	11.17	2.01	0.19	313.30	$4.5_{\pm0.7}$	23	$10.8_{\pm0.1}$	$10.8_{\pm0.1}$	0.50	0.75	0.75	$1.9_{\pm0.2}$	$1.9_{\pm0.2}$
	$1.4 \le z < 1.8$	23	9	1.57	11.22	2.21	0.20	311.27	$6.3_{\pm1.2}$	28	$10.9_{\pm0.1}$	$10.9_{\pm0.1}$	0.47	0.77	0.78	$2.1_{\pm0.1}$	$2.2_{\pm0.2}$
	$1.8 \le z < 2.2$	35	14	1.98	11.22	2.35	0.15	312.98	$8.4_{\pm3.0}$	23	$11.0_{\pm0.2}$	$11.1_{\pm0.1}$	0.42	0.65	0.67	$1.7_{\pm0.1}$	$1.8_{\pm0.2}$
	$2.2 \le z < 2.6$	35	13	2.35	11.26	2.52	0.24	310.17	$9.3_{\pm1.9}$	26	$11.1_{\pm0.1}$	$11.1_{\pm0.1}$	0.42	0.59	0.62	$1.5_{\pm0.1}$	$1.6_{\pm0.1}$
	$2.6 \le z < 3.0$	26	12	2.82	11.22	2.57	0.22	297.10	$9.0_{\pm1.8}$	37	$11.0_{\pm0.1}$	$11.1_{\pm0.1}$	0.72	0.79	0.87	$1.1_{\pm0.1}$	$1.5_{\pm0.1}$
	$3.0 \le z < 3.4$	9	5	3.19	11.16	2.76	0.38	271.01	$8.8_{\pm1.5}$	30	$11.0_{\pm0.1}$	$11.0_{\pm0.1}$	1.39	1.60	1.60	$2.6_{\pm0.2}$	$2.5_{\pm0.2}$
$11.0 \le \log_{10}$	$0.6 \le z < 1.4$	17	0	0.97	11.17	1.62	−0.03	270.21	$2.0_{\pm0.9}$	5	$10.4_{\pm0.2}$	$10.5_{\pm0.2}$	0.83	0.92	1.02	$1.4_{\pm0.7}$	$2.0_{\pm0.9}$
$M_\star < 12.0$	$1.4 \le z < 2.2$	20	7	1.84	11.19	2.18	0.00	301.15	$3.8_{\pm2.1}$	13	$10.7_{\pm0.2}$	$10.7_{\pm0.2}$	0.69	0.81	0.87	$1.5_{\pm0.2}$	$1.9_{\pm0.2}$
(off the phase	$2.2 \le z < 2.6$	13	6	2.39	11.20	2.40	0.11	284.18	$7.7_{\pm1.9}$	17	$11.0_{\pm0.1}$	$11.0_{\pm0.1}$	0.72	0.77	0.80	$0.9_{\pm0.1}$	$1.2_{\pm0.2}$
center)	$2.6 \le z < 3.0$	8	3	2.80	11.20	2.55	0.19	277.93	$7.4_{\pm1.8}$	16	$11.0_{\pm0.1}$	$11.0_{\pm0.1}$	0.98	1.13	1.17	$1.8_{\pm0.2}$	$2.1_{\pm0.3}$
	$3.0 \le z < 3.4$	6	3	3.18	11.19	2.72	0.33	259.30	$9.3_{\pm1.4}$	15	$11.1_{\pm0.1}$	$11.1_{\pm0.1}$	1.29	1.57	1.57	$2.9_{\pm0.2}$	$2.9_{\pm0.3}$
$10.5 \le \log_{10}$	$0.4 \le z < 0.8$	57	4	0.67	10.69	1.43	0.18	316.73	$0.8_{\pm0.5}$	5	$10.1_{\pm0.2}$	$10.1_{\pm0.2}$	0.60	0.82	0.84	$1.6_{\pm0.7}$	$1.7_{\pm0.8}$
$M_\star < 11.0$	$0.8 \le z < 1.1$	73	2	0.92	10.72	1.58	0.06	298.96	$1.3_{\pm0.9}$	9	$10.3_{\pm0.3}$	$10.3_{\pm0.3}$	0.62	0.85	0.87	$1.9_{\pm0.2}$	$2.0_{\pm0.4}$
	$1.1 \le z < 1.4$	81	12	1.25	10.71	1.83	0.08	274.75	$2.9_{\pm0.6}$	26	$10.6_{\pm0.1}$	$10.6_{\pm0.1}$	0.55	0.64	0.68	$1.2_{\pm0.1}$	$1.4_{\pm0.2}$
	$1.4 \le z < 1.7$	63	6	1.55	10.72	1.99	0.11	299.42	$1.7_{\pm0.6}$	14	$10.4_{\pm0.2}$	$10.4_{\pm0.1}$	0.68	0.73	0.73	$1.0_{\pm0.5}$	$1.0_{\pm0.2}$
	$1.7 \le z < 2.0$	59	6	1.85	10.69	1.96	−0.02	284.15	$2.7_{\pm0.6}$	6	$10.6_{\pm0.1}$	$10.6_{\pm0.1}$	0.54	1.08	1.04	$3.3_{\pm0.4}$	$3.1_{\pm0.8}$
	$2.0 \le z < 2.4$	51	6	2.19	10.72	2.07	−0.04	282.95	$2.0_{\pm0.5}$	8	$10.4_{\pm0.1}$	$10.5_{\pm0.1}$	0.80	0.90	0.94	$1.8_{\pm0.4}$	$2.6_{\pm0.7}$
	$2.4 \le z < 3.0$	62	8	2.69	10.69	2.16	−0.02	279.43	$2.8_{\pm0.6}$	13	$10.6_{\pm0.1}$	$10.5_{\pm0.1}$	0.81	0.98	1.01	$2.2_{\pm0.2}$	$2.0_{\pm0.4}$
	$3.0 \le z < 3.6$	43	7	3.22	10.70	2.10	−0.12	269.51	$3.2_{\pm1.1}$	16	$10.6_{\pm0.1}$	$10.7_{\pm0.1}$	0.63	0.88	0.96	$2.1_{\pm0.2}$	$2.3_{\pm0.2}$
$10.0 \le \log_{10}$	$0.4 \le z < 0.8$	103	0	0.67	10.26	1.24	0.11	302.70	$0.5_{\pm0.5}$	3	$9.9_{\pm0.4}$	$10.1_{\pm0.2}$	0.75	1.26	1.65	$3.0_{\pm1.1}$	$4.3_{\pm2.2}$
$M_\star < 10.5$	$0.8 \le z < 1.1$	131	0	0.94	10.23	1.34	0.02	299.47	$0.7_{\pm0.2}$	4	$10.0_{\pm0.1}$	$9.8_{\pm0.3}$	0.63	1.24	0.88	$3.7_{\pm0.7}$	$2.1_{\pm1.1}$
	$1.1 \le z < 1.4$	95	0	1.24	10.24	1.48	−0.04	270.81	$0.8_{\pm0.8}$	8	$10.1_{\pm0.4}$	$10.2_{\pm0.3}$	0.68	0.73	1.03	$0.8_{\pm0.7}$	$2.7_{\pm0.7}$
	$1.4 \le z < 1.7$	114	1	1.54	10.22	1.67	0.06	289.10	$1.4_{\pm0.2}$	9	$10.3_{\pm0.1}$	$10.4_{\pm0.1}$	0.71	0.82	0.94	$1.4_{\pm0.3}$	$2.2_{\pm0.5}$
	$1.7 \le z < 2.0$	79	1	1.85	10.21	1.67	−0.04	278.14	$0.9_{\pm0.2}$	5	$10.1_{\pm0.1}$	$10.2_{\pm0.1}$	0.76	0.91	1.08	$1.7_{\pm0.7}$	$2.7_{\pm1.2}$
	$2.0 \le z < 2.4$	92	1	2.18	10.22	1.62	−0.14	284.62	$1.1_{\pm0.4}$	4	$10.2_{\pm0.1}$	$10.3_{\pm0.1}$	0.40	0.67	0.71	$1.9_{\pm0.4}$	$2.1_{\pm0.7}$
	$2.4 \le z < 3.0$	79	0	2.74	10.24	1.80	−0.10	269.94	$2.2_{\pm0.9}$	4	$10.5_{\pm0.2}$	$10.4_{\pm0.2}$	0.58	1.20	0.91	$3.5_{\pm0.2}$	$2.3_{\pm1.2}$
	$3.0 \le z < 3.6$	100	1	3.30	10.20	1.79	−0.11	261.39	$1.7_{\pm0.3}$	6	$10.4_{\pm0.1}$	$10.4_{\pm0.1}$	0.84	1.11	1.27	$2.3_{\pm0.7}$	$3.0_{\pm1.2}$

Notes. (1) Stellar mass bin, (2) redshift bin, (3) number of stacked galaxies, (4) number of individually detected stacked galaxies, (5) mean redshift, (6) mean stellar mass, (7) mean SFR, (8) mean ΔMS, (9) mean observed frequency, (10) mean L_{850} inferred from the *uv* domain, (11) peak S/N on the image, (12) mean gas mass inferred from the *uv*-domain, and (13) from the image domain, (14) circularized synthesized beam FWHM, (15) circularized intrinsic FWHM from the *uv* domain, (16) circularized intrinsic FWHM from the image domain, (17) circularized half-light radii from the *uv* domain, and (18) from the image domain.

mass and redshift dependences of evolution of the molecular gas fraction of MS galaxies, we fitted our measurements, together with the local reference, following Liu et al. (2019b), that is,

$$\begin{aligned}\log_{10}\mu_{\rm mol} = &(a + ak\times\log_{10}(M_\star/10^{10}))\times\Delta\mathrm{MS}\\ &+ b\times\log_{10}(M_\star/10^{10})\\ &+ (c + ck\times\log_{10}(M_\star/10^{10}))\times t_{\rm cosmic}\\ &+ d,\end{aligned} \tag{8}$$

where $t_{\rm cosmic}$ is the cosmic time in units of Gyr, and $M_\star$ is in units of $M_\odot$. Because our analysis does not probe a large dynamic range in ΔMS, we fixed a and ak to the values reported by Liu et al. (2019b) (i.e., $a = 0.4195$ and $ak = 0.1195$, respectively). To constrain the remaining parameters of Eq. (8), we then performed a standard Bayesian analysis using the python Markov chain Monte Carlo (MCMC) package `emcee` (Foreman-Mackey et al. 2013). In this analysis, we accounted for the redshift, stellar mass, and ΔMS of each galaxy in a given stacked bin, that is, in each MCMC step, we compared our stacked measurements, $\langle M^i_{\rm gas}\rangle$, to $\langle f(t^i_{\rm cosmic}, M^i_\star, \Delta\mathrm{MS}^i)\rangle$ and not $f(\langle t^i_{\rm cosmic}\rangle, \langle M^i_\star\rangle, \langle\Delta\mathrm{MS}^i\rangle)$, where i is the ith galaxy of our stacked bin and f is the fitted function. This avoids averaging biases that could arise if one would simply fit our stacked measurements using $\langle t^i_{\rm cosmic}\rangle$, $\langle M^i_\star\rangle$, and $\langle\Delta\mathrm{MS}^i\rangle$. Results of this MCMC analysis are shown in Fig. 6, with $b = -0.468^{+0.070}_{-0.070}$, $c = -0.122^{+0.008}_{-0.008}$, $d = 0.572^{+0.059}_{-0.060}$, and $ck = 0.002^{+0.011}_{-0.011}$. These results unambiguously demonstrate that the molecular gas fraction of MS galaxies decreases with stellar masses (i.e., $b < 0$) while it increases with redshifts (i.e., $c < 0$; see blue solid lines in Fig. 4). We note that repeating this MCMC analysis while fixing $a = 0$ and $ak = 0$ (i.e., considering that our measurements are for ΔMS = 0 galaxies), the likelihood of our fit decreases but the inferred gas fraction evolution remains qualitatively consistent with our previous fit, albeit with a somewhat flatter stellar mass dependence (i.e., $b = -0.252^{+0.072}_{-0.072}$, $c = -0.114^{+0.008}_{-0.008}$, $d = 0.481^{+0.061}_{-0.061}$, and $ck = -0.016^{+0.011}_{-0.011}$).

By comparing our results with those from the A^{3}COSMOS catalog, one immediately notices that these individually detected galaxies systematically lie above our measurements. This systematic offset results from an observational bias. First of all, at a given redshift and stellar mass, the A^{3}COSMOS catalog mostly contains galaxies on the upper part of the MS because those galaxies have higher molecular gas mass ($a > 0$ in Eq. 8) and are thus more likely to be individually detected. This observational bias was, however, accounted for when fitting the A^{3}COSMOS population using Eq. (8). This "correction" can be seen in Fig. 4 by noticing that the A^{3}COSMOS analytical predictions for MS galaxies systematically lies below the A^{3}COSMOS data-points. Nevertheless, at a given redshift, stellar mass, and ΔMS, the A^{3}COSMOS catalog could still be biased toward galaxies with a bright millimeter emission and thus high molecular gas mass (see discussion in Liu et al. 2019b). Our measurements, which are not affected by this bias and which lie systematically below those of Scoville et al. (2017), Liu et al. (2019b), and Tacconi et al. (2020), clearly demonstrate the presence of this residual observational bias in these literature studies. By averaging at a given redshift and stellar mass all MS galaxies in the field, our stacking analysis reveals their true mean molecular gas mass. Taken at face value, our findings imply that previous studies might have systematically overestimated by at least 10–40% the gas content of MS galaxies in redshift and stellar mass bins with relatively high detection fraction (i.e., mostly $M_\star > 10^{11}\,M_\odot$),

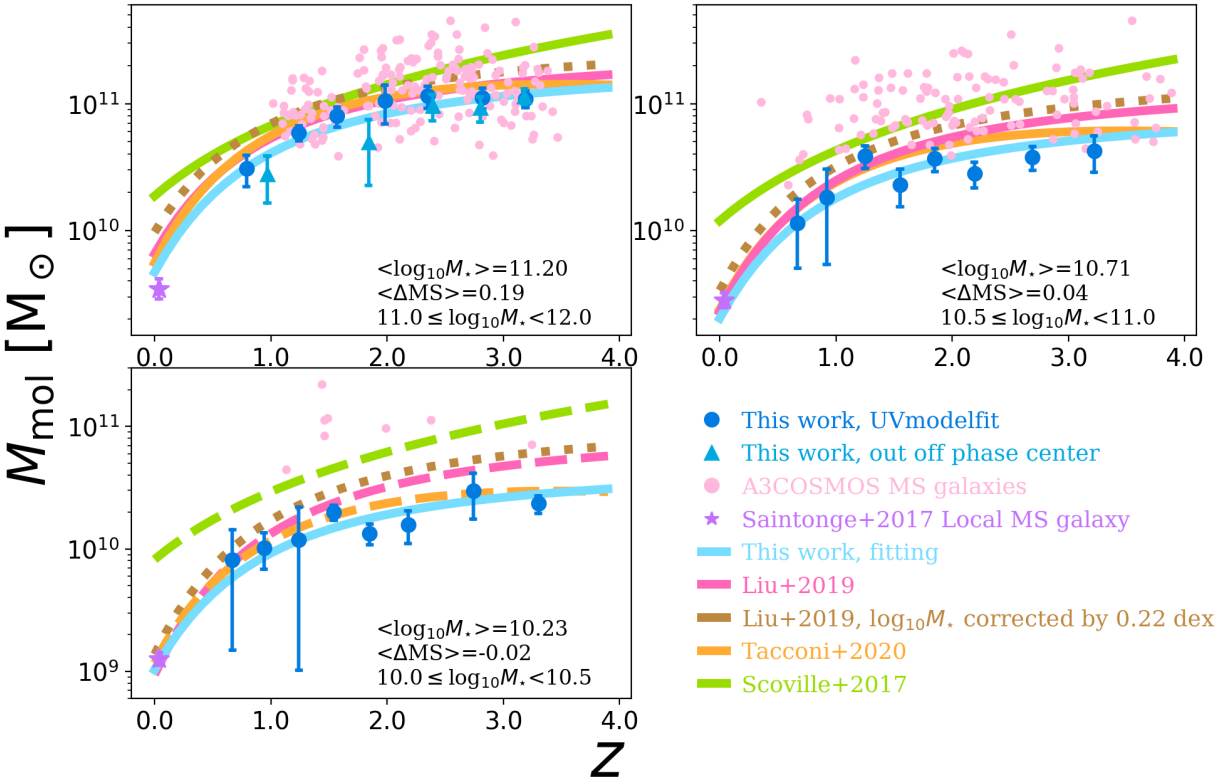

Fig. 4. Redshift evolution of the mean molecular gas mass of MS galaxies in three stellar mass bins, i.e., $10^{11} \leq M_\star/M_\odot < 10^{12}$, $10^{10.5} \leq M_\star/M_\odot < 10^{11}$, and $10^{10} \leq M_\star/M_\odot < 10^{10.5}$. Blue circles show our *uv*-domain measurements, while in the highest stellar mass bin blue triangles show those obtained after excluding ALMA primary-target galaxies from our stacked sample (see Sect. 2.2). Pink circles are individually detected MS galaxies taken from the A^{3}COSMOS catalog (Liu et al. 2019b), while purple stars present the local reference taken from Saintonge et al. (2017). Lines show the analytical evolution of the gas fraction as inferred from our work (blue), from Scoville et al. (2017, green), from Liu et al. (2019b, pink), from Tacconi et al. (2020, orange), and from Liu et al. (2019b, dotted brown line) but this time accounting for the systematic 0.22 dex offset observed between their and our stellar mass estimates. In our lower stellar mass bin, lines from the literature are dashed as they mostly rely on extrapolations. We note that here and in all following figures, the values of $\langle M_\star \rangle$ and $\langle \Delta\mathrm{MS} \rangle$ given in each panel are simply used to plot the analytical evolution of the gas fraction. These values naturally vary for each stacked measurements and are accounted for by our MCMC analysis. This avoids averaging biases that could arise if one simply fit our stacked measurements using $\langle t_\mathrm{cosmic} \rangle$, $\langle M_\star \rangle$, and $\langle \Delta\mathrm{MS} \rangle$.

and by 10–60% in bins with low detection fraction. While significant, one should, however, acknowledge that these offsets remain reasonable considering all the selection biases affecting these previous studies. The impact of this finding for galaxy evolution models is discussed in Sect. 5.

4.2. The molecular gas depletion time of MS galaxies

The redshift evolution of the molecular gas depletion time (i.e., $\tau_\mathrm{mol} = M_\mathrm{mol}/\mathrm{SFR}$) of MS galaxies as inferred from our stacking analysis is shown in Fig. 7, together with analytical predictions from Scoville et al. (2017), Liu et al. (2019b), and Tacconi et al. (2020) as well as the local reference for MS galaxies taken from Saintonge et al. (2017). In addition, in Fig. 8, we compare the redshift evolution of the molecular gas depletion time as inferred for our three stellar mass bins. Again, to obtain a more quantitative constraint on the stellar mass and redshift dependences of the molecular gas depletion time of MS galaxies, we fitted our measurements, together with the local reference, following Liu et al. (2019b), that is,

$$\begin{aligned}\log_{10}\tau_\mathrm{mol} = {} & (a + ak \times \log_{10}(M_\star/10^{10})) \times \Delta\mathrm{MS} \\ & + b \times \log_{10}(M_\star/10^{10}) \\ & + (c + ck \times \log_{10}(M_\star/10^{10})) \times t_\mathrm{cosmic} \\ & + d.\end{aligned} \tag{9}$$

Our analysis does not probe a large dynamic range in ΔMS, we thus fixed a and ak to the values reported by Liu et al. (2019b), that is, $a = -0.5724$ and $ak = 0.1120$. Results of our MCMC analysis are shown in Fig. 9, with $b = 0.055^{+0.069}_{-0.071}$, $c = 0.049^{+0.008}_{-0.008}$, $d = -0.643^{+0.056}_{-0.057}$, and $ck = 0.016^{+0.010}_{-0.010}$. Because the depletion time is the ratio of M_mol by SFR, we also display in Fig. 7 the redshift evolution of depletion time as one would infer by dividing $M_\mathrm{gas}(z, M_*, \Delta\mathrm{MS})$ from Eq. (8) by the $\mathrm{SFR_{MS}}(z, M_*, \Delta\mathrm{MS})$ from Leslie et al. (2020, dash-dotted light-blue line).

In all our stellar mass bins, the molecular gas depletion time of MS galaxies decreases by a factor of ∼3–4 from $z \sim 0$ to $z \sim 3.2$, with, however, most of this decrease happening at $z \lesssim 1.0$. At $z \gtrsim 1$, the molecular gas depletion time of MS galaxies remains instead roughly constant with redshifts and stellar masses with a value of ∼300–500 Myr. While such evolution is qualitatively predicted by all literature studies, its amplitude as well as its exact redshift and stellar mass dependences quantitatively disagree (see Fig. 7). For example, our measurements and those from Liu et al. (2019b) agree at high stellar masses, but differ by ∼30–40% in our lower stellar mass bins. These differences are likely explained by the observational biased discussed in Sect. 4.1, which implies that the mean molecular gas mass and thus depletion time of MS galaxies inferred by Liu et al. (2019b) are slightly overestimated especially at low stellar masses. The same effect likely explains the ∼20–30% overestimation of the

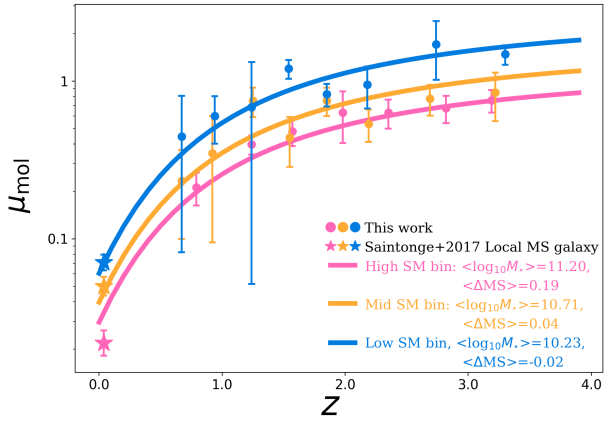

Fig. 5. Redshift evolution of the mean molecular gas fraction of MS galaxies. Circles show the mean molecular gas fraction from our work. Stars present the local reference taken from Saintonge et al. (2017). Lines display the analytical evolution of the molecular gas fraction inferred from our work. Symbols and lines are color-coded by stellar mass, i.e., pink for $10^{11} \leq M_\star/M_\odot < 10^{12}$, orange for $10^{10.5} \leq M_\star/M_\odot < 10^{11}$, and blue for $10^{10} \leq M_\star/M_\odot < 10^{10.5}$.

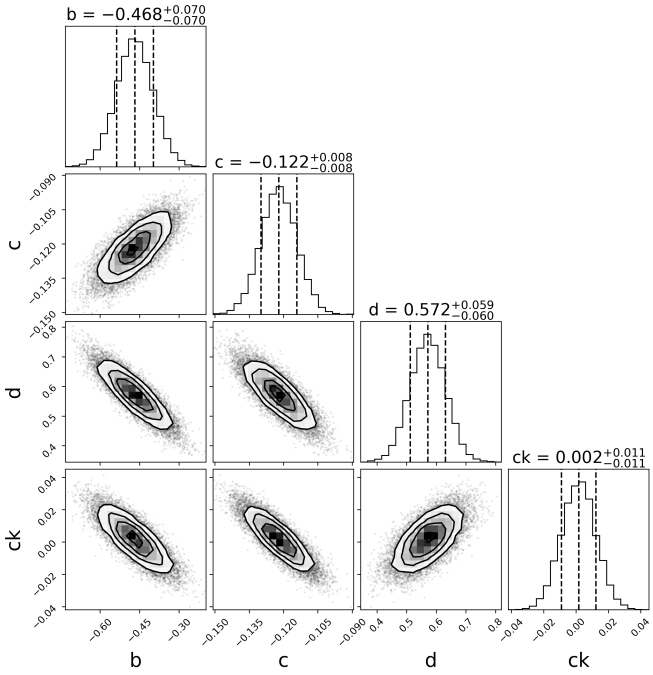

Fig. 6. Probability distributions of the parameters in Eq. (8), as found by fitting our stacked measurements using an MCMC analysis. The dashed vertical lines show the 16th, 50th, and 84th percentiles of each distribution.

molecular gas depletion time inferred in Tacconi et al. (2020) in most redshift–stellar mass bins probed here. While our direct analytical fit of the redshift/stellar mass evolution of the molecular gas depletion time (solid blue lines in Fig. 7) matches relatively well the local reference from Saintonge et al. (2017), this is not the case of our fit inferred by simply dividing $M_{\rm gas}(z, M_*, \Delta{\rm MS})$ from Eq. (8) by ${\rm SFR_{MS}}(z, M_*, \Delta{\rm MS})$ from Leslie et al. (2020, dash-dotted light-blue line). This disagreement between predictions and observations at $z \sim 0$ is entirely attributed to a miss-match in ${\rm SFR_{MS}}(z, M_*, \Delta{\rm MS})$, that is, at a given stellar mass, the mean SFR of $z \sim 0$ MS galaxies as predicted by Leslie et al. (2020) does not match that observed by Saintonge et al. (2017). This disagreement is, however, not unexpected as the sample used in Leslie et al. (2020) was restricted to $z > 0.3$ galaxies.

In general, we conclude that our depletion times agree at high stellar masses with Liu et al. (2019b), that is, where their study relies on a large and robust amount of ALMA-based measurements of MS galaxies; while our depletion time agree better at low stellar masses with Tacconi et al. (2020), that is, where their study, contrary to that of Liu et al. (2019b), still relies on some observational measurements of MS galaxies thanks to their *Herschel* stacking analysis. Like our measurements, those from Tacconi et al. (2020) predict only a minor evolution of the molecular gas depletion time of MS galaxies with stellar masses. This implies that the flattening of the MS at high stellar masses observed in most studies (i.e., $\log_{10}\ {\rm SFR^{MS}} = 0.7 \times \log_{10}\ M_\star^{\rm MS} + {\rm C}$) is not associated with or due to lower SFEs (i.e., $1/\tau_{\rm mol}$) in massive systems but rather lower molecular gas fraction (see Sect. 4.1). This is further discussed in Sect. 5. In addition, we note that extrapolating our molecular gas depletion time predictions to $z \sim 5$, that is, $\tau_{\rm mol}^{\rm pred} = 250$ Myr (from Eq. (9)) or $\tau_{\rm mol}^{\rm pred} = 620$ Myr (from Eq. (8)/specific ${\rm SFR_{MS}}$), our prediction qualitatively agrees with the latest observational constraints from the ALPINE [C II] ALMA large project (i.e., $\tau_{\rm mol}^{\rm obs} = 520 \pm 70$ Myr) (Dessauges-Zavadsky et al. 2020).

Finally, we note that the accuracy of the depletion times relies not only on accurate gas masses but also on accurate SFRs. In our study, the latter were estimated using the so-called ladder of SFR indicators, that is, by applying to each galaxy the best dust-corrected star-formation indicator available (Sect. 2.2). In particular, among the 1376 galaxies in our final sample with stellar mass $>10^{10}\,M_\odot$, 852 (62%) have very robust dust-corrected SFRs based on the combination of infrared and ultraviolet measurements. Of the remaining 524 galaxies whose SFRs are solely based on their ultraviolet-to-optical fits, most (470) should also have robust SFRs, as they falls below the $\sim 100\,M_\odot\,{\rm yr}^{-1}$ limit above which ${\rm SFR_{SED}}$ starts to be systematically underestimated (Fig. 2). We verified that our results remain unchanged (within the uncertainties) when excluding from our stacking analysis these 54 galaxies with ${\rm SFR_{SED}} > 100\,M_\odot\,{\rm yr}^{-1}$ and without infrared detection.

4.3. The FIR sizes of MS galaxies

Our stacking analysis provides the first measurements of the mean FIR size of MS galaxies across cosmic time. These mean FIR (at the observed-frame 850–1300 μm) sizes of MS galaxies are presented in Fig. 10, and compared to optical, FIR and radio sizes measurements from van der Wel et al. (2014), Barro et al. (2016), Rujopakarn et al. (2016), Elbaz et al. (2018), Jiménez-Andrade et al. (2019), Suess et al. (2019), Chang et al. (2020), and Tadaki et al. (2020). Because most of the FIR and radio size measurements from the literature were made on the image-plane, we displayed in Fig. 10 our 2D Gaussian image-plane measurements inferred using PyBDSF. Displaying instead our *uv*-plane size measurements would, however, not change any of our conclusions, as both agree within their uncertainties with no apparent systematic offset between them.

These FIR sizes do not seem to evolve significantly with redshift or stellar mass, with a mean circularized effective – equivalently half-light – radius of 2.2 kpc (i.e., corresponding

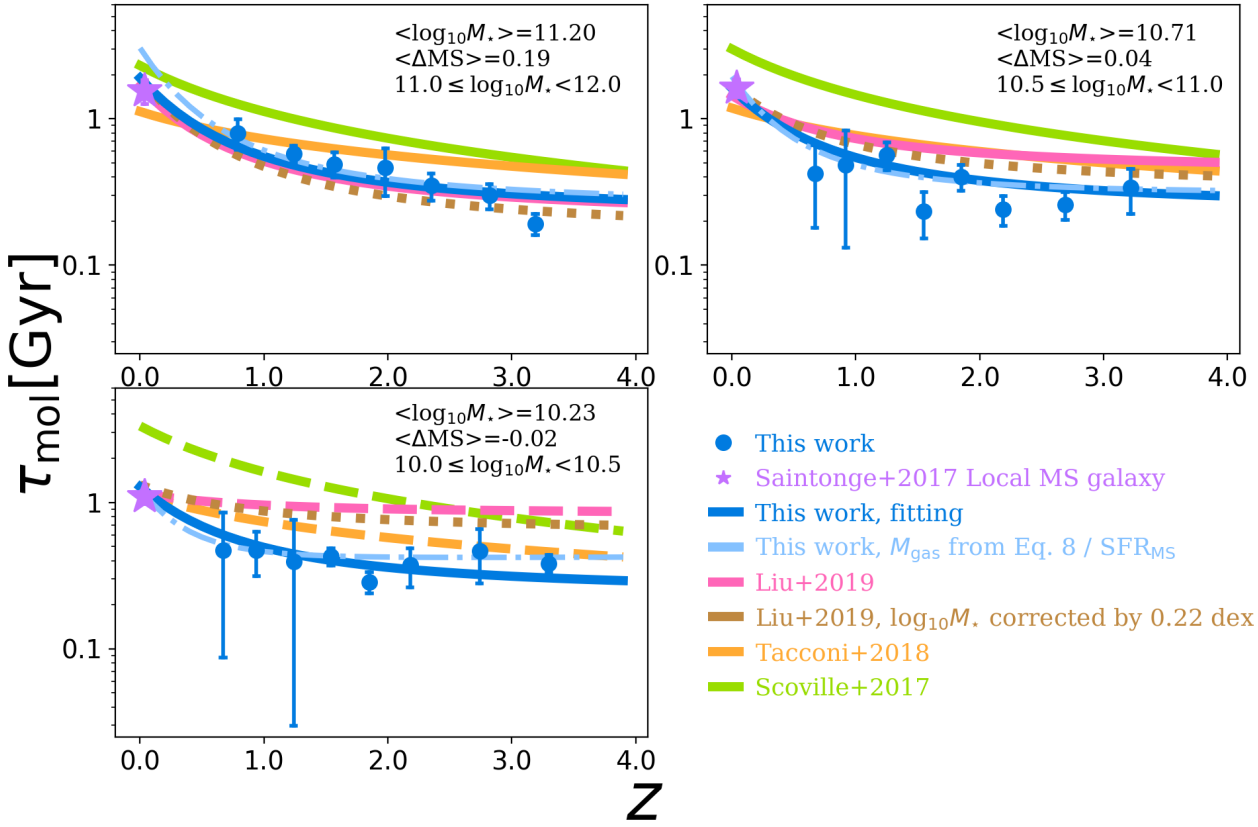

Fig. 7. Redshift evolution of the molecular gas depletion time of MS galaxies in three stellar mass bins, i.e., $10^{11} \leq M_\star/M_\odot < 10^{12}$, $10^{10.5} \leq M_\star/M_\odot < 10^{11}$, and $10^{10} \leq M_\star/M_\odot < 10^{10.5}$. Blue circles show our *uv*-domain molecular gas mass measurements divided by the mean SFR of each of these stacked samples. Purple stars show the local MS reference taken from Saintonge et al. (2017). Lines present the analytical evolution of the molecular gas depletion time as inferred from our work (blue lines; see text for details), from Liu et al. (2019b, pink line), from Scoville et al. (2017, green line), and from Tacconi et al. (2020, orange line). In our lower stellar mass bin, lines from the literature are dashed as they mostly rely on extrapolations.

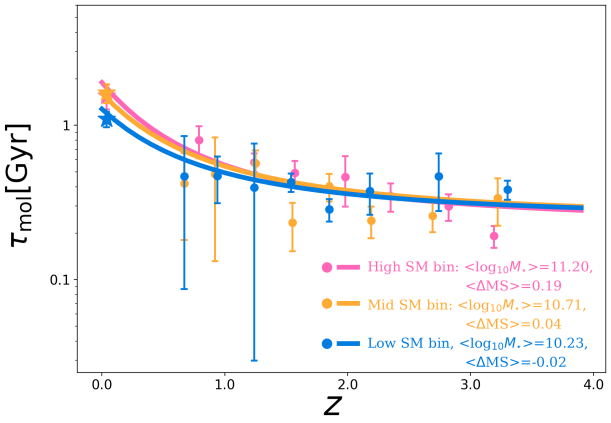

Fig. 8. Redshift evolution of the molecular gas depletion time of MS galaxies. Circles show the mean molecular gas depletion time from our work. Stars show the local MS reference taken from Saintonge et al. (2017). Lines display the analytical evolution of the molecular gas fraction inferred from our work. Symbols and lines are color-coded by stellar mass, i.e., pink for $10^{11} \leq M_\star/M_\odot < 10^{12}$, orange for $10^{10.5} \leq M_\star/M_\odot < 10^{11}$, and blue for $10^{10} \leq M_\star/M_\odot < 10^{10.5}$.

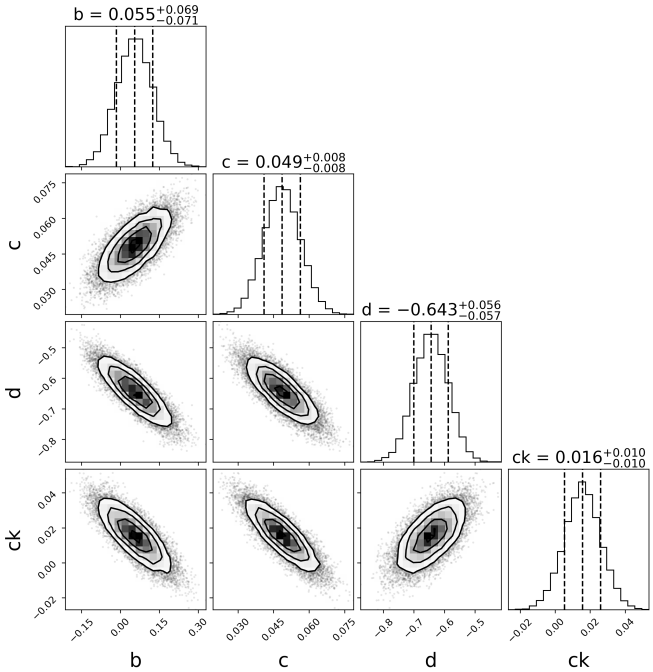

Fig. 9. Probability distributions of the parameters in Eq. (9) as found by fitting our stacked measurements using an MCMC analysis. The dashed vertical lines show the 16th, 50th, and 84th percentiles of each distribution.

to a median angular size-to-synthesized beam FWHM ratio of 1.5). Because there is a possible mismatch between our stacked position and the actual millimeter position of the sources (e.g., Elbaz et al. 2018), these average FIR sizes could, however, be

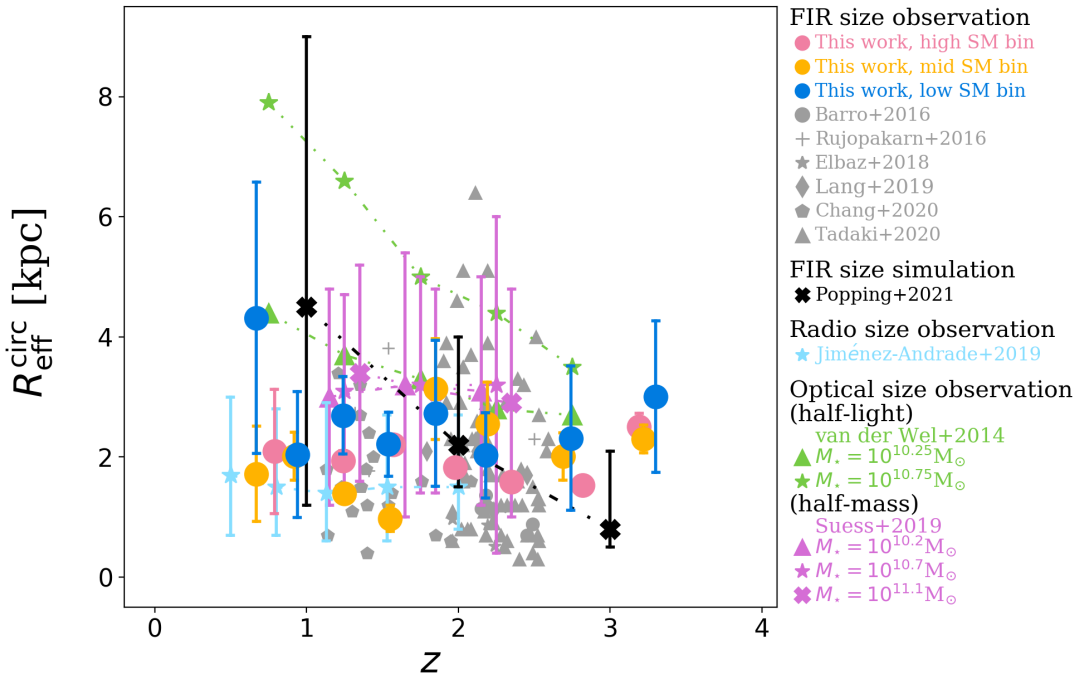

Fig. 10. Redshift evolution of the half-light (or half-mass) radius of MS galaxies. Pink, orange, and blue circles present our stacking results for our high, mid, and low stellar mass bins, i.e., $10^{11} \leq M_\star/M_\odot < 10^{12}$, $10^{10.5} \leq M_\star/M_\odot < 10^{11}$, and $10^{10} \leq M_\star/M_\odot < 10^{10.5}$, respectively. The gray data points are the FIR sizes of MS galaxies from Barro et al. (2016, dots), Rujopakarn et al. (2016, pluses), Elbaz et al. (2018, stars), Lang et al. (2019, diamonds), Chang et al. (2020, pentagons), and Tadaki et al. (2020, triangles); light blue stars are radio sizes of MS galaxies from Jiménez-Andrade et al. (2019). The black crosses are the FIR sizes of $M_\star = 10^{10.5}\,M_\odot$ MS galaxies from the simulations of Popping et al. (2022). The green triangles and stars are the optical half-light sizes of $M_\star = 10^{10.25}\,M_\odot$ and $M_\star = 10^{11.25}\,M_\odot$ MS galaxies from van der Wel et al. (2014). Finally, the purple triangles, stars, and crosses are the optical half-mass sizes of $M_\star = 10^{10.25}\,M_\odot$, $M_\star = 10^{10.75}\,M_\odot$, and $M_\star = 10^{11.25}\,M_\odot$ MS galaxies from Suess et al. (2019). Because most of these literature studies relied on image-plane fits, the stacked FIR sizes displayed here are those from our 2D Gaussian image-plane fits done using `PyBDSF`.

slightly overestimated. Nevertheless, such bias does not seem to be significant as our measurements agree qualitatively and quantitatively with the mean star-forming size of massive ($M_\star \sim 10^{10.7-11.7}\,M_\odot$) MS galaxies inferred by the most recent literature studies. In contrast, the half-light stellar size of massive MS galaxies is typically larger than these FIR extents by a factor of 2 and 4 at $z \sim 3$ and 1, respectively (see Fig. 10; van der Wel et al. 2014). In lower-mass MS galaxies (i.e., $M_\star \sim 10^{10.3}\,M_\odot$), larger half-light stellar size than FIR extents are also observed but mostly at low redshifts. As discussed in Sect. 5, this apparent discrepancy between optical and FIR sizes of MS galaxies does not, however, necessarily translate into stellar half-mass radius discrepancy, as complex obscuration biases need to be accounted for when converting half-light stellar radius into half-mass stellar radius (e.g., Lang et al. 2019; Suess et al. 2019; Popping et al. 2022). For example, the FIR sizes inferred in our study agree quantitatively with the mean redshift-independent half-mass stellar radius of SFGs measured by Suess et al. (2019).

4.4. The Kennicutt-Schmidt relation

Combining our half-light FIR radii (from our image-plane fits), molecular gas mass, and SFR measurements, we study in Fig. 11 the relation between the SFR and gas mass surface densities of MS galaxies (i.e., $\Sigma_{\rm SFR} = {\rm SFR}/(2\pi\,R_{\rm eff-py}^{\rm circ\ 2})$ versus $\Sigma_{M_{\rm mol}} = M_{\rm mol}/(2\pi\,R_{\rm eff-py}^{\rm circ\ 2})$; the so-called KS relation). We compare our estimates with results from the literature: local normal and starburst galaxies from Kennicutt (1998a, hereafter K98) and de los Reyes & Kennicutt (2019) (taking only their molecular gas phase measurements and thus excluding contribution from the atomic gas phase) as well as the global fit of the KS relation from K98; $\langle z \rangle = 1.2$ MS galaxies from Daddi et al. (2010) as well as their MS-only galaxies fit of the KS relation; $\langle z \rangle = 1.5$ MS galaxies from Davis et al. (2007), Noeske et al. (2007), and Tacconi et al. (2010); $\langle z \rangle = 2.3$ MS galaxies from Erb et al. (2006); and finally the MS-only galaxies fit of the KS relation from Genzel et al. (2010). We note that here we take the FIR size of galaxies as a proxy of their SFRs and gas mass distributions (under the hypothesis that the dust and gas are co-spatial). This assumption is justified by recent simulations in which the FIR half-light radius of galaxies is found to be consistent with the radius containing half their star formation and to be only slightly more compact than the radius containing half their molecular gas mass, at least in $z \lesssim 2$ galaxies (Popping et al. 2022).

There is a tight correlation between the $\Sigma_{M_{\rm mol}}$ and $\Sigma_{\rm SFR}$ of MS galaxies, with no significant dependences of this relation on stellar mass or redshift; in other words, at a given $\Sigma_{M_{\rm mol}}$, measurements from different stellar mass or redshift bins agree within their uncertainties. Our measurements are consistent with previous individually detected MS galaxy estimates while they fall below those from individually detected starbursts. In general, at a given redshift, MS galaxies with higher stellar masses are located at the higher end of the $\Sigma_{\rm SFR} - \Sigma_{M_{\rm mol}}$ relation due to the increase in their molecular gas content and the absence of significant size evolution with stellar mass, which translates into an overall increase in their $\Sigma_{M_{\rm mol}}$. Similarly, at a given stellar mass, MS galaxies at higher redshifts are mostly located at the higher end of the $\Sigma_{\rm SFR} - \Sigma_{M_{\rm mol}}$ relation due to the increase in their molecular gas content and the absence of significant size evolution

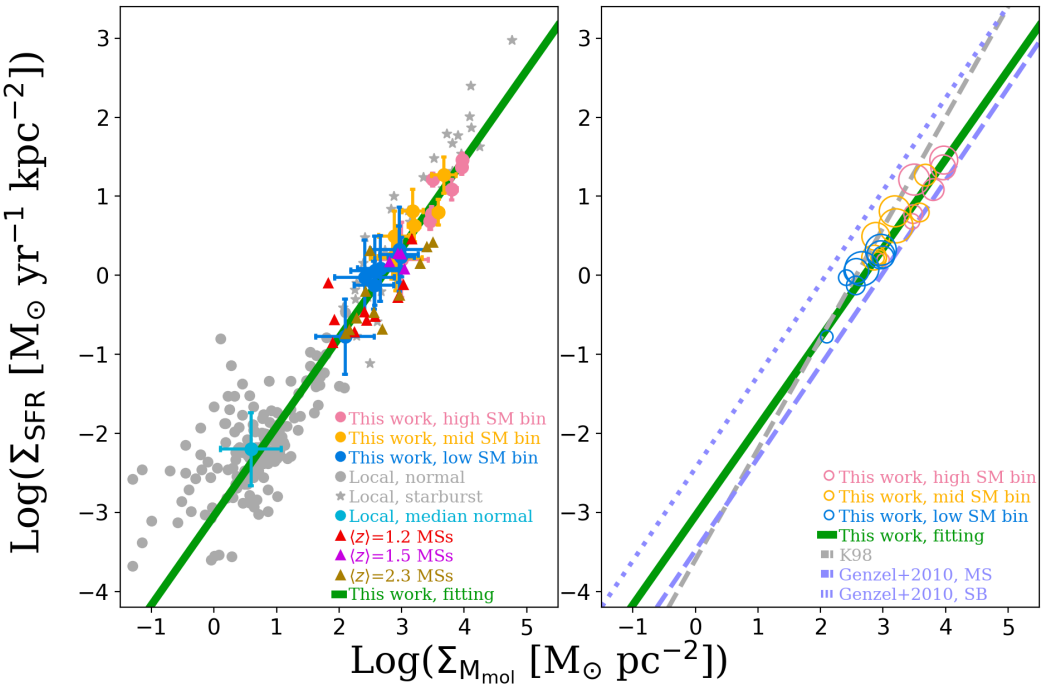

Fig. 11. Relation between the SFR and gas mass densities of SFGs, i.e., the so-called KS relation. *Left*: our stacking results for our high, mid, and low stellar mass bins, i.e., $10^{11} \leq M_\star/M_\odot < 10^{12}$, $10^{10.5} \leq M_\star/M_\odot < 10^{11}$, and $10^{10} \leq M_\star/M_\odot < 10^{10.5}$, respectively, shown by pink, orange, and blue circles. Gray circles and stars are normal and starburst local galaxies from K98 and de los Reyes & Kennicutt (2019, taking only their molecular gas mass estimates, i.e., excluding the atomic phase). Red, purple, and brown triangles are $\langle z \rangle = 1.2$ (Daddi et al. 2010), $\langle z \rangle = 1.5$ (Davis et al. 2007; Noeske et al. 2007; Tacconi et al. 2010), and $\langle z \rangle = 2.3$ (Erb et al. 2006) MS galaxies, respectively. The green line is a fit to the KS relation considering only MS galaxies, i.e., our measurements together with the K98 normal local galaxy average (turquoise dot). *Right*: comparison of our MS-only KS relation to the global fit of K98, the MS-only (long dashed blue line) and starburst-only (dotted blue line) fits of Genzel et al. (2010). Open circles show our measurements, with symbol size increasing with redshift and color-coded by stellar masses.

with redshifts, which also translates into an overall increase in their $\Sigma_{M_{\rm mol}}$.

We performed a linear fit of the KS relation of MS-only galaxies in log-log space, combining our high-redshift MS galaxies measurements with those from the local Universe obtained by K98 and de los Reyes & Kennicutt (2019),

$$\log_{10}\Sigma_{\rm SFR} = (1.13 \pm 0.09) \cdot \log_{10}\Sigma_{M_{\rm mol}} - (3.06 \pm 0.33). \quad (10)$$

The inferred power index of the MS-only KS relation (i.e., $\alpha = 1.13$) is smaller than that found by Daddi et al. (2010) considering MS-only galaxies ($\alpha = 1.42$), but similar to that found by Genzel et al. (2010) for MS-only galaxies ($\alpha = 1.17$). We note that previous high-redshift investigations (i.e., Daddi et al. 2010; Genzel et al. 2010) were only based on relatively small samples of massive high-redshift SFGs (i.e., $N < 50$, $z > 1$, and $M_\star > 10^{11}\,M_\odot$), and are thus likely limited by selection biases. A power law index for the MS-only KS relation that is greater than unity implies that the depletion time (i.e., $\tau_{\rm mol}$) – equivalently, the SFE (i.e., $1/\tau_{\rm mol}$) – of MS galaxies is controlled by their $\Sigma_{M_{\rm mol}}$. In other words, the evolution of the depletion time with redshift and stellar mass seen in Fig. 7 can be predicted from their $\Sigma_{M_{\rm mol}}$ and this universal redshift-independent MS-only KS relation. The KS of MS-only galaxies remains thus one of the most fundamental relation to understand the stellar mass growth of the Universe over the last 10 Gyr.

Finally, as already pointed out by, for example, Daddi et al. (2010) and Genzel et al. (2010), we found that MS galaxies seems to follow a KS relation that at high $\Sigma_{M_{\rm mol}}$ falls below the relation followed by starburst galaxies. In this high $\Sigma_{M_{\rm mol}}$ regime, starbursts exhibit SFEs that are two to three times higher.

We note that in this analysis we implicitly assume that the dust and gas are co-spatial. However, this assumption might not always be verified, as suggested by some ALMA high-resolution observations of submillimeter-selected galaxies (e.g., Chen et al. 2017; Calistro Rivera et al. 2018), which revealed around two times more compact dust continuum emission than gas CO emission. Increasing our FIR sizes by a factor of 2 would shift our data points toward lower surface densities along the one-to-one line in the log-log space but would not significantly change the slope of the inferred KS relation. However, such a large offset or discrepancy in spatial distribution would also translate into very uncertain dust-based gas mass measurements and would thus impact in a more complex way the inferred KS relation. Regardless, submillimeter-selected galaxies are extreme object located far above the MS (e.g., Magnelli et al. 2012a; Casey et al. 2014) and MS galaxies do not seem to exhibit any significant discrepancies between their gas and dust sizes (Puglisi et al. 2019).

4.5. Limitations and uncertainties

Naturally, our analysis suffers from a number of limitations and uncertainties. Those can be mostly divided into two categories: those inherent to all studies measuring molecular gas masses from single RJ dust continuum flux densities; and those specifically associated with our stacking analysis that are related to the averaged nature of our stacked measurements. In the following, we try to exhaustively list these limitations and uncertainties, and discuss their impact on the main conclusions of our analysis.

4.5.1. From observed-frame flux densities to molecular gas masses

To convert observed-frame flux densities into molecular gas masses, we applied a two-step approach, first converting observed-frame flux densities into rest-frame 850 µm luminosities using a standard SED template (the so-called k-correction) and then converting these rest-frame luminosities into molecular gas masses using a standard L_{850}-to-$M_{\rm mol}$ relation. To study how these particular choices of SED templates and L_{850}-to-$M_{\rm mol}$ relations influence our results, we repeated our analysis using alternatives commonly adopted in the literature.

Instead of using the SED template of Béthermin et al. (2012) to perform our k-corrections, we repeated our analysis using the SED template of Schreiber et al. (2018) or a single gray-body emission with $T_{\rm dust} = 25$ K and $\beta = 1.8$ (as it is assumed in, e.g., Scoville et al. 2016). These two k-correction methods yield molecular gas masses that are, respectively, 12% higher and 16% lower at $z \sim 0.6$ than our original calculation and 5% higher and 5% lower at $z \sim 3.2$ than our original calculation. Because our original k-corrections are bracket by these alternatives and because the inferred offsets are in any cases well within the uncertainties of our original constraints, we conclude that the specific choice of this SED template has no significant impact on our results.

As extensively discussed in Liu et al. (2019b), systematic offsets are found between all different metallicity-dependent or -independent L_{850}-to-$M_{\rm mol}$ relations. We evaluate the impact of these relations on our results in Appendix B by repeating our analysis using instead of the metallicy-independent L_{850}-to-$M_{\rm mol}$ relation of Hughes et al. (2017, hereafter H17), (i) the H17 relation inferred assuming a $\alpha_{\rm CO}$ of 4.35 $M_\odot\,(\mathrm{K\,km\,s^{-1}\,pc^2})^{-1}$ (hereafter H17$_{\alpha_{\rm CO}=4.35}$) instead of 6.5 $M_\odot\,(\mathrm{K\,km\,s^{-1}\,pc^2})^{-1}$; (ii) the metallicity-independent L_{850}-to-$M_{\rm mol}$ relation of Scoville et al. (2016, hereafter S16), (iii) a L_{850}-to-$M_{\rm dust}$ relation assuming $T_{\rm dust} = 25$ K and $\beta = 1.8$ combined to the metallicity-dependent $M_{\rm dust}$-to-$M_{\rm mol}$ relation of Bertemes et al. (2018, hereafter B18) and finally (iv) a L_{850}-to-$M_{\rm dust}$ relation assuming $T_{\rm dust} = 25$ K and $\beta = 1.8$ combined to the metallicity-dependent $M_{\rm dust}$-to-$M_{\rm gas}$ relation of Leroy et al. (2011, hereafter $\delta_{\rm GDR}$). As for our k-corrections, our original calculation (i.e., H17) yields estimates that are bracket by these alternatives: H17$_{\alpha_{\rm CO}=4.35}$ produces estimates that are systematically lower than ours by ∼0.17 dex, B18 gives values that are systematically lower than ours by ∼0.17 dex; S16 yields values that are consistent with those reported here within ∼0.04 dex; while the $\delta_{\rm GDR}$ method produces estimates that are systematically higher than ours by ∼0.13 dex. In addition to this global offsets, the metallicity-dependent methods (i.e., $\delta_{\rm GDR}$ and B18) introduces redshift- and stellar mass-dependent trends, which are due to the fact that lower-mass and higher-redshift galaxies have increasingly lower metallicities. Consequently, the offsets between our measurements and those inferred with the $\delta_{\rm GDR}$ method increase toward lower masses and higher redshifts, while the offsets with B18 decrease toward lower masses and higher redshifts. Even if present, these stellar mass- and redshift-dependent trends do not qualitatively change the main conclusions of our papers: irrespective of the assumed methods: (i) the molecular gas fraction of MS galaxies still increases with redshifts and decreases with stellar masses; (ii) their depletion time still remains mostly dependent on their redshifts and not their stellar masses and finally, (iii) MS galaxies still evolve along a seemingly universal MS-only KS relation. These evolutions are, however, quantitatively changed, with, for example, the molecular gas fraction of MS galaxies increasing by a factor of ∼15, ∼45, ∼33, and ∼17 from $z \sim 0$ to $z \sim 3.2$ for the H17$_{\alpha_{\rm CO}=4.35}$, $\delta_{\rm GDR}$, S16, and B18 gas mass calibrations, respectively, as compared to the factor of 24 found for the H17 method; and their molecular gas depletion time being 200–300, 400–600, 400–700, and 200–500 Myr for the H17$_{\alpha_{\rm CO}=4.35}$, $\delta_{\rm GDR}$, S16, and B18 gas mass calibrations, respectively, instead of 300–500 Myr for our original calculation. Again, our original constraints are roughly bracket by these alternatives and values are consistent within 1–2σ.

We note that combining the local measurements from Saintonge et al. (2017) with our high-redshift H17 estimates yields a redshift evolution of the molecular gas content of SFGs that is in very good agreement with that of Tacconi et al. (2020) at high stellar masses (Fig. 4), where this latter can be considered as the reference as it is based on a fairly complete sample of massive SFGs across cosmic time and a thorough cross-calibration of the CO- and dust-based methods. This agreement could seem surprising as the L_{850}-to-$M_{\rm mol}$ relation of H17 was calibrated using $\alpha_{\rm CO} = 6.5$, while our local reference (i.e., Saintonge et al. 2017) converted their CO measurements into molecular gas masses using $\alpha_{\rm CO} \sim 4$ (at the high stellar masses of our study). This agreement between our high-redshift H17 measurements and those from Tacconi et al. (2020) is due to the fact that using $\alpha_{\rm CO} = 6.5$ instead of 4.3 to calibrate the local L_{850}-to-$M_{\rm mol}$ relation corrects indirectly (and to first order) for the fact that at a given stellar mass, high-redshift galaxies have lower metallicities than local galaxies, and thus have a higher gas-to-dust ratio (e.g., Leroy et al. 2011) and consequently should have a lower L_{850}-to-$M_{\rm mol}$ ratio.

Finally, we note that the particular choice of a L_{850}-to-$M_{\rm mol}$ relation cannot explain the differences observed between the molecular gas masses of MS galaxies at a given stellar mass and redshift inferred by our study and that from Liu et al. (2019b) and Scoville et al. (2016). Indeed, Liu et al. (2019b) also used H17 to infer their molecular gas mass estimates, while the method used in Scoville et al. (2017) (i.e., S16) provides consistent results with H17 (within ∼0.04 dex). In both cases, differences between our and their measurements are likely caused by the fact that these literature studies were largely biased toward individually detected MS galaxies with massive gas reservoirs.

4.5.2. Limitation and uncertainties associated with stacking

Stacking in the *uv* domain is a difficult task and could be subject to a series of potential downfalls when applied to the heterogeneous A^{3}COSMOS database. To test the reliability of our stacking analysis, we used realistic simulations, in which mock sources with different flux densities and sizes were introduced in an A^{3}COSMOS-like interferometric database and subsequently stacked using the same procedure as the real sources. The results of these simulations, which are shown in Appendix A, unambiguously demonstrate the reliability of our stacking analysis to accurately retrieve the intrinsic flux densities and sizes of a stacked population. As a reminder, performing such a stacking analysis on images with drastically different spatial resolutions would be virtually impossible or very uncertain.

While our simulations demonstrated that we were able to accurately measure the mean flux density of a galaxy population, one still has to remember that these stacked measurements are averaged values for galaxy populations with intricate stellar mass, SFR, and redshift distributions. How these mean molecular gas measurements, $\langle M_{\rm mol}\rangle$, can be related to $\langle t_{\rm cosmic}\rangle$, $\langle M_\star\rangle$, and $\langle\Delta{\rm MS}\rangle$ to infer $\mu_{\rm gas}(M_*, t_{\rm cosmic}, \Delta{\rm MS})$ and $\tau_{\rm mol}(M_*, t_{\rm cosmic}, \Delta{\rm MS})$ is an none trivial question and depends on

the intrinsic stellar mass, SFR, and redshift distributions of each stacked populations. To address this issue, we applied a Bayesian analysis in which using the true distributions of these stacked populations we estimated the likelihood to measure their stacked $\langle M_{\rm mol}\rangle$ for a given analytical functions of $\mu_{\rm gas}(M_*, t_{\rm cosmic}, \Delta{\rm MS})$ and $\tau_{\rm mol}(M_*, t_{\rm cosmic}, \Delta{\rm MS})$. Without such an approach (i.e., simply inferring $\mu_{\rm gas}(M_*, t_{\rm cosmic}, \Delta{\rm MS})$ and $\tau_{\rm mol}(M_*, t_{\rm cosmic}, \Delta{\rm MS})$ by fitting $\langle M_{\rm mol}\rangle$, $\langle t_{\rm cosmic}\rangle$, $\langle M_\star\rangle$, and $\langle\Delta{\rm MS}\rangle$), those analytical functions would differ from our original calculation by up to 25%. While this approach is currently the best way to deal with this averaging issue, only future high-sensitivity ALMA observations that individually detect all our MS galaxies would be able to definitively constrain $\mu_{\rm gas}(M_*, t_{\rm cosmic}, \Delta{\rm MS})$ and $\tau_{\rm mol}(M_*, t_{\rm cosmic}, \Delta{\rm MS})$.

Recent findings in the literature suggests that there might exist an mean offset of 0.″2 between the optical position and the actual (sub)millimeter position of our sources (e.g., Elbaz et al. 2018). While we verified via simulations that such an offset does not affect significantly our stacked flux density and size measurements, one should at worst consider our molecular gas sizes as upper limits or more realistically keep in mind that those should be corrected from this extra convolution kernel. We decided, however, not to correct our size measurements from this effect in Table 1 because this optical-to-FIR position offset still needs to be confirmed and because deconvolving those intrinsic sizes (i.e., $\theta^{\rm circ}_{{\rm mol}-uv}$ or $\theta^{\rm circ}_{{\rm mol}-{\rm py}}$) by an Gaussian kernel with a FWHM of 0.″2 would only have lowered them by ∼6%, leaving all our results unchanged.

5. Discussion

Our analysis reveals that (i) the molecular gas fraction of MS galaxies increases with redshift and decreases with stellar mass; (ii) the depletion time of MS galaxies does not depend on their stellar masses but mostly on their redshift, increasing from 0.4 Gyr at $z \sim 3.6$ to 1.3 Gyr at $z \sim 0$; (iii) the FIR size of MS galaxies does not evolve with redshifts nor stellar masses, with a mean half-light radius of 2.2 kpc; and finally, (iv) MS galaxies evolve along a seemingly universal MS-only KS relation with a slope of ∼1.13.

In the following, we discuss some of these results in light of recent observational findings and galaxy evolution scenarios.

5.1. A universal Kennicutt-Schmidt relation

It is crucial to accurately measure the relation between the SFR and gas (surface) densities of galaxies because it provides theoretical models with key information about the mechanisms and efficiency with which these galaxies turn their gas into stars. The pioneering work of Schmidt (1959) suggests that in the Galactic plane the SFR volume density ($\rho_{\rm SFR}$) is proportional to the gas volume density ($\rho_{\rm gas}$) with a power law index of ∼2. This power law index directly reflects the physical conditions for star formation and can be studied, assuming a constant gas scale height, via the observationally more convenient $\Sigma_{\rm gas}$–$\Sigma_{\rm SFR}$ relation (i.e., the so-called KS relation). At sub-kiloparsec scales, this power law index is found to vary from $\alpha \sim 0.75$ to 2, rendering difficult any theoretical interpretation of this relation at small scales (e.g., Wong & Blitz 2002; Schuster et al. 2007; Bigiel et al. 2008; Leroy et al. 2013; Momose et al. 2013; Miura et al. 2014; Shetty et al. 2014; Wilson et al. 2019; Wang & Hwang 2020; Ellison et al. 2021; Pessa et al. 2021; Sánchez et al. 2021). For example, a power law index of ∼0.75 is expected if giant molecular clouds (GMCs) convert all their gas into stars over a free-fall time (e.g., Krumholz & McKee 2005), while a power index of ∼2.0 is expected if star formation is mostly induced by collisions of small clouds of gas (e.g., Wyse 1986; Wong & Blitz 2002).

K98 provides the first accurate measurement of the $\Sigma_{\rm gas}$–$\Sigma_{\rm SFR}$ relation at global scales by combining data from both normal and starburst galaxies. K98 find $\alpha = 1.4$, which is near the expected value of 1.5 for self-gravitating disks if the SFR scales as the ratio of gas volume density ($\rho_{\rm gas}$) to the free-fall timescale ($\rho_{\rm gas}^{-0.5}$). However, Bigiel et al. (2008) argue that the conditions for star formation in starbursts are too different to be combined with normal galaxies (e.g., Gao & Solomon 2004; Rosolowsky & Blitz 2005) and find $\alpha = 1.0$ when considering only kiloparsec-scale star-forming regions of nearby spirals. They conclude that stars are forming in GMCs with relatively uniform properties and that at supra-kiloparsec scales, star formation remains unresolved and $\Sigma_{\rm SFR}$ becomes thus more a measure of the filling fraction of GMCs than changes in conditions for star formation. Recent studies at high redshift and global scales support this conclusion (e.g., Genzel et al. 2010; Miettinen et al. 2017a). In particular, Genzel et al. (2010) argue that normal and starburst galaxies seem to follow two different KS relations both with a near-unity power law index but with different normalization, the latter galaxy population being more efficient in turning gas into stars. Our analysis also supports the existence of a universal KS relation for MS galaxies with a near-unity power law index. Our results are the first to extend this finding up to $z \sim 3.6$ and using a mass-complete sample of $>10^{10}\,M_\odot$ MS galaxies. We note in particular that the extension of our analysis to very high redshift is crucial because high-redshift MS galaxies have sufficiently high $\Sigma_{\rm gas}$ to provide adequate leverage to accurately constrain the power law index of the KS relation on global scales. The high $\Sigma_{\rm gas}$ of these high-redshift MS galaxies also allow us to compare their SFE with that of local starbursts that have similarly high $\Sigma_{\rm gas}$ (see local starbursts in Fig. 11 from K98 and de los Reyes & Kennicutt 2019).

While the power law index of the KS relation for MS galaxies found in our analysis is consistent with that of Genzel et al. (2010), our normalization differs by about 0.2 dex (see right panel of Fig. 11), with our findings predicting shorter depletion times for MS galaxies than theirs. This difference can most likely be explained by the same limitation as that affecting Liu et al. (2019b) and Tacconi et al. (2020): literature studies on the KS relation are based on individually detected CO galaxy observations and are thus likely biased toward gas-rich galaxies at fixed $\Sigma_{\rm SFR}$. Naturally, one cannot rule out that part of this offset is due to some remaining offset between CO-based and dust-based molecular gas mass estimates (e.g., Tacconi et al. 2020).

5.2. Molecular gas depletion time

The molecular gas depletion time is defined as the time that a galaxy would need to deplete its molecular gas reservoir through star formation, provided a constant SFR and no gas accretion (i.e., $\tau_{\rm mol} = M_{\rm mol}/{\rm SFR}$). It can theoretically be written as $\tau_{\rm mol} = M_{\rm mol}/{\rm SFR} = t_{\rm ff}/\varepsilon_{\rm ff}$, where $t_{\rm ff}$ is the free-fall time and $\varepsilon_{\rm ff}$ is a dimensionless measure of the SFR efficiency, linking the mass of gas available for star formation and that effectively turning into stars (Krumholz et al. 2012). Theoretically, $\varepsilon_{\rm ff}$ is supposed to be roughly constant (≈0.01), rendering any variations in depletion time mostly due to variations in $t_{\rm ff}$ (Krumholz et al. 2012).

Observationally, the molecular depletion time of SFGs was found to follow tight scaling relations with their ΔMS, redshifts,

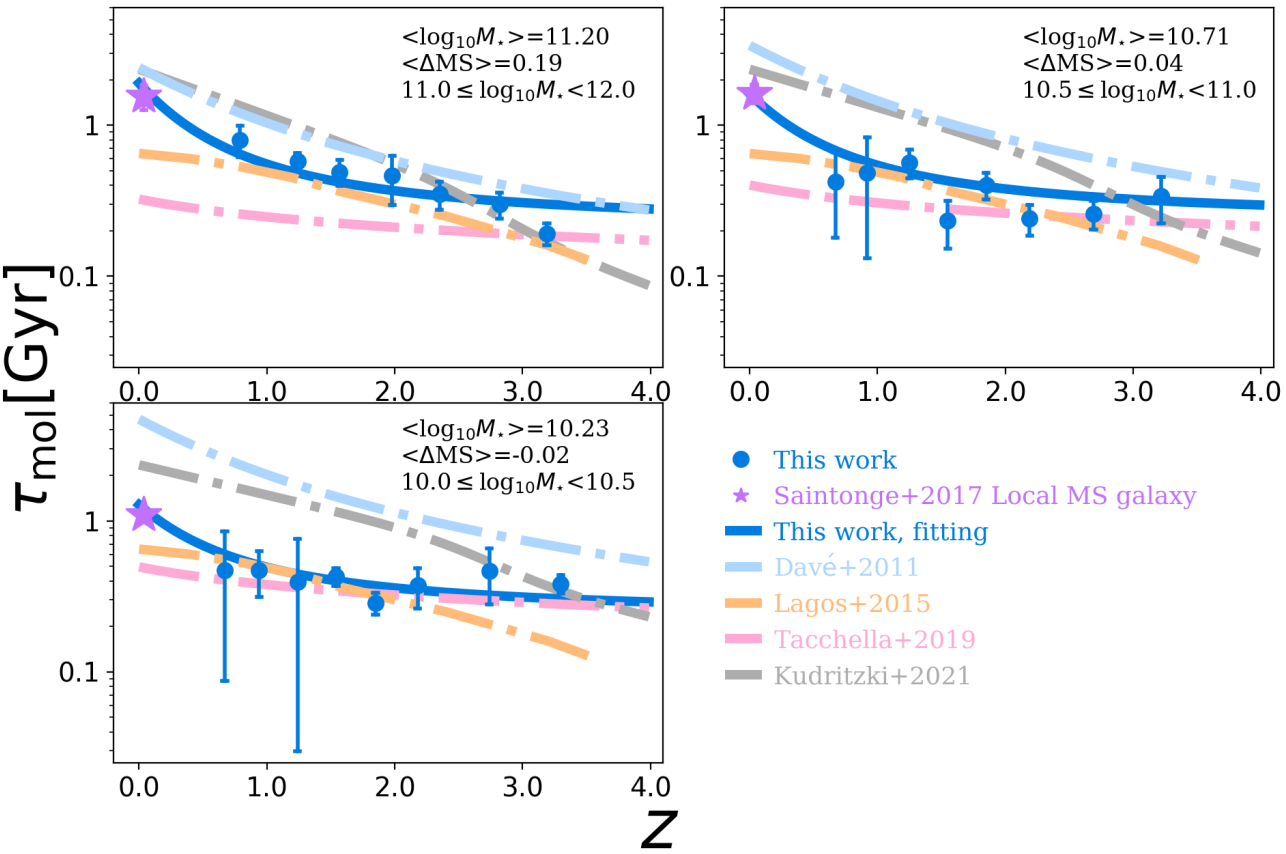

Fig. 12. Same as Fig. 7, but comparing our results to predictions from the cosmological hydrodynamic simulations of Davé et al. (2011, dash-dotted light-blue line), Lagos et al. (2015, dash-dotted orange line), Tacchella et al. (2016, dash-dotted pink line), and Kudritzki et al. (2021, dash-dotted gray line).

and stellar masses, providing thereby key information for models of galaxy evolution (e.g., Saintonge et al. 2016; Tacconi et al. 2018, 2020; Liu et al. 2019b; Hunt et al. 2020; Popesso et al. 2020). For example, the depletion time of galaxies situated well above the MS (i.e., ×4) was found to be significantly shorter (∼0.1 Gyr) than that of MS galaxies, suggesting a different star-formation mode for this galaxy population, likely triggered by the major merger of two gas-rich galaxies (e.g., Genzel et al. 2010; Hayward et al. 2011; Alaghband-Zadeh et al. 2012; Riechers et al. 2013). In addition, the depletion time of MS galaxies was found to slightly decrease with redshift up to $z \sim 3$ (e.g., Schinnerer et al. 2016; Tacchella et al. 2016; Tacconi et al. 2018, 2020; Padmanabhan & Loeb 2020). Our analysis, which confirms this finding, reveals that this apparent evolution is, however, not associated per se with a redshift evolution of the star-formation mode of MS galaxies but rather to the increase in their gas content with redshift, a relatively constant star-forming extent, and a seemingly universal KS relation with a power law index of ∼1.13: at a given stellar mass, the gas content of MS galaxies increases with redshift while their star-forming size remains roughly constant; their $\Sigma_{M_{\rm mol}}$ increases thus smoothly with redshift, shifting toward higher $\Sigma_{\rm SFR}$ to $\Sigma_{M_{\rm mol}}$ ratios. The molecular gas depletion time of MS galaxies was finally found to slightly decrease with stellar masses (e.g., Saintonge et al. 2016; Tacconi et al. 2018, 2020; Padmanabhan & Loeb 2020). On the contrary, our analysis finds that the evolution of their depletion time is mostly independent from their stellar masses. We note that this stellar mass-independent evolution of the depletion time suggests that the flattening of the MS at high stellar masses ($>10^{10.5}\,M_\odot$) and $z \lesssim 2.5$ (Leslie et al. 2020) is mostly due to their lower gas content rather than lower SFEs (see Sect. 5.4).

The scaling relations between the molecular gas depletion time of MS galaxies and their redshifts and stellar masses provide stringent constraints to hydrodynamic simulations performed in a cosmological context. In Fig. 12, we compare our findings to predictions from the simulations of Davé et al. (2011), Lagos et al. (2015), Tacchella et al. (2016), and Kudritzki et al. (2021). Overall, all these simulations predict a decrease in the molecular gas depletion time of MS galaxies with redshift and stellar mass, in qualitative agreement with our observations. However, the slope and overall normalization of these scaling relations vary by at least a factor of 3 between all these simulations and none can accurately reproduce the observed relations. As discussed in Kudritzki et al. (2021), predictions of the molecular depletion time are indeed strongly affected by the exact star formation, accretion and feedback models implemented in these simulations. The large disagreement between simulations and with the observations demonstrates that our understanding of these complex mechanisms across cosmic time is far from being complete and it also demonstrates the power of simple scaling relations to constrain models of galaxy evolution.

Finally, irrespective of the exact slope of these various scaling relations, all observations point toward relatively short molecular gas depletion times (∼0.5–1 Gyr) for MS galaxies of any stellar masses and redshifts. Without a constant replenishment of their gas reservoirs, the population of MS galaxies observed at, for example, $z \sim 2$, would thus have fully disappeared by $z = 1.5$ (see, e.g., Walter et al. 2020). These findings

strongly support the so-called gas regulator models (e.g., Erb 2008; Bouché et al. 2010; Davé et al. 2012; Lilly et al. 2013; Peng & Maiolino 2014; Rathaus & Sternberg 2016), in which galaxy growth is mostly driven by a continuous supply of fresh gas from the cosmic web (Dekel et al. 2009).

5.3. Compact star-forming extent

Our analysis as well as numerous recent studies have revealed that the star-forming half-light radius of MS galaxies is relatively compact (i.e., 1–3 kpc) and does not evolve significantly with redshift nor stellar mass (e.g., Barro et al. 2016; Rujopakarn et al. 2016; Elbaz et al. 2018; Lang et al. 2019; Jiménez-Andrade et al. 2019; Chang et al. 2020; Tadaki et al. 2020). In contrast, Fujimoto et al. (2017) found that the FIR size of MS galaxies evolves slightly with redshift. However, as stressed in their study, their individually detected ALMA sample is SFR-selected and could therefore be biased at high redshift toward compact SFGs (i.e., galaxies with high surface brightness). In any cases, the optical half-light radius of late-type galaxies of similar masses and at $z \lesssim 3$ is found to be about two times larger (∼3–8 kpc) than their star-forming extent (Sect. 4.3 van der Wel et al. 2014; Fujimoto et al. 2017; Elbaz et al. 2018; Lang et al. 2019; Jiménez-Andrade et al. 2019, 2021; Chen et al. 2020; Tadaki et al. 2020). This centrally enhanced star formation is usually interpreted in the literature as a sign that the cold gas accreted by MS galaxies falls preferentially onto their central region and triggers the formation of their bulge (e.g., Fisher 2006; Goldbaum et al. 2016; Tonini et al. 2016). These bulges would therefore grow from inside out and quench in the latest evolutionary stage of MS galaxies, leaving solely the outer disk with star-formation activities (e.g., Tacchella et al. 2015; Ellison et al. 2018; Rowlands et al. 2018; Colombo et al. 2020). While possible for massive SFGs, which are known to have massive central bulges (e.g., Leslie et al. 2020), such an interpretation seems less likely for less massive MS galaxies (i.e., $M_\star < 10^{11.0}\,M_\odot$) that are explored for the first time here. Using high-resolution ALMA and *Hubble* Space Telescope observations of 20 submillimeter-selected galaxies, Lang et al. (2019) argues instead that the discrepancy between FIR and optical sizes is mostly due to observational biases in which important radial color gradients yield very discrepant half-light and half-mass radii. This observational finding has recently been supported by The Next Generation Illustris 50 (TNG50) simulations coupled with state-of-the-art radiative transfer code to study the FIR, optical, and half-mass radius of thousands high-redshift 10^9–$10^{11}\,M_\odot$ MS galaxies (Popping et al. 2022). Indeed, in these simulations it is found that while the FIR half-light radius correlates with the radius containing half the star formation in galaxies, strong and un-corrected obscuration of the stellar light toward the galaxy center increases significantly the apparent extent of the disk sizes in the optical. Popping et al. (2022) conclude that the compact dust-continuum emission of MS galaxies with respect to the optical size is not necessarily evidence of the buildup of a dense central stellar component. Future high-resolution near-infrared observations performed by the *James Webb* Space Telescope will certainly play a key role in validating or invalidating these later findings.

5.4. The flattening of the MS relation at high masses

It is now relatively well established that the slope of the MS of SFGs flattens at high stellar masses, with this flattening becoming more and more prominent at $z \lesssim 2.5$ (e.g., Schreiber et al. 2015; Popesso et al. 2019; Leslie et al. 2020). Such a flattening of the MS is usually associated with the so-called mass-quenching model (e.g., Peng et al. 2010; Nelson et al. 2018; Wright et al. 2019). In this model, massive galaxies with their high gravitational potential hold a large accretion rate, growing their core rapidly in a few gigayears. As the core keeps growing, however, the ever larger gravitational potential could shock heat and/or an AGN could heat the new infalling gas, slowing down the gas accretion rate and reducing thereby the specific SFR of massive galaxies (e.g., Dekel & Birnboim 2006; Rodríguez Montero et al. 2019; Donnari et al. 2021). On the other hand, less massive galaxies could take more than a Hubble time to trigger such feedback and could thus efficiently accrete fresh cold gas even at low redshift. Our analysis reveals that the molecular gas fraction of our MS galaxies decreases with stellar mass at a rate mirroring than that of the flattening of the MS, yielding almost constant depletion time (equivalently SFE) with stellar mass. This implies that the slow downfall of the star formation in massive MS galaxies is principally due to an decrease in their molecular gas content rather than a decrease in their SFE, in agreement with recent observations of low-redshift galaxies (Colombo et al. 2020). Our findings support thus an interpretation in which the flattening of the MS at high masses is primarily controlled by the ability of galaxies to efficiently accrete or not accrete gas from the intergalactic medium.

Finally, we note that Leslie et al. (2020) found that the flattening of the MS must be linked with changes in the morphological composition of galaxies: bulge-dominated late-type galaxies, which dominate the SFG population at high stellar masses, show a flattening of the MS, while disk-dominated late-type galaxies have align on a SFR-M_* sequence with a slightly higher normalization and with a power law index in the log-log space close to unity. Although this result seems to favor a scenario in which the gas in bulge-dominated MS galaxies is stabilized against fragmentation (so-called morphological quenching; Martig et al. 2013), our findings suggest that the gas is instead simply not present to form stars in these galaxies: either it has been removed by feedback or cold gas is no longer able to be accreted efficiently onto bulge-dominated late-type galaxies.

6. Summary

We have investigated the evolution of the molecular gas content of MS galaxies from $z \sim 3.6$ to $z \sim 0.4$. We applied an innovative *uv*-based stacking analysis to a large set of ALMA observations toward a mass-complete sample of $>10^{10}\,M_\odot$ MS galaxies. This *uv*-based stacking analysis, performed on the RJ dust continuum emission of these galaxies, provides an accurate measurement of their mean molecular gas content (Hughes et al. 2017). With this unique data set and innovative approach, we constrain the redshift and stellar mass evolution of the mean molecular gas mass, molecular gas fraction, molecular gas depletion time, and molecular gas size of MS galaxies down to $10^{10}\,M_\odot$ and up to $z \sim 3.4$. Finally, we have also studied for the first time – using a mass-complete sample of MS galaxies – the KS relation at high redshift. Our main findings are:

1. The mean molecular gas mass of MS galaxies evolves significantly with redshift and depends on the stellar mass. At all stellar masses, the molecular gas fraction (i.e., $\mu_{\rm gas} = M_{\rm mol}/M_\star$) decreases by a factor of ∼24 from $z \sim 3.2$ to $z \sim 0$. In addition, at a given redshift, $\mu_{\rm gas}$ decreases with stellar mass at roughly the same rate as the decrease in the specific SFR (i.e., SSFR = SFR/$M_\star$) of MS galaxies.

2. Our mean molecular gas mass measurements are generally lower (∼10–60%) than literature estimates (e.g., Scoville et al. 2017; Liu et al. 2019b; Tacconi et al. 2020), especially at low stellar masses. Literature measurements, which have mostly relied on individually detected galaxies, were likely biased toward gas-rich galaxies.

3. The molecular gas depletion time (i.e., $\tau_{\rm mol} = M_{\rm mol}/{\rm SFR}$) of MS galaxies remains mostly constant at $z > 0.5$ with a value of 300–500 Myr, but increases by a factor of ∼3 by $z \sim 0$.

4. The mean FIR size of MS galaxies does not seem to evolve significantly with redshift or stellar mass, with a mean circularized half-light radius of ∼2.2 kpc. This result agrees qualitatively and quantitatively with the star-forming extent of MS galaxies measured in Jiménez-Andrade et al. (2019) using high-resolution radio observations of the COSMOS field (i.e., $R^{\rm circ}_{\rm radio} \sim 1.5^{+1.5}_{-0.8}$ kpc).

5. The redshift evolution of $\tau_{\rm mol}$ can be accurately predicted from the redshift evolution of the molecular gas surface density (i.e., $\Sigma_{M_{\rm mol}}$) of MS galaxies and a seemingly universal MS-only $\Sigma_{M_{\rm mol}} - \Sigma_{M_{\rm mol}}$ relation with a slope of ∼1.13, the KS relation.

Our findings provide key constraints for galaxy evolution models, as $>10^{10}\,M_\odot$ MS galaxies are known to have been responsible for the bulk of the star-forming activity of the Universe over the last 10 Gyr. To first order, it seems that the molecular gas content of MS galaxies regulates the evolution of their star-formation activity across cosmic time, while variation in their SFE (i.e., $1/\tau_{\rm mol}$) plays only a secondary role. The short depletion time of the molecular gas reservoir of MS galaxies (<1 Gyr) contrasts with the long duty cycle inherent to the existence of the MS itself. This suggests that the continuous replenishment of the molecular gas reservoir of MS galaxies plays a fundamental role in regulating star formation across cosmic time. Finally, despite large variations in the gas content and SFR of MS galaxies over the last 10 Gyr, their star formation seems to take place in their inner 2 kpc radius and to follow a seemingly universal MS-only $\Sigma_{M_{\rm mol}} - \Sigma_{\rm SFR}$ relation.

Acknowledgements. This research was carried out within the Collaborative Research Centre 956, sub-project A1, funded by the Deutsche Forschungsgemeinschaft (DFG) – project ID 184018867. E.S. and D.L. acknowledge funding from the European Research Council (ERC) under the European Union's Horizon 2020 research and innovation programme (grant agreement No. 694343). ALMA is a partnership of ESO (representing its member states), NSF (USA) and NINS (Japan), together with NRC (Canada), MOST and ASIAA (Taiwan), and KASI (Republic of Korea), in cooperation with the Republic of Chile. The Joint ALMA Observatory is operated by ESO, AUI/NRAO and NAOJ. This paper makes use of the following ALMA data: ADS/JAO.ALMA#2015.1.00026.S, ADS/JAO.ALMA#2015.1.00055.S, ADS/JAO.ALMA#2015.1.00122.S, ADS/JAO.ALMA#2015.1.00137.S, ADS/JAO.ALMA#2015.1.00260.S, ADS/JAO.ALMA#2015.1.00379.S, ADS/JAO.ALMA#2015.1.00388.S, ADS/JAO.ALMA#2015.1.00540.S, ADS/JAO.ALMA#2015.1.00568.S, ADS/JAO.ALMA#2015.1.00664.S, ADS/JAO.ALMA#2015.1.00695.S, ADS/JAO.ALMA#2015.1.00704.S, ADS/JAO.ALMA#2015.1.00928.S, ADS/JAO.ALMA#2015.1.01074.S, ADS/JAO.ALMA#2015.1.01105.S, ADS/JAO.ALMA#2015.1.01111.S, ADS/JAO.ALMA#2015.1.01171.S, ADS/JAO.ALMA#2015.1.01212.S, ADS/JAO.ALMA#2015.1.01345.S, ADS/JAO.ALMA#2015.1.01495.S, ADS/JAO.ALMA#2016.1.00279.S, ADS/JAO.ALMA#2016.1.00463.S, ADS/JAO.ALMA#2016.1.00478.S, ADS/JAO.ALMA#2016.1.00624.S, ADS/JAO.ALMA#2016.1.00646.S, ADS/JAO.ALMA#2016.1.00778.S, ADS/JAO.ALMA#2016.1.00804.S, ADS/JAO.ALMA#2016.1.01012.S, ADS/JAO.ALMA#2016.1.01040.S, ADS/JAO.ALMA#2016.1.01184.S, ADS/JAO.ALMA#2016.1.01208.S, ADS/JAO.ALMA#2016.1.01240.S, ADS/JAO.ALMA#2016.1.01355.S, ADS/JAO.ALMA#2016.1.01426.S, ADS/JAO.ALMA#2016.1.01559.S, ADS/JAO.ALMA#2016.1.01604.S, ADS/JAO.ALMA#2017.1.00326.S, ADS/JAO.ALMA#2017.1.00413.S, ADS/JAO.ALMA#2017.1.00428.L, ADS/JAO.ALMA#2017.1.01020.S, ADS/JAO.ALMA#2017.1.01176.S, ADS/JAO.ALMA#2017.1.01276.S, ADS/JAO.ALMA#2017.1.01358.S, ADS/JAO.ALMA#2017.1.01451.S, ADS/JAO.ALMA#2017.1.01618.S, ADS/JAO.ALMA#2017.1.00046.S, ADS/JAO.ALMA#2017.1.01217.S, ADS/JAO.ALMA#2017.1.01259.S, ADS/JAO.ALMA#2018.1.00085.S, ADS/JAO.ALMA#2018.1.00216.S, ADS/JAO.ALMA#2018.1.00681.S, ADS/JAO.ALMA#2018.1.00992.S, ADS/JAO.ALMA#2018.1.01044.S, ADS/JAO.ALMA#2018.1.01359.S.

References

Alaghband-Zadeh, S., Chapman, S. C., Swinbank, A. M., et al. 2012, MNRAS, 424, 2232
Algera, H. S. B., Smail, I., Dudzevičiūtė, U., et al. 2020, ApJ, 903, 138
Barro, G., Kriek, M., Pérez-González, P. G., et al. 2016, ApJ, 827, L32
Berta, S., Lutz, D., Genzel, R., et al. 2016, A&A, 587, A73
Bertemes, C., Wuyts, S., Lutz, D., et al. 2018, MNRAS, 478, 1442
Béthermin, M., Daddi, E., Magdis, G., et al. 2012, ApJ, 757, L23
Béthermin, M., Daddi, E., Magdis, G., et al. 2015, A&A, 573, A113
Bigiel, F., Leroy, A., Walter, F., et al. 2008, AJ, 136, 2846
Bolatto, A. D., Wolfire, M., & Leroy, A. K. 2013, ARA&A, 51, 207
Bouché, N., Dekel, A., Genzel, R., et al. 2010, ApJ, 718, 1001
Bourne, N., Dunne, L., Bendo, G. J., et al. 2013, MNRAS, 436, 479
Bourne, N., Dunlop, J. S., Merlin, E., et al. 2017, MNRAS, 467, 1360
Bouwens, R. J., Illingworth, G. D., Oesch, P. A., et al. 2015, ApJ, 803, 34
Brinchmann, J., Charlot, S., White, S. D. M., et al. 2004, MNRAS, 351, 1151
Bruzual, G., & Charlot, S. 2003, MNRAS, 344, 1000
Calistro Rivera, G., Hodge, J. A., Smail, I., et al. 2018, ApJ, 863, 56
Cappelluti, N., Brusa, M., Hasinger, G., et al. 2009, A&A, 497, 635
Carilli, C. L., & Walter, F. 2013, ARA&A, 51, 105
Casey, C. M., Narayanan, D., & Cooray, A. 2014, Phys. Rep., 541, 45
Cassata, P., Liu, D., Groves, B., et al. 2020, ApJ, 891, 83
Chabrier, G. 2003, PASP, 115, 763
Chang, Y.-Y., Le Floc'h, E., Juneau, S., et al. 2020, ApJ, 888, 44
Chary, R., & Elbaz, D. 2001, ApJ, 556, 562
Chen, C.-C., Hodge, J. A., Smail, I., et al. 2017, ApJ, 846, 108
Chen, C.-C., Harrison, C. M., Smail, I., et al. 2020, A&A, 635, A119
Colombo, D., Sanchez, S. F., Bolatto, A. D., et al. 2020, A&A, 644, A97
da Cunha, E., Charlot, S., & Elbaz, D. 2008, MNRAS, 388, 1595
da Cunha, E., Walter, F., Smail, I. R., et al. 2015, ApJ, 806, 110
Daddi, E., Elbaz, D., Walter, F., et al. 2010, ApJ, 714, L118
Davé, R., Finlator, K., & Oppenheimer, B. D. 2011, MNRAS, 416, 1354
Davé, R., Finlator, K., & Oppenheimer, B. D. 2012, MNRAS, 421, 98
Davis, M., Guhathakurta, P., Konidaris, N. P., et al. 2007, ApJ, 660, L1
Dekel, A., & Birnboim, Y. 2006, MNRAS, 368, 2
Dekel, A., Birnboim, Y., Engel, G., et al. 2009, Nature, 457, 451
de los Reyes, M. A. C., & Kennicutt, R. C. 2019, ApJ, 872, 16
Dessauges-Zavadsky, M., Ginolfi, M., Pozzi, F., et al. 2020, A&A, 643, A5
Dole, H., Lagache, G., Puget, J.-L., et al. 2006, A&A, 451, 417
Donnari, M., Pillepich, A., Joshi, G. D., et al. 2021, MNRAS, 500, 4004
Elbaz, D., Dickinson, M., Hwang, H. S., et al. 2011, A&A, 533, A119
Elbaz, D., Leiton, R., Nagar, N., et al. 2018, A&A, 616, A110
Ellison, S. L., Sánchez, S. F., Ibarra-Medel, H., et al. 2018, MNRAS, 474, 2039
Ellison, S. L., Lin, L., Thorp, M. D., et al. 2021, MNRAS, 501, 4777
Erb, D. K. 2008, ApJ, 674, 151
Erb, D. K., Steidel, C. C., Shapley, A. E., et al. 2006, ApJ, 647, 128
Faucher-Giguère, C.-A., Kereš, D., & Ma, C.-P. 2011, MNRAS, 417, 2982
Feltre, A., Maseda, M. V., Bacon, R., et al. 2020, A&A, 641, A118
Fisher, D. B. 2006, ApJ, 642, L17
Foreman-Mackey, D., Hogg, D. W., Lang, D., et al. 2013, PASP, 125, 306
Fudamoto, Y., Oesch, P. A., Faisst, A., et al. 2020, A&A, 643, A4
Fujimoto, S., Ouchi, M., Shibuya, T., et al. 2017, ApJ, 850, 83
Gabányi, K. É., Frey, S., & Perger, K. 2021, MNRAS, 506, 3641
Gao, Y., & Solomon, P. M. 2004, ApJ, 606, 271
Genzel, R., Tacconi, L. J., Gracia-Carpio, J., et al. 2010, MNRAS, 407, 2091
Genzel, R., Tacconi, L. J., Lutz, D., et al. 2015, ApJ, 800, 20
Goldbaum, N. J., Krumholz, M. R., & Forbes, J. C. 2016, ApJ, 827, 28
Gowardhan, A., Riechers, D., Pavesi, R., et al. 2019, ApJ, 875, 6
Groves, B. A., Schinnerer, E., Leroy, A., et al. 2015, ApJ, 799, 96
Gruppioni, C., Béthermin, M., Loiacono, F., et al. 2020, A&A, 643, A8
Hayward, C. C., Kereš, D., Jonsson, P., et al. 2011, ApJ, 743, 159
Hughes, T. M., Ibar, E., Villanueva, V., et al. 2017, MNRAS, 468, L103
Hunt, L. K., De Looze, I., Boquien, M., et al. 2019, A&A, 621, A51
Hunt, L. K., Tortora, C., Ginolfi, M., et al. 2020, A&A, 643, A180
Jiménez-Andrade, E. F., Magnelli, B., Karim, A., et al. 2019, A&A, 625, A114
Jiménez-Andrade, E. F., Murphy, E. J., Heywood, I., et al. 2021, ApJ, 910, 106
Jin, S., Daddi, E., Liu, D., et al. 2018, ApJ, 864, 56
Johnston, R., Vaccari, M., Jarvis, M., et al. 2015, MNRAS, 453, 2540
Johnston, R. S., Stil, J. M., & Keller, B. W. 2021, ApJ, 909, 73
Kaasinen, M., Scoville, N., Walter, F., et al. 2019, ApJ, 880, 15
Karim, A., Schinnerer, E., Martínez-Sansigre, A., et al. 2011, ApJ, 730, 61

Kashino, D., Silverman, J. D., Rodighiero, G., et al. 2013, ApJ, 777, L8
Kennicutt, R. C. 1998a, ApJ, 498, 541
Kennicutt, R. C. 1998b, ARA&A, 36, 189
Koekemoer, A. M., Aussel, H., Calzetti, D., et al. 2007, ApJS, 172, 196
Krumholz, M. R., & McKee, C. F. 2005, ApJ, 630, 250
Krumholz, M. R., Dekel, A., & McKee, C. F. 2012, ApJ, 745, 69
Kudritzki, R.-P., Teklu, A. F., Schulze, F., et al. 2021, ApJ, 910, 87
Lagos, C. del P., Crain, R. A., Schaye, J., et al. 2015, MNRAS, 452, 3815
Laigle, C., McCracken, H. J., Ilbert, O., et al. 2016, ApJS, 224, 24
Lang, P., Schinnerer, E., Smail, I., et al. 2019, ApJ, 879, 54
Le Floc'h, E., Aussel, H., Ilbert, O., et al. 2009, ApJ, 703, 222
Leroy, A. K., Bolatto, A., Gordon, K., et al. 2011, ApJ, 737, 12
Leroy, A. K., Walter, F., Sandstrom, K., et al. 2013, AJ, 146, 19
Leslie, S. K., Schinnerer, E., Liu, D., et al. 2020, ApJ, 899, 58
Lilly, S. J., Carollo, C. M., Pipino, A., et al. 2013, ApJ, 772, 119
Lindroos, L., Knudsen, K. K., Vlemmings, W., et al. 2015, MNRAS, 446, 3502
Lindroos, L., Knudsen, K. K., Fan, L., et al. 2016, MNRAS, 462, 1192
Liu, D., Daddi, E., Dickinson, M., et al. 2018, ApJ, 853, 172
Liu, D., Schinnerer, E., Groves, B., et al. 2019a, ApJ, 887, 235
Liu, D., Lang, P., Magnelli, B., et al. 2019b, ApJS, 244, 40
Luo, W., Yang, X., & Zhang, Y. 2014, ApJ, 789, L16
Lutz, D., Poglitsch, A., Altieri, B., et al. 2011, A&A, 532, A90
Madau, P., & Dickinson, M. 2014, ARA&A, 52, 415
Magdis, G. E., Rigopoulou, D., Huang, J.-S., et al. 2010, MNRAS, 401, 1521
Magdis, G. E., Daddi, E., Béthermin, M., et al. 2012, ApJ, 760, 6
Magnelli, B., Saintonge, A., Lutz, D., et al. 2012a, A&A, 548, A22
Magnelli, B., Lutz, D., Santini, P., et al. 2012b, A&A, 539, A155
Magnelli, B., Lutz, D., Saintonge, A., et al. 2014, A&A, 561, A86
Magnelli, B., Ivison, R. J., Lutz, D., et al. 2015, A&A, 573, A45
Magnelli, B., Boogaard, L., Decarli, R., et al. 2020, ApJ, 892, 66
Marchesi, S., Civano, F., Elvis, M., et al. 2016, ApJ, 817, 34
Martig, M., Crocker, A. F., Bournaud, F., et al. 2013, MNRAS, 432, 1914
McMullin, J. P., Waters, B., Schiebel, D., Young, W., & Golap, K. 2007, in Astronomical Data Analysis Software and Systems XVI, eds. R. A. Shaw, F. Hill, & D. J. Bell, ASP Conf. Ser., 376, 127
Miettinen, O., Delvecchio, I., Smolčić, V., et al. 2017a, A&A, 602, L9
Miettinen, O., Delvecchio, I., Smolčić, V., et al. 2017b, A&A, 606, A17
Millard, J. S., Eales, S. A., Smith, M. W. L., et al. 2020, MNRAS, 494, 293
Miura, R. E., Kohno, K., Tosaki, T., et al. 2014, ApJ, 788, 167
Mohan, N., & Rafferty, D. 2015, PyBDSF: Python Blob Detection and Source Finder, Astrophysics Source Code Library [record ascl:1502.007]
Momose, R., Koda, J., Kennicutt, R. C., et al. 2013, ApJ, 772, L13
Nelson, D., Kauffmann, G., Pillepich, A., et al. 2018, MNRAS, 477, 450
Noeske, K. G., Weiner, B. J., Faber, S. M., et al. 2007, ApJ, 660, L43
Novak, M., Smolčić, V., Delhaize, J., et al. 2017, A&A, 602, A5
Oliver, S. J., Bock, J., Altieri, B., et al. 2012, MNRAS, 424, 1614
Padmanabhan, H., & Loeb, A. 2020, MNRAS, 496, 1124
Pannella, M., Carilli, C. L., Daddi, E., et al. 2009, ApJ, 698, L116
Pearson, W. J., Wang, L., Hurley, P. D., et al. 2018, A&A, 615, A146
Peng, Y. J., & Maiolino, R. 2014, MNRAS, 443, 3643
Peng, Y. J., Lilly, S. J., Kovač, K., et al. 2010, ApJ, 721, 193
Pessa, I., Schinnerer, E., Belfiore, F., et al. 2021, A&A, 650, A134
Planck Collaboration XIII 2016, A&A, 594, A13
Popesso, P., Morselli, L., Concas, A., et al. 2019, MNRAS, 490, 5285
Popesso, P., Concas, A., Morselli, L., et al. 2020, MNRAS, 496, 2531
Popping, G., Pillepich, A., Calistro Rivera, G., et al. 2022, MNRAS, 510, 3321
Puglisi, A., Daddi, E., Liu, D., et al. 2019, ApJ, 877, L23
Qin, J., Zheng, X. Z., Wuyts, S., et al. 2019, MNRAS, 485, 5733
Rathaus, B., & Sternberg, A. 2016, MNRAS, 458, 3168
Rémy-Ruyer, A., Madden, S. C., Galliano, F., et al. 2014, A&A, 563, A31
Riechers, D. A., Bradford, C. M., Clements, D. L., et al. 2013, Nature, 496, 329
Rodighiero, G., Daddi, E., Baronchelli, I., et al. 2011, ApJ, 739, L40
Rodighiero, G., Renzini, A., Daddi, E., et al. 2014, MNRAS, 443, 19
Rodríguez Montero, F., Davé, R., Wild, V., et al. 2019, MNRAS, 490, 2139
Rosolowsky, E., & Blitz, L. 2005, ApJ, 623, 826
Rowlands, K., Heckman, T., Wild, V., et al. 2018, MNRAS, 480, 2544
Rujopakarn, W., Dunlop, J. S., Rieke, G. H., et al. 2016, ApJ, 833, 12
Saintonge, A., Catinella, B., Cortese, L., et al. 2016, MNRAS, 462, 1749
Saintonge, A., Catinella, B., Tacconi, L. J., et al. 2017, ApJS, 233, 22
Saintonge, A., Wilson, C. D., Xiao, T., et al. 2018, MNRAS, 481, 3497
Sánchez, S. F., Barrera-Ballesteros, J. K., Colombo, D., et al. 2021, MNRAS, 503, 1615
Sanders, D. B., Salvato, M., Aussel, H., et al. 2007, ApJS, 172, 86
Santini, P., Maiolino, R., Magnelli, B., et al. 2014, A&A, 562, A30
Sargent, M. T., Béthermin, M., Daddi, E., et al. 2012, ApJ, 747, L31
Sargent, M. T., Daddi, E., Béthermin, M., et al. 2014, ApJ, 793, 19
Schinnerer, E., Sargent, M. T., Bondi, M., et al. 2010, ApJS, 188, 384
Schinnerer, E., Groves, B., Sargent, M. T., et al. 2016, ApJ, 833, 112
Schmidt, M. 1959, ApJ, 129, 243
Schreiber, C., Pannella, M., Elbaz, D., et al. 2015, A&A, 575, A74
Schreiber, C., Elbaz, D., Pannella, M., et al. 2018, A&A, 609, A30
Schuster, K. F., Kramer, C., Hitschfeld, M., et al. 2007, A&A, 461, 143
Scoville, N., Aussel, H., Brusa, M., et al. 2007, ApJS, 172, 1
Scoville, N., Aussel, H., Sheth, K., et al. 2014, ApJ, 783, 84
Scoville, N., Sheth, K., Aussel, H., et al. 2016, ApJ, 820, 83
Scoville, N., Lee, N., Vanden Bout, P., et al. 2017, ApJ, 837, 150
Shetty, R., Kelly, B. C., Rahman, N., et al. 2014, MNRAS, 437, L61
Smolčić, V., Novak, M., Bondi, M., et al. 2017, A&A, 602, A1
Sobral, D., Best, P. N., Smail, I., et al. 2014, MNRAS, 437, 3516
Speagle, J. S., Steinhardt, C. L., Capak, P. L., et al. 2014, ApJS, 214, 15
Suess, K. A., Kriek, M., Price, S. H., et al. 2019, ApJ, 877, 103
Szokoly, G. P., Bergeron, J., Hasinger, G., et al. 2004, ApJS, 155, 271
Tacchella, S., Carollo, C. M., Renzini, A., et al. 2015, Science, 348, 314
Tacchella, S., Dekel, A., Carollo, C. M., et al. 2016, MNRAS, 457, 2790
Tacconi, L. J., Genzel, R., Neri, R., et al. 2010, Nature, 463, 781
Tacconi, L. J., Genzel, R., Saintonge, A., et al. 2018, ApJ, 853, 179
Tacconi, L. J., Genzel, R., & Sternberg, A. 2020, ARA&A, 58, 157
Tadaki, K., Belli, S., Burkert, A., et al. 2020, ApJ, 901, 74
Tan, Q., Daddi, E., Magdis, G., et al. 2014, A&A, 569, A98
Taniguchi, Y., Scoville, N., Murayama, T., et al. 2007, ApJS, 172, 9
Tomczak, A. R., Quadri, R. F., Tran, K.-V. H., et al. 2016, ApJ, 817, 118
Tonini, C., Mutch, S. J., Croton, D. J., et al. 2016, MNRAS, 459, 4109
van der Wel, A., Franx, M., van Dokkum, P. G., et al. 2014, ApJ, 788, 28
Walter, F., Carilli, C., Neeleman, M., et al. 2020, ApJ, 902, 111
Walther, M., Oñorbe, J., Hennawi, J. F., et al. 2019, ApJ, 872, 13
Wang, T.-M., & Hwang, C.-Y. 2020, A&A, 641, A24
Whitaker, K. E., Franx, M., Leja, J., et al. 2014, ApJ, 795, 104
Wiklind, T., Ferguson, H. C., Guo, Y., et al. 2019, ApJ, 878, 83
Wilson, C. D., Elmegreen, B. G., Bemis, A., et al. 2019, ApJ, 882, 5
Wong, T., & Blitz, L. 2002, ApJ, 569, 157
Wright, R. J., Lagos, C. del P., Davies, L. J. M., et al. 2019, MNRAS, 487, 3740
Wuyts, S., Förster Schreiber, N. M., Lutz, D., et al. 2011, ApJ, 738, 106
Wyse, R. F. G. 1986, ApJ, 311, L41
Zahid, H. J., Dima, G. I., Kewley, L. J., et al. 2012, ApJ, 757, 54
Zamojski, M. A., Schiminovich, D., Rich, R. M., et al. 2007, ApJS, 172, 468
Zheng, X. Z., Bell, E. F., Rix, H.-W., et al. 2006, ApJ, 640, 784

Appendix A: Reliability of the stacked flux density and size measurements

To test the reliability of the flux densities and sizes measured by stacking in the *uv* and image domain, we used simulations tailored to reproduce the peculiar properties of the A^{3}COSMOS archive (i.e., with a heterogeneous frequency, depth, and spatial resolution). The logic of our approach is to (i) simulate 100 realistic ALMA observations of a galaxy population with a given intrinsic flux density and size properties, (ii) stack these 100 mock observations, and (iii) finally compare the measured stacked flux density and size to the intrinsic ones. For a given set of flux density and size properties, we judge the reliability of our stacking analysis by computing $(S_{\rm in} - S_{\rm out})/S_{\rm in}$ and $(R^{\rm circ}_{\rm in} - R^{\rm circ}_{\rm out})/R^{\rm circ}_{\rm in}$ (i.e., the error on the retrieved stacked flux density and size, respectively).

Our mock ALMA observations were generated using the CASA task `simobserve`. To realistically reproduce the heterogeneity of the A^{3}COSMOS archive, the observing properties of each simulation (i.e., frequency resolution, integration time, and antenna positions) were randomly picked from one of the A^{3}COSMOS data set. Then, the stacked position of the mock galaxies were randomly selected within a radius of 3″from the simulated phase center. Finally, to account for possible mismatches between the stacked position and the actual millimeter position of the stacked sources, we randomly placed these mock galaxies around their stacked position, following a 2D Gaussian distribution with a dispersion of 0.″2 (e.g., Elbaz et al. 2018). We note that here we do not test the effect of the observed-frame flux density to rest-frame luminosities conversion discussed in Sect. 3.1. Indeed, from a technical point of view this conversion is strictly equivalent to a simple multiplication and thus a noise increase or decrease in the initial to-be-stacked data set. Our simulation already test the effect of stacking data set with different noise, redistributing this noise distribution is thus unnecessary.

Results of these Monte Carlo simulations for three realistic angular sizes (i.e., point source, $FWHM$ = 0.″5 and $FWHM$ = 1.″0) and twelves flux densities combinations, are shown in Fig. A.1 and A.2. These results demonstrate the reliability of our stacked flux density and size measurements. Indeed, all size-flux density combinations that yield a detection have $(S_{\rm in} - S_{\rm out})/S_{\rm in}$ and $(R^{\rm circ}_{\rm in} - R^{\rm circ}_{\rm out})/R^{\rm circ}_{\rm in}$ values consistent with 0 within the measured uncertainties. We only notice a slight systematic overestimation of our stacked flux densities by 6% and 4% when inferred from the *uv* and image domain, respectively. Such an offset is virtually insignificant with respect to the measured uncertainties. Lastly, we note that galaxies with larger intrinsic sizes (i.e., 1.″0) do not yield a detection down to our lowest flux density combination. This is not inherent to our stacking analysis but simply to the spreading of the flux densities of these galaxies over several synthesized beams.

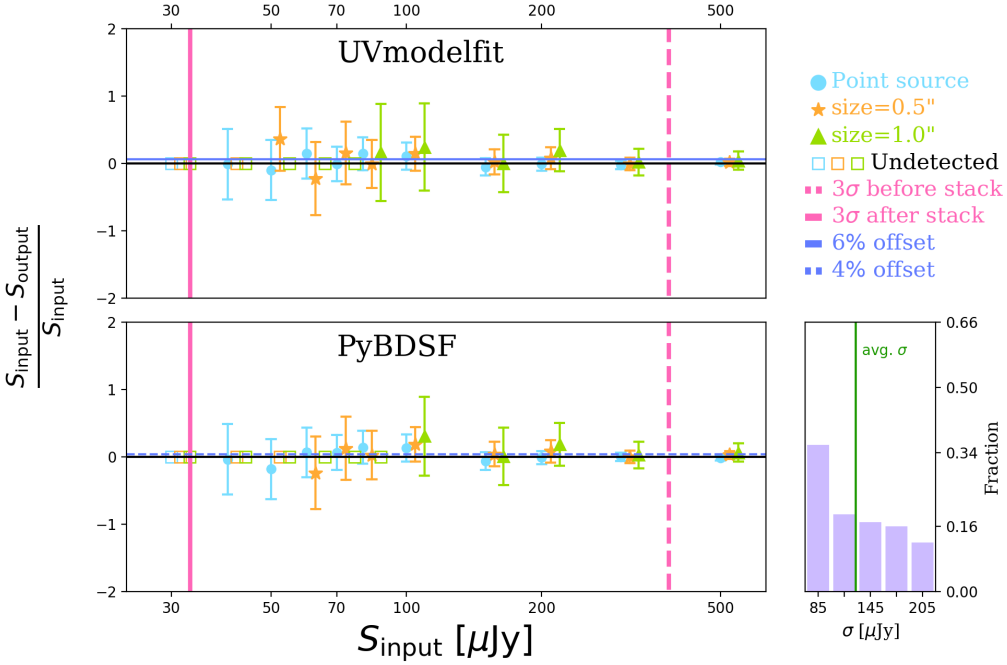

Fig. A.1. Uncertainty on the *uv*-domain (upper panel) and image-domain (lower panel) stacked flux density measurements of 100 simulated galaxies as a function of their intrinsic flux densities and sizes. The vertical pink dashed line shows the average "point source" 3σ detection threshold of the measurement sets to be stacked, while the lower right subpanel displays their 1σ distribution. The vertical solid pink line presents the point source 3σ detection threshold in the stacked measurement set. Our stacking analysis allows accurate mean flux density measurements (i.e., $(S_{\rm in} - S_{\rm out})/S_{\rm in} \sim 0$) for galaxy populations that are otherwise individually undetected, i.e., with intrinsic flux densities lower than the vertical pink dashed line. Stacked flux densities are in average underestimated by 6% and 4% in the *uv* domain and image domain, respectively, as illustrated by the dark blue solid and dashed horizontal lines, respectively.

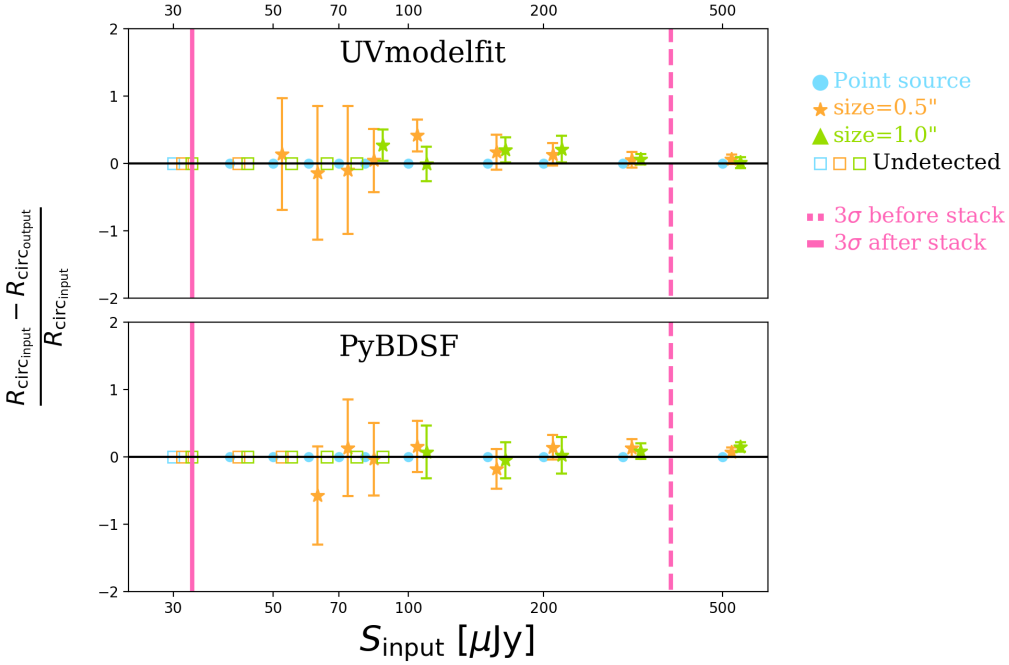

Fig. A.2. Uncertainty on the *uv*-domain (upper panel) and image-domain (lower panel) stacked size measurements of 100 simulated galaxies as a function of their intrinsic flux densities and sizes. Lines and symbols are the same as in Fig. A.1. Our stacking analysis allows accurate mean size measurements (i.e., $(R_{\mathrm{in}}^{\mathrm{circ}} - R_{\mathrm{out}}^{\mathrm{circ}})/R_{\mathrm{in}}^{\mathrm{circ}} \sim 0$) for galaxy populations that are otherwise individually undetected, i.e., with intrinsic flux densities lower than the vertical dashed pink line.

Appendix B: Different gas mass calibrations

The results of our study could naturally be influenced by the particular assumptions made here to convert stacked rest-frame 850 μm luminosities into molecular gas masses (see, e.g., discussion in Liu et al. 2019b). To evaluate the impact of these assumption on our results, we compare molecular gas masses obtained here using the metallicity-independent L_{850}-to-$M_{\rm mol}$ relation of H17 with those obtained using others relations commonly applied in the literature (Fig. B.1).

H17 inferred two L_{850}-to-$M_{\rm mol}$ relations: the one used in the core of our paper was calibrated using a CO-to-$M_{\rm mol}$ conversion factor (i.e., $\alpha_{\rm CO}$) that assumes that the density and properties in the gas reservoirs of high-redshift galaxies are similar to Milky Way GMCs (i.e., $\alpha_{\rm CO}$=6.5 $M_\odot$ (K km s^{-1} pc^2)$^{-1}$); and another relation calibrated instead using $\alpha_{\rm CO}$=4.35 (H17$_{\alpha_{\rm CO}=4.35}$), which is the standard value for the Milky Way. These relations have the same slope and only differ in terms of normalization. Molecular gas masses obtained with H17$_{\alpha_{\rm CO}=4.35}$ are thus shifted to lower values by 0.17 dex (Fig. B.1). This yields a quantitatively different evolution of the molecular gas mass fraction and depletion time with redshift than those inferred with H17 (Fig. B.2). However, the main conclusions of our analysis remains unchanged: the molecular gas fraction of MS galaxies still increases significantly with redshifts and decreases with stellar masses; and their depletion time still decrease more moderately with redshifts and remains mostly independent from their stellar mass.

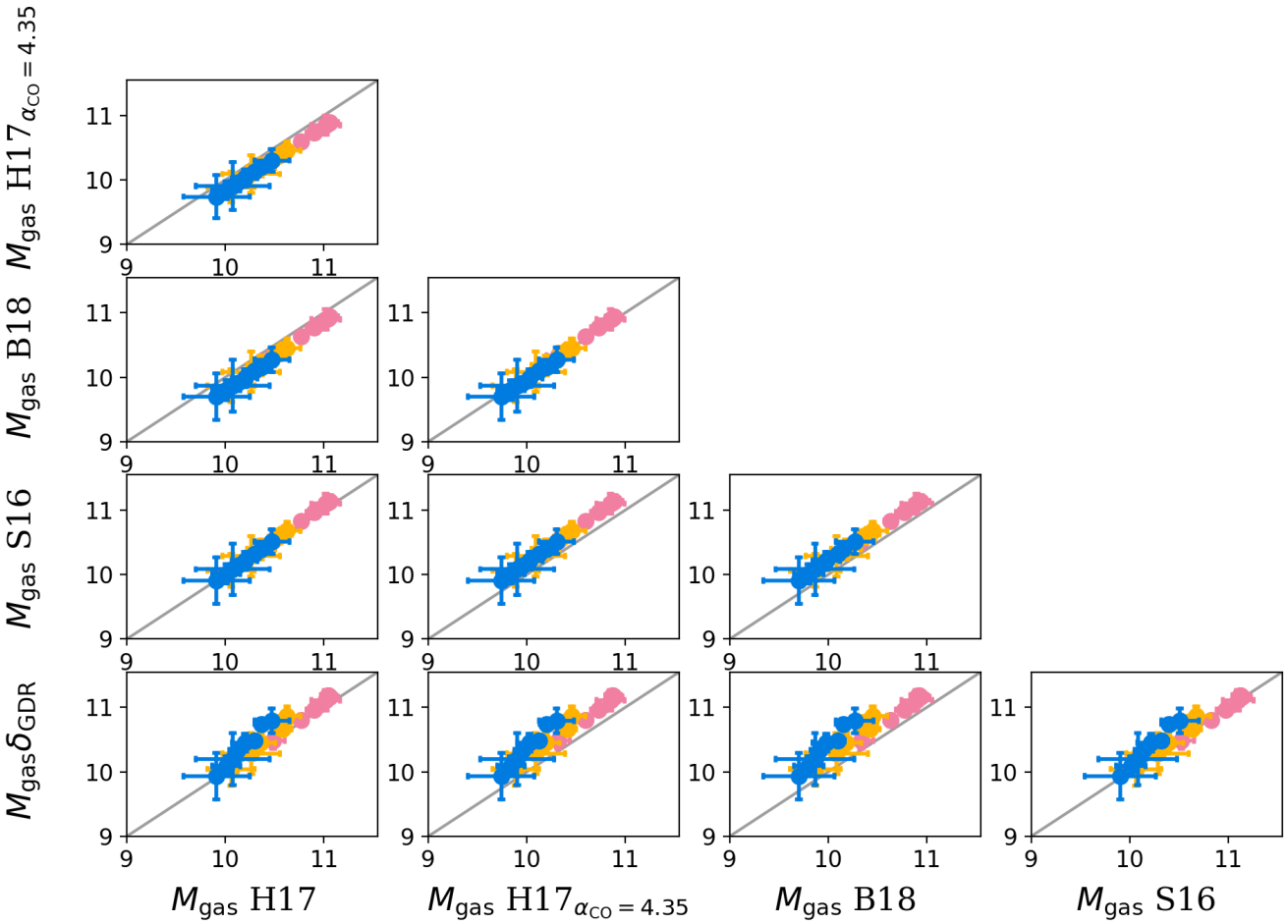

Fig. B.1. Comparisons between four molecular gas mass calibrations, i.e., from Hughes et al. (2017) assuming $\alpha_{\rm CO}$ = 6.5 (H17; used throughout our paper), Hughes et al. (2017) assuming $\alpha_{\rm CO}$ = 4.35 (H17$_{\alpha_{\rm CO}=4.35}$), Scoville et al. (2016, S16), Bertemes et al. (2018, B18), and Leroy et al. (2011, $\delta_{\rm GDR}$). In each panel, the solid gray line is the one-to-one relation. Symbol colors have the same meaning as in Fig. 11.

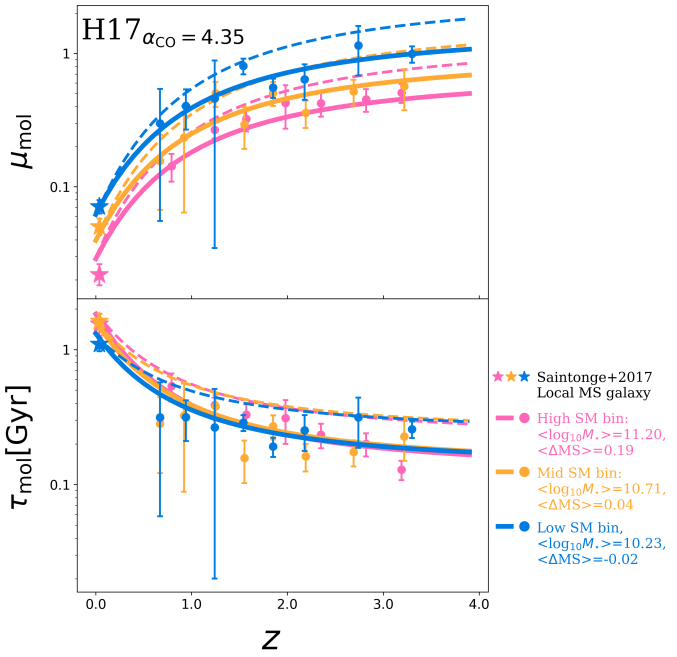

Fig. B.2. Redshift evolution of the mean molecular gas fraction and molecular gas depletion time of MS galaxies, with the M_{gas} from the H17$_{\alpha_{CO}=4.35}$ gas mass calibration. Dots show the mean molecular gas fraction and molecular gas depletion time from our work. Stars represent the local reference taken from Saintonge et al. (2017). Solid lines display the analytical evolution of the molecular gas fraction and molecular gas depletion time inferred with the H17$_{\alpha_{CO}=4.35}$ gas mass calibration. Dashed lines show the analytical evolution of the molecular gas fraction and molecular gas depletion time inferred with the H17 gas mass calibration (used throughout the paper). Symbols and lines are color-coded by stellar mass.

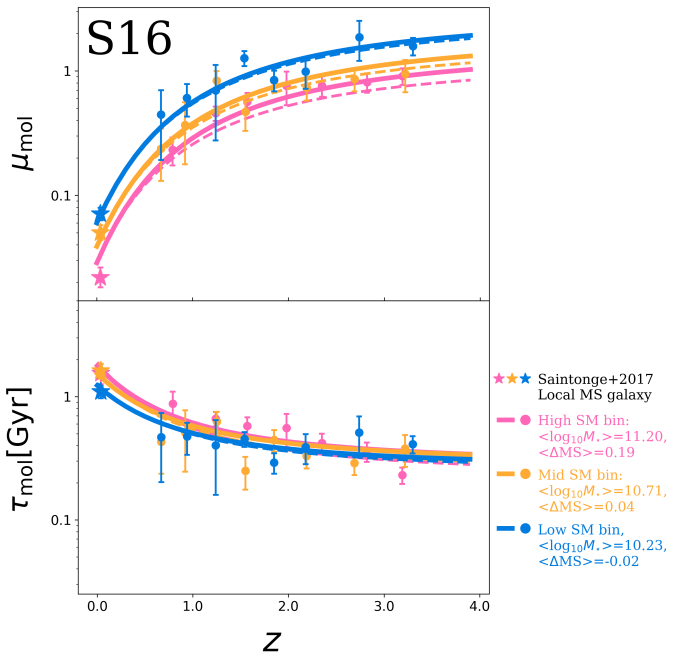

Fig. B.3. Same as Fig. B.2 but for the gas mass calibration from S16.

Besides the H17 gas mass calibration, S16 also provides a metallicity-independent L_{850}-to-M_{mol} relation calibrated on a sample of 70 SFGs with both dust RJ and CO measurements. Then, assuming a constant mass-weighted dust temperature of 25 K, a dust emissivity, β, of 1.8, and α_{CO}=6.5 $M_\odot$ (K km s^{-1} pc^2)$^{-1}$, they calibrated a light-to-mass relation

$$\log(M_{mol}) = \log(L_{850}) - 19.83, \quad \text{(B.1)}$$

where M_{mol} and L_{850} are in units of $M_\odot$ and erg s^{-1} Hz^{-1}, respectively. This relation yields molecular gas masses in very good agreement with those inferred here (Fig. B.1), with only a systematic offset of +0.04 dex for S16. The redshift evolution of the molecular gas mass fraction and depletion time inferred using S16 are shown in Fig. B.3. Those agree qualitatively and quantitatively with the original findings of our study.

One can also measure the molecular gas mass of SFGs by applying first a standard L_{850}-to-M_{dust} relation and then a metallicity-dependent M_{dust}-to-M_{mol} relation. To begin with, we thus convert our stacked rest-frame 850 μm luminosities into M_{dust} following Magnelli et al. (2020), who assumed a constant mass-weighted dust temperature of 25 K, a dust emissivity of 1.8, and a photon cross section to dust mass ratio at rest-frame 850 μm, κ_{850}, of 0.0431 m^2 kg^{-1},

$$\log(M_{dust}) = \log(L_{850}) - 21.86, \quad \text{(B.2)}$$

where M_{dust} is in unit of $M_\odot$. This dust mass can then be converted into molecular gas mass using the metallicity-dependent M_{dust}-to-M_{mol} relation of, for example, B18, which was calibrated using 78 local SFGs with known gas-phase metallicity,

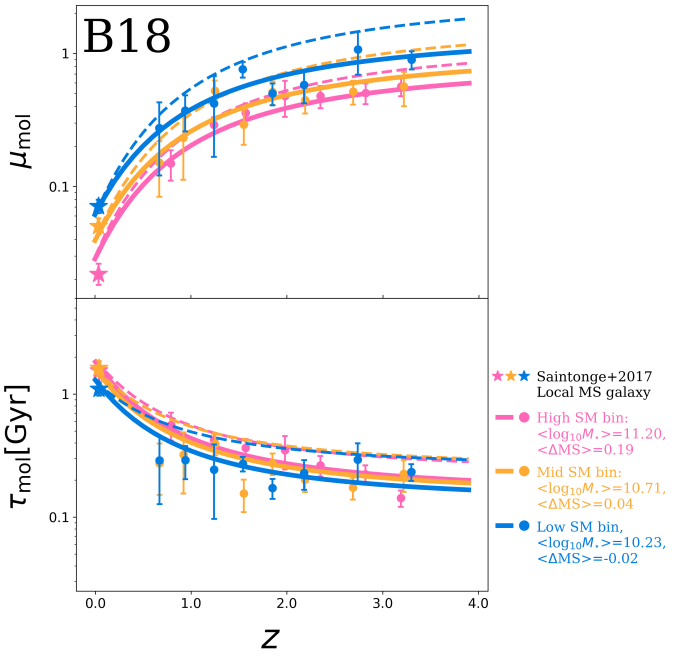

Fig. B.4. Same as Fig. B.2 but for the gas mass calibration from B18.

$$\log(M_{mol}) = \log(M_{dust}) + 1.83 + 0.12 \times ((12 + \log(O/H)) - 8.67), \quad \text{(B.3)}$$

where the gas-phase metallicity, 12+log(O/H), can be inferred using the redshift- and stellar mass-dependent relation given in Liu et al. (2019b),

$$12 + \log(O/H) = \begin{cases} a & \text{if } \log(M_\star/M_\odot) \geq b(z), \\ a - 0.087 \times (\log(M_\star/M_\odot) - b(z))^2, & \text{else,} \end{cases} \quad \text{(B.4)}$$

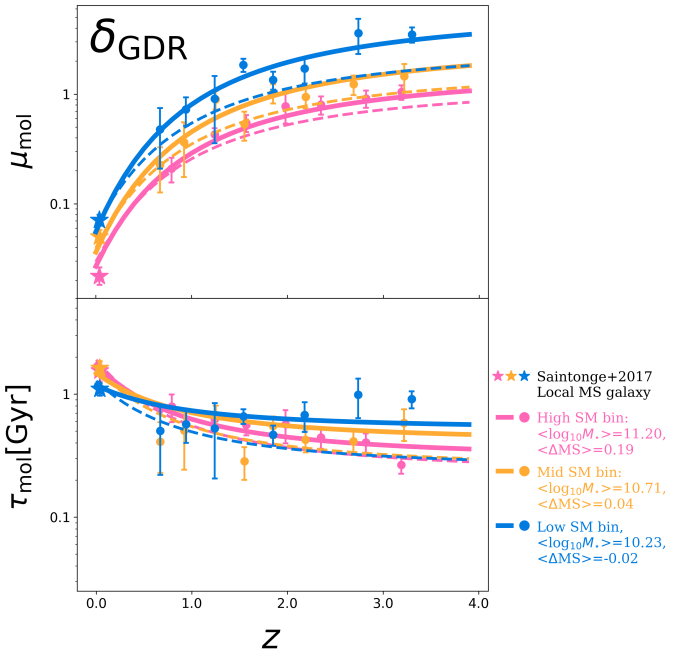

Fig. B.5. Same as Fig. B.2 but for the gas mass calibration from Leroy et al. (2011, δ_{GDR}).

Table B.1. Best-fit coefficients for the molecular gas fraction (Eq. 8) and molecular gas depletion time (Eq. 9) functions.

$\log_{10}\mu_{mol}$ with a = 0.4195 and ak = 0.1195 from Liu et al. (2019b)				
	b	c	ck	d
H17	$-0.468^{+0.070}_{-0.070}$	$-0.122^{+0.008}_{-0.008}$	$0.572^{+0.059}_{-0.060}$	$0.002^{+0.011}_{-0.011}$
$H17_{\alpha_{CO}=4.35}$	$-0.463^{+0.070}_{-0.071}$	$-0.102^{+0.008}_{-0.008}$	$0.311^{+0.061}_{-0.058}$	$0.000^{+0.010}_{-0.010}$
B18	$-0.353^{+0.069}_{-0.069}$	$-0.099^{+0.008}_{-0.008}$	$0.266^{+0.057}_{-0.057}$	$-0.008^{+0.010}_{-0.010}$
S16	$-0.396^{+0.070}_{-0.070}$	$-0.123^{+0.008}_{-0.008}$	$0.584^{+0.059}_{-0.058}$	$-0.004^{+0.011}_{-0.011}$
L11	$-0.679^{+0.068}_{-0.067}$	$-0.152^{+0.008}_{-0.008}$	$0.948^{+0.057}_{-0.057}$	$0.017^{+0.010}_{-0.010}$
$\log_{10}\tau_{mol}$ [Gy^{-1}] with a = −0.5724 and ak = 0.1120 from Liu et al. (2019b)				
	b	c	ck	d
H17	$0.055^{+0.069}_{-0.071}$	$0.049^{+0.008}_{-0.008}$	$-0.643^{+0.056}_{-0.057}$	$0.016^{+0.010}_{-0.010}$
$H17_{\alpha_{CO}=4.35}$	$0.054^{+0.071}_{-0.069}$	$0.069^{+0.008}_{-0.008}$	$-0.899^{+0.055}_{-0.057}$	$0.014^{+0.010}_{-0.011}$
B18	$0.168^{+0.069}_{-0.067}$	$0.072^{+0.008}_{-0.008}$	$-0.947^{+0.057}_{-0.057}$	$0.006^{+0.010}_{-0.010}$
S16	$-0.125^{+0.070}_{-0.067}$	$0.047^{+0.008}_{-0.008}$	$-0.628^{+0.058}_{-0.058}$	$0.010^{+0.010}_{-0.010}$
L11	$-0.157^{+0.068}_{-0.070}$	$0.019^{+0.008}_{-0.008}$	$-0.265^{+0.059}_{-0.057}$	$0.031^{+0.010}_{-0.011}$

where a=8.74 and $b(z)$=10.4+4.46×log(1+z)-1.78×(log(1+z))^2. Using this molecular gas mass calibration (i.e., B18) yields estimates that are ∼0.17 dex lower than those from H17 (Fig. B.1). In addition to this global offset, this metallicity-dependent approach yields quantitatively different evolution of the molecular gas mass fraction and depletion time with redshift than those inferred with H17 (Fig. B.4). However, the main conclusions of our analysis remains unchanged: the molecular gas fraction of MS galaxies still increases significantly with redshifts and decreases with stellar masses; and their depletion time still decreases more moderately with redshifts and remains mostly independent from their stellar mass.

Finally, we converted the dust masses from Eq. B.2 into molecular gas masses using instead the standard metallicity-dependent M_{dust}-to-M_{mol} relation of Leroy et al. (2011, δ_{GDR}), which was calibrated using high-resolution observations of five local group galaxies,

$$\log(M_{mol}) = \log(M_{dust}) + 9.4 - 0.85 \times (12 + \log(O/H)). \quad (B.5)$$

We note that while this relation formally account for both molecular and atomic gas masses, we implicitly assume here that the gas in high-redshift ($z > 0.5$) SFGs is dominated by their molecular phase Tacconi et al. (see discussion in 2018); Liu et al. (see discussion in 2019b). Overall, the molecular gas masses inferred using the δ_{GDR} method are about ∼0.13 dex higher than those obtained from H17 (Fig. B.1). As for B18, this gas mass calibration also yields slightly different, yet qualitatively consistent, molecular gas mass fraction and depletion time redshift evolution (Fig. B.5) than those inferred with H17.

To summarize, the gas mass calibrations are: $M_{mol}^{H17_{\alpha_{CO}=4.35}} \approx M_{mol}^{B18} < M_{mol}^{H17} \approx M_{mol}^{S16} < M_{mol}^{\delta_{GDR}}$. The redshift evolution of the molecular gas fraction and depletion time obtained from S16 agree qualitatively and quantitatively with those from H17, while those measured using $H17_{\alpha_{CO}=4.35}$, B18 and δ_{GDR} agree only qualitatively with those from H17 (see Table B.1). However, because the main conclusion of our paper are not qualitatively affected by the particular choice of a given relation and because the H17 approach yield measurements that are bracket by others, we decided to use H17 in our paper.

The choice of using the L_{850}-to-M_{mol} relation from H17 could seem at odds since this relation was calibrated using α_{CO}=6.5, while our local reference (i.e., Saintonge et al. 2017) converted their CO measurements into molecular gas masses using α_{CO} ∼4 (at the high stellar masses of our study). Despite this apparent inconsistency, the redshift evolution of the molecular gas content of massive SFGs inferred by combining this local reference with our high-redshift H17 measurements is in much better agreement with Tacconi et al. (2020) than when combining this local reference with our high-redshift $H17_{\alpha_{CO}=4.35}$ measurements (see Fig. 4 and B.1). Because at high stellar masses results from Tacconi et al. (2020) can be considered as the reference (as they are based in a fairly complete sample of massive SFGs and a thorough cross-calibration of the CO- and dust-based methods), we decided to use in the core of our paper the L_{850}-to-M_{mol} relation from H17. The agreement between these high-redshift H17 measurements and those from Tacconi et al. (2020) is explained by the fact that using α_{CO}=6.5 instead of 4.3 to calibrate the local L_{850}-to-M_{mol} relation corrects indirectly (and to first order) for the fact that at a given stellar mass, high-redshift galaxies have lower metallicities than local galaxies, and thus have a higher gas-to-dust ratio (e.g., Leroy et al. 2011) and consequently should have lower L_{850}-to-M_{mol} ratio. This seems also confirmed by the good agreement at high stellar masses between our H17 measurements and those from the metallicity-dependent δ_{GDR} method.

APPENDIX C

A^{3}COSMOS: Dissecting the gas content of star-forming galaxies across the main sequence at 1.2 $\leq z <$ 1.6

The publication *Wang et al. A&A (2023), 47219-23 (Forthcoming Article)* is reproduced below in its original form with permission by ESO.

Astronomy & Astrophysics manuscript no. output
November 20, 2023

A^{3}COSMOS: Dissecting the gas content of star-forming galaxies across the main sequence at $1.2 \leq z < 1.6$

Tsan-Ming Wang[1], Benjamin Magnelli[2], Eva Schinnerer[3], Daizhong Liu[4], Eric Faustino Jiménez-Andrade[5], Christos Karoumpis[1], Sylvia Adscheid[1], and Frank Bertoldi[1]

[1] Argelander-Institut für Astronomie, Universität Bonn, Auf dem Hügel 71, 53121 Bonn, Germany
e-mail: twan@uni-bonn.de
[2] Université Paris-Saclay, Université Paris Cité, CEA, CNRS, AIM, 91191, Gif-sur-Yvette, France
[3] Max-Planck-Institut für Astronomie, Königstuhl 17, 69117 Heidelberg, Germany
[4] Max-Planck-Institut für extraterrestrische Physik, Gießenbachstraße 1, 85748 Garching b. München, Germany
[5] Instituto de Radioastronomía y Astrofísica, Universidad Nacional Autónoma de México, Antigua Carretera a Pátzcuaro # 8701, Ex-Hda. San José de la Huerta, Morelia, Michoacán, México C.P. 58089

Received xxx; accepted xxx

ABSTRACT

Aims. We aim to understand the physical mechanisms that drive star formation in a sample of mass-complete ($>10^{9.5} M_\odot$) star-forming galaxies (SFGs) at $1.2 \leq z < 1.6$.
Methods. We selected SFGs from the COSMOS2020 catalog and applied a *uv*-domain stacking analysis to their archival Atacama Large Millimeter/submillimeter Array (ALMA) data. Our stacking analysis provides precise measurements of the mean molecular gas mass and size of SFGs down to a stellar mass of $M_\star \sim 10^{9.5} M_\odot$, even though at these stellar mass galaxies on the main sequence (MS) are no longer detected individually in the archival ALMA data. We also applied an image-domain stacking analysis on their *HST* *i*-band and UltraVISTA *J*- and K_s-band images. This allowed us to trace the distribution of their stellar component. Correcting these rest-frame optical sizes using the $R_{\rm half-stellar-light}$-to-$R_{\rm half-stellar-mass}$ conversion at rest 5000Å, we obtain the stellar mass size of MS galaxies and compare them to the sizes of their star-forming component obtained from our ALMA stacking analysis.
Results. Across the MS ($-0.2 < \Delta{\rm MS} = \log({\rm SFR}/{\rm SFR_{MS}}) < 0.2$), the mean molecular gas fraction of SFGs increases by a factor of $\sim$1.4, while their mean molecular gas depletion time decreases by a factor of $\sim$1.8. The scatter of the MS could thus be caused by variations in both the star formation efficiency and molecular gas fraction of galaxies. The mean molecular gas fraction of MS galaxies decreases by a factor of $\sim$7 from $M_\star \sim 10^{9.7} M_\odot$ to $\sim 10^{11.3} M_\odot$, while their mean molecular gas depletion time remains roughly the same at all stellar masses. This finding could be a hint that the bending of the MS at $z \sim 1.4$ is primarily driven by variations in cold gas accretion. The majority of the galaxies lying on the MS have $R_{\rm FIR} \approx R_{\rm stellar}$. Their central regions are subject to large dust attenuation. Starbursts (SBs, $\Delta{\rm MS} > 0.7$) have a mean molecular gas fraction $\sim$2.1 times larger and mean molecular gas depletion time $\sim$3.3 times shorter than MS galaxies. Additionally, they have more compact star-forming regions ($\sim$2.5 kpc for MS galaxies vs. $\sim$1.4 kpc for SBs) and systematically disturbed rest-frame optical morphologies, which is consistent with their association with major-mergers. SBs and MS galaxies follow the same relation between their molecular gas mass and star formation rate surface densities with a slope of $\sim 1.1 - 1.2$, that is, the so-called Kennicutt-Schmidt relation.

Key words. galaxies: evolution – galaxies: high-redshift – galaxies: ISM

1. Introduction

Parts of the evolutionary history of the Universe have been revealed to us in the last decades by modern telescopes. In particular, it has been found that the cosmic star formation rate density (SFRD) increases from early cosmic times, reaches a peak at cosmic noon, i.e., $z \sim 2$, and smoothly decreases by a factor of ~ 10 by $z \sim 0$ (e.g., Madau & Dickinson 2014; Novak et al. 2017; Liu et al. 2018; Gruppioni et al. 2020; Leslie et al. 2020). In the star formation rate (SFR) versus stellar mass ($M_\star$) plane, star-forming galaxies (SFGs) can be broadly classified into two populations. The first and largest population resides on a tight correlation between SFR and stellar mass, which accounts for about 80% of the cosmic SFRD, the so-called main sequence (MS) of SFGs (e.g., Noeske et al. 2007; Elbaz et al. 2011; Magnelli et al. 2014; Schreiber et al. 2015; Leslie et al. 2020; Leja et al. 2022; Popesso et al. 2022). The MS has a scatter of $\sim$0.3 dex and a normalization that decreases by a factor of 20 from $z \sim 2$ to $z \sim 0$ (e.g., Schreiber et al. 2015; Leslie et al. 2020; Leja et al. 2022; Popesso et al. 2022). The MS is also found to bend at high stellar mass (e.g., Schreiber et al. 2015; Popesso et al. 2019; Leslie et al. 2020; Delvecchio et al. 2021), but this flattening becomes less prominent with increasing redshift and almost vanishes by $z \sim 2$. SFGs on the MS are thought to evolve in isolation with long star-forming duty cycles, sustained by continuous cold gas accretion (e.g., Liu et al. 2019a; Tacconi et al. 2020; Wang et al. 2022). The second population, known as starbursts (SBs), exhibits intense star formation activities and is offset above the MS with $\Delta{\rm MS}$ ($\log_{10}({\rm SFR}/{\rm SFR_{MS}}) > 0.7$ (e.g., Schreiber et al. 2015; Silverman et al. 2018). These galaxies make up only 5% of the SFG population and contribute 10% of the SFRD out to $z \sim 4$ (e.g., Rodighiero et al. 2011; Sargent et al. 2012; Lamastra et al. 2013; Schreiber et al. 2015). Their enhanced star formation is believed to result from mergers, interactions between galaxies, or disk instabilities of galaxies (e.g., Davé et al. 2010; Hodge et al. 2012; Porter et al. 2014; Wilkinson et al. 2018; Calabrò et al.

2019; Cibinel et al. 2019; Renaud et al. 2022). Despite the well-established classification of SFGs based on their SFRs and stellar masses up to $z \sim 6$, the underlying mechanisms causing the evolution of the normalization of the MS (leading to the dispersion of the MS) and the triggering of SBs remain debated. Deeper insight into the mechanisms behind these scaling relations can be gained from precise measurements of their molecular gas reservoir, which serves as the fuel for star formation.

In the local universe, carbon monoxide (CO) emission from the molecular gas is widely used to measure the molecular gas content of galaxies (see Bolatto et al. 2013, for a review). However, obtaining the molecular gas mass of SFGs through CO observations at high redshifts is a challenge considering the sensitivity of even the latest (sub)millimeter and radio interferometers, e.g., Atacama Large Millimeter/submillimeter Array (ALMA), Northern Extended Millimeter Array (NOEMA), and Karl G. Jansky Very Large Array (JVLA). To alleviate this limitation, a new approach to measure gas mass for high-redshift galaxies from dust continuum observations has been developed in recent years. This approach relies on standard gas-to-dust mass relations and well-calibrated dust mass measurements, which can be achieved by using either multiwavelength dust spectral energy distribution (SED) fits (e.g., Magdis et al. 2012; Santini et al. 2014; Hunt et al. 2019; Kokorev et al. 2021; Suzuki et al. 2021) or a single Rayleigh–Jeans (RJ) flux density conversion (e.g., Scoville et al. 2014, 2016; Liu et al. 2019a; Magnelli et al. 2020; Millard et al. 2020; Dye et al. 2022; Wang et al. 2022). A plethora of literature studies have since used this approach to measure the molecular gas mass of massive SFGs up to $z \sim 5$ (e.g., Scoville et al. 2016; Liu et al. 2019a; Tacconi et al. 2020; Suzuki et al. 2021; Wang et al. 2022). Among these, that of Wang et al. (2022) is the first to statistically constrain (through stacking) the molecular gas content of a mass-complete sample of MS galaxies down to $10^{10}\,M_\odot$ and up to $z \sim 3.5$, thus avoiding any selection bias that could potentially affect previous studies. With this approach, they accurately measured that the mean molecular gas fraction, i.e., $\mu_{\rm mol} = M_{\rm mol}/M_\star$, of MS galaxies decreases with increasing stellar mass and decreases by a factor of ~ 20 from $z \sim 3$ to $z \sim 0$. Additionally, they found that the molecular gas depletion time (i.e., $\tau_{\rm mol} = M_{\rm mol}/{\rm SFR}$) of MS galaxies remains roughly constant at $z > 0.5$ with a value of $300 - 500$ Myr, and it only increases by a factor of ~ 3 from $z \sim 0.5$ to $z \sim 0$. This suggests that to the first order, the molecular gas content of MS galaxies regulates their star formation across cosmic time, while variation of their star formation efficiency plays a secondary role.

Although the study of Wang et al. (2022) has provided us with an accurate estimate of the redshift evolution of the molecular gas content of MS galaxies as a whole population, they did not study how the molecular content of SFGs evolves across and well above the MS. Therefore, while it is generally accepted that SBs partly have a higher star formation efficiency and partly a higher molecular gas content than MS galaxies (e.g., Genzel et al. 2010; Liu et al. 2019a; Tacconi et al. 2020), the exact balance between these two distinct effects is still uncertain, mainly because current studies on the evolution of the molecular gas content of SFGs with ΔMS are still not based on mass-complete samples and are thus potentially affected by selection biases. As a consequence, we are missing a complete picture of the physical mechanisms that drive and regulate the dispersion of ~ 0.3 dex of the MS and that drive galaxies well above the MS. To make progress on these topics, a detailed study of the evolution of the molecular gas content of a mass-complete sample SFGs as a function of ΔMS is needed.

To gain a better understanding of the mechanisms that drive the evolution of SFGs, it is also essential to accurately measure the extent of their gas reservoir. Indeed, such measurements allow us to investigate the fundamental scaling relationship between the SFR and gas surface densities of SFGs, the so-called Kennicutt-Schmidt (KS) relation (Kennicutt 1998a). Wang et al. (2022) found, for example, that the moderate redshift evolution of the molecular gas depletion time of MS galaxies could be predicted from the evolution of their molecular gas surface density and a universal KS relation with a slope of ~ 1.13. In addition, some observations suggest that the most extreme SBs follow a different KS relation, characterized by a slope of ~ 1.13 but with a normalization ~ 10 times higher than that of MS galaxies (e.g., Daddi et al. 2010; Genzel et al. 2010). This latter result is, however, still debated because it remains unclear whether the KS relation is truly bimodal (MS vs. SB) or whether it evolves smoothly with ΔMS. To make further progress on this topic, a detailed study of the evolution of the molecular gas mass and size of a mass-complete sample SFGs as a function of ΔMS is needed.

In this work, we thus derived the mean molecular gas mass and extent of SFGs across the MS at $M_\star > 10^{9.5} M_\odot$ and $1.2 \leq z \leq 1.6$ using a stacking analysis. This redshift range was chosen as it yields detection with the highest significance level in Wang et al. (2022), i.e., we can further dissect the mean molecular gas mass of the SFGs in different ΔMS. We selected our mass-complete sample of SFGs in the Cosmic Evolution Survey (COSMOS) field using their latest optical-to-near-infrared catalog (i.e., the COSMOS2020 catalog; Weaver et al. 2021) and the super-deblended far-infrared-to-millimeter catalog of Jin et al. (2018). These SFGs were then subdivided into different stellar mass and ΔMS bins. In each bin, we performed a *uv*-domain stacking analysis on the ALMA band 6 and 7 dataset and measured their mean molecular gas mass and size. This allowed us to constrain the KS relation for a mass-complete ($> 10^{9.5}\,M_\odot$) sample of galaxies probing a wide range of ΔMS for the first time and thereby gain insights into the mechanisms that regulate the dispersion of the MS and that drive galaxies well above the MS. Finally, we compared the dust-obscured star-forming sizes of our MS galaxies to the size of their stellar component using data from the *Hubble* Space Telescope (*HST*) and UltraVISTA. This allowed us to better understand the processes leading to the structural evolution of SFGs (e.g., Wilman et al. 2020). We verified, in particular, if the recent finding of compact star-forming regions relative to the mass-size relation of late type galaxies with ALMA (e.g., Ikarashi et al. 2015; Simpson et al. 2015; Hodge et al. 2016; Fujimoto et al. 2017; Elbaz et al. 2018; Lang et al. 2019; Rujopakarn et al. 2019; Puglisi et al. 2019; Chang et al. 2020; Chen et al. 2020; Franco et al. 2020; Tadaki et al. 2020; Puglisi et al. 2021; Gómez-Guijarro et al. 2022a; Wang et al. 2022) is due to dust attenuation biasing current measurements of the mass-size relation at high redshift or not.

Our paper is organized as follows. Sect. 2 introduces our mass-complete sample of SFGs and their ALMA, *HST*, and UltraVISTA observations; Sect. 3 details the stacking method used to measure their mean molecular gas masses, star-forming sizes, and stellar sizes; Sect. 4 presents our results, and Sect. 5 discusses the implication of our findings; finally, Sect. 6 presents our conclusions.

We assumed a flat Λ cold dark matter cosmology with $H_0 = 67.8$ km s^{-1} Mpc^{-1}, $\Omega_{\rm M} = 0.308$, and $\Omega_\Lambda = 0.692$ (Planck Collaboration et al. 2016). A Chabrier (2003) initial mass function is assumed for all stellar masses and SFRs.

2. Data

2.1. Parent sample and ALMA data

The latest optical-to-near-infrared catalog in the COSMOS field, i.e., the COSMOS2020 catalog (Weaver et al. 2021), provides accurate photometry, photometric redshift, stellar mass, and SFR measurements for more than 966,000 sources. The astrometry of all these sources is aligned to *Gaia,* and their photometry were obtained using a new photometric extraction tool (`THE FARMER`). This catalog provides highly reliable photometric redshift even for faint galaxies, that is, with a redshift precision ($\Delta z/(1+z)$) of 0.036 for galaxies with an i-band apparent magnitude between 25.0 and 27.0.

We selected galaxies at $1.2 \leq z < 1.6$ in `THE FARMER` catalog. Then, we classified galaxies into star-forming and quiescent galaxies following the standard rest-frame near-ultraviolet-r/r-J selection method from Ilbert et al. (2013) and selected only the SFGs. We excluded galaxies below the mass-completeness limit of the COSMOS2020 catalog, which is $10^{8.5} M_\odot$ at $z \sim 1.2$ and $\sim 10^{8.7} M_\odot$ at $z \sim 1.6$. In addition, we excluded galaxies classified as active galactic nuclei (AGNs) to avoid contamination. We excluded AGNs based on their X-ray luminosity ($L_X \geq 10^{42}$ erg s^{-1}; Szokoly et al. 2004) and the latest COSMOS X-ray catalog of Marchesi et al. (2016). We then excluded galaxies classified as AGNs from their optical SED using the catalog of Stemo et al. (2020). Finally, we excluded galaxies classified as radio AGNs in the VLA-COSMOS 3 GHz AGN catalog (Delvecchio et al. 2017). This parent sample of SFGs at $1.2 \leq z < 1.6$ contains 62,681 galaxies.

The A^{3}COSMOS dataset (Liu et al. 2019b) gathers all ALMA archive projects available in the COSMOS field, making it ideal for studying the dust RJ-tail luminosity emitted by galaxies, which is a proxy of their molecular gas content. In this work, we used the A^{3}COSMOS data version 20220105 (Adscheid et al. in prep.), i.e., all public COSMOS ALMA datasets released by the 5 January 2022. The A^{3}COSMOS database contains the ALMA calibrated measurement sets, the cleaned images, and a value-added catalogue, which gathers all the galaxies individually detected in these images (i.e., with a signal-to-noise ratio > 4.35 following Liu et al. 2019b). As stressed in Wang et al. (2022), the definition of weights on visibilities after ALMA cycle 2 is different from the definition of the previous ALMA cycle. Therefore, we only used the ALMA data from band 6 (~243 GHz) and band 7 (~324 GHz) that were observed after ALMA cycle 2. We cross-matched our parent sample with the A^{3}COSMOS database, and excluded galaxies that were not covered by any ALMA observations, i.e., those located in regions with a primary beam response under 0.5. This reduces our sample to 1,971 galaxies. Finally, in order to avoid contamination from bright nearby sources during our stacking analysis, we excluded galaxy pairs (< 2.″0) with $S^1_{\rm ALMA}/S^2_{\rm ALMA} > 2$ or $M^1_\star/M^2_\star > 3$[1]. There are 1,688 galaxies in this final sample.

The SFR of our galaxies was obtained following Kennicutt (1998b) for a Chabrier (2003) initial mass function,

$$\mathrm{SFR_{UV+IR}[M_\odot\,yr^{-1}]} = 1.09\times10^{-10}(L_{\rm IR}[\mathrm{L_\odot}]+3.3\times L_{\rm UV}[\mathrm{L_\odot}]), \quad (1)$$

where the rest-frame $L_{\rm UV}$ at 2300Å was taken from the COSMOS2020 catalog, and the rest-frame $L_{\rm IR} = L(8-1000\,\mu\mathrm{m})$ was calculated by following the ladder of SFR indicator as advocated by Wuyts et al. (2011); i.e., we used the best infrared luminosity indicator available for each galaxy. To this end, we used the mid-infrared (MIR) and far-infrared (FIR) photometry from the super-deblended catalog (Jin et al. 2018), which provides *Spitzer* and *Herschel* photometries without contamination from nearby sources by iteratively deblending source emission with prior information, SED prediction, and residual source detection techniques. For galaxies with FIR and MIR photometry, their $L_{\rm IR}$ was obtained by fitting their MIR and/or FIR SED with the template of Chary & Elbaz (2001) (see details in Sect. 2.2 of Wang et al. (2022)). For galaxies without any MIR or FIR photometry, their SFRs were taken directly from the COSMOS2020 catalog. We note that Wang et al. (2022) have verified that the SFRs obtained from UV+IR measurements agree with the COSMOS2020 SFRs at intermediate SFRs (see their Fig. 2.), i.e., where the MIR/FIR detection rate of galaxies starts to decrease. From the SFR and stellar mass of each of our galaxies, we measured their offset from the MS, i.e., $\Delta\mathrm{MS} = \log(\mathrm{SFR}(z, M_\star)/\mathrm{SFR_{MS}}(z, M_\star))$, using the MS calibration of Leslie et al. (2020).

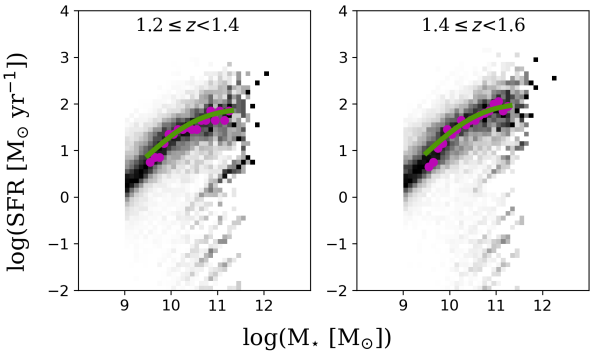

Fig. 1. Number density of galaxies from COSMOS2020 catalog in SFR-$M_\star$ plane, with SFRs determined by the approach used in our study. The darkest color indicates the highest number density of galaxies for a given stellar mass, which is further highlighted by purple circles in the stellar mass range of $10^{9.5} M_\odot \leq M_\star < 10^{11.3} M_\odot$. These number density peaks correspond to the MS for our SFR tracer and can be compared to the MS from Leslie et al. (2020, green solid lines), where the SFRs were measured from three GHz radio-continuum observations.

The SFR indicator used in our study differs from that of Leslie et al. (2020), who used 3 GHz radio-continuum to measure the SFR of their SFG. In Fig. 1, we show a test we did to determine whether these different SFR indicators could introduce bias into our study, and in particular lead to different definitions of the MS. To this end, we selected all $M_\star \geq 10^{9.0} M_\odot$ galaxies with $1.2 \leq z < 1.6$ in the COSMOS2020 catalog and calculated their SFR based on the ladder of SFR indicators used in our study. At $10^{9.5} M_\odot \leq M_\star < 10^{11.3} M_\odot$, we then defined the peak of the number density of galaxies at each stellar mass (purple circles in Fig. 1) as "our" MS. Finally, we compared our MS with that of Leslie et al. (2020, green solid lines in Fig. 1) and found an average offset of 0.02 dex and no offset greater than 0.2 dex in any of our specific stellar mass bins. This demonstrates that the use of the MS from Leslie et al. is appropriate and leads to accurate measurements of ΔMS.

2.2. HST and UltraVISTA data

We studied the size of the stellar component of our galaxies using their optical-to-near-infrared emission. First, we used the *HST*/Advanced Camera for Surveys (ACS) i-band images of Koekemoer et al. (2007) and Massey et al. (2010). The *HST*/ACS

[1] 1 and 2 denote the brighter and fainter objects in a pair system.

i band has a wavelength centered at 8,333 Å and a PSF full width at half maximum ($FWHM$) of 0.095 arcsec. At the redshift of our galaxies, this corresponds to the rest-frame wavelength of ~3,470 Å and thus traces the near UV emitted by young O/B stars. Second, we used the Ultra Visible and Infrared Survey Telescope for Astronomy (UltraVISTA) J- and K_s-band images of McCracken et al. (2012). The UltraVISTA J and K_s bands have wavelengths centered on 12,525 and 21,557 Å. At the redshift of our galaxies, these images correspond to the rest-frame wavelengths of ~5,210 Å and ~8,980 Å and thus trace the bulk of the stellar population of these galaxies. Because VISTA is a ground-based telescope, there is variation of the seeing across the mosaics. However, McCracken et al. (2012) stressed that such seeing variation is small (~0.05 arcsec) compared to the average seeing. In our paper, we thus used the PSF $FWHM$s of McCracken et al. (2012), which are 0.77 and 0.78 arcsec for the J and K_s bands, respectively.

3. Method

The high-sensitivity of ALMA has revolutionized our ability to measure the gas content (from RJ dust continuum emission) of high-stellar-mass, high-ΔMS, and low-redshift galaxies. However, with the time restriction of each ALMA project, galaxies at high redshift, low stellar mass, and low ΔMS remain difficult to detect individually with ALMA (e.g., see Table 1 of Wang et al. (2022)). To statistically measure the mean value of our mass-complete sample of SFGs at z ~1.4, we therefore used a stacking analysis. However, stacking the A^{3}COSMOS dataset is a challenge because the different ALMA projects were observed at different frequencies and spatial resolutions (e.g., Wang et al. 2022). On the contrary, stacking the *HST* or UltraVISTA datasets is straightforward because each of these datasets corresponds to only one frequency and one angular resolution. Below, we describe the steps to perform the uv-domain stacking analysis on our ALMA data and the steps to perform the image-domain stacking analysis on the *HST* and UltraVISTA data.

3.1. The stacking analysis

We followed the same approach as Wang et al. (2022) to perform the uv-domain stacking analysis of our ALMA dataset. Details regarding these steps can be found in their Sects. 3.1 and 3.2. We first scaled the observed ALMA visibility amplitudes of each galaxy to its rest-frame luminosity at 850 μm (i.e., $L_{850}^{\rm rest}$) using the SED templates of Béthermin et al. (2012) and the Common Astronomy Software Applications package (CASA; McMullin et al. 2007) tasks `gencal` and `applycal`. In practice, this scaling was performed using both the MS and SB galaxy SED templates of Béthermin et al. (2012). Then, for a galaxy with ΔMS <0.4, we kept the scaling obtained with the MS galaxy SED template; for a galaxy with ΔMS > 0.7, we kept that measured with the SB galaxy SED template; and, finally, for a galaxy with 0.4 < ΔMS < 0.7, we used a linear interpolation in the log-space between the MS and SB galaxy SED template scalings. For each galaxy, we then shifted the phase center of its visibilities to its coordinates by using a CASA based package: the `STACKER` (Lindroos et al. 2015). The visibilities of the galaxies in each $M_\star$–ΔMS bin were then stacked together using the CASA task `concat`. The cleaned image was generated from the stacked measurement set with the CASA task `tclean` using Briggs $n = 2$ weighting and cleaning the image down to 3σ. Finally, we measured the stacked $L_{850}^{\rm rest}$ and its beam-deconvolved distribution with the CASA task `uvmodelfit` (uv-domain) and the Python Blob Detector and Source Finder (`PyBDSF`) package (Mohan & Rafferty 2015) (image-domain). Both `uvmodelfit` and `PyBDSF` fit a single Gaussian component to the source. We express the mean size of the stacked galaxies in the form of circularized radii, $R_{\rm eff}^{\rm circ}$:

$$R_{\rm eff}^{\rm circ} = R_{\rm eff} \times \sqrt{\frac{b}{a}}, \tag{2}$$

where b/a is the axis ratio measured with `uvmodelfit` or `PyBDSF` and $R_{\rm eff}$ is the effective radius (following Murphy et al. (2017) and Jiménez-Andrade et al. (2019), $R_{\rm eff} \approx FWHM_{\rm Gaussian}/2.43$, where $FWHM_{\rm Gaussian}$ is the beam deconvolved $FWHM$ of the single Gaussian component fitted to the source).

We followed the standard resampling method from Wang et al. (2022) to derive the uncertainties in these $L_{850}^{\rm rest}$ and size measurements (see their Sect. 3.2). This gives us the uncertainties from both the instrumental noise and the intrinsic distribution of the stacked population. These uncertainties are marked as thin error bars in the following figures. We also measured the uncertainties from the instrumental noise alone by simulating galaxies with the same $L_{850}^{\rm rest}$ and size measured in each stacked $M_\star$–ΔMS bin. These simulated galaxies were placed at 3.″0 from the phase center in each realization of our resampling method. Then, by measuring the physical properties of these simulated galaxies, we obtained the uncertainties from the instrumental noise alone. This uncertainty is marked by thick error bars in the following figures.

To obtain the mean molecular gas mass of each $M_\star$–ΔMS bin, we first converted their stacked $L_{850}^{\rm rest}$ to dust mass. This was performed by scaling the MS and SB galaxy SED templates of Béthermin et al. (2012) to the stacked $L_{850}^{\rm rest}$, calculating the corresponding $L_{\rm IR}$, and applying the $L_{\rm IR}$-to-dust mass conversion provided by Béthermin et al. (2012) for each of these SED templates. Then, for bins with ΔMS <0.4, we kept the dust mass measured with the MS galaxy SED template; for bins with ΔMS > 0.7, we kept that measured with the SB galaxy SED template; and, finally, for bins with 0.4 < ΔMS < 0.7, we used a linear interpolation in the log-space between the MS and SB galaxy SED template measurements. Because these dust mass measurements considered the ΔMS of each bin, it takes into account the different dust grain temperatures within MS and SB galaxies. We then converted these dust masses into molecular gas masses using the gas-to-dust mass ratio versus metallicity relation of Leroy et al. (2011), i.e., $\delta_{\rm GDR}$ method:

$$\log(M_{\rm mol}) = \log(M_{\rm dust}) + 9.4 - 0.85 \times (12 + \log({\rm O/H})), \tag{3}$$

where the gas-phase metallicity, 12+log(O/H), was obtained following the redshift- and stellar mass-dependent relation given in Liu et al. (2019a):

$$12 + \log({\rm O/H}) = \begin{cases} a & \text{if } \log(M_\star/M_\odot) \geq b(z), \\ a - 0.087 \times (\log(M_\star/M_\odot) - b(z))^2, & \text{else,} \end{cases} \tag{4}$$

where a=8.74 and $b(z)$=10.4+4.46×log(1+z)-1.78×(log(1+z))^2.

As mentioned above, images in the COSMOS field obtained by the *HST* or UltraVISTA telescope have uniform sensitivity and PSF. In these cases, stacking in the image domain is straightforward and appropriate. For each telescope, we stacked the images using the noise-weighted method:

$$I_{\rm stack} = \frac{\Sigma\, I_i\, \sigma_i^{-2}}{\Sigma \sigma_i^{-2}}, \tag{5}$$

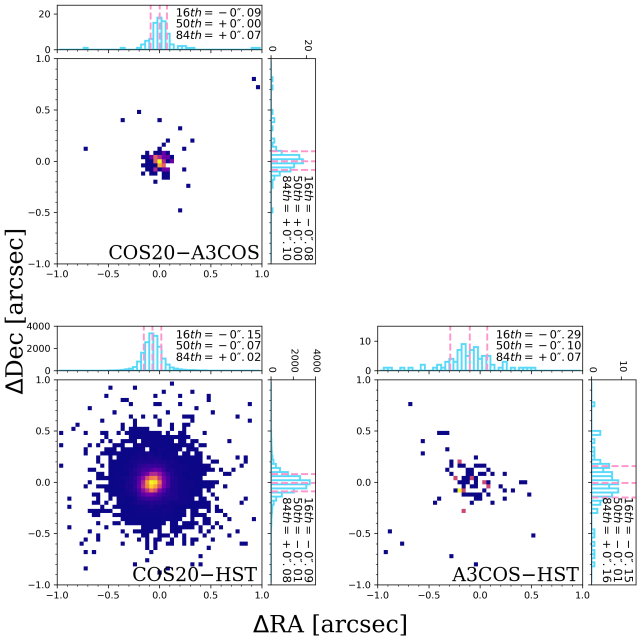

Fig. 2. Astrometric offsets between COSMOS-2020 (Weaver et al. 2021), *HST*-ACS-COSMOS (Leauthaud et al. 2007), and A^{3}COSMOS catalogs (Liu et al. 2019b). Each panel shows the R.A. and Dec. offset distribution for sources presented in both catalogs. The top and right axes of each panel display the histograms of these R.A. and Dec. offsets. Pink dashed vertical lines are the 16th, 50th, and 84th percentiles of each distribution.

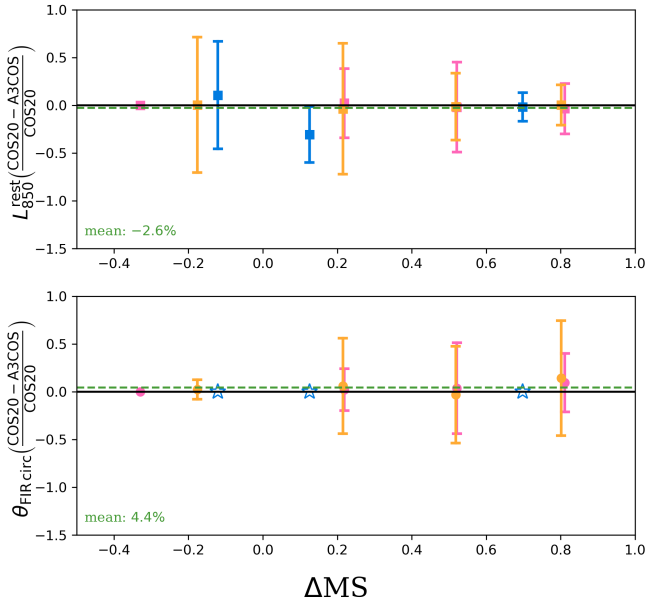

Fig. 3. Relative differences on rest-frame 850μm luminosity ($L_{850}^{\rm rest}$) and FIR beam-deconvolved size of the stacked galaxies based on astrometry from the COSMOS-2020 catalog (Weaver et al. 2021) or A^{3}COSMOS catalog (Liu et al. 2019b). Squares show the relative difference on the stacked $L_{850}^{\rm rest}$. Circles display the relative difference on the FIR size for the resolved stacked galaxies, while stars show the bins where the stacks are spatially unresolved (i.e., point sources). Symbols are color-coded by stellar mass, i.e., pink for $10^{11} \leq M_\star/{\rm M}_\odot < 10^{12}$, orange for $10^{10.5} \leq M_\star/{\rm M}_\odot < 10^{11}$, and blue for $10^{10} \leq M_\star/{\rm M}_\odot < 10^{10.5}$. The green dashed lines are the average uncertainties in each panel, while values are given on the bottom left of each panel. Overall, using either optically-based or (sub)millimeter-based positions in stacking analysis yields consistent results.

where $I_{\rm stack}$ is the pixel intensity in the stacked image, I_i is the pixel intensity of the i-th galaxies, and σ_i is the pixel noise of the i-th galaxies. We compare the radial profile of the stacked ALMA, *HST*, and UltraVISTA images in Sect. 4.2.

3.2. Uncertainties from the mismatch of position and selection of astrometry

The use of accurate galaxy coordinates is critical for obtaining high-quality results from our stacking analysis. In Fig. 2, we compare the astrometry offset between sources in the COSMOS2020 and *HST*-ACS-COSMOS catalog and show a 0.07 arcsec offset in R.A. This systematic offset is not due to an intrinsic mismatch between the *HST* and COSMOS2020 emitting regions of our galaxies, but rather a misalignment between the astrometric references of the two catalogs. Despite being small, this misalignment is still larger than the PSF size of the stacked *HST* image and cannot be neglected. To account for this, a 0.07 arcsec offset in R.A. was taken into consideration when we performed the image-domain stacking analysis on the *HST* i-band image.

A possible intrinsic mismatch of $\sim 0\farcs2$ between the optical and FIR emitting regions of SFGs was reported in some literature studies (e.g., Elbaz et al. 2018). This would translate into a dispersion between the FIR and optical positions of SFGs and could lead to artificially large FIR sizes when stacking the FIR data using optical positions. We investigated the existence of such systematic positional mismatch by comparing the astrometry of the COSMOS2020 catalog (optical-based; positions used in our ALMA stacking analysis) and A^{3}COSMOS catalog (Liu et al. 2019b, (sub)millimeter-based) in Fig. 2. We find that the positional dispersions between these catalogs is relatively small compared to the beam size of our stacked ALMA dataset (i.e., dispersion < 1/3 $FWHM$ of the typical ALMA stacked beam). We then studied the impact of this dispersion on our results further by repeating our stacking analysis but limiting it to the source individually detected by ALMA and using their A^{3}COSMOS position instead of their COSMOS2020 position. We find that using the A^{3}COSMOS positions changes by their measured stacked luminosities and sizes (Fig. 3) at most 5%, which is relatively little compared to our uncertainties. Based on this finding, we conclude that the mismatch between the optical-based position and (sub)millimeter-based position would only have a minor effect on the FIR luminosities and sizes inferred from our stacking analysis.

4. Results

4.1. Molecular gas content and star-forming size

The results of our ALMA stacking analysis are shown in Fig. 4 and Fig. 5 and are summarized in Tab. 1. In high $M_\star$–ΔMS bins, i.e., $M_\star > 10^{10.5} M_\odot$ and $\Delta{\rm MS} > 0.4$, more than 60% of the stacked sources are detected individually by ALMA. The stacks for these bins thus yield a detection with a high signal-to-noise ratio, i.e., S/N>17. The detection rate ($N_{D\,{\rm ALMA}}/N$) decreases with decreasing stellar mass and ΔMS, reaching a minimum of 0% in our lowest stellar mass bins. Our stacking analysis allows, however, for the detection at reasonable significance (i.e., S/N >

Table 1. Molecular gas mass and size properties of the stacked galaxies.

$M_\star$	ΔMS	N	$N_{D\,\mathrm{ALMA}}$	$\langle z \rangle$	$\langle M_\star \rangle$ $\log_{10}\mathrm{M}_\odot$	$\langle \Delta\mathrm{MS} \rangle$	$\langle L^{\mathrm{rest}}_{850-uv} \rangle$ $10^{30}\,\mathrm{erg\,s^{-1}\,Hz^{-1}}$	$\mathrm{S/N_{peak}}$	$M_{\mathrm{mol-uv}}$ $\log_{10}\mathrm{M}_\odot$	$M_{\mathrm{mol-py}}$ $\log_{10}\mathrm{M}_\odot$	$\theta^{\mathrm{circ}}_{\mathrm{beam}}$ arcsec	$\theta^{\mathrm{circ}}_{\mathrm{decon.-uv}}$ arcsec	$\theta^{\mathrm{circ}}_{\mathrm{decon.-py}}$ arcsec	$R^{\mathrm{circ}}_{\mathrm{eff-uv}}$ kpc	$R^{\mathrm{circ}}_{\mathrm{eff-py}}$ kpc
(1)	(2)	(3)	(4)	(5)	(6)	(7)	(8)	(9)	(10)	(11)	(12)	(13)	(14)	(15)	(16)
$11.0 \leq \log_{10} M_\star < 12.0$	$0.7 \leq \Delta\mathrm{MS} < 1.1$	5	5	1.38	11.25	0.81	$11.4_{\pm 2.6}$	27	$11.0_{\pm 0.1}$	$11.0_{\pm 0.1}$	0.61	0.26	0.32	$0.9_{\pm 0.3}$	$1.1_{\pm 0.3}$
	$0.4 \leq \Delta\mathrm{MS} < 0.7$	26	23	1.40	11.29	0.54	$7.5_{\pm 1.0}$	46	$10.8_{\pm 0.1}$	$10.8_{\pm 0.1}$	0.51	0.31	0.37	$1.1_{\pm 0.1}$	$1.3_{\pm 0.1}$
	$0.0 \leq \Delta\mathrm{MS} < 0.4$	28	16	1.36	11.27	0.20	$4.0_{\pm 0.9}$	24	$10.7_{\pm 0.1}$	$10.8_{\pm 0.1}$	0.52	0.48	0.51	$1.7_{\pm 0.3}$	$1.8_{\pm 0.3}$
	$-0.6 \leq \Delta\mathrm{MS} < 0.0$	8	1	1.43	11.26	-0.30	$2.6_{\pm 1.9}$	17	$10.6_{\pm 0.3}$	$10.6_{\pm 0.3}$	0.94	0.44	0.49	$1.6_{\pm 1.2}$	$1.7_{\pm 1.2}$
$10.5 \leq \log_{10} M_\star < 11.0$	$0.7 \leq \Delta\mathrm{MS} < 1.0$	6	5	1.45	10.83	0.80	$6.3_{\pm 1.6}$	21	$10.8_{\pm 0.1}$	$10.8_{\pm 0.1}$	0.68	0.20	0.34	$0.7_{\pm 0.6}$	$1.2_{\pm 0.6}$
	$0.4 \leq \Delta\mathrm{MS} < 0.7$	10	6	1.31	10.78	0.50	$5.8_{\pm 1.2}$	17	$10.7_{\pm 0.1}$	$10.8_{\pm 0.1}$	0.66	0.27	0.35	$0.9_{\pm 0.4}$	$1.2_{\pm 0.4}$
	$0.0 \leq \Delta\mathrm{MS} < 0.4$	49	8	1.35	10.74	0.17	$1.8_{\pm 1.2}$	16	$10.5_{\pm 0.3}$	$10.5_{\pm 0.3}$	0.69	0.40	0.48	$1.4_{\pm 0.3}$	$1.7_{\pm 0.3}$
	$-0.7 \leq \Delta\mathrm{MS} < 0.0$	41	3	1.34	10.71	-0.22	$1.2_{\pm 0.8}$	5	$10.3_{\pm 0.3}$	$10.5_{\pm 0.2}$	0.70	0.58	0.86	$2.0_{\pm 1.9}$	$3.0_{\pm 2.0}$
$10.0 \leq \log_{10} M_\star < 10.5$	$0.4 \leq \Delta\mathrm{MS} < 0.9$	11	1	1.39	10.19	0.72	$1.4_{\pm 0.4}$	4	$10.3_{\pm 0.1}$	$10.4_{\pm 0.1}$	0.56	-	-	-	$< 2.0^{\dagger}$
	$0.0 \leq \Delta\mathrm{MS} < 0.4$	48	3	1.37	10.25	0.14	$0.9_{\pm 0.2}$	6	$10.2_{\pm 0.1}$	$10.4_{\pm 0.1}$	0.87	0.56	0.85	$2.0_{\pm 1.4}$	$3.0_{\pm 1.4}$
	$-0.7 \leq \Delta\mathrm{MS} < 0.0$	82	1	1.38	10.22	-0.28	$0.6_{\pm 0.3}$	4	$10.1_{\pm 0.2}$	$10.2_{\pm 0.2}$	0.73	0.91	1.00	$3.2_{\pm 1.6}$	$3.5_{\pm 1.6}$
$9.5 \leq \log_{10} M_\star < 10.0$	$0.4 \leq \Delta\mathrm{MS} < 1.3$	20	0	1.40	9.69	0.59	$0.6_{\pm 0.4}$	4	$10.1_{\pm 0.3}$	$10.2_{\pm 0.3}$	1.14	-	-	-	$< 4.0^{\dagger}$
	$0.0 \leq \Delta\mathrm{MS} < 0.4$	74	0	1.34	9.73	0.18	$0.4_{\pm 0.2}$	4	$10.0_{\pm 0.2}$	$9.9_{\pm 0.2}$	1.07	-	-	-	$< 3.8^{\dagger}$
	$-0.7 \leq \Delta\mathrm{MS} < 0.0$	129	0	1.38	9.72	-0.29	$< 0.3^{\dagger\dagger}$	-	-	$< 10.0^{\dagger\dagger}$	0.61	-	-	-	-

Notes. (1) Stellar mass bin, (2) ΔMS bin, (3) number of stacked galaxies, (4) number of individually detected stacked galaxies, (5) mean redshift, (6) mean stellar mass, (7) mean ΔMS, (8) mean L^{rest}_{850} inferred from the *uv*-domain, (9) peak S/N on the image, (10) mean molecular gas mass inferred from the *uv*-domain, and (11) from the image-domain, (12) circularized synthesized beam $FWHM$, (13) circularized deconvolved $FWHM$ from the *uv*-domain, and (14) from the image-domain, (15) circularized half-light radii from the *uv*-domain, and (16) from the image-domain.
†Size upper limit inferred from its circularized synthesized beam $FWHM$.
†† L_{850} and molecular gas mass upper limit inferred from the 5σ noise on the image.

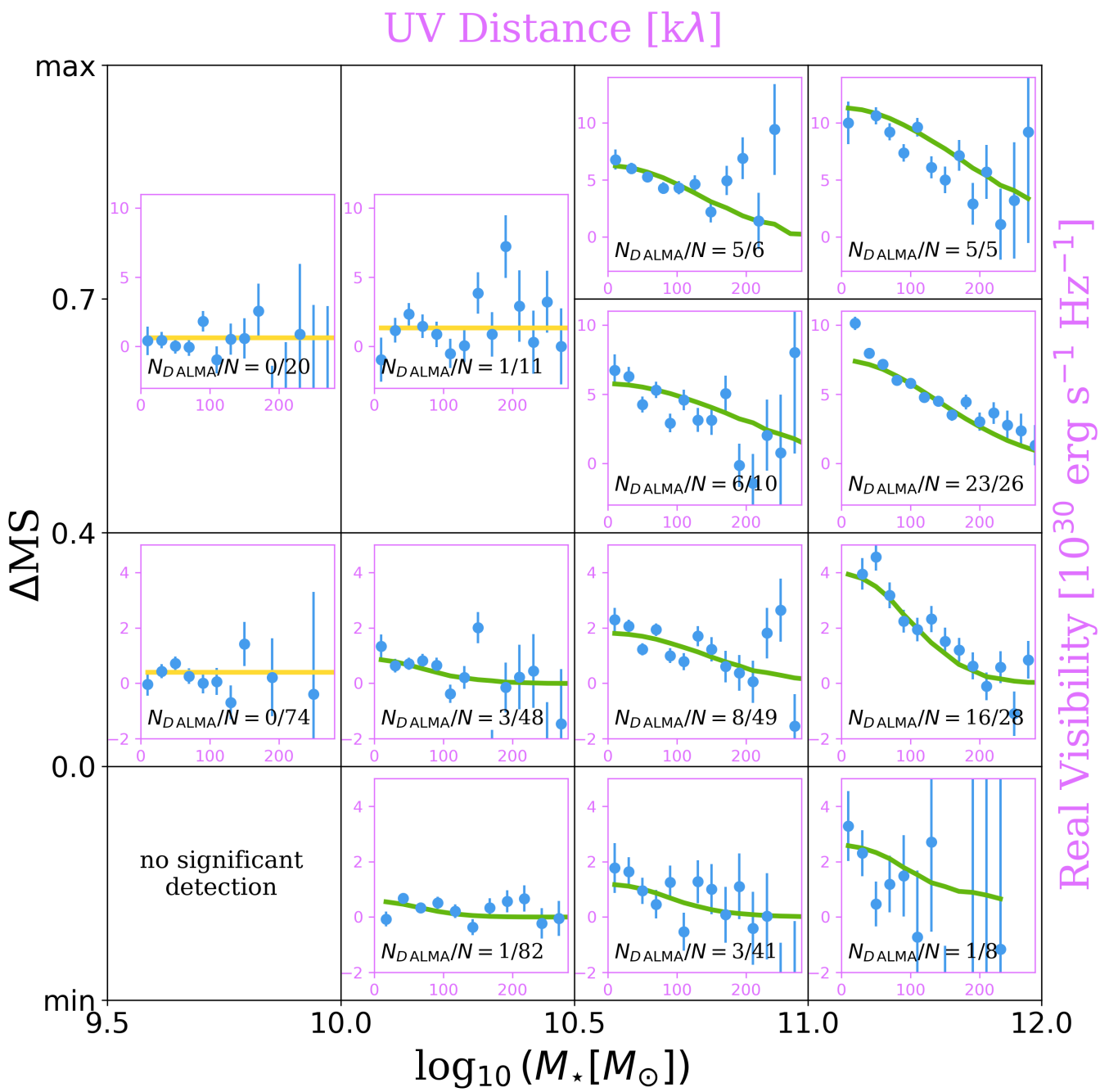

Fig. 4. Results in *uv*-domain of our ALMA stacking analysis. In each panel, a single component model (green solid line for Gaussian profile and yellow solid line for point source) has been fit to the mean visibility amplitudes (blue filled circles) using the CASA task `uvmodelfit`. The maximun values of ΔMS from the lowest to highest stellar mass bins are 1.3, 0.9, 1.0, and 1.1; and the minimum values from the lowest to highest stellar mass bins are -0.7, -0.7, -0.7, and -0.6, respectively. The number of individually detected galaxies in the ALMA archival images ($N_{D\,\mathrm{ALMA}}$) and the number of stacked galaxies (N) is also reported in each panel.

4) in most of these low $M_\star$–ΔMS bins. Yet, there is no significant detection in the lowest stellar mass and ΔMS bin, i.e., $10^{9.5} M_\odot \leq M_\star < 10^{10.0} M_\odot$ and ΔMS < 0. For this bin, we instead infer an 5σ upper limit on the mean molecular gas mass.

In the *uv* domain, most of the stacked visibilities are well fit by an elliptical Gaussian component, except for our lowest stellar mass bins and the highest ΔMS bin at $10^{10.0} M_\odot \leq M_\star < 10^{10.5} M_\odot$. Indeed, for the latter, a fit with an elliptical Gaussian component with `uvmodelfit` led to an axis ratio with a value close to 0. These bins have instead the properties of a point source, as also suggested by the relatively constant value of their visibility amplitude as a function of the *uv* distance. For these bins, we simply fit a point-source model and conservatively used their circularized synthesized beam $FWHM$ as an upper limit to their FIR size.

Finally, we note that the mean molecular gas mass and size measured by `uvmodelfit` in the *uv* domain and by `PyBDSF` in the image domain are in agreement within the uncertainties (see

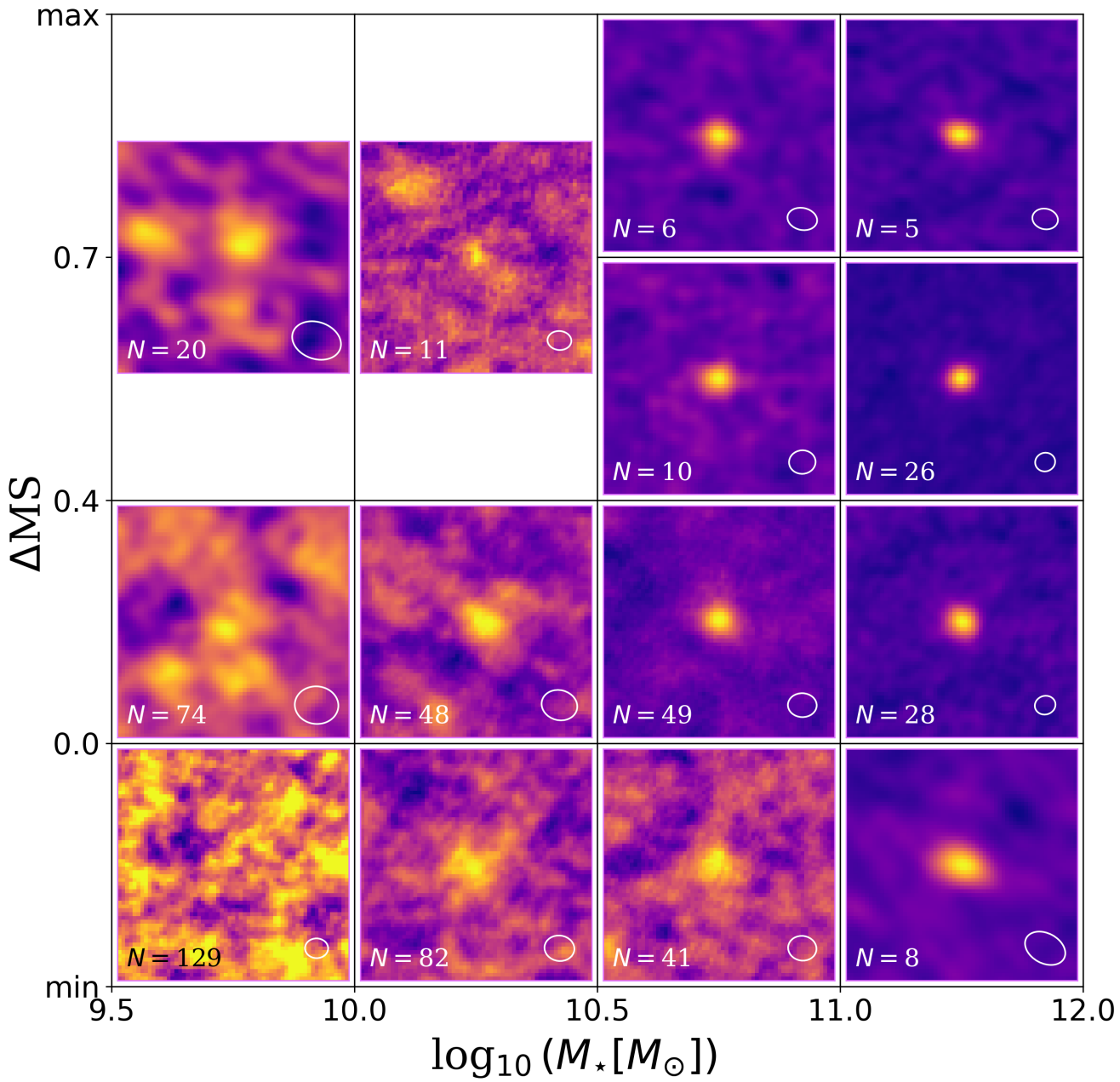

Fig. 5. Results in image-domain of our ALMA stacking analysis in *uv*-domain. The maximun values of ΔMS from the lowest to highest stellar mass bins are 1.3, 0.9, 1.0, and 1.1; and the minimum values from the lowest to highest stellar mass bins are -0.7, -0.7, -0.7, and -0.6, respectively. Each panel has a size of 6 arcsec × 6 arcsec. The synthesized beam of the image is shown in the right-bottom corner of each panel.

Tab. 1). Such an agreement is perfectly in line with the findings and simulations presented in Wang et al. (2022).

4.1.1. Molecular gas fraction and depletion time of SFGs

The mean molecular gas fraction ($\mu_{\rm mol}$=$M_{\rm gas}/M_\star$) and mean molecular gas depletion time ($\tau_{\rm mol}$=$M_{\rm gas}$/SFR) of our stacked galaxies for different ΔMSs are shown in Fig. 6 and Fig. 7, respectively, along with the analytical relations of Liu et al. (2019a), Tacconi et al. (2020), and Wang et al. (2022). Our measurements show that the mean molecular gas fraction of galaxies increases by a factor of ∼2.1 from MS galaxies (ΔMS∼0) to SB galaxies (ΔMS∼0.8), and the mean molecular gas depletion time decreases by a factor of ∼3.3 from MS galaxies to SB galaxies. These findings are consistent with those of Scoville et al. (2023), who find that the mean molecular gas fraction increases by a factor of ∼1.7 from MS galaxies to SB galaxies, while the mean molecular gas depletion time decreases by a factor of ∼3.7. These findings suggest that the variation in star formation efficiency ($1/\tau_{\rm mol}$) and the variation in gas content are roughly similar when galaxies move from being MS to SB. Meanwhile, the mean molecular gas fraction of galaxies increases by a factor of

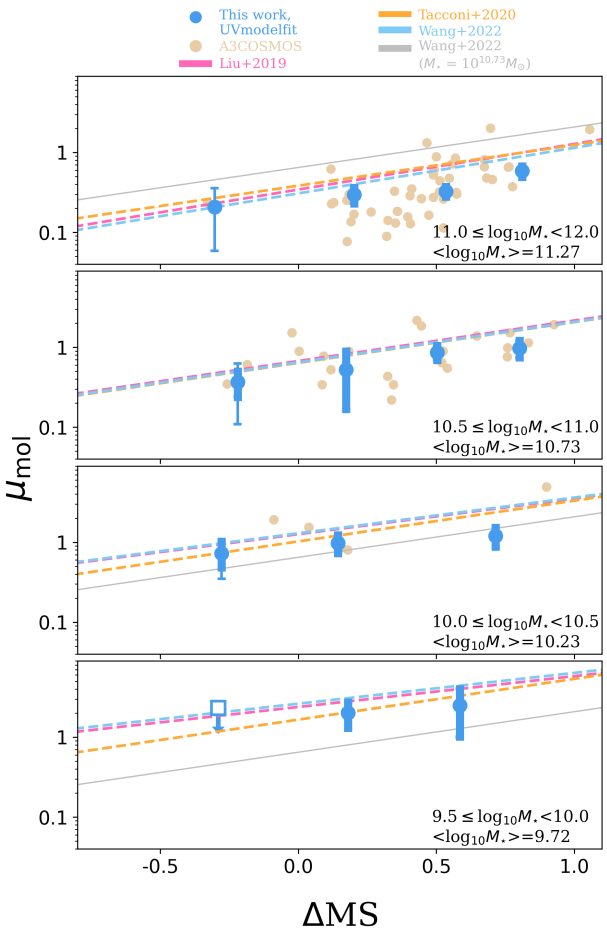

Fig. 6. Molecular gas fraction (i.e., $\mu_{\rm mol} = M_{\rm gas}/M_\star$) of SFGs at z ~1.4 as a function of their distance to the MS (i.e., ΔMS) and their stellar mass. Blue circles show the mean molecular gas fraction from our work. The square displays the upper limit for the bin with no detection in both the *uv* domain and image domain. The thick error bars display the instrumental uncertainty in each bin, while the thin error bars show the total uncertainty, i.e., including both the instrumental noise and the uncertainties due to the intrinsic dispersion of the molecular gas fraction within the stacked population. Salmon-colored circles represent individually detected galaxies taken from the latest A^{3}COSMOS catalog ($S/N > 4.35$; Adscheid et al. in prep.), applying the same method used here to convert these flux densities into molecular gas mass. Dashed lines display the analytical relations of the molecular gas fraction at different stellar mass and ΔMS from Liu et al. (2019a, pink), Tacconi et al. (2020, orange), and Wang et al. (2022, blue). Gray lines show the analytical relation from Wang et al. (2022) at $M_\star = 10^{10.73} M_\odot$ as a reference, which is the same stellar mass as in the second panel.

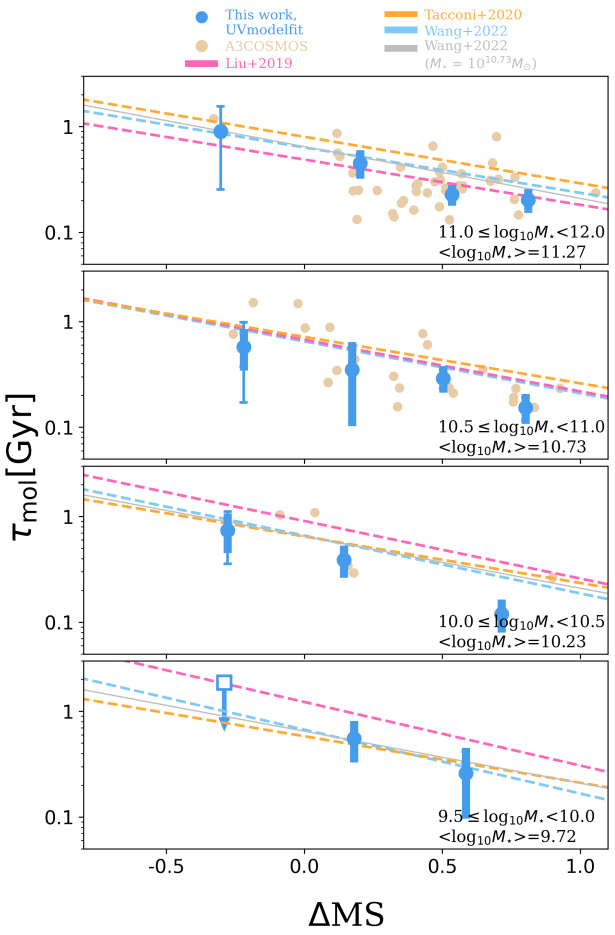

Fig. 7. Same as Fig. 6, but for the molecular gas depletion time (i.e., $\tau_{\rm mol} = M_{\rm gas}/{\rm SFR}$).

~1.4 across the MS (-0.2 < ΔMS < 0.2), and the mean molecular gas depletion time decreases by a factor of ~1.8 across the MS. Our findings indicate that the change of gas content and star formation efficiency play again roughly a similar role when SFGs oscillate within the MS. This disagrees with the findings of Sargent et al. (2014), who found that the oscillation is mainly due to variations in their gas content. This discrepancy likely comes from the fact that the "2-star formation mode" model of Sargent et al. (2014) was fit to a relatively small number of data points, mixing different redshifts and stellar masses and restricting the variation of the depletion time of MS galaxies to their SFR. Finally, we find that the mean molecular gas fraction of galaxies decreases by a factor of ~7 from $M_\star \sim 10^{9.7} M_\odot$ to $\sim 10^{11.3} M_\odot$, while their mean molecular gas depletion time does not change with stellar mass. Our results support the scenario that the bending of the MS at z ~1.4, which at this redshift appears at $M_\star > 10^{10.5} M_\odot$, is due to a variation in the cold gas accretion of these galaxies that decreases their gas fraction (e.g., Daddi et al. 2022) rather than changes in their star formation efficiency.

Our mean molecular gas fraction for MS galaxies are in qualitative and quantitative agreement with the analytical relations of Liu et al. (2019a), Tacconi et al. (2020), and Wang et al. (2022). Regarding our mean molecular gas depletion time for MS galaxies, they are in agreement with the analytical relations of Tacconi et al. (2020) and Wang et al. (2022) at all stellar masses. However, our results only agree with the analytical relation of Liu et al. (2019a) for $M_\star > 10^{10.5} M_\odot$. Interestingly, our results on the mean molecular gas fraction agree with those of Liu et al. (2019a) at $M_\star < 10^{10.5} M_\odot$. The molecular gas depletion time being the ratio between the molecular gas mass and SFR, the discrepancy between our results and the analytical relation of Liu et al. (2019a) at $M_\star < 10^{10.5} M_\odot$ can only be explained by the use of different ${\rm SFR_{MS}}$ calibrations. We note that at $z \sim 1.4$ and $M_\star < 10^{10.5} M_\odot$, the results from Liu et al. (2019a) are mostly based on extrapolations.

Finally, we find that the slopes of the $\mu_{\rm mol}$ − ΔMS relations might be slightly shallower compared to those found in Liu et al. (2019a), Tacconi et al. (2020), and Wang et al. (2022); while the slopes of the $\tau_{\rm mol}$ − ΔMS relations appear to be slightly steeper

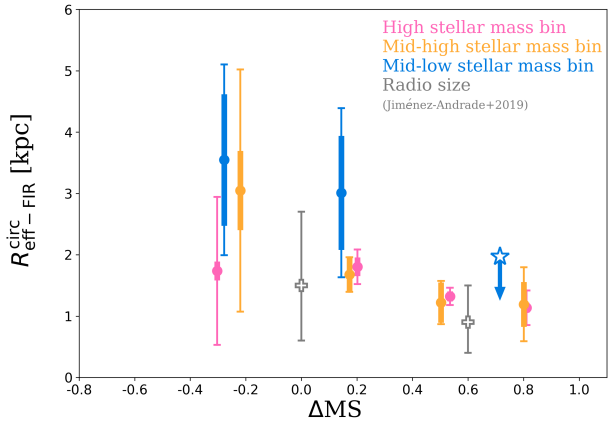

Fig. 8. Circularized effective FIR radius as a function of distance to the MS. Circles and stars show the mean and upper limit FIR sizes for the resolved and unresolved stacked galaxies, respectively. Error bars are the same as in Fig. 6, but for the circularized effective FIR radius. Crosses are the mean radio sizes of SFGs at $M_\star > 10^{10.5} M_\odot$ from Jiménez-Andrade et al. (2019).

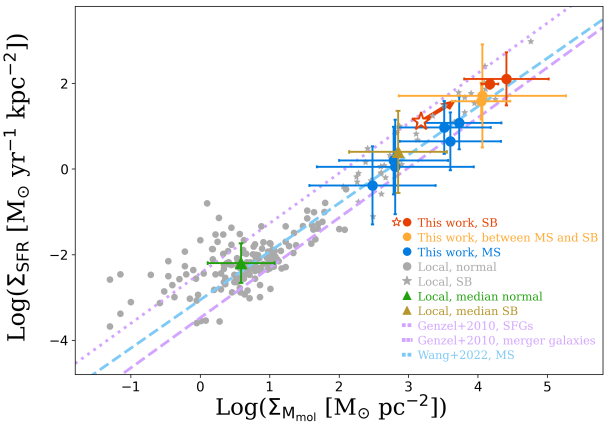

Fig. 9. Relation between SFR surface density ($\Sigma_{\rm SFR}$) and molecular gas mass surface density ($\Sigma_{\rm M_{mol}}$) of SFGs, i.e., the so-called KS relation. Blue, orange, and red circles represent our stacking results for MS galaxies, in between MS and SB galaxies, and SB galaxies, i.e., ΔMS < 0.4, $0.4 \leq$ ΔMS < 0.7, and $0.7 \leq$ ΔMS, respectively. The red star with the arrow is the lower limit of $\Sigma_{\rm SFR}$ and $\Sigma_{\rm M_{mol}}$ in our highest ΔMS and $10^{10.0} \leq M_\star/M_\odot < 10^{10.5}$ bin because their star-forming size is not resolved. Gray circles and stars are local normal and SB galaxies from Kennicutt (1998a) and de los Reyes & Kennicutt (2019). Green and brown triangles are the median values of these local normal and SB galaxies. The blue dashed line is the MS-only KS relation from Wang et al. (2022). Purple dashed and dotted lines are the KS relations for SFGs and mergers from Genzel et al. (2010).

compared to those found in the aforementioned studies. Specifically, while the slopes of the $\mu_{\rm mol}-\Delta$MS and $\tau_{\rm mol}-\Delta$MS relations in logarithm space are 0.51 and −0.49 in Tacconi et al. (2020), we found that slopes of ~ 0.40 and ~ -0.65 would provide a better fit to our measurements, respectively. As SFGs move from the MS to SB, their mean molecular gas fraction increases and the mean molecular gas depletion time decreases slightly more than anticipated by these analytical relations.

4.1.2. Star-forming size of SFGs

The circularized effective FIR size of our stacked galaxies in different $M_\star-\Delta$MS bins is shown in Fig. 8. Although still uncertain, these measurements suggest that the FIR size decreases from 2.5 kpc to 1.4 kpc when going from ΔMS∼0 to ΔMS∼0.8, especially when considering only the uncertainties from the instrumental noise (thick error bars in Fig. 8). This finding is in qualitative agreement with Jiménez-Andrade et al. (2019), who studied the radio size of massive ($>10^{10.5} M_\odot$) $z \sim 1.5$ SFGs as a function of ΔMS. SBs have thus more compact star-forming region compared to MS galaxies, potentially linked to the merger events that triggered them (see Sect. 4.2). Indeed, simulations suggest that galaxy mergers can trigger the inflow of gas towards the central region and create compact star-forming regions (e.g., Springel et al. 2005; Sparre & Springel 2016; Blumenthal & Barnes 2018; Byrne-Mamahit et al. 2023).

We also find that the relative dispersion of sizes within the SB population is smaller than within the MS population (see thin error bars in Fig. 8; see also Jiménez-Andrade et al. (2019)). A small size dispersion within the SB population may seem at odds with the diversity of orientation, size, and mass ratio that a merging system can have and thus the diversity of gas tidal tails or bridges it can exhibit. Our results therefore support a scenario in which the inflow of gas to a central, coalescent, and compact region is short during a merger, i.e., < 0.3 Gyr (e.g., Sparre et al. 2022). On the other hand, the relatively large size dispersion within the MS population, especially for the low ΔMS population, could indicate the presence of a hidden and compact SB population within the normal and extended MS galaxies (see also Elbaz et al. 2018; Jiménez-Andrade et al. 2019; Puglisi et al. 2021; Gómez-Guijarro et al. 2022b).

4.1.3. The Kennicutt-Schmidt relation

In Fig. 9, we show the relation between the SFR and molecular gas mass surface densities (the so-called KS relation) of our stacked galaxies by combining their SFR, molecular gas mass, and FIR size measurements. We also compare these measurements with results from the literature: molecular gas phase measurement of local normal and starburst galaxies from Kennicutt (1998a) and de los Reyes & Kennicutt (2019) and the KS relation for SFGs from Genzel et al. (2010) and Wang et al. (2022).

The KS relation of our stacked MS galaxies is fully consistent with the relation for SFGs from Genzel et al. (2010) and for MS-only galaxies from Wang et al. (2022). SBs roughly fall on the same KS relation as MS galaxies. Indeed, the increase of the mean star formation efficiency of SBs compared to MS galaxies (see Sect. 4.1.1) is in part explained by the combination of their ∼2-3 times more compact FIR sizes (shifting their molecular gas mass surface densities to higher values by a factor ∼4-9), ∼2.1 times larger molecular gas mass fraction (shifting their molecular gas mass surface densities to higher values by a factor ∼2.1), and the slope of 1.1–1.2 of the KS relation.

Our SBs deviate by ∼0.5 dex from the KS relation for mergers from Genzel et al. (2010). The reason for this difference could be threefold. (i) Genzel et al. (2010) used CO-based gas mass measurements and an $\alpha_{\rm CO}$ specific for mergers. This particular $\alpha_{\rm CO}$ could underestimate their molecular gas mass by a factor of ∼0.5 dex. (ii) Genzel et al. (2010) averaged the size measurements from Hα, optical, UV, and CO as a representative of star-forming size and report ∼2 times larger sizes compared to our FIR measurements. (iii) Genzel et al. (2010) restricted their

SB sample to mergers, while we defined SB based on their distance from the MS.

4.2. Stellar population size and morphology

Results of our image-domain stacking analysis on the *HST* *i*-band dataset are displayed in Fig. 10. All the *HST* stacked images have significant detection with a S/N > 5. In addition, while galaxies on the MS (ΔMS < 0.4) exhibit disk-like morphology, it is clear from our stacked *HST* images that galaxies above the MS have disturbed morphology associated with multiple stellar components. To further characterize these disk-like and merger-like morphologies, we measured the Gini and M20 coefficients of the 195 individual galaxies with $M_\star > 10^{10} M_\odot$ that are sufficiently bright[2] using the python package `statmorph` (Rodriguez-Gomez et al. 2019, 2022). The Gini describes the relative pixel distribution, while the M20 corresponds to the second-order moment of the brightest 20% of the pixels of a galaxy (Lotz et al. 2004). If a galaxy has a merger-like morphology, it has a relatively high Gini and low M20 coefficient compared to disk-like galaxies. The Gini and M20 coefficient measured on the *HST* *i*-band image of each of our galaxies and on their stacked *HST* *i*-band images are shown in Fig. 11. The uncertainties associated with these Gini and M20 coefficient measurements were obtained using Monte Carlo simulations. For each galaxy, we created 100 realizations, each containing the modeled galaxy obtained by `statmorph` and a random background noise consistent with that found on the residual map of `statmorph`. We then measured the Gini and M20 coefficients on these 100 realizations and used their distributions as uncertainties. To distinguish merging, spiral, and elliptical galaxies, we used the morphological classification from Lotz et al. (2008). Since we aim to compare the morphology and size of the stacked galaxies that have at least one FIR size measurement in the stellar mass bin, we did not measure the morphology of galaxies with $M_\star < 10^{10} M_\odot$.

For individual galaxies (left panel of Fig 11), we find that SBs have indeed a merger-like morphology (see also Fig. 12 in which we show examples of these *HST* *i*-band images) For our stacked images (right panel of Fig 11), this separation is less clear as the stacking analysis naturally erases the irregularity of the merging system and thus decreases their Gini and increases their M20 values. Yet stacked SBs are located closer to the merger separation than MS galaxies, and thus still retain some information from their merger origin. We note that this is due to the small number statistic of our SB sample, and we can expect these irregularities to be largely erased in future studies stacking large numbers of SBs.

We show the image-domain stacking analysis for the UltraVISTA dataset in Fig. 13 (UltraVISTA *J*-band) and Fig. 14 (UltraVISTA K_s-band). The stacked images of the UltraVISTA dataset have significant detection with a S/N > 5. As a sanity check, in Fig. 15 we compare the mass–size relation at a rest-frame wavelength of 5, 000Å inferred from our stacking analysis (i.e., fitting 2D Gaussian profiles to our UltraVISTA *J*-band stacks, our sample being at $z \sim 1.4$) to that inferred by van der Wel et al. (2014) using *HST* images of the CANDELS fields. We find a very good agreement between these two mass–size relations. This demonstrates that, despite the use of a seeing-limited image and of a stacking analysis, we can still obtain accurate estimates of the mean size of SFGs.

[2] Above this stellar mass, 119 galaxies, mostly at low ΔMS, remain undetected in the *HST* *i* band and are thus excluded from our analysis.

This unique FIR, *HST* *i*-band, UltraVISTA *J*-band, and UltraVISTA K_s-band stacking analysis enables us to compare the size of stacked galaxies at different wavelengths, which in turn reflects the distribution of their various components, such as their young and old stars. Because our stacked FIR and optical images have different spatial resolution, before performing any comparison, we matched the PSFs by convolving each image with different kernels to ensure that all images have the same final resolution. The optical and FIR radial profiles in each $M_\star$–ΔMS bin after this PSF-matching are shown in Fig. 16. These radial profiles were created by measuring the mean intensity value at different radii and normalizing these mean values with the intensity measured in the central pixel.

In Fig. 16, most of the radial light profiles are more extended than the matched PSF, except for the FIR radial profile in the highest ΔMS and $10^{10} \leq M_\star/\mathrm{M}_\odot < 10^{10.5}$ bin. This indicates that except for the latter, all the other bins have spatially resolved emission at optical and FIR wavelengths. However, the spatial extents in these different wavelength are not always the same and we typically found at $M_\star > 10^{10.5} M_\odot$: *HST* *i*-band > UltraVISTA *J*-band > UltraVISTA K_s-band > ALMA. To quantify the size ratio between these bands, we measured their deconvolved $FWHM$ (i.e., $\sqrt{FWHM^2 - \theta^2_{\mathrm{target}}}$) and converted it to an effective radius following Jiménez-Andrade et al. (2019), i.e., $R_{\mathrm{eff}} \approx FWHM\,(\mathrm{deconvolved})/2.43$. The effective radius of each band (R_{band}) and its ratio to the FIR size is displayed in Fig. 17. We note that the FIR sizes inferred using this simple beam deconvolution of the light profile are consistent with those inferred using single Gaussian fit to our original (before kernel convolution) stacked ALMA images, with a mean offset of ∼5% (see blue square in Fig. 17).

We find that the FIR and rest-frame optical sizes of MS galaxies are generally in agreement with each other at $M_\star < 10^{10.5} M_\odot$. Above this stellar mass, their rest-frame optical sizes are usually larger than their FIR sizes. The finding of $R_{\mathrm{optical}} > R_{\mathrm{FIR}}$ could be interpreted as evidence that we are witnessing the formation of the central bulge in these massive MS galaxies. However, this interpretation depends on which optical sizes we consider, as those tend to decrease when measured at longer wavelengths (*HST* *i*-band > UltraVISTA *J*-band > UltraVISTA K_s-band; see also, e.g., van der Wel et al. 2014; Suess et al. 2022). It is thus highly probable that our rest-frame optical sizes, even when measured in the longest band available (i.e., UltraVISTA K_s-band), are still affected by large dust attenuation at the center of these galaxies and could therefore be overestimated. To obtain an accurate comparison between the size of the star-forming component of these galaxies (i.e., their FIR size) and their stellar component, it is thus necessary to determine their half-stellar mass radius from our observed rest-frame optical effective radius. To do so, we corrected our effective radius at rest of ∼0.5 μm (UltraVISTA *J*-band) using the $R_{\mathrm{half-stellar-light}}$-to-$R_{\mathrm{half-stellar-mass}}$ ratio versus stellar mass relation calibrated at rest of 0.5 μm by Suess et al. (2019). The corrected half-stellar mass size of MS galaxies (i.e., those with ΔMS<0.4) are consistent with their stacked FIR size, with $\langle R_{\mathrm{stellar}_{(M_\star,\Delta\mathrm{MS})}}/R_{\mathrm{FIR}_{(M_\star,\Delta\mathrm{MS})}}\rangle$=0.9±0.3. This result agrees with the simulation of Popping et al. (2022), which found that the half-stellar mass sizes of SFGs are consistent with the half-light size of the dust continuum emission (and their half SFR size).

At ΔMS>0.4, using the relation of Suess et al. (2019) to correct half-light size to half-stellar mass size is probably inappropriate as this relation has not been calibrated specifically for SBs. Nevertheless, the fact that at ΔMS>0.4 even the corrected half-

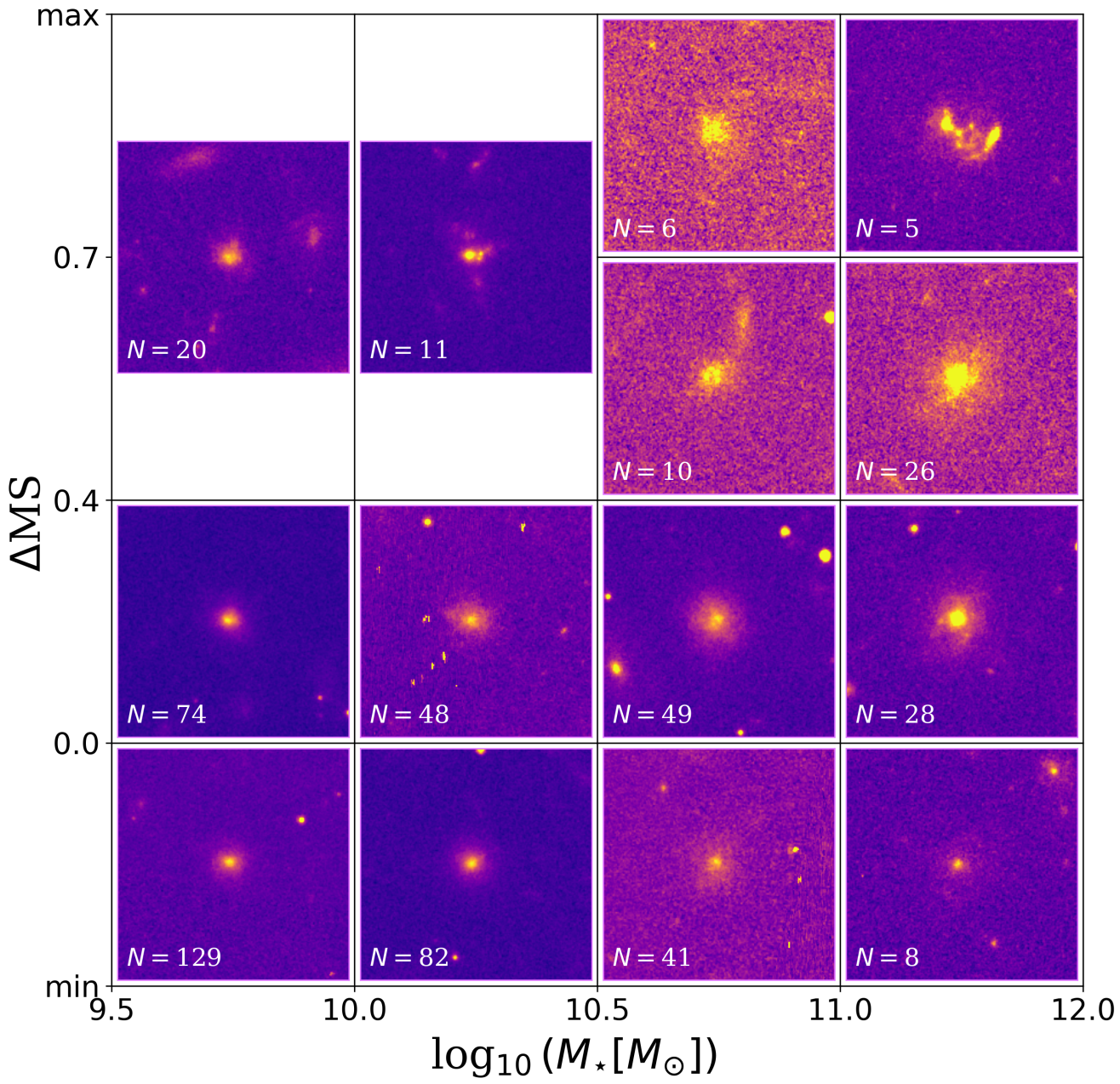

Fig. 10. Same as Fig. 5, but for the image stacking on the *HST* *i*-band data.

stellar mass sizes are larger than the FIR sizes is probably best explained by the fact that these galaxies are dominated by merging systems. In this case, the rest-frame optical sizes are likely dominated by the disrupted morphology of the merging stellar components, whereas the FIR sizes are likely dominated by the coalescing star-forming region as, for example, in the local antennae galaxies (e.g., Bigiel et al. 2015).

5. Discussion

Our analysis reveals several key properties of SFGs at z ~1.4: (i) their mean molecular gas fraction increases and their mean molecular gas depletion time decreases continuously and at similar rates across the MS (-0.2 < ΔMS < 0.2) and into the SB region (i.e., up to ΔMS~0.8); (ii) their FIR size decreases from 2.5 kpc at ΔMS~0 to 1.4 kpc at ΔMS~0.8; (iii) MS galaxies and SBs fall roughly on the same KS relation with a slope of 1.13; (iv) SBs tend to have a merger-like morphology, while MS galaxies tend to have a disk-like morphology; (v) at $M_\star > 10^{10.5} M_\odot$, their optical sizes are usually $R_{HST\,i\text{−band}} > R_{\mathrm{UltraVISTA}\,J\text{−band}} > R_{\mathrm{UltraVISTA}\,K_s\text{−band}}$, consistently with the so-called negative color gradient; (vi) after having statistically corrected these rest-frame optical sizes for dust attenuation using an empirical relation from Suess et al. (2019), the stellar mass sizes of MS galaxies are similar to their FIR sizes.

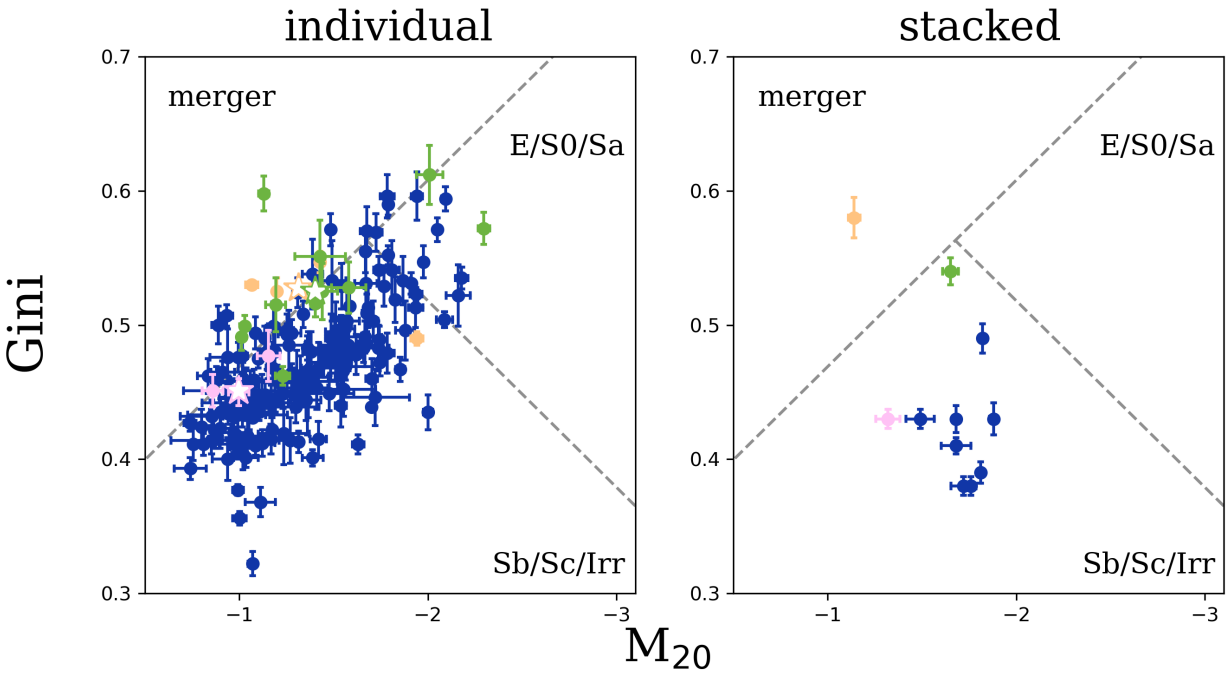

Fig. 11. Morphological classification of our $M_\star > 10^{10} M_\odot$ SFGs measured on their *HST* *i*-band images. Circles in the left panel are the Gini and M20 coefficient measured on *HST* *i*-band images of each individual galaxy, while the right panel shows the Gini and M20 coefficient measured for the stacked images of the different stellar mass and ΔMS bin. Orange, pink, green, and dark blue show SBs (ΔMS > 0.7) at $10^{11} \leq M_\star/\mathrm{M}_\odot < 10^{12}$, SBs at $10^{10.5} \leq M_\star/\mathrm{M}_\odot < 10^{11}$, SBs at $10^{10} \leq M_\star/\mathrm{M}_\odot < 10^{10.5}$, and $M_\star > 10^{10} M_\odot$ SFGs without SBs (ΔMS < 0.7), respectively. Stars in the left panel are the median Gini and M20 coefficients of SBs in these three stellar mass bins. Gray dashed lines are the morphology classification from Lotz et al. (2008).

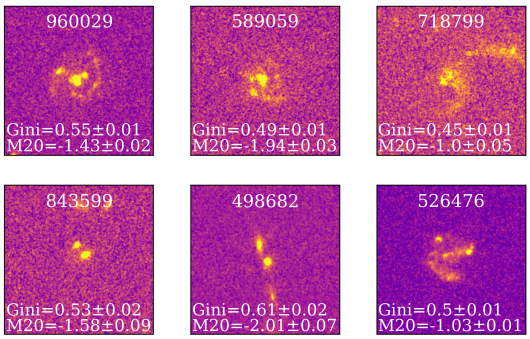

Fig. 12. Examples of *HST* *i*-band images of individual SB. Numbers on each image show their COSMOS2020 ID and measured Gini and M20 coefficients. Each image has a size of 6″ × 6″.

5.1. The dispersion of the MS

At all redshifts and stellar masses, a constant dispersion of ∼0.3 dex of the MS has been observed (e.g., Schreiber et al. 2015; Leslie et al. 2020; Leja et al. 2022). Simulations by Tacchella et al. (2016, 2020) suggest that the mechanisms behind the dispersion of the MS could be complex. For example, gas compaction induced by minor mergers or disk instabilities could enhance the star formation efficiency of galaxies, raise their SFR, and thus increase their ΔMS (e.g., Cacciato et al. 2012; Dekel & Burkert 2014; Lapiner et al. 2023). On the other hand, the depletion of gas due to star formation or supernova feedback could reduce the gas fraction in galaxies, suppress their SFR, and thus decrease their ΔMS (e.g., Feldmann & Mayer 2015; Spilker et al. 2019). Most star-forming galaxies would thus experience cycles of the aforementioned mechanisms and oscillate on the MS for a few gigayears, finally quenching into quiescence if the inflow of fresh gas from the the cosmic web cannot support its star formation (e.g., Feldmann & Mayer 2015; Williams et al. 2021). During these oscillations within the MS, simulations of Tacchella et al. (2016, see also Tacchella et al. 2020) predict that the variation in molecular gas fraction and star formation efficiency play a similar role. Our findings of both higher molecular gas fraction and lower depletion time as galaxies move across the MS support this scenario. Although still tentative, the observation of slightly more compact FIR sizes at ΔMS∼ 0.2 than at ΔMS∼ −0.2 (see Fig. 8) is also consistent with this scenario.

5.2. Compact star-forming size or dust attenuation effect

To understand the mechanisms leading to the disk growth of SFGs along the MS, one needs to compare their current morphologies (i.e., those of their stellar components) to the distribution of their ongoing star formation. In this context, many studies have investigated the Hα extent ($R_{\mathrm{H}\alpha}$), i.e., star-forming size, and optical extent (R_{optical}), i.e., stellar size, of SFGs at different redshifts and stellar masses (e.g., Nelson et al. 2016; Wilman et al. 2020; Matharu et al. 2022). They found that $R_{\mathrm{H}\alpha}/R_{\mathrm{optical}}$ is usually >1, and that this ratio decreases with decreasing stellar mass. These results suggest that the growth of SFGs follow the so-called inside-out scenario, i.e., where new stars form mainly at large radii. However, recent ALMA observations have contradicted this picture of large star-forming size compared to stellar size at least at the high-mass end ($\geq 10^{10.5} M_\odot$) of high-redshift ($z \geq 1$) SFGs, as those have mostly revealed compact

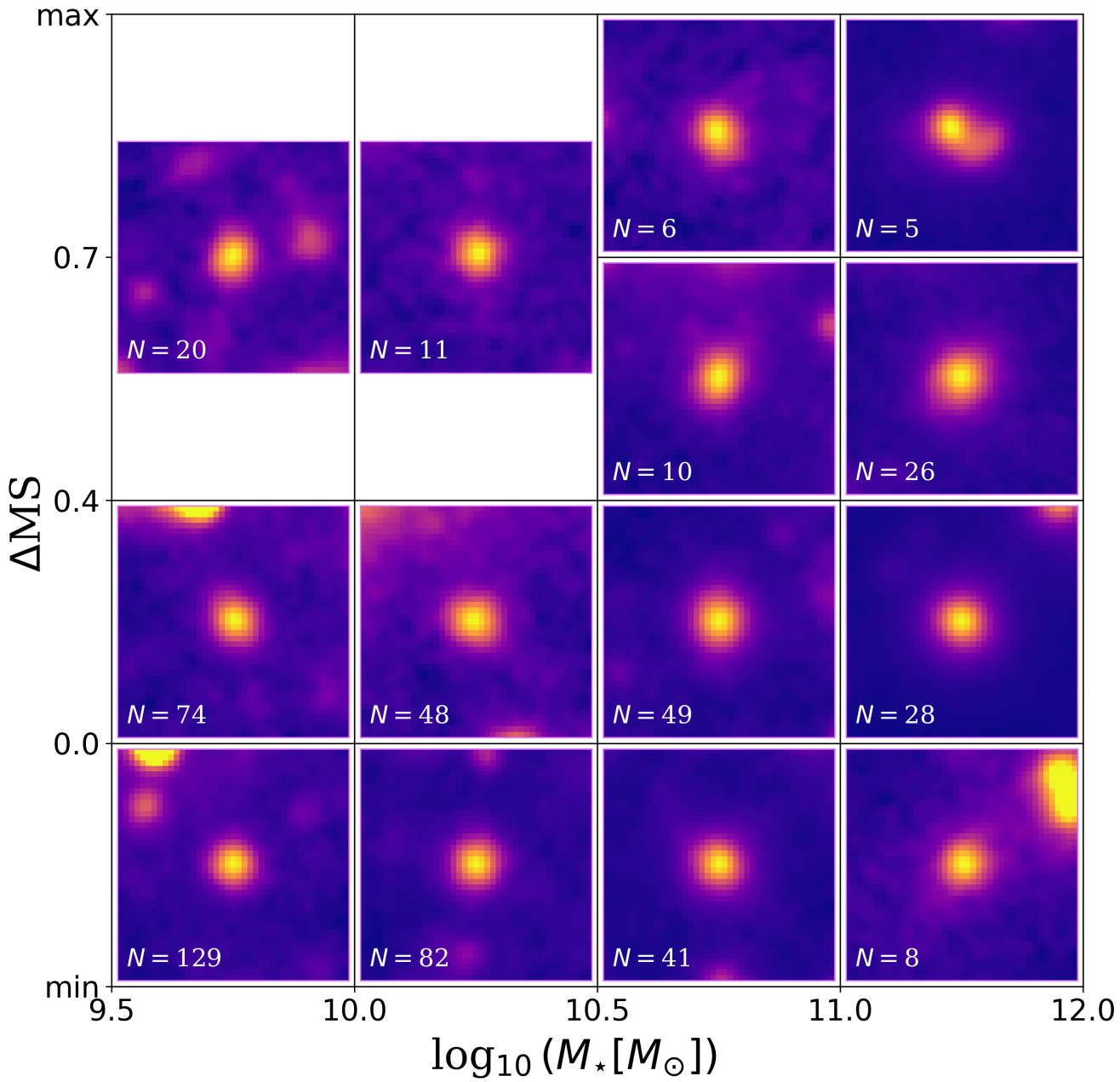

Fig. 13. Same as Fig. 5, but for the image stacking on the UltraVISTA J-band data.

star-forming regions compared to their rest-frame optical extent (e.g., Elbaz et al. 2018; Tadaki et al. 2020; Puglisi et al. 2021; Gómez-Guijarro et al. 2022a; Wang et al. 2022). This discovery of such compact star-forming regions is usually interpreted as the formation of stellar bulges in SFGs (e.g., Zolotov et al. 2015; Tacchella et al. 2016). Recent TNG50 simulations by Popping et al. (2022) suggest instead that the observed compact star-forming size in massive SFGs, when compared to their optical sizes, could primarily result from large dust attenuation in the central region. This attenuation strongly affects the estimation of their stellar extent based on rest-frame optical observations. Here we probe for the first time with a mass-complete sample the optical and FIR sizes of MS galaxies down to $M_\star$~$10^{10.0} M_\odot$. We found that their star-forming size is similar to their stellar mass size, i.e., $\langle R_{\rm stellar_{(M_\star,\Delta MS)}}/R_{\rm FIR_{(M_\star,\Delta MS)}}\rangle$=0.9±0.3, when accounting for dust attenuation. Our finding supports the interpretation that the observed larger optical size compared to the star-forming size in MS galaxies may be primarily due to dust extinction.

5.3. Which mechanism(s) trigger SBs?

Starbursts are believed to mostly originate from the major merger of two gas-rich galaxies (e.g., Moreno et al. 2019; Renaud et al. 2022; Petersson et al. 2023). During a merger, the molecular gas clouds of galaxies can interact with each other and fall into the central region of the merging system (e.g., We-

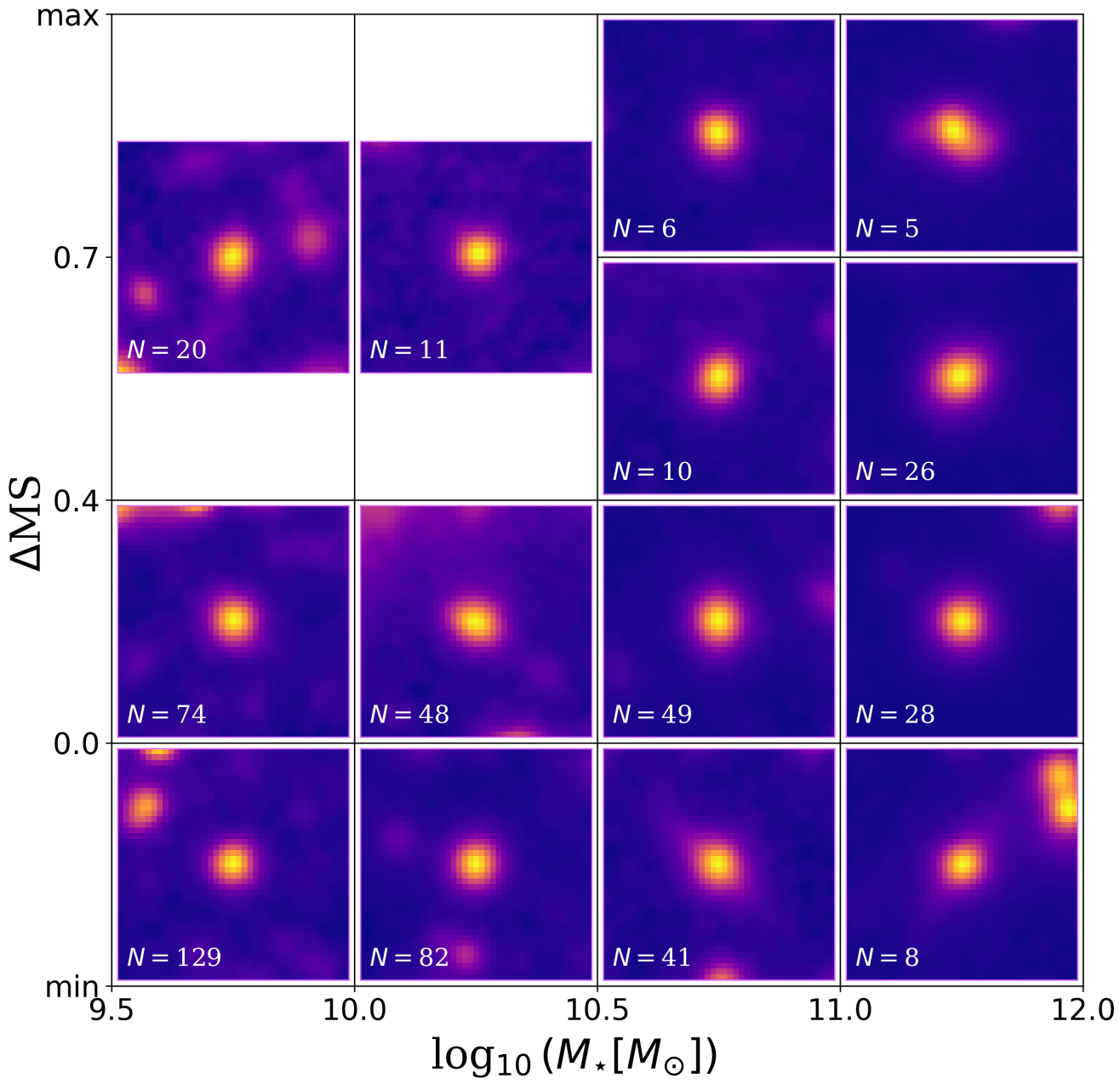

Fig. 14. Same as Fig. 5, but for the image stacking on the UltraVISTA K_s-band data.

ston et al. 2017; Blumenthal & Barnes 2018; Sivasankaran et al. 2022). The fact that most of the individual SBs have merger-like morphology in the rest-frame optical and the stacked SBs have compact FIR size support such a merger-driven scenario. We note that literature studies also suggest that a portion of SBs could be induced without major merger, such as galaxy interactions or disk instabilities (e.g., Porter et al. 2014; Wilkinson et al. 2018). Our finding that a few individual galaxies do not exhibit merger-like morphologies in their rest-frame optical images (left panel of Fig. 11) supports this interpretation.

While mergers appear to be the dominating driver for the formation of SBs, the exact way galaxy mergers enhance star formation in such systems is debated. Mergers could enhance solely the star formation efficiency (e.g., Di Matteo et al. 2007; Sargent et al. 2014). This scenario is observationally supported by the finding in Genzel et al. (2010) of a distinct KS relation for SBs with ten times higher normalization compared to the KS relation for SFGs. On the other hand, the molecular gas fraction of SFGs could also be elevated by a factor of >2 during a merger, which is revealed by both simulations (e.g., Teyssier et al. 2010; Renaud et al. 2014) and observations in the local Universe (e.g., Pan et al. 2018; Violino et al. 2018; Lisenfeld et al. 2019). Indeed, during a merger, the extended H I reservoir of the merging galaxies (e.g., Neeleman et al. 2017; Walter et al. 2020) can be compressed and transformed into molecular gas (e.g., Yu et al. 2022), thereby enhancing the molecular gas frac-

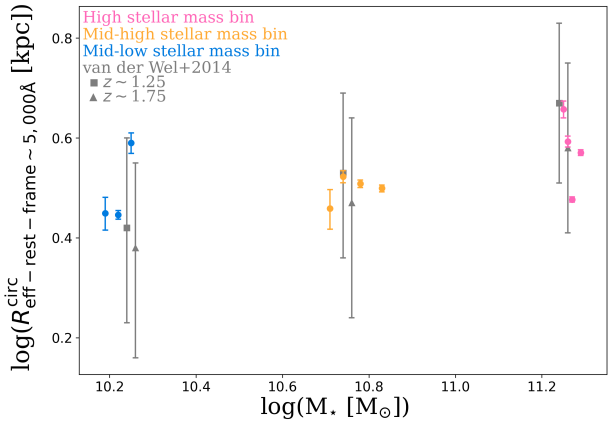

Fig. 15. Circularized effective radius at rest-frame wavelength of 5,000Å as a function of stellar mass. Circles show the UltraVISTA J-band sizes from our stacking analysis, corresponding roughly to a rest-frame wavelength of 5,000Å for our $z \sim 1.4$ sample. Squares ($z \sim 1.25$) and triangles ($z \sim 1.75$), along with their error bars, show the 16th, 50th, and 84th percentiles from van der Wel et al. (2014) for late-type galaxies as inferred using *HST* images of the CANDELS fields.

tion in merging systems. We found that the mean molecular gas fraction increases by a factor of ~2.1 from the MS to SBs, while the mean molecular gas depletion time decreases by a factor of ~3.3. These findings support the scenario where H I gas from the reservoir flows into the gravitational well of the merging system and subsequently converts into molecular gas during the merger, thereby leading to a higher molecular gas fraction in SBs. This mechanism is nearly as important as the variation in star formation efficiency to explain the increase in SFR at a given stellar mass when SFGs move from the MS to the SB regime.

6. Summary

We investigated the molecular gas mass properties of a mass-complete sample ($>10^{9.5} M_\odot$) of SFGs at $1.2 \leq z < 1.6$, and in particular the variation of these properties with the distance of these galaxies from the main sequence of SFGs (i.e., ΔMS). We applied a *uv*-domain stacking analysis to all archival ALMA data available for the COSMOS field to accurately measure the RJ-based molecular gas mass and size of SFGs in multiple stellar mass and ΔMS bins. With this approach, we studied, for the first time, the molecular gas fraction, molecular gas star formation efficiency, and the KS relation of MS galaxies (-0.7 < ΔMS < 0.4) and SBs (ΔMS > 0.7). Additionally, we performed an image-domain stacking analysis on the *HST* i-band and UltraVISTA J- and K_s-band images of these galaxies and measured, thereby, the size and morphology of their stellar component. Our main findings are listed below.

1. The mean molecular gas fraction of SFGs increases by a factor of ~2.1, while their mean molecular gas depletion time decreases by a factor of ~3.3, as they move from the MS (ΔMS ~ 0) to SB (ΔMS ~ 0.8).
2. Across the MS (-0.2 < ΔMS < 0.2), the mean molecular gas fraction of SFGs increases by a factor of ~1.4, while their mean molecular gas depletion time decreases by a factor of ~1.8.
3. Although still uncertain, the mean FIR size of SFGs seems to decrease from ~2.5 kpc at the MS to ~1.4 kpc at the SB.
4. Main-sequence galaxies and SBs follow the same near-linear KS relation, with a slope of 1.1 − 1.2.
5. The measured optical size decreases with wavelength for $M_\star > 10^{10.5} M_\odot$, with *HST* i-band > UltraVISTA J-band > UltraVISTA K_s-band. This is consistent with the so-called negative color gradient described in the literature and is likely due to dust attenuation.
6. When accounting for dust attenuation by converting the half-light radius of MS galaxies in the UltraVISTA J band into half-mass radius using the relation of Suess et al. (2019), the size of the stellar component of MS galaxies is similar to that of their star-forming component.
7. Starbursts tend to have merger-like morphology, while MS galaxies have disk-like morphology, as revealed by their Gini-M20 coefficient of their optical *HST* i-band images.

Overall, the evolution of SFGs across and above the MS is a complex combination of variations in their molecular gas fraction, mean molecular gas depletion time, and mean star-forming size. Variations in both the molecular gas fraction and star formation efficiency seem to drive the oscillation of SFGs within the MS, likely through cycles of compaction, depletion, and outflow, as predicted by Tacchella et al. (2016, see also Tacchella et al. 2020). SFGs move into the SB region as a result of galaxy mergers that yield to a more compact star-forming region and larger gas fraction that may originate from the transformation of the surrounding HI reservoir into molecular gas. This in turn leads to higher $\Sigma_{M_{mol}}$ and thus higher star formation efficiency as SBs follow the universal KS relation with a slope of 1.1–1.2.

Acknowledgements. This research was carried out within the Collaborative Research Centre 956, sub-project A1, funded by the Deutsche Forschungsgemeinschaft (DFG) – project ID 184018867. ES acknowledges funding from the European Research Council (ERC) under the European Union's Horizon 2020 research and innovation programme (grant agreement No. 694343). This work was supported by UNAM-PAPIIT IA102023. ALMA is a partnership of ESO (representing its member states), NSF (USA) and NINS (Japan), together with NRC (Canada), MOST and ASIAA (Taiwan), and KASI (Republic of Korea), in cooperation with the Republic of Chile. The Joint ALMA Observatory is operated by ESO, AUI/NRAO and NAOJ. This paper makes use of the following ALMA data: ADS/JAO.ALMA#2015.1.00055.S, ADS/JAO.ALMA#2015.1.00137.S, ADS/JAO.ALMA#2015.1.00260.S, ADS/JAO.ALMA#2015.1.00299.S, ADS/JAO.ALMA#2015.1.00379.S, ADS/JAO.ALMA#2015.1.00388.S, ADS/JAO.ALMA#2015.1.00568.S, ADS/JAO.ALMA#2015.1.00664.S, ADS/JAO.ALMA#2015.1.00704.S, ADS/JAO.ALMA#2015.1.01074.S, ADS/JAO.ALMA#2015.1.01105.S, ADS/JAO.ALMA#2015.1.01212.S, ADS/JAO.ALMA#2015.1.01495.S, ADS/JAO.ALMA#2016.1.00279.S, ADS/JAO.ALMA#2016.1.00463.S, ADS/JAO.ALMA#2016.1.00478.S, ADS/JAO.ALMA#2016.1.00624.S, ADS/JAO.ALMA#2016.1.00646.S, ADS/JAO.ALMA#2016.1.00735.S, ADS/JAO.ALMA#2016.1.00778.S, ADS/JAO.ALMA#2016.1.00804.S, ADS/JAO.ALMA#2016.1.01012.S, ADS/JAO.ALMA#2016.1.01040.S, ADS/JAO.ALMA#2016.1.01208.S, ADS/JAO.ALMA#2016.1.01426.S, ADS/JAO.ALMA#2016.1.01454.S, ADS/JAO.ALMA#2016.1.01559.S, ADS/JAO.ALMA#2016.1.01604.S, ADS/JAO.ALMA#2017.1.00326.S, ADS/JAO.ALMA#2017.1.00413.S, ADS/JAO.ALMA#2017.1.00428.L, ADS/JAO.ALMA#2017.1.01176.S, ADS/JAO.ALMA#2017.1.01276.S, ADS/JAO.ALMA#2017.1.01358.S, ADS/JAO.ALMA#2017.1.00046.S, ADS/JAO.ALMA#2017.1.01217.S, ADS/JAO.ALMA#2017.1.01259.S, ADS/JAO.ALMA#2018.1.00085.S, ADS/JAO.ALMA#2018.1.00164.S, ADS/JAO.ALMA#2018.1.00251.S, ADS/JAO.ALMA#2018.1.00635.S, ADS/JAO.ALMA#2018.1.00681.S, ADS/JAO.ALMA#2018.1.00933.S, ADS/JAO.ALMA#2018.1.00992.S, ADS/JAO.ALMA#2018.1.01044.S, ADS/JAO.ALMA#2018.1.01605.S, ADS/JAO.ALMA#2018.1.01871.S, ADS/JAO.ALMA#2019.1.00399.S, ADS/JAO.ALMA#2019.1.00477.S, ADS/JAO.ALMA#2019.1.00964.S, ADS/JAO.ALMA#2019.1.01142.S, ADS/JAO.ALMA#2019.1.01634.L, ADS/JAO.ALMA#2019.1.01702.S. Based in part on data products produced by TERAPIX and the Cambridge Astronomy Survey Unit on behalf of the UltraVISTA consortium.

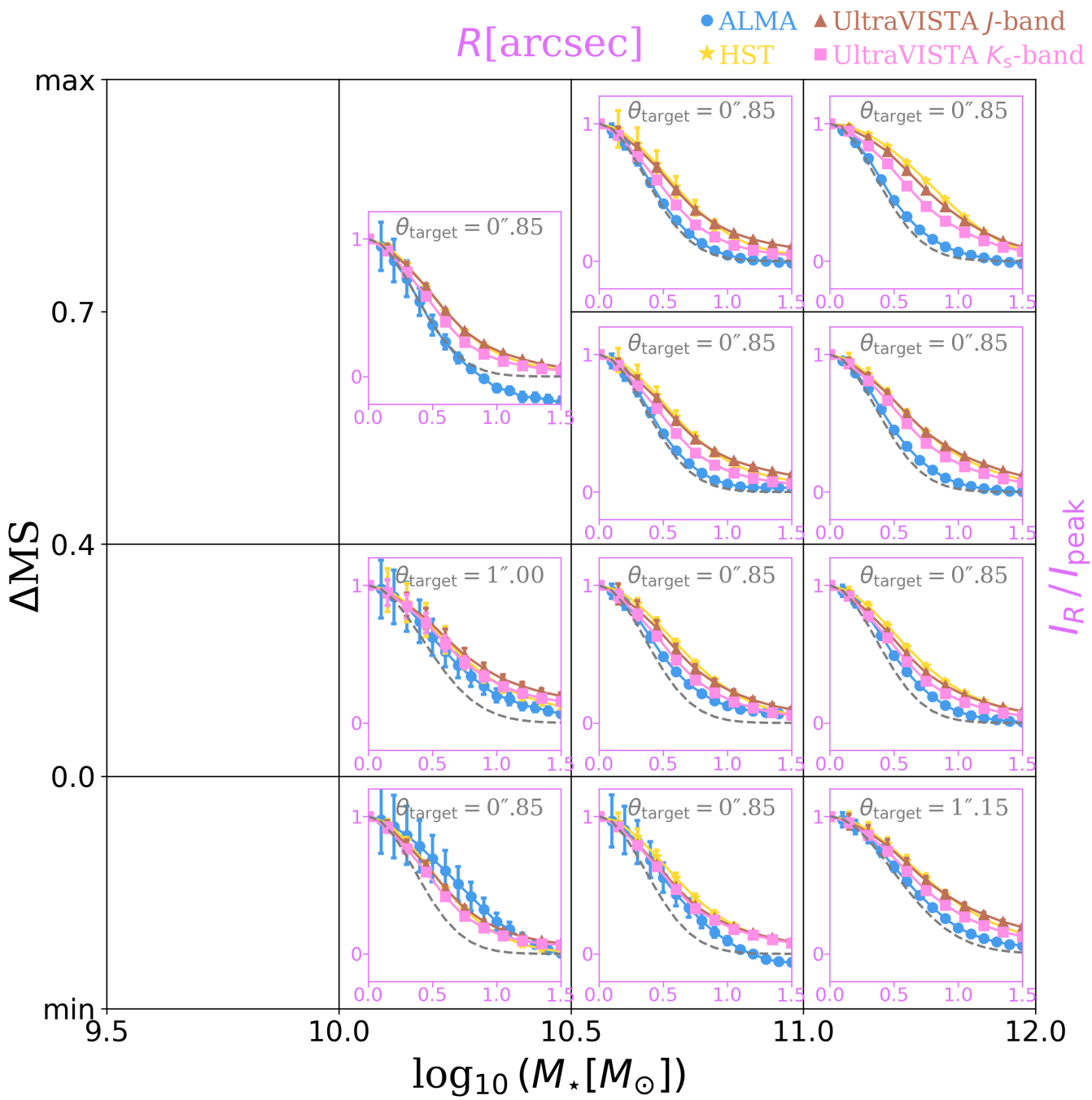

Fig. 16. Normalized radial light profile of stacked ALMA (blue circles), *HST* (yellow stars), UltraVISTA *J*-band (brown triangles), and UltraVISTA K_s-band (pink squares) images in different $M_\star$–ΔMS bins. All stacked images are matched to the same PSF, i.e., $\theta_{\rm target}$ (gray dashed line). The maximum value of ΔMS for the mid-low, mid-high, and high stellar mass bins are 0.9, 1.0, and 1.1; and the minimum value for the mid-low, mid-high, and high stellar mass bins are -0.7, -0.7, and -0.6, respectively. At the lowest stellar mass, we do not present radial light profiles of the stacked galaxies as they are either unresolved or undetected in our ALMA stacked images.

References

Béthermin, M., Daddi, E., Magdis, G., et al. 2012, ApJ, 757, L23. doi:10.1088/2041-8205/757/2/L23

Bigiel, F., Leroy, A. K., Blitz, L., et al. 2015, ApJ, 815, 103. doi:10.1088/0004-637X/815/2/103

Blumenthal, K. A. & Barnes, J. E. 2018, MNRAS, 479, 3952. doi:10.1093/mnras/sty1605

Bolatto, A. D., Wolfire, M., & Leroy, A. K. 2013, ARA&A, 51, 207. doi:10.1146/annurev-astro-082812-140944

Byrne-Mamahit, S., Hani, M. H., Ellison, S. L., et al. 2023, MNRAS, 519, 4966. doi:10.1093/mnras/stac3674

Cacciato, M., Dekel, A., & Genel, S. 2012, MNRAS, 421, 818. doi:10.1111/j.1365-2966.2011.20359.x

Calabrò, A., Daddi, E., Fensch, J., et al. 2019, A&A, 632, A98. doi:10.1051/0004-6361/201935778

Chabrier, G. 2003, PASP, 115, 763. doi:10.1086/376392

Chang, Y.-Y., Le Floc'h, E., Juneau, S., et al. 2020, ApJ, 888, 44. doi:10.3847/1538-4357/ab595b

Chary, R. & Elbaz, D. 2001, ApJ, 556, 562. doi:10.1086/321609

Chen, C.-C., Harrison, C. M., Smail, I., et al. 2020, A&A, 635, A119. doi:10.1051/0004-6361/201936286

Cibinel, A., Daddi, E., Sargent, M. T., et al. 2019, MNRAS, 485, 5631. doi:10.1093/mnras/stz690

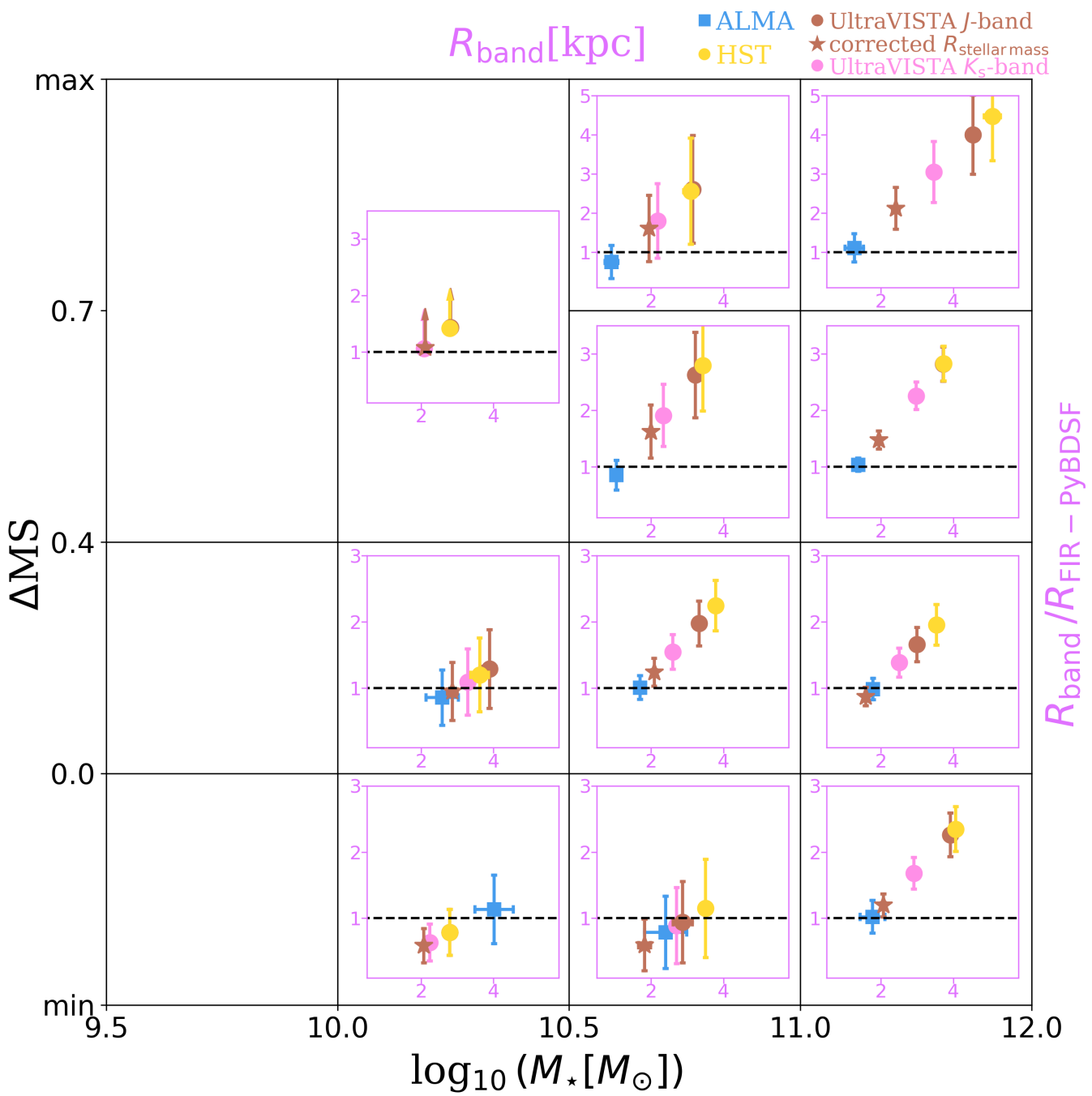

Fig. 17. Ratio of effective radius in different bands to effective radius in FIR measured by fitting a single Gaussian to our original ALMA stacked images. Yellow, brown, and pink circles correspond the optical size measured from the *HST* *i*-band, UltraVISTA *J*-band, and UltraVISTA $K_{\rm s}$-band light profiles, respectively. Blue squares display the FIR size measured from the ALMA light profile. Brown stars show the stellar mass effective radius inferred by correcting our UltraVISTA *J*-band sizes with a $R_{\rm half-stellar-light}$-to-$R_{\rm half-stellar-mass}$ relation at rest 5000 Å from Suess et al. (2019). We provide lower limits of the size ratio in the highest ΔMS and $10^{10.0} \leq M_\star/{\rm M}_\odot < 10^{10.5}$ bin because these galaxies are unresolved in our ALMA stacked images. The maximun value of ΔMS for the mid-low, mid-high, and high stellar mass bin are 0.9, 1.0, and 1.1; and the minimum value for the mid-low, mid-high, and high stellar mass bin are -0.7, -0.7, and -0.6, respectively.

Daddi, E., Elbaz, D., Walter, F., et al. 2010, ApJ, 714, L118. doi:10.1088/2041-8205/714/1/L118

Daddi, E., Delvecchio, I., Dimauro, P., et al. 2022, A&A, 661, L7. doi:10.1051/0004-6361/202243574

Davé, R., Finlator, K., Oppenheimer, B. D., et al. 2010, MNRAS, 404, 1355. doi:10.1111/j.1365-2966.2010.16395.x

Dekel, A. & Burkert, A. 2014, MNRAS, 438, 1870. doi:10.1093/mnras/stt2331

Delvecchio, I., Smolčić, V., Zamorani, G., et al. 2017, A&A, 602, A3. doi:10.1051/0004-6361/201629367

Delvecchio, I., Daddi, E., Sargent, M. T., et al. 2021, A&A, 647, A123. doi:10.1051/0004-6361/202039647

de los Reyes, M. A. C. & Kennicutt, R. C. 2019, ApJ, 872, 16. doi:10.3847/1538-4357/aafa82

Di Matteo, P., Combes, F., Melchior, A.-L., et al. 2007, A&A, 468, 61. doi:10.1051/0004-6361:20066959

Dye, S., Eales, S. A., Gomez, H. L., et al. 2022, MNRAS, 510, 3734. doi:10.1093/mnras/stab3569

Elbaz, D., Dickinson, M., Hwang, H. S., et al. 2011, A&A, 533, A119. doi:10.1051/0004-6361/201117239

Elbaz, D., Leiton, R., Nagar, N., et al. 2018, A&A, 616, A110. doi:10.1051/0004-6361/201732370
Feldmann, R. & Mayer, L. 2015, MNRAS, 446, 1939. doi:10.1093/mnras/stu2207
Franco, M., Elbaz, D., Zhou, L., et al. 2020, A&A, 643, A30. doi:10.1051/0004-6361/202038312
Fujimoto, S., Ouchi, M., Shibuya, T., et al. 2017, ApJ, 850, 83. doi:10.3847/1538-4357/aa93e6
Genzel, R., Tacconi, L. J., Gracia-Carpio, J., et al. 2010, MNRAS, 407, 2091. doi:10.1111/j.1365-2966.2010.16969.x
Gómez-Guijarro, C., Elbaz, D., Xiao, M., et al. 2022, A&A, 659, A196. doi:10.1051/0004-6361/202142352
Gómez-Guijarro, C., Elbaz, D., Xiao, M., et al. 2022, A&A, 658, A43. doi:10.1051/0004-6361/202141615
Gruppioni, C., Béthermin, M., Loiacono, F., et al. 2020, A&A, 643, A8. doi:10.1051/0004-6361/202038487
Hodge, J. A., Carilli, C. L., Walter, F., et al. 2012, ApJ, 760, 11. doi:10.1088/0004-637X/760/1/11
Hodge, J. A., Swinbank, A. M., Simpson, J. M., et al. 2016, ApJ, 833, 103. doi:10.3847/1538-4357/833/1/103
Hunt, L. K., De Looze, I., Boquien, M., et al. 2019, A&A, 621, A51. doi:10.1051/0004-6361/201834212
Ikarashi, S., Ivison, R. J., Caputi, K. I., et al. 2015, ApJ, 810, 133. doi:10.1088/0004-637X/810/2/133
Ilbert, O., McCracken, H. J., Le Fèvre, O., et al. 2013, A&A, 556, A55. doi:10.1051/0004-6361/201321100
Jiménez-Andrade, E. F., Magnelli, B., Karim, A., et al. 2019, A&A, 625, A114. doi:10.1051/0004-6361/201935178
Jin, S., Daddi, E., Liu, D., et al. 2018, ApJ, 864, 56. doi:10.3847/1538-4357/aad4af
Kennicutt, R. C. 1998, ApJ, 498, 541. doi:10.1086/305588
Kennicutt, R. C. 1998, ARA&A, 36, 189. doi:10.1146/annurev.astro.36.1.189
Kennicutt, R. C. & De Los Reyes, M. A. C. 2021, ApJ, 908, 61. doi:10.3847/1538-4357/abd3a2
Koekemoer, A. M., Aussel, H., Calzetti, D., et al. 2007, ApJS, 172, 196. doi:10.1086/520086
Kokorev, V. I., Magdis, G. E., Davidzon, I., et al. 2021, ApJ, 921, 40. doi:10.3847/1538-4357/ac18ce
Lamastra, A., Menci, N., Fiore, F., et al. 2013, A&A, 552, A44. doi:10.1051/0004-6361/201220754
Lang, P., Schinnerer, E., Smail, I., et al. 2019, ApJ, 879, 54. doi:10.3847/1538-4357/ab1f77
Lapiner, S., Dekel, A., Freundlich, J., et al. 2023, MNRAS. doi:10.1093/mnras/stad1263
Leauthaud, A., Massey, R., Kneib, J.-P., et al. 2007, ApJS, 172, 219. doi:10.1086/516598
Leja, J., Speagle, J. S., Ting, Y.-S., et al. 2022, ApJ, 936, 165. doi:10.3847/1538-4357/ac887d
Leroy, A. K., Bolatto, A., Gordon, K., et al. 2011, ApJ, 737, 12. doi:10.1088/0004-637X/737/1/12
Leslie, S. K., Schinnerer, E., Liu, D., et al. 2020, ApJ, 899, 58. doi:10.3847/1538-4357/aba044
Lindroos, L., Knudsen, K. K., Vlemmings, W., et al. 2015, MNRAS, 446, 3502. doi:10.1093/mnras/stu2344
Lisenfeld, U., Xu, C. K., Gao, Y., et al. 2019, A&A, 627, A107. doi:10.1051/0004-6361/201935536
Liu, D., Daddi, E., Dickinson, M., et al. 2018, ApJ, 853, 172. doi:10.3847/1538-4357/aaa600
Liu, D., Schinnerer, E., Groves, B., et al. 2019, ApJ, 887, 235. doi:10.3847/1538-4357/ab578d
Liu, D., Lang, P., Magnelli, B., et al. 2019, ApJS, 244, 40. doi:10.3847/1538-4365/ab42da
Lotz, J. M., Primack, J., & Madau, P. 2004, AJ, 128, 163. doi:10.1086/421849
Lotz, J. M., Davis, M., Faber, S. M., et al. 2008, ApJ, 672, 177. doi:10.1086/523659doi:10.1111/j.1365-2966.2008.14004.x
Madau, P. & Dickinson, M. 2014, ARA&A, 52, 415. doi:10.1146/annurev-astro-081811-125615
Magdis, G. E., Daddi, E., Béthermin, M., et al. 2012, ApJ, 760, 6. doi:10.1088/0004-637X/760/1/6
Magnelli, B., Lutz, D., Saintonge, A., et al. 2014, A&A, 561, A86. doi:10.1051/0004-6361/201322217
Magnelli, B., Boogaard, L., Decarli, R., et al. 2020, ApJ, 892, 66. doi:10.3847/1538-4357/ab7897
Marchesi, S., Civano, F., Elvis, M., et al. 2016, ApJ, 817, 34. doi:10.3847/0004-637X/817/1/34
Matharu, J., Papovich, C., Simons, R. C., et al. 2022, ApJ, 937, 16. doi:10.3847/1538-4357/ac8471
Massey, R., Stoughton, C., Leauthaud, A., et al. 2010, MNRAS, 401, 371. doi:10.1111/j.1365-2966.2009.15638.x
McCracken, H. J., Milvang-Jensen, B., Dunlop, J., et al. 2012, A&A, 544, A156. doi:10.1051/0004-6361/201219507
McMullin J. P., Waters B., Schiebel D., Young W., Golap K., 2007, in Shaw R. A., Hill F., Bell D. J., eds, Astronomical Society of the Pacific Conference Series Vol. 376, Astronomical Data Analysis Software and Systems XVI. p. 127
Millard, J. S., Eales, S. A., Smith, M. W. L., et al. 2020, MNRAS, 494, 293. doi:10.1093/mnras/staa609
Mohan, N., & Rafferty, D. 2015, PyBDSF: Python Blob Detection and Source Finder, ascl:1502.007
Moreno, J., Torrey, P., Ellison, S. L., et al. 2019, MNRAS, 485, 1320. doi:10.1093/mnras/stz417
Murphy, E. J., Momjian, E., Condon, J. J., et al. 2017, ApJ, 839, 35. doi:10.3847/1538-4357/aa62fd
Neeleman, M., Kanekar, N., Prochaska, J. X., et al. 2017, Science, 355, 1285. doi:10.1126/science.aal1737
Nelson, E. J., van Dokkum, P. G., Förster Schreiber, N. M., et al. 2016, ApJ, 828, 27. doi:10.3847/0004-637X/828/1/27
Noeske, K. G., Weiner, B. J., Faber, S. M., et al. 2007, ApJ, 660, L43. doi:10.1086/517926
Novak, M., Smolčić, V., Delhaize, J., et al. 2017, A&A, 602, A5. doi:10.1051/0004-6361/201629436
Pan, H.-A., Lin, L., Hsieh, B.-C., et al. 2018, ApJ, 868, 132. doi:10.3847/1538-4357/aaeb92
Petersson, J., Renaud, F., Agertz, O., et al. 2023, MNRAS, 518, 3261. doi:10.1093/mnras/stac3136
Planck Collaboration, Ade, P. A. R., Aghanim, N., et al. 2016, A&A, 594, A13. doi:10.1051/0004-6361/201525830
Popesso, P., Morselli, L., Concas, A., et al. 2019, MNRAS, 490, 5285. doi:10.1093/mnras/stz2635
Popesso, P., Concas, A., Cresci, G., et al. 2022, MNRAS. doi:10.1093/mnras/stac3214
Popping, G., Pillepich, A., Calistro Rivera, G., et al. 2022, MNRAS, 510, 3321. doi:10.1093/mnras/stab3312
Porter, L. A., Somerville, R. S., Primack, J. R., et al. 2014, MNRAS, 444, 942. doi:10.1093/mnras/stu1434
Puglisi, A., Daddi, E., Liu, D., et al. 2019, ApJ, 877, L23. doi:10.3847/2041-8213/ab1f92
Puglisi, A., Daddi, E., Valentino, F., et al. 2021, MNRAS, 508, 5217. doi:10.1093/mnras/stab2914
Renaud, F., Bournaud, F., Kraljic, K., et al. 2014, MNRAS, 442, L33. doi:10.1093/mnrasl/slu050
Renaud, F., Segovia Otero, Á., & Agertz, O. 2022, MNRAS, 516, 4922. doi:10.1093/mnras/stac2557
Rodighiero, G., Daddi, E., Baronchelli, I., et al. 2011, ApJ, 739, L40. doi:10.1088/2041-8205/739/2/L40
Rodriguez-Gomez, V., Snyder, G. F., Lotz, J. M., et al. 2019, MNRAS, 483, 4140. doi:10.1093/mnras/sty3345
Rodriguez-Gomez, V., Lotz, J., & Snyder, G. 2022, Astrophysics Source Code Library. ascl:2201.010
Rujopakarn, W., Daddi, E., Rieke, G. H., et al. 2019, ApJ, 882, 107. doi:10.3847/1538-4357/ab3791
Santini, P., Maiolino, R., Magnelli, B., et al. 2014, A&A, 562, A30. doi:10.1051/0004-6361/201322835
Sargent, M. T., Béthermin, M., Daddi, E., et al. 2012, ApJ, 747, L31. doi:10.1088/2041-8205/747/2/L31
Sargent, M. T., Daddi, E., Béthermin, M., et al. 2014, ApJ, 793, 19. doi:10.1088/0004-637X/793/1/19
Schreiber, C., Pannella, M., Elbaz, D., et al. 2015, A&A, 575, A74. doi:10.1051/0004-6361/201425017
Scoville, N., Aussel, H., Sheth, K., et al. 2014, ApJ, 783, 84. doi:10.1088/0004-637X/783/2/84
Scoville, N., Sheth, K., Aussel, H., et al. 2016, ApJ, 820, 83. doi:10.3847/0004-637X/820/2/83
Scoville, N., Faisst, A., Weaver, J., et al. 2023, ApJ, 943, 82. doi:10.3847/1538-4357/aca1bc
Shen, S., Mo, H. J., White, S. D. M., et al. 2003, MNRAS, 343, 978. doi:10.1046/j.1365-8711.2003.06740.x
Silverman, J. D., Rujopakarn, W., Daddi, E., et al. 2018, ApJ, 867, 92. doi:10.3847/1538-4357/aae25e
Simpson, J. M., Smail, I., Swinbank, A. M., et al. 2015, ApJ, 799, 81. doi:10.1088/0004-637X/799/1/81
Sivasankaran, A., Blecha, L., Torrey, P., et al. 2022, MNRAS, 517, 4752. doi:10.1093/mnras/stac2759
Sparre, M. & Springel, V. 2016, MNRAS, 462, 2418. doi:10.1093/mnras/stw1793
Sparre, M., Whittingham, J., Damle, M., et al. 2022, MNRAS, 509, 2720. doi:10.1093/mnras/stab3171

Spilker, J. S., Bezanson, R., Weiner, B. J., et al. 2019, ApJ, 883, 81. doi:10.3847/1538-4357/ab3804
Springel, V., Di Matteo, T., & Hernquist, L. 2005, MNRAS, 361, 776. doi:10.1111/j.1365-2966.2005.09238.x
Stemo, A., Comerford, J. M., Barrows, R. S., et al. 2020, ApJ, 888, 78. doi:10.3847/1538-4357/ab5f66
Suess, K. A., Kriek, M., Price, S. H., et al. 2019, ApJ, 877, 103. doi:10.3847/1538-4357/ab1bda
Suess, K. A., Bezanson, R., Nelson, E. J., et al. 2022, ApJ, 937, L33. doi:10.3847/2041-8213/ac8e06
Suzuki, T. L., Onodera, M., Kodama, T., et al. 2021, ApJ, 908, 15. doi:10.3847/1538-4357/abd4e7
Szokoly, G. P., Bergeron, J., Hasinger, G., et al. 2004, ApJS, 155, 271. doi:10.1086/424707
Tacchella, S., Dekel, A., Carollo, C. M., et al. 2016, MNRAS, 457, 2790. doi:10.1093/mnras/stw131
Tacchella, S., Forbes, J. C., & Caplar, N. 2020, MNRAS, 497, 698. doi:10.1093/mnras/staa1838
Tacconi, L. J., Genzel, R., & Sternberg, A. 2020, ARA&A, 58, 157. doi:10.1146/annurev-astro-082812-141034
Tadaki, K.-. ichi ., Belli, S., Burkert, A., et al. 2020, ApJ, 901, 74. doi:10.3847/1538-4357/abaf4a
Teyssier, R., Chapon, D., & Bournaud, F. 2010, ApJ, 720, L149. doi:10.1088/2041-8205/720/2/L149
van der Wel, A., Franx, M., van Dokkum, P. G., et al. 2014, ApJ, 788, 28. doi:10.1088/0004-637X/788/1/28
Violino, G., Ellison, S. L., Sargent, M., et al. 2018, MNRAS, 476, 2591. doi:10.1093/mnras/sty345
Walter, F., Carilli, C., Neeleman, M., et al. 2020, ApJ, 902, 111. doi:10.3847/1538-4357/abb82e
Wang, T.-M., Magnelli, B., Schinnerer, E., et al. 2022, A&A, 660, A142. doi:10.1051/0004-6361/202142299
Weaver, J. R., Kauffmann, O., Shuntov, M., et al. 2021, A&A, 23721506W
Weston, M. E., McIntosh, D. H., Brodwin, M., et al. 2017, MNRAS, 464, 3882. doi:10.1093/mnras/stw2620
Wilkinson, C. L., Pimbblet, K. A., Stott, J. P., et al. 2018, MNRAS, 479, 758. doi:10.1093/mnras/sty1493
Williams, C. C., Spilker, J. S., Whitaker, K. E., et al. 2021, ApJ, 908, 54. doi:10.3847/1538-4357/abcbf6
Wilman, D. J., Fossati, M., Mendel, J. T., et al. 2020, ApJ, 892, 1. doi:10.3847/1538-4357/ab7914
Wuyts, S., Förster Schreiber, N. M., Lutz, D., et al. 2011, ApJ, 738, 106. doi:10.1088/0004-637X/738/1/106
Yu, Q., Fang, T., Feng, S., et al. 2022, ApJ, 934, 114. doi:10.3847/1538-4357/ac78e6
Zolotov, A., Dekel, A., Mandelker, N., et al. 2015, MNRAS, 450, 2327. doi:10.1093/mnras/stv740

List of Figures

List of Tables

Acknowledgements

I would like to thank my advisor, Prof. Dr. Frank Bertoldi, for his guidance in my work, conference presentations, and writing. He taught me how to organize my thoughts and express them fluently.

I thank Dr. Benjamin Magnelli for his daily guidance and support throughout my doctoral research. He regularly reviewed my work and provided invaluable comments that enabled me to successfully complete two first-author publications and this dissertation. From Benjamin, I learned not only how to conduct research, but also how to think logically.

I would like to thank Dr. Eva Schinnerer and Dr. Daizhong Liu for their assistance in commenting on my two first-author publications.

I am grateful to all my friends at AIfA, especially my officemate, Christos Karoumpis. I discussed scientific issues with Christos, and I shared many wonderful trips and memories with him.

I am deeply thankful for the support from my family. Every time I have been stuck with my work and felt depressed, their warm encouragement has helped me to move forward positively.

Finally, I am grateful for the financial support through the DFG Collaborative Research Centre 956, Project number 184018867.

Without all the assistance from these people, this thesis would not have been possible.